

INTO THE VOID:
SIMULATIONS OF PROTOSTELLAR JETS FROM KEPLERIAN DISCS
EXTENDED TO OBSERVATIONAL LENGTH SCALES

by

Jonathan Paul Ramsey

A thesis submitted to

Saint Mary's University, Halifax, Nova Scotia

in partial fulfillment of the requirements for the degree of

Doctor of Philosophy in Astronomy

July, 2011, Halifax, Nova Scotia

Copyright © Jonathan Paul Ramsey, 2011

Approved: _____
Dr. David A. Clarke
Supervisor

Approved: _____
Dr. Rob J. Thacker
Examiner

Approved: _____
Dr. Luigi C. Gallo
Examiner

Approved: _____
Dr. Tom W. Jones
External Examiner

Date: July 25, 2011



Library and Archives
Canada

Published Heritage
Branch

395 Wellington Street
Ottawa ON K1A 0N4
Canada

Bibliothèque et
Archives Canada

Direction du
Patrimoine de l'édition

395, rue Wellington
Ottawa ON K1A 0N4
Canada

Your file Votre référence
ISBN: 978-0-494-81006-4
Our file Notre référence
ISBN: 978-0-494-81006-4

NOTICE:

The author has granted a non-exclusive license allowing Library and Archives Canada to reproduce, publish, archive, preserve, conserve, communicate to the public by telecommunication or on the Internet, loan, distribute and sell theses worldwide, for commercial or non-commercial purposes, in microform, paper, electronic and/or any other formats.

The author retains copyright ownership and moral rights in this thesis. Neither the thesis nor substantial extracts from it may be printed or otherwise reproduced without the author's permission.

In compliance with the Canadian Privacy Act some supporting forms may have been removed from this thesis.

While these forms may be included in the document page count, their removal does not represent any loss of content from the thesis.

AVIS:

L'auteur a accordé une licence non exclusive permettant à la Bibliothèque et Archives Canada de reproduire, publier, archiver, sauvegarder, conserver, transmettre au public par télécommunication ou par l'Internet, prêter, distribuer et vendre des thèses partout dans le monde, à des fins commerciales ou autres, sur support microforme, papier, électronique et/ou autres formats.

L'auteur conserve la propriété du droit d'auteur et des droits moraux qui protègent cette thèse. Ni la thèse ni des extraits substantiels de celle-ci ne doivent être imprimés ou autrement reproduits sans son autorisation.

Conformément à la loi canadienne sur la protection de la vie privée, quelques formulaires secondaires ont été enlevés de cette thèse.

Bien que ces formulaires aient inclus dans la pagination, il n'y aura aucun contenu manquant.


Canada

Contents

| | |
|--|-------|
| Contents | ii |
| List of Figures | vi |
| List of Tables | xviii |
| Acknowledgments | xxi |
| Abstract | xxii |
| 1 Introduction | 1 |
| 1.1 Observational studies of protostellar jets | 1 |
| 1.2 Theoretical studies of protostellar jets | 7 |
| 1.3 Numerical studies of protostellar jets | 15 |
| 1.4 This work | 25 |
| 2 AZEuS: An Adaptive Zone Eulerian Scheme | 34 |
| 2.1 Introduction | 34 |
| 2.2 Preamble | 38 |
| 2.2.1 Underlying numerical method | 38 |
| 2.2.2 Conventions and Notation | 39 |
| 2.3 Restriction | 42 |
| 2.3.1 Conservative Overwrite | 43 |
| 2.3.2 Flux Corrections | 45 |

| | | |
|----------|--|------------|
| 2.4 | Prolongation | 50 |
| 2.4.1 | Spatial interpolation | 51 |
| 2.4.2 | Temporal interpolation | 57 |
| 2.4.3 | Monotonicity | 58 |
| 2.5 | Boundary conditions | 59 |
| 2.5.1 | Physical Boundaries | 60 |
| 2.5.2 | Adjacent Boundaries | 63 |
| 2.6 | Grid creation and adaptation | 65 |
| 2.7 | Numerical Tests | 67 |
| 2.7.1 | 1-D shock tubes | 67 |
| 2.7.2 | 2-D tests | 71 |
| 2.7.3 | A 3-D test: self-gravitational hydrodynamical collapse | 80 |
| 2.8 | Summary | 82 |
| 2.A | Curvilinear Coordinates | 83 |
| 2.A.1 | Restriction | 86 |
| 2.A.2 | Prolongation | 89 |
| 2.B | The Vector Potential | 93 |
| 2.C | Schematic overview of the AMR module | 97 |
| 3 | Simulating protostellar jets simultaneously at launching and observational scales | 101 |
| 3.1 | Introduction | 101 |
| 3.2 | Initialisation | 103 |
| 3.2.1 | The atmosphere | 104 |
| 3.2.2 | Boundary Conditions | 106 |
| 3.2.3 | Scaling Relations | 107 |
| 3.3 | Results for $\beta_1 = 40$ | 108 |

| | | |
|----------|---|------------|
| 3.4 | Comparing simulations and observations | 111 |
| 3.4.1 | Proper motion | 111 |
| 3.4.2 | Toroidal velocity | 114 |
| 3.4.3 | Jet radius and mass flux | 115 |
| 3.5 | Discussion | 115 |
| 4 | Additional results from simulations of protostellar jets | 118 |
| 4.1 | Introduction | 118 |
| 4.2 | Description of simulations | 120 |
| 4.2.1 | Simulation A: $\beta_i = 0.1$ | 121 |
| 4.2.2 | Simulation B: $\beta_i = 0.4$ | 127 |
| 4.2.3 | Simulation C: $\beta_i = 1.0$ | 132 |
| 4.2.4 | Simulation D: $\beta_i = 2.5$ | 132 |
| 4.2.5 | Simulation E: $\beta_i = 10$ | 136 |
| 4.2.6 | Simulation F: $\beta_i = 40$ | 137 |
| 4.2.7 | Simulation G: $\beta_i = 160$ | 139 |
| 4.2.8 | Simulation H: $\beta_i = 640$ | 140 |
| 4.2.9 | Qualitative trends | 143 |
| 4.3 | The “knot” generator | 149 |
| 4.4 | Numerical Challenges | 155 |
| 4.5 | The driving mechanism | 159 |
| 4.5.1 | Steady-state constants | 160 |
| 4.5.2 | Centrifugal versus magnetic mechanisms | 162 |
| 4.5.3 | Establishing a magnetic environment | 173 |
| 4.6 | Trends in B_i | 176 |
| 4.6.1 | Speeds | 176 |
| 4.6.2 | Jet Radii | 183 |

| | | |
|----------|---|------------|
| 4.6.3 | Fluxes | 185 |
| 4.7 | Linking simulations to observations | 194 |
| 4.7.1 | Comparisons with current observations | 194 |
| 4.7.2 | Comparisons with future observations | 197 |
| 4.8 | Discussion | 199 |
| 5 | Conclusions | 203 |
| | References | 208 |

List of Figures

- | | | |
|-----|---|----|
| 1.1 | False colour image of the HH 34 complex in the Orion nebula, obtained with the VLT. The HH34 jet is characterised by the narrow and bright red feature, seen slightly off-centre, and the two oppositely directed bow shocks. Blue corresponds to the visual B filter, green to $H\alpha$, and red to [SII]. Image credit: ESO. | 5 |
| 1.2 | Schematic representation of the magneto-centrifugal launching mechanism in cylindrical coordinates. Adapted from Spruit (1996). | 9 |
| 1.3 | Three characteristic profiles for a magnetic field line with footprint r_0 . See the text for descriptions of field lines A, B, and C. Adapted from Spruit (1996). | 10 |
| 1.4 | Figure 1 from “Magnetohydrodynamic simulations of outflows from accretion disks” (Ustyugova <i>et al.</i> 1995) demonstrating a jet launched from a disc as a boundary condition at the bottom edge of each frame. Poloidal velocity vectors (top) and contours of toroidal velocity (bottom) are plotted at different times. Also plotted are the fast magnetosonic surface (long dashed line), the Alfvén surface (dashed line), and slow magnetosonic surface (dot-dashed line). This figure is reproduced with kind permission of the original authors and the AAS. | 17 |

-
- 1.5 Results from “Numerical simulations of astrophysical jets from Keplerian disks. II. Episodic outflows” (Ouyed & Pudritz 1997b; Figure 2) showing episodic knot-like features. Twenty logarithmically spaced contours of density (left) and twenty linearly spaced contours of the toroidal magnetic field (right) are plotted at four different times. The disc as a boundary condition is on the left-hand side of each frame. This figure is reproduced with kind permission of the original authors and the AAS. 18
- 1.6 Results from one of the 3-D simulations of “Three-dimensional simulations of jets from Keplerian disks: self-regulatory stability” (Ouyed, Clarke, & Pudritz 2003; Figure 3). Shown are false colour representations of $\int \rho dl$ (top) and $\int (\nabla \cdot \vec{v}) dl$ (bottom). The disk is on the left-hand side of the image (not shown), and the jet propagates from left to right. This figure is reproduced with kind permission of the original authors and the AAS. . . . 23
- 1.7 False colour images of the HH 30 (top left), HH 34 (top right), and HH 47 jets (bottom) taken with the Hubble space telescope. HH 47 exhibits clear non-axisymmetric behaviour while HH 30 and HH34 appear more axisymmetric. The images were taken with WFPC2 in visible light, and the scales in the bottom left of each panel correspond to 1000 AU. Top left credit: J. Morse/STScI, and NASA. Top right credit: J. Hester (Arizona State University), the WFPC 2 Investigation Definition Team, and NASA. Bottom credit: C. Burrows (STScI & ESA), the WFPC 2 Investigation Definition Team, and NASA. 27
- 2.1 On a fully-staggered grid, scalars (ρ , e_T , e , p) are zone-centred, primitive vectors (\vec{v} , \vec{B}) are face-centred, and derived vectors ($\vec{E} = -\vec{v} \times \vec{B}$, $\vec{J} = \nabla \times \vec{B}$) are edge-centred. 36

| | | |
|-----|--|----|
| 2.2 | On a fully-staggered grid, all variables have two boundary values. In addition, for each direction, one component of a face-centred vector and two components of an edge-centred vector have one skin value. | 40 |
| 2.3 | The regions of influence (ROI) (shaded) for: (a) zone-centred variables, (b) face-centred and volume-conserved variables, and (c) face-centred and area-conserved variables. A refinement ratio of $\nu = 4$ is shown. | 41 |
| 2.4 | The different cases for flux corrections on a staggered grid, including: (a) zone-centred quantities; (b, c, and d) the three different cases for face-centred, volume-conserved momenta; and (e) area-conserved magnetic field corrections via the EMFs. Note that in this figure, all arrows correspond to components of fluxes or EMFs. | 46 |
| 2.5 | Schematic representation of the directionally unsplit Li & Li algorithm for calculating fine values of \vec{b} between coarse grid faces when $\nu = 4$ | 55 |
| 2.6 | A single coarse zone in the $z = 0$ boundary with zone centre at $r(J) = r$ and with refinement ratio of $\nu = 2$ | 61 |
| 2.7 | Two grids that originally abut (panel a) are made to overlap by at least one coarse zone (panel b). | 67 |
| 2.8 | Static grid solution to problem (4a) of RJ95 at time $t = 0.45$. The initial left and right states are $(\rho, v_1, v_2, v_3, B_2, B_3, p) = (1, 0, 0, 0, 1, 0, 1)$ and $(0.2, 0, 0, 0, 0, 0, 0.1)$, with $B_1 = 1$. From left to right, the physical features are: (1) fast rarefaction, (2) slow rarefaction, (3) contact discontinuity, (4) slow shock, and (5) “switch-on” shock. <i>Left panels:</i> uniform “fine” grid solution; <i>middle panels:</i> same solution with two fine, static grids (gray) overlying the coarse grid; <i>right panel:</i> percent difference between the uniform and static grid solutions. Solid lines are the analytical solutions from the Riemann solver described in RJ95. | 69 |

-
- 2.9 AZEuS solution to problem (2a) of RJ95 at $t = 0.20$. The initial left and right states are $(\rho, v_1, v_2, v_3, B_2, B_3, p) = (1.08, 1.2, 0.01, 0.5, 3.6/\sqrt{4\pi}, 2/\sqrt{4\pi}, 0.95)$ and $(1, 0, 0, 0, 4/\sqrt{4\pi}, 2/\sqrt{4\pi}, 1)$, with $B_1 = 2/\sqrt{4\pi}$. The physical features, from left to right, are: (1) fast shock, (2) rotational discontinuity, (3) slow shock, (4) contact discontinuity, (5) slow shock, (6) rotational discontinuity, and (7) fast shock. Shaded regions indicate the location of finer grids, with the level of shading indicating the level of refinement. $\Psi = \tan^{-1}(B_3/B_2)$ is the angle between the transverse field components. The solid lines are the analytical solution from the Riemann solver described in RJ95. 70
- 2.10 AZEuS solution for the 2-D MHD blast problem at $t = 0.02$ using 2 levels of refinement. *Top left:* gas pressure; *bottom left:* magnetic pressure ($p_B = |B|^2/2$); *top right:* gas density; and *bottom right:* distribution of AMR grids at $t = 0.02$ 72
- 2.11 Uniform and adaptive grid solutions for the Orszag-Tang MHD vortex at $t = 1/2$. Plotted are 20 evenly spaced contours of the gas pressure with range $[0.03, 0.50]$. *Top left:* uniform grid solution with 256^2 zones; *top right:* uniform grid solution with 512^2 zones; *bottom left:* AMR solution with a base grid resolution of 128^2 and 2 levels of refinement; and *bottom right:* distribution of grids at level 3 in the AMR solution. 75
- 2.12 1-D slices of the gas pressure at $t = 1/2$ and $y = 0.4277$ in the Orszag-Tang MHD vortex problem. From top to bottom, uniform 256^2 grid, uniform 512^2 grid, AMR solution with 2 levels of refinement and an effective resolution of 512^2 zones. 76

-
- 2.13 The “beard of AZEuS”: Results of MHD accretion torus simulations in (r, ϑ) coordinates at $t = 300$, where the vertical axis is the rotation axis. Plotted are contours of poloidal magnetic field (left) and logarithmic density (right). Top panels are for the uniform grid, bottom panels the AMR solution with one level of refinement. Borders of the adaptive grids are shown with black lines. 79
- 2.14 AZEuS results for the Truelove problem with a 10% amplitude perturbation at $t = 0.598133 = 1.215t_{\text{ff}}$, where t_{ff} is the free-fall time. *Left*: Equatorial x_1 - x_2 slice of logarithmic density with velocity vectors over-plotted. The highest resolution shown here is R_{8192} . *Right*: Equatorial x_1 - x_2 slice of logarithmic density of the upper fragment. The highest resolution in this plot is R_{32768} ; there is one additional level of refinement not shown. Black lines denote the borders of AMR grids and the units of density are g cm^{-3} . For each panel, 20 evenly spaced contours are plotted with ranges $\log \rho = [-16.10, -9.905]$ (left) and $[-14.30, -9.604]$ (right). 82
- 2.15 The effects of differencing a parabolic interpolation of \vec{A} twice to calculate $\vec{J} \times \vec{B}$ forces. Left panel: the solution immediately before a grid adaptation step. Right panel: the solution a few time steps after. Plotted are 20 evenly spaced contours of the toroidal magnetic field (top) and velocity divergence (bottom) with ranges $B_\varphi = [-0.035, 0.0]$ and $\nabla \cdot \vec{v} = [-0.15, 0.15]$, respectively. 97
- 3.1 Nested images of a $\beta_i = 40$ jet at $t = 100$ yr. Colours indicate temperature, white contours magnetic field lines, maroon contours the slow surface, and arrows the velocity. Dashed lines denote grid boundaries, and $x_1 = z$, $x_2 = r$. 109

-
- 3.2 (a) $\langle\beta\rangle$ as a function of time for different β_i . (b) v_{jet} (diamonds) and $\langle v_\varphi\rangle$ (triangles) of each jet as a function of B_i . Best fit power-law coefficients for these data are $\alpha = 0.44 \pm 0.01$ (v_{jet} , solid line) and 0.66 ± 0.01 ($\langle v_\varphi\rangle$, dashed line). 112
- 4.1 Nested images of simulation A at $t = 42.37$ yr. Colours indicate temperature, white contours magnetic field lines, black contours the slow magnetosonic surface, and arrows the poloidal velocity. Dashed lines indicate grid boundaries. The dimensions of the top panel are $z = x_1 \in [0, 4096]$ AU and $r = x_2 \in [0, 256]$ AU. 123
- 4.2 A radial slice from simulation A at $z = 100$ AU and $t = 42.37$ yr. Plotted on the left are, from top to bottom, logarithmic density, poloidal velocity, and poloidal magnetic field. Plotted on the right, from top to bottom, are logarithmic temperature, toroidal velocity, and toroidal field. Successively darker shading indicates a higher level of refinement; no shading corresponds to level $l = 2$. The highest resolution available at this height above the disc is level $l = 4$ 124
- 4.3 A radial slice from simulation A at $z = 1000$ AU and $t = 42.37$ yr. Plotted on the left are, from top to bottom, logarithmic density, poloidal velocity, poloidal field, and the z -component of the magnetic field. Plotted on the right, from top to bottom, are logarithmic temperature, toroidal velocity, and toroidal field, and logarithmic β . At this height above the disc, the highest resolution data available is at level $l = 1$ 126
- 4.4 Nested images of simulation B at $t = 60.53$ yr. See Figure 4.1 for a description of the plotted quantities. The dimensions of the top panel are $z \in [0, 4096]$ AU and $r \in [0, 256]$ AU. 130

-
- 4.5 An axial slice through simulation B at $r = 1.0$ AU showing the structure of the knots. Plotted on the left, from top to bottom, are logarithmic density, poloidal velocity, poloidal field, slow magnetosonic Mach number, and Alfvénic Mach number. Plotted on the right, from top to bottom, are logarithmic temperature, toroidal velocity, toroidal field, logarithmic β , and fast magnetosonic Mach number. Successively darker shading indicates a higher level of refinement; no shading corresponds to level $l = 4$ 131
- 4.6 Nested images of simulation C at $t = 74.92$ yr. See Figure 4.1 for a description of the plotted quantities. The dimensions of the top panel are $z \in [0, 4096]$ AU and $r \in [0, 256]$ AU. 133
- 4.7 Nested images of simulation D at $t = 92.68$ yr. See Figure 4.1 for a description of the plotted quantities. Note that the contour levels for this Figure (and subsequent Figures) have changed from Figure 4.6. The dimensions of the top panel are $z \in [0, 4096]$ AU and $r \in [0, 256]$ AU. 135
- 4.8 A radial cut at $z = 3.9$ AU and levels $l = 8, 9$ from simulation D. Plotted on the top are logarithmic density and temperature, and on the bottom, the z and r -components of velocity. The two knots can be seen distinctly in the density and temperature. 136
- 4.9 Nested images of simulation E at $t = 100$ yr. See Figure 4.1 for a description of the plotted quantities. 138
- 4.10 A representative example of knot production in simulation E at $t = 60.29$ yr. Temperature is plotted in colour, the slow magnetosonic surface with black contours, magnetic field lines in white, and arrows denote the poloidal velocity. 139
- 4.11 Nested images of simulation G at $t = 76.18$ yr. See Figure 4.1 for a description of the plotted quantities. 141

-
- 4.12 Nested images of simulation H at $t = 100$ yr. See Figure 4.1 for a description of the plotted quantities. 142
- 4.13 A radial slice from simulation H at $t = 100$ yr. Plotted on the left, from top to bottom, are the logarithmic density, poloidal velocity, poloidal magnetic field, and fast magnetosonic Mach number. Plotted on the right, from top to bottom, are the logarithmic temperature, toroidal velocity, toroidal field, and logarithmic β 144
- 4.14 Two snapshots in time from simulation H. On the left, before an eruption event. On the right, immediately after. β is plotted in colour, magnetic field lines in white, and velocity vectors in black. 145
- 4.15 Images of the knot-like structures observed in simulations A – H on the highest resolution grid. Simulations A – D are arranged from top to bottom on the left, and simulations E – H are similarly arranged on the right. Colour contours denote the temperature, white the plasma- β surface, and black the Alfvénic Mach surface. The dimensions of each panel are $z \in [0, 4]$, $r \in [0, 1]$ AU. Unlike Figures 4.1 – 4.12, all panels use the same temperature scale. 146
- 4.16 The toroidal velocity, v_ϕ , in simulations A – H (top to bottom), plotted when they reach a height of 1000 AU above the disc. Black contours denote the fast magnetosonic surface ($M_f = 1$). All plots have dimensions $z \in [0, 1025]$, $r \in [0, 110]$ AU. 147
- 4.17 The poloidal velocity, v_p , in simulations A – H (top to bottom), plotted at simulation time $t = 42.65$ yr. Black contours denote the fast magnetosonic surface ($M_f = 1$). All plots have dimensions $z \in [0, 4070]$, $r \in [0, 245]$ AU. 148

-
- 4.18 The knot generator in the “on” position. Top left panel: plasma- β is plotted in colour, the slow Mach surface in black, and velocity vectors in white. Bottom left panel: the z -component of the velocity is plotted in colour, magnetic field lines in black, and the net poloidal acceleration vectors in white. Top and middle right panels: the launching angle θ and the poloidal velocity, just above the disc surface at $z = 0.01$ AU, as a function of radius. Bottom right panel: The net radial acceleration at the location of the knot generator ($z \simeq 0.04$ AU). The dashed red line denotes the inner disc radius $r_i = 0.05$ AU. 150
- 4.19 Knot generator in the “off” position. See Figure 4.18 for a description of the plotted variables. 151
- 4.20 Two successive snapshots in time illustrating the numerical instability due to insufficient resolution of gradients in B_φ . From top to bottom, plotted are contours of velocity divergence, temperature, and toroidal magnetic field. The instability leads to the localised explosion observed at $z \simeq 184$ AU. 156
- 4.21 An axial slice from simulation F at $z = 0.1$ AU and level $l = 9$. Plotted are logarithmic density (left) and Alfvén speed (right). The highest Alfvén speeds correspond to regions between knots. 158

-
- 4.22 The different speeds and fractional variations of the steady-state constants along a field line anchored at $r_0 \simeq 1.0$ AU in simulation A. In the left panel, v_p is the poloidal velocity, v_φ is the toroidal velocity, $a_{A,p}$ is the (poloidal) Alfvén speed, $a_{A,\varphi}$ is the toroidal Alfvén speed, a_f is the fast magnetosonic speed, and $v_{\text{esc}} = \sqrt{2GM/r_0}$ is the local escape speed for footprint r_0 . The triangle (square) denotes the location of the Alfvén (fast) point. Plotted in the right panel are the fractional variations of the steady-state constants from their analytical values: η is the mass load, Ω is the field line rotation rate, L is the angular momentum constant, and E is the energy constant (equations 4.6 – 4.9). These data are taken at $t = 42.95$ yr, but do not strongly vary in time. 163
- 4.23 A representative example of a field line from simulation A which is *not* in steady-state ($r_0 \simeq 0.20$ AU). Note the difference in scale of the right panel relative to Figure 4.22. For a description of plotted quantities, see the caption of Figure 4.22. 164
- 4.24 Various speeds and fractional variation of the steady-state constants along a field line with footprint at $r_0 \simeq 1.0$ AU from simulation B. See Figure 4.22 for additional information. 165
- 4.25 Various speeds and fractional variation of the steady-state constants along a field line with footprint at $r_0 \simeq 1.0$ AU from simulation C. See Figure 4.22 for additional information. 165
- 4.26 Various speeds and fractional variation of the steady-state constants along a field line with footprint at $r_0 \simeq 1.0$ AU from simulation D. See Figure 4.22 for additional information. 166
- 4.27 Various speeds and fractional variation of the steady-state constants along a field line with footprint at $r_0 \simeq 1.0$ AU from simulation E. See Figure 4.22 for additional information. 166

| | | |
|------|---|-----|
| 4.28 | Various speeds and fractional variation of the steady-state constants along a field line with footprint at $r_0 \simeq 1.0$ AU from simulation F. See Figure 4.22 for additional information. | 167 |
| 4.29 | Various speeds and fractional variation of the steady-state constants along a field line with footprint at $r_0 \simeq 1.0$ AU from simulation G. See Figure 4.22 for additional information. | 167 |
| 4.30 | Various speeds and fractional variation of the steady-state constants along a field line with footprint at $r_0 \simeq 1.0$ AU from simulation H. See Figure 4.22 for additional information. This field line is clearly <i>not</i> in steady-state, and is only included for completeness. | 168 |
| 4.31 | $ B_\varphi /B_p$ as a function of radius just above the disc surface in each simulation. The data are taken at the end of the simulations (t_{end}). | 170 |
| 4.32 | The net acceleration (black) and poloidal Lorentz acceleration (red) along a field line with foot print $r_0 \simeq 1.0$ AU for simulations A and G (left and right panels, respectively). The Alfvén and fast points are denoted by dashed lines, and 1% of the maximum acceleration is denoted by the green dash-dot line. | 173 |
| 4.33 | Different measures of plasma- β as a function of time. Top left panel: $\langle\beta_p\rangle = 8\pi\langle p\rangle/\langle B_p^2\rangle$ (poloidal). Top right panel: $\langle\beta_\varphi\rangle = 8\pi\langle p\rangle/\langle B_\varphi^2\rangle$ (toroidal). Bottom left panel: an updated version of Figure 3.2a for $\langle\beta_T\rangle = 8\pi\langle p\rangle/\langle B^2\rangle$ (total). Bottom right panel: a close-up of simulation G showing its asymptotic approach to $\langle\beta_T\rangle = 1$ | 174 |
| 4.34 | The ratio $ B_\varphi /B_p$ in simulations A – H (top to bottom), all plotted when they reach a height of 1000 AU above the disc. Black contours denote where $ B_\varphi /B_p = 1$. All plots have dimensions $z \in [0, 1025]$, $r \in [0, 110]$ AU. . . . | 180 |

| | | |
|------|---|-----|
| 4.35 | The height of the jet bow shock (z_{jet}) above the disc as a function of time and β_i . The proper motions of Figure 3.2b and Tables 3.2 & 4.4 are determined from the asymptotic slope of these data. | 182 |
| 4.36 | Top panel: the maximum jet radius r_{jet} as a function of time for simulations A – G. Simulation H is excluded for reasons already discussed. Bottom panel: the maximum jet radius at select times as a function of B_i . The uncertainty for each measurement of r_{jet} is ± 1.6 AU, which is the resolution of the grid from whence these data were extracted. This is also the cause of the step-like appearance of the curves in the top panel. | 184 |
| 4.37 | Plot of mass, momentum, kinetic energy, and angular momentum flux for simulation A as a function of time at different heights above the disc. A boxcar average width of $\simeq 0.09$ yr has been applied to the data to smooth over short-period fluctuations which can obscure the overall trends. The kinetic energy flux was smoothed with a width of $\simeq 0.21$ yr. | 186 |
| 4.38 | The same as Figure 4.37, but for simulation B. | 187 |
| 4.39 | The same as Figure 4.37, but for simulation C. | 188 |
| 4.40 | The same as Figure 4.37, but for simulation D. | 189 |
| 4.41 | The same as Figure 4.37, but for simulation E. | 191 |
| 4.42 | The same as Figure 4.37, but for simulation F. | 192 |
| 4.43 | The same as Figure 4.37, but for simulation G. | 193 |
| 4.44 | The same as Figure 4.37, but for simulation H. | 195 |

List of Tables

| | | |
|-----|--|-----|
| 1.1 | A summary of observed characteristics of protostellar jets. | 6 |
| 1.2 | Several properties from simulations of protostellar jets launched from a disc as a boundary condition. | 25 |
| 2.1 | Extrema for density, ρ , gas pressure, p , and magnetic pressure, p_B , in AMR and uniform grid solutions of the 2-D MHD blast problem at $t = 0.02$ | 73 |
| 2.2 | The metric scaling factors in AZEuS for Cartesian, cylindrical, and spherical polar coordinates. | 84 |
| 3.1 | Selected observational characteristics of protostellar jets. References: Reipurth & Bally (2001), Ray <i>et al.</i> (2007), McKee & Ostriker (2007). | 111 |
| 3.2 | Simulation “observables” v_{jet} and $\langle v_\phi \rangle$ are asymptotic values while r_{jet} and \dot{M}_{jet} are measured at $z = 200$ AU and $t = 20$ yr. Uncertainties in α are from the fitting procedure. | 114 |
| 4.1 | Initial static grid set up for these simulations. The zones are everywhere uniform in shape (<i>i.e.</i> , $\Delta z = \Delta r$). | 119 |
| 4.2 | Summary of simulation times. The simulation end time, t_{end} , denotes when the jet leaves the computational domain or $t = 100$ yr, whichever comes first. | 120 |
| 4.3 | The measured and calculated periods, and the measured slow magnetosonic speed, of the knot generator, as a function of B_i . Individual knots are not produced for in simulations A, G, and H. The estimated average relative uncertainty in $\tau_{\text{knot,obs}}$ and a_s is $\sim 20\%$ | 154 |

| | | |
|------|---|-----|
| 4.4 | The different velocities measured in simulations A – G. More detailed explanations are given in the text; see also Section 3.4.1. Although I have included simulation H results in the table, this simulation does not follow the same trends as the others, and I have elected to leave it out of the power-law fits. | 178 |
| 4.5 | The variation of α in $r_{\text{jet,max}} \propto B_i^\alpha$ as a function of time. The last time slice is at $t = 40$ yr because the simulation A jet leaves the domain shortly thereafter. | 186 |
| 4.6 | Time-averaged mass $\langle \dot{M} \rangle$ ($10^{-6} M_\odot \text{yr}^{-1}$), momentum $\langle \dot{S} \rangle$ ($10^{-4} M_\odot \text{yr}^{-1} \text{km s}^{-1}$), kinetic energy $\langle \dot{K} \rangle$ ($10^{33} \text{erg s}^{-1}$), and angular momentum fluxes $\langle \dot{L} \rangle$ ($10^{-3} M_\odot \text{yr}^{-1} \text{AU km s}$ with power-law fits α , measured at $z = 100$ AU above the disc for the different values of β_i . The data for simulation H is included in the table for completeness, but is excluded from the power-law fits (see Table 4.4). . . . | 190 |
| 4.7 | The same as Table 4.6, but measured at $z = 200$ AU above the disc. $\langle \dot{M} \rangle$ has units of $10^{-6} M_\odot \text{yr}^{-1}$, $\langle \dot{S} \rangle$ units of $10^{-4} M_\odot \text{yr}^{-1} \text{km s}^{-1}$, $\langle \dot{K} \rangle$ units of $10^{33} \text{erg s}^{-1}$, and $\langle \dot{L} \rangle$ units of $10^{-3} M_\odot \text{yr}^{-1} \text{AU km s}^{-1}$ | 194 |
| 4.8 | The same as Table 4.6, but measured at $z = 500$ AU above the disc. $\langle \dot{M} \rangle$ has units of $10^{-6} M_\odot \text{yr}^{-1}$, $\langle \dot{S} \rangle$ units of $10^{-4} M_\odot \text{yr}^{-1} \text{km s}^{-1}$, $\langle \dot{K} \rangle$ units of $10^{33} \text{erg s}^{-1}$, and $\langle \dot{L} \rangle$ units of $10^{-3} M_\odot \text{yr}^{-1} \text{AU km s}^{-1}$ | 194 |
| 4.9 | The same as Table 4.6, but measured at $z = 1000$ AU above the disc. Due to fluxes from simulations G and H barely registering at 1000 AU above the disc, we exclude this data from the fits for this height only. $\langle \dot{M} \rangle$ has units of $10^{-6} M_\odot \text{yr}^{-1}$, $\langle \dot{S} \rangle$ units of $10^{-4} M_\odot \text{yr}^{-1} \text{km s}^{-1}$, $\langle \dot{K} \rangle$ units of $10^{33} \text{erg s}^{-1}$, and $\langle \dot{L} \rangle$ units of $10^{-3} M_\odot \text{yr}^{-1} \text{AU km s}^{-1}$ | 196 |
| 4.10 | A review of selected observational characteristics of protostellar jets. | 196 |

| | |
|---|-----|
| 4.11 The ranges of fluxes in the simulations A – H. We have ignored fluxes from simulation G and H at $z = 1000$ AU in determining these values; see Table 4.9. | 197 |
|---|-----|

Acknowledgements

I would like to thank Marsha Berger for providing us with her AMR subroutines, and Sasha Men'shchikov for early work on AZEuS. Use of MPFIT by C. B. Markwardt for curve fitting, and JETGET by J. Staff, M. A. S. G. Jørgenson, and R. Ouyed for integrating along field lines, is acknowledged. This work was supported by the Natural Sciences and Engineering Research Council of Canada (NSERC) and Saint Mary's University. Computing resources were provided by ACEnet, which is funded by the Canadian Fund for Innovation (CFI), the Atlantic Canada Opportunities Agency (ACOA), and the provinces of Nova Scotia, Newfoundland & Labrador, and New Brunswick.

Thank you to Dr. David Clarke for the years of support, guidance, generosity, and seemingly endless patience with me as I worked through this project. Thanks also must go to my fellow graduate students, in no particular order: Ashley, Steve, Catherine, Mina, Chris, Aaron, Tomomi, Andy, Kathleen, Bobby, Dave, Mike, James, Michael, Chris, Jason, Larkin, Liz, Dan (especially Dan!), Jon, Nick, Anneya, and even Diego. Indeed, thank you to all of the members of the Department of Astronomy & Physics during my time at Saint Mary's. The atmosphere was always friendly, positive, and social, and I consider myself very lucky to be given such a great environment to study and work in.

Thank you to my wife and best friend, Andrea, for taking care of me during the writing of this thesis, and for being patient and understanding with me. I am not sure what I would have done without you. Thank you to my parents and siblings for your support over the years, and to my Mother-in-law for her kindness and generosity. Thanks to Ingram for keeping me company, and for forcing me to take breaks even when I did not want to. Last but not least, thanks to Caffeine: you've been a good friend.

Abstract

INTO THE VOID:

SIMULATIONS OF PROTOSTELLAR JETS FROM KEPLERIAN DISCS

EXTENDED TO OBSERVATIONAL LENGTH SCALES

by

Jonathan Paul Ramsey

In this work, I present the first simulations to investigate the formation and propagation of protostellar jets that simultaneously include the launching mechanism at < 0.1 AU and the much larger observational length scales at $> 10^3$ AU. This is accomplished through the development and application of AZEuS, a new adaptive mesh refinement (AMR) version of the *ZEUS-3D* magnetohydrodynamics (MHD) fluid code. AMR has been adapted for a fully-staggered mesh, and a description of the methods employed is given. By simulating protostellar jets over 5 orders of magnitude in length, I find relationships between conditions at the disc surface and observable quantities such as jet proper motion, rotational velocity, jet radius, and mass, momentum, kinetic energy, and angular momentum fluxes. I also find that two mechanisms for jet launching are required to understand the simulation results. For strong fields, the traditional magneto-centrifugal mechanism is applicable, while for weak fields, the jet is accelerated by gradients in toroidal magnetic pressure. The jets presented here establish a magnetically-dominated region early in their evolution, regardless of the initial magnetic field strength, implying that plasma- $\beta < 1$ is required for jet launching to occur. Over time, the plasma- $\beta \rightarrow 1$, and the jets approach equipartition between thermal pressure and magnetic forces. These results demonstrate that outflows launched magnetically from discs are capable, by themselves, of producing realistic protostellar jets.

July 25, 2011

Chapter 1

Introduction

1.1 Observational studies of protostellar jets

It has been more than 50 years since the initial discovery of Herbig-Haro (HH) objects, small nebulae with characteristic optical emission, found in or around regions of star formation (Herbig 1950, 1951; Haro 1952, 1953). While these objects were originally believed to be reflection nebulae, or even the sites of active star formation, by the late 1970s it was becoming clear they were instead the optical manifestations of low-excitation shocks (see the review of Schwartz 1983). Then, in the early 1980s, CO measurements of L1551 IRS 5 by Snell *et al.* (1980) revealed oppositely directed blue- and red-shifted lobes, inside which HH objects were embedded. These authors subsequently proposed a model whereby HH objects are produced inside a bipolar outflow which has itself been ejected from an obscured young star and accretion disc. It did not take long for additional observations of well-collimated bipolar outflows in regions of star formation to appear (*e.g.*, Mundt *et al.* 1983; Mundt & Fried 1983; Mundt *et al.* 1984), further lending support to the outflow model.

At around the same time, radio emission at centimetre wavelengths was detected from HH objects 1 and 2, as well as from an optically invisible source lying in between (Pravdo *et al.* 1985). The spectral power index of the invisible central source is consistent

with an ionised stellar wind, again pointing towards an outflow origin for HH objects. Similar radio jets, explainable by thermal free-free emission, have since been discovered in numerous other bipolar outflows (*e.g.*, Anglada *et al.* 1998).

In the mid-1990s, through the increasing availability of wide-field and high resolution CCDs, it was discovered that a number of protostellar jets were associated with HH objects at *much* larger length scales than previously believed (*e.g.*, Bally & Devine 1994). Several of these so-called giant HH outflows have since been observed stretching over several *parsecs*, leaving their parent molecular cores, and injecting energy and momentum into the interclump medium (*e.g.*, Reipurth *et al.* 1997b). In fact, more recent studies of giant outflows imply that the amount of energy and momentum deposited can actually maintain the supersonic turbulence observed in molecular clouds (*e.g.*, Quillen *et al.* 2005).

The influence of protostellar outflows is not limited to the parent core or cloud: they also have a profound influence on the chemistry of the surrounding medium by destroying dust grains, dissociating molecules, and generally injecting thermal energy via shock heating. Moreover, they strongly affect the accretion disc and young star from whence they are launched by extracting mass and angular momentum. This link with the accretion disc is of particular importance because it relates the properties of the jet to conditions near the disc, as well as to the accretion history of the central driving object.

Further adding to the importance of protostellar outflows is the frequency with which they are observed: Reipurth (1999) has catalogued 600 HH objects, while Wu *et al.* (2004) lists almost 400 molecular outflows. Indeed, jets and outflows are observed not only in

regions of star formation, but in a wide range of other astrophysical settings, from brown dwarfs to X-ray binaries to active galactic nuclei (Livio 2009).

Although observations tell us a great deal about protostellar outflows, there are a few areas wherein they encounter difficulties. For example, observed opening angles of protostellar jets imply the launching region is < 5 AU in size (Ray *et al.* 2007). Ignoring for the moment that the majority of protostars and accretion discs are obscured by a thick layer of dust and gas, 5 AU is still smaller than the finest resolution possible for the nearest star formation regions with current telescope technology. In fact, only recently have observations begun to routinely probe length scales below 100 AU (*e.g.*, Hartigan, Edwards, & Pierson 2004, Coffey *et al.* 2008).

It has also proven difficult to observe definitively the presence of rotation in protostellar jets, a critical measurement if one wishes to determine the angular momentum transported by a jet. While radial velocity gradients across jets are observed to be in the $5\text{--}25 \pm 5$ km s⁻¹ range (*e.g.*, Woitas *et al.* 2005), and it is becoming generally accepted that protostellar jets do rotate, these asymmetries can be explained away by other phenomena, such as an interaction between the jet and a warped disc (Soker 2005), or magnetohydrodynamic shocks in a helical field (Fendt 2011).

The detection of magnetic fields in protostellar outflows is another area in which observations continue to experience difficulty. While there are a number of observations of circular polarisation in protostellar jets (*e.g.*, Chrysostomou *et al.* 2007) which give clues to the magnetic field structure, to date there are only two actual measurements of field strengths in a protostellar jet. The first comes from non-thermal cyclotron radio

emission in T Tauri S (\sim a few Gauss; Ray *et al.* 1997), and the second is from polarised synchrotron emission in HH 80-81 (\sim 0.2 mG; Carrasco-González *et al.* 2010). As discussed below, the most successful theoretical models for protostellar outflows require magnetic fields, and to test these models, additional measurements of field strengths are needed.

Application of the ‘BE’ technique (Bacciotti & Eisloffel 1999) shows that the ionisation fraction (the ratio between electron and total number densities) in the outflow varies between 0.03 – 0.6, with the highest values concentrated near the jet base (Ray *et al.* 2007). While strong magnetic fields have been observed in the inner regions of protostellar discs (\sim kG strengths; *e.g.*, Donati *et al.* 2005), the lack of magnetic field measurements in protostellar jets implies that, although the jet may be driven by strong magnetic fields near the central star, on larger scales these fields are weak and no longer dynamically important (Hartigan *et al.* 2007).

Figure 1.1 shows a false colour image of HH 34, a well-known giant outflow in the Orion nebula which is nearly 3 pc in length (Reipurth *et al.* 2002). This object displays many of the characteristic features of a typical protostellar jet including a high degree of collimation (\sim 0.4° opening angle), large flow speeds (\lesssim 200 km s⁻¹) along its length, strong emission in forbidden lines (*e.g.*, [SII]), episodic “knots” in emission along the jet length, a strongly axisymmetric appearance, and two oppositely directed bow shocks far ($>$ 40000 AU) from the central source (Reipurth *et al.* 2002). The central source itself is obscured behind a thick torus of dust and gas, and invisible at optical wavelengths, thus limiting the information we have on both the protostar and the physical mechanism producing the jet.

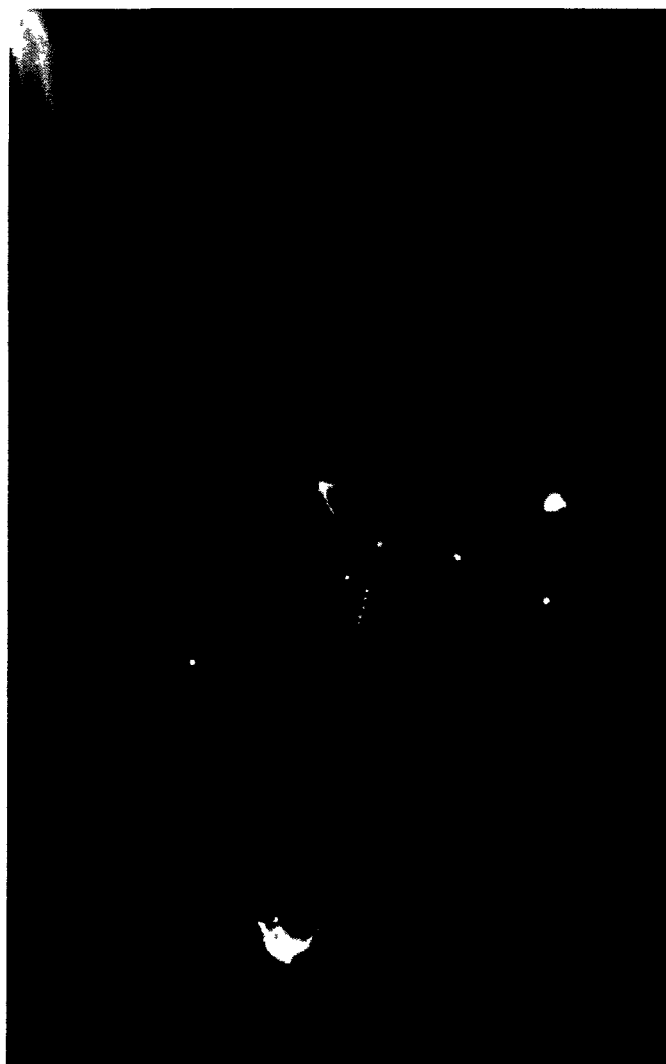


Figure 1.1 False colour image of the HH 34 complex in the Orion nebula, obtained with the VLT. The HH34 jet is characterised by the narrow and bright red feature, seen slightly off-centre, and the two oppositely directed bow shocks. Blue corresponds to the visual B filter, green to $H\alpha$, and red to [SII]. Image credit: ESO.

The emission observed in protostellar jets is typically dominated by line emission from atomic Hydrogen (*e.g.*, $H\alpha$; green in Figure 1.1) and forbidden transitions in atoms such as Oxygen (*e.g.*, [OIII]), Sulfur (*e.g.*, [SII]; red in Figure 1.1), and others. Molecular

emission is also commonly observed around outflows (*e.g.*, rotational transitions of CO), primarily in material which has been entrained by a fast-moving jet such as HH 34 (see Arce *et al.* 2007 for a review).

Together, line and molecular emission provide a wealth of information on protostellar jets and the surrounding conditions into which the jet propagates. From this information, characteristic properties of protostellar jets can be derived. These include the mass-loss rate, the ionisation fraction, and the total gas density, among others. Summarised in Table 1.1, these general characteristics furnish us with most of the information necessary to develop physical models for protostellar jets, the topic I turn to now.

| | |
|---|--|
| proper motion (km s^{-1}) | 100 – 200 (500 max.) |
| rotational velocity (km s^{-1}) | $(5 - 25) \pm 5$ |
| FWHM jet width (AU) | 30 – 80 (at 200 AU) |
| mass-loss rate ($M_{\odot} \text{ yr}^{-1}$) | 10^{-6} – 10^{-5} |
| momentum fluxes ($M_{\odot} \text{ yr}^{-1} \text{ km s}^{-1}$) | 10^{-5} |
| angular momentum fluxes ($M_{\odot} \text{ yr}^{-1} \text{ AU km s}^{-1}$) | 10^{-6} – 10^{-5} |
| mechanical luminosity (erg s^{-1}) | $(2.7 - 16) \times 10^{33}$ |
| $\dot{M}_{\text{jet}}/\dot{M}_{\text{acc}}$ | 0.05 – 0.1 |
| opening angles | 20 – 30° inside 50 AU \lesssim few ° beyond 50 AU |
| ionisation fraction | 0.03 – 0.6; decreasing along jet |
| total density, n_H | up to 10^6 cm^{-3} |
| jet overpressure factor | $10^2 - 10^4 \times$ the ambient |

Table 1.1 A summary of observed characteristics of protostellar jets.

References. — Hartigan, Morse, & Raymond (1994); Reipurth & Bally (2001); Podio *et al.* (2006); McKee & Ostriker (2007); Ray *et al.* (2007); Coffey *et al.* (2008, 2011).

1.2 Theoretical studies of protostellar jets

There are several theoretical models in the literature which can, at least partially, account for the properties of observed protostellar outflows. However, those which employ magnetic fields and accretion discs have, by far, been the most successful. Indeed, accretion discs coupled to magnetic fields are now argued by some to be the common mechanism producing most, if not all, types of astrophysical jets (*e.g.*, Livio 2009).

Two models which have received serious attention, but that have fallen out of favour, are purely hydrodynamical and radiation pressure-driven jets. Hydrodynamical models have demonstrated that an infalling envelope of gas can form a nozzle and collimate a wind (*e.g.*, Delamarter *et al.* 2000), but the base wind must be weak in order to reach the high degree of collimation observed in protostellar jets. Further, hydrodynamical models do not treat the underlying mechanism, but instead rely on an already existing wind.

Radiation pressure is expected to play an important role in outflows from massive and luminous central stars. For low-luminosity sources however, around which collimated protostellar outflows are commonly observed, the momentum contained in the outflow is $\sim 100\times$ greater than the momentum provided by the radiation pressure (Lada 1985), and purely radiative models can be ruled out.

Theories of magnetically-powered winds date back to the work of Schatzman (1962), Weber & Davis (1967), and Mestel (1968) in the context of stellar winds. An important result of these studies was that magnetic winds can remove a significant amount of angular momentum from a rotating star. Michel (1969) further demonstrated that, with regard to pulsars, magnetic fields can also power a high speed outflow. Applying

these ideas to accretion discs around black holes, Bisnovatyi-Kogan & Ruzmaikin (1976), Lovelace (1976), and Blandford (1976) almost simultaneously proposed that discs could also launch a magnetic outflow, carrying with it energy and angular momentum. It was not until Blandford & Payne (1982; BP82), however, that self-similar quantitative models of “magneto-centrifugal” disc winds became available. This seminal study demonstrated that magnetic field lines which make an angle of less than 60° with the surface of a cold accretion disc will launch an outflow parallel to the disc rotation axis. The usefulness of this mechanism lies in its ability to convert the gravitational potential energy of disc material into kinetic energy of a wind, removing significant amounts of angular momentum along magnetic field lines, and thus increasing the rate at which matter can accrete onto the central object. While BP82 focused on jets in the extragalactic context, it was Pudritz & Norman (1983), however, who first proposed that a magneto-centrifugal wind could power protostellar jets.

Following Spruit (1996), consider a thin accretion disc lying in the $z = 0$ plane of a cylindrical (z, r, φ) coordinate system, threaded by a magnetic field \vec{B} (Figure 1.2). Assume the disc is a Keplerian rotator ($v_\varphi = v_K = \sqrt{GM_*/r}$, where M_* is the mass of the central object, G is the gravitational constant), and the atmosphere above the disc is cold enough that the thermal pressure p can effectively be ignored.

Although not a requirement (*e.g.*, Fendt & Čemeljić 2002), I will assume the gas is sufficiently ionised for the ideal magnetohydrodynamics (MHD) approximation to apply. Thus, the magnetic field lines and the gas are perfectly coupled, the field lines are anchored in the disc and forced to rotate with the disc. For a “strong” magnetic field near the disc

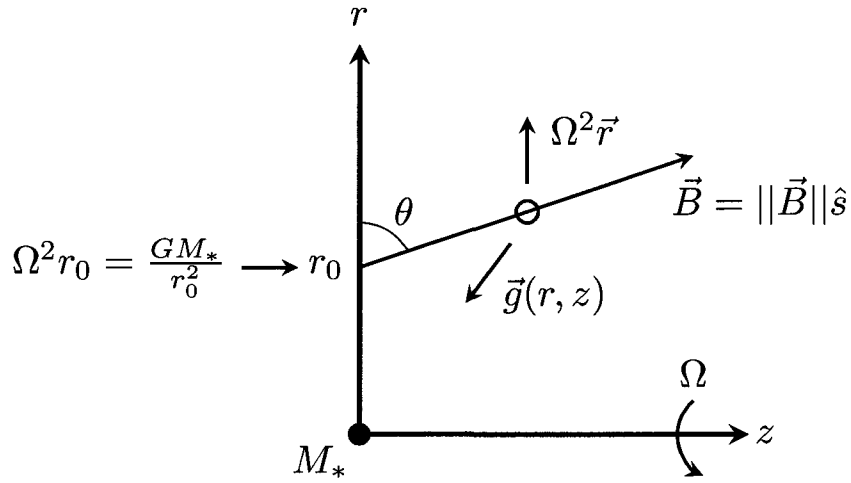


Figure 1.2 Schematic representation of the magneto-centrifugal launching mechanism in cylindrical coordinates. Adapted from Spruit (1996).

surface (*i.e.*, the plasma- $\beta = 8\pi p/B^2 < 1$, $4\pi\rho v^2/B^2 < 1$, where p is the gas pressure and ρ is the density), I can assume that the atmosphere is forced to co-rotate with the field.

In a reference frame co-rotating with the accretion disc, the velocity will be parallel to the magnetic field: $\vec{v} \parallel \vec{B}$, and the Lorentz force ($F_L = q\vec{v} \times \vec{B}$) along a field line will be zero. Under the assumption of a strong magnetic field ($\beta < 1$), the field lines can be considered to be rigid, and fluid particles are free to move like a “bead on a frictionless wire” (Henriksen & Rayburn 1971).

Under the assumption of Keplerian rotation, gravity *just* balances the centrifugal force at the footprint of a field line (r_0), where the centrifugal force is given by $F_c \propto v_K^2/r_0 = \Omega^2 r_0$, and Ω is the angular speed. Since the field lines rotate with the disc, the centrifugal force along a field line will behave like solid body rotation and increase with radius. If a fluid particle is then raised up off the disc along a field line, and

the component of the centrifugal force exceeds the gravitational force, the fluid will be accelerated outward.

What conditions must be satisfied for this to occur? Consider the effective potential of a fluid particle tied to a field line:

$$\Phi_{\text{eff}}(s) = -\frac{GM_*}{R(s)} - \frac{1}{2}\Omega^2 r^2(s), \quad (1.1)$$

where $R = \sqrt{r^2 + z^2}$ is the spherical radius, s is the coordinate along a magnetic field line ($\vec{B} = \|\vec{B}\|\hat{s}$), and $\Omega^2 = GM_*/r_0^3$ assuming co-rotation of the field line and a Keplerian disc. Depending on the inclination angle θ of the field line along which the fluid particle is tied, Φ_{eff} takes on three different characteristic profiles (Figure 1.3).

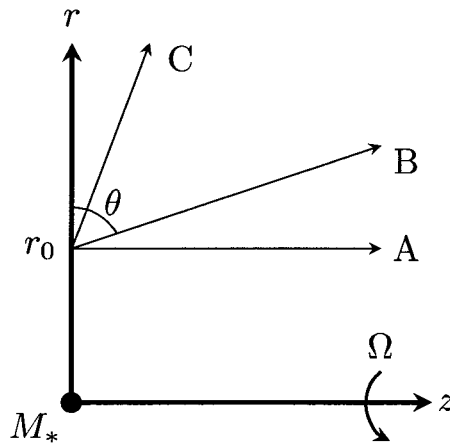


Figure 1.3 Three characteristic profiles for a magnetic field line with footprint r_0 . See the text for descriptions of field lines A, B, and C. Adapted from Spruit (1996).

First, for a perfectly vertical field line ($\theta = \pi/2$; case A), the rotational term $-\frac{1}{2}\Omega^2 r^2(s)$ is constant, and the effective potential monotonically increases away from the disc, making it difficult to overcome gravity and launch a wind. For field lines with an intermediate inclination angle (case B), the effective potential has a global maximum relatively near the disc surface, beyond which the centrifugal force along the field line overcomes gravity. In this case, it is possible to launch a wind so long as a means to move fluid particles beyond the global maximum can be found. Finally, for field lines relatively close to the disc surface (case C), the effective potential monotonically decreases, and the centrifugal term immediately overpowers the gravitational force, allowing a wind to launch directly from the disc surface.

To determine when launching directly from the disc is possible, one needs to know the location of the boundary between the second and third cases: *i.e.*, when the global maximum of Φ_{eff} is at the disc surface: $\partial^2 \Phi_{\text{eff}} / \partial s^2 |_{s=0} = 0$. Since $r = s \cos \theta + r_0$, and $R^2 = s^2 + r_0^2 + 2sr_0 \cos \theta$ by the law of cosines (Figure 1.2), it can be shown that

$$\left. \frac{\partial^2 \Phi_{\text{eff}}}{\partial s^2} \right|_{s=0} = 0 = \Omega^2 (\sin^2 \theta - 3 \cos^2 \theta). \quad (1.2)$$

Solving for θ , the critical angle to launch a wind directly from the disc surface is: $\theta_{\text{crit}} = 60^\circ$ (BP82).

This centrifugal launching action will continue to operate so long as the magnetic field can enforce co-rotation with the fluid. This assumption loses its validity when the poloidal kinetic energy of the fluid is greater than the magnetic energy: $M_A^2 = 4\pi\rho v_p^2/B_p^2 > 1$, *i.e.*, when the Alfvénic Mach number (M_A) is greater than one. The location along a field

line where $M_A = 1$ is called the Alfvén point. In addition, I have used here the *poloidal* magnetic field and velocity, which, in cylindrical coordinates, are components of the total magnetic and velocity vectors, given by:

$$\vec{B} = \vec{B}_p + B_\varphi \hat{\varphi} \quad \text{and} \quad \vec{v} = \vec{v}_p + v_\varphi \hat{\varphi}. \quad (1.3)$$

It is important to note that a magneto-centrifugal jet *can* be launched for inclination angles $\theta > 60^\circ$; the fluid just needs a push to get past the maximum of the effective potential. Means of accomplishing this include an outward thermal pressure gradient or an “evaporation” speed from the disc into the wind, both of which serve to move the fluid from the disc past the maximum of the effective potential. I have ignored these effects here, but they are factors for some of the simulations presented in Chapters 3 and 4.

So far, the reference frame is assumed to co-rotate with the accretion disc. However, an alternative viewpoint for the magneto-centrifugal mechanism can be developed if one instead works in the inertial reference frame.

In the co-rotating frame, $\vec{v} \parallel \vec{B}$, and the Lorentz force along the field line is zero. In the inertial frame however, it is the poloidal velocity which is parallel to the poloidal field ($\vec{v}_p \parallel \vec{B}_p$), and the centrifugal force term disappears, while the poloidal Lorentz force density is:

$$\begin{aligned} \vec{F}_{L,p} &= \frac{1}{4\pi} \left((\nabla \times \vec{B}_p) \times \vec{B}_p \right) \\ &= -\frac{1}{4\pi} \left(\frac{B_\varphi^2}{r} \hat{r} + \frac{1}{2} \nabla B_\varphi^2 \right), \end{aligned} \quad (1.4)$$

where $\vec{B}_\varphi = B_\varphi \hat{\varphi}$. For a wind to be launched via the poloidal Lorentz force, one requires that the combination of toroidal magnetic pressure gradient ∇B_φ^2 and inwardly directed magnetic tension $B_\varphi^2 \hat{r}/r$ result in a net outward force along the field line.

These two viewpoints are equivalent and related by a relatively simple coordinate transformation. The stationary equation of motion for ideal MHD in the inertial frame is:

$$\rho \vec{v} \cdot \nabla \vec{v} = -\nabla p - \rho \nabla \Phi + \frac{1}{4\pi} (\nabla \times \vec{B}) \times \vec{B}. \quad (1.5)$$

Along a field line, the magnetic force is then given by $(\vec{v}_p/v_p) \cdot \vec{F}_{L,p}$, where $\vec{F}_{L,p}$ is given by equation (1.4). If we define the rotating reference frame with:

$$\vec{v}' = \vec{v} - r\Omega \hat{\varphi}, \quad (1.6)$$

and substitute into equation (1.5), then the equation of motion in the rotating frame is (equation 23 of Spruit (1996)):

$$\rho \vec{v}' \cdot \nabla \vec{v}' = -\nabla p - \rho \nabla \Phi + \frac{1}{4\pi} (\nabla \times \vec{B}) \times \vec{B} + \rho \Omega^2 r \hat{r} + 2\rho \vec{v}' \times (\Omega \hat{z}), \quad (1.7)$$

where $\rho \Omega^2 r$ is the centrifugal term, and $2\rho \vec{v}' \times (\Omega \hat{z})$ is the Coriolis term. Along a field line, where the velocity and magnetic field are parallel, the Coriolis term will everywhere be perpendicular to the field line and $(\vec{B}/B) \cdot (\vec{v}' \times [\Omega \hat{z}])$ will be zero. The Lorentz force is also perpendicular to \vec{B} , and by the same argument, also disappears, leaving only the pressure, gravitational, and centrifugal terms. Thus, we have two forms of the equation

of motion: one which involves a centrifugal force (equation 1.7), the other which involves a magnetic force due to the toroidal field (equation 1.5).

Which point of view one should adopt depends on the conditions in the flow: If the approximation of co-rotation is reasonable, then the centrifugal picture is the most useful. However, when co-rotation is not applicable, the toroidal field dominates over the poloidal field, and the acceleration mechanism is best viewed with the magnetic picture. For the simulations presented in Chapters 3 and 4, both of these viewpoints have proven useful in understanding our results.

Time-independent theoretical models are valuable for determining the overall structure of a jet, including collimation, terminal wind speeds, location of the critical surfaces (*e.g.*, the Alfvén point), magnetic field structure, and even the amount of mass or angular momentum removed from the accretion disc (see Pudritz *et al.* 2007 for a review). However, being stationary, these models cannot accommodate time-dependent phenomena, in particular, the jet formation process, the episodic emission observed in some outflows (*e.g.*, HH 34; Figure 1.1), and the time-variable turbulent structure of the jet bow shock (*e.g.*, Hartigan *et al.* 2011). In order to remain tractable, theoretical models have been restricted to a relatively small portion of parameter space, and require assumptions which are not always physically realistic (*e.g.*, self-similar models exclude the jet symmetry axis and assume the jet radius extends to infinity). For answering questions about the clearly non-stationary aspects of protostellar jets, the only effective tool available is direct numerical integration of the time-dependent MHD equations.

1.3 Numerical studies of protostellar jets

The first numerical simulations of a magneto-centrifugal jet launched from an accretion disc were presented by Uchida & Shibata (1985) and Shibata & Uchida (1986). These authors modelled a magnetised, sub-Keplerian disc around a gravitational point source in axisymmetric (2.5-D), cylindrical coordinates using the equations of ideal magnetohydrodynamics (MHD). They demonstrated that material can be launched perpendicular to the disc by an initially poloidal magnetic field which has been wound-up into a toroidal field by the rotating disc.

The pioneering simulations of Uchida & Shibata proved to be the beginning of a veritable industry of numerical simulations of protostellar outflows. These subsequent studies generally break down into two groups: Those which include the time evolution of the accretion disc, and those which take the accretion disc as a boundary condition.

Ultimately, the self-consistent inclusion of the accretion disc is important for understanding the interaction between disc, central mass, and outflow. However, the spatial and temporal scales required to simulate all three components self-consistently is restrictive, and as a result this type of simulation has so far been limited to relatively small spatial and temporal scales (*e.g.*, Miller & Stone 1997; Kudoh *et al.* 1998; Matt *et al.* 2002; Casse & Keppens 2004; Kigure & Shibata 2005; Romanova *et al.* 2005; Meliani *et al.* 2006; Zanni *et al.* 2007; Tzeferacos *et al.* 2009).

Alternatively, the outflow problem can be simplified by treating the accretion disc as a boundary condition, and setting some or all of the MHD variables to prescribed values. Pioneered by Ustyugova *et al.* (1995), this approach is computationally less expensive,

and allows focus to be placed on the process of launching and collimating an outflow. This tactic has since been the basis for a large number of simulations across a range of physical conditions, and below, I summarise some of these studies and their important results.

The study of Ustyugova *et al.* (1995) finds that an outflow is launched along the rotation axis of the disc, driven and collimated by magnetic forces (Figure 1.4). Although the flow is sub-slow at the disc, it is accelerated to super-fast magnetosonic speeds by gradients in the toroidal field, which have built up through twisting of the initially poloidal magnetic field (*c.f.* Uchida & Shibata 1985).

In a series of papers, Ouyed & Pudritz (1997a,b, 1999) present axisymmetric ideal MHD calculations of centrifugally launched jets, with a time-independent Keplerian disc for a boundary condition, and initial conditions which are magnetically force-free and in hydrostatic equilibrium (HSE). They obtain solutions which are either stationary ($\partial/\partial t \simeq 0$) or unsteady, depending on the mass load at the disc surface ($\eta(\psi) = \rho v_p/B_p$; see Section 4.5.1). Even though a steady mass inflow is used, the unsteady simulations produce episodic ejections which are characterised as “knots” (*e.g.*, Figure 1.5). These ejections have radii ~ 1 AU, and it is speculated they may explain the much larger clumpy structures observed in some protostellar jets (*e.g.*, HH 111; Raga *et al.* 2002). Their simulations are also effective at removing angular momentum from the disc: the ratio of accretion rate to the wind mass loss rate is found to be $\dot{m}_a/\dot{m}_w \simeq 6$.

Employing the same initial conditions as Ouyed & Pudritz (1997a), Vitorino *et al.* (2002, 2003) apply random and sinusoidal perturbations to the velocity at the disc surface,

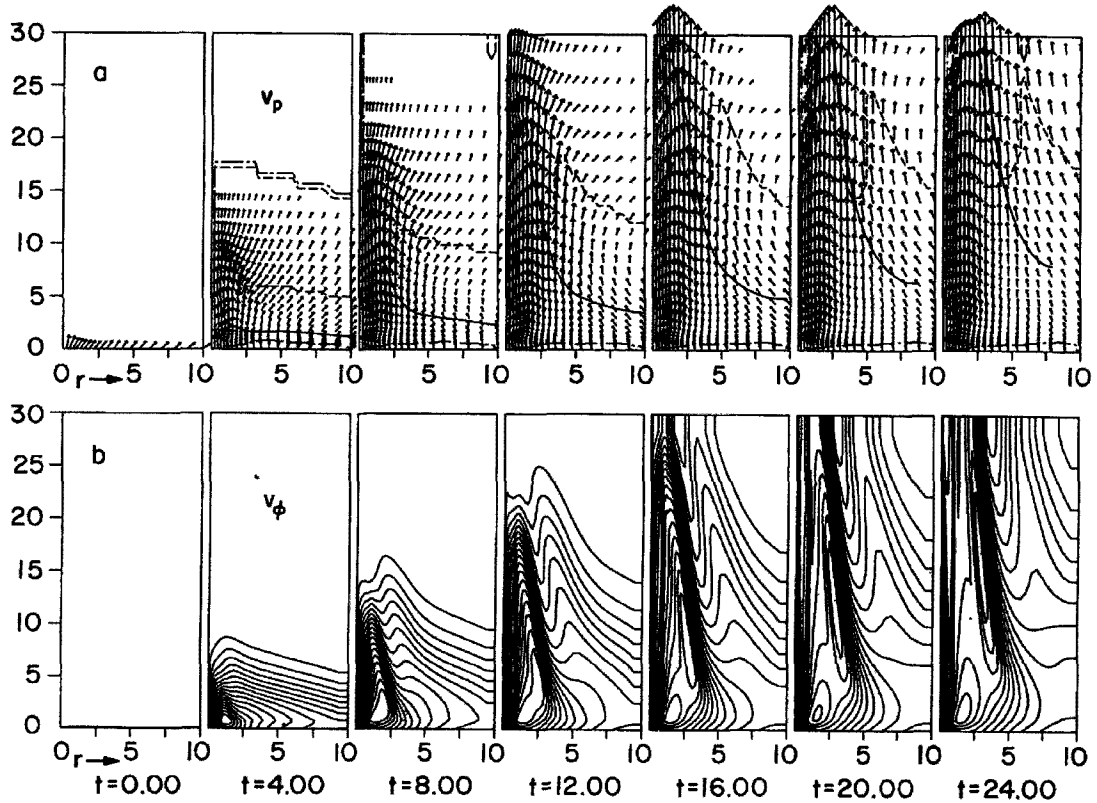


Figure 1.4 Figure 1 from “Magnetohydrodynamic simulations of outflows from accretion disks” (Ustyugova *et al.* 1995) demonstrating a jet launched from a disc as a boundary condition at the bottom edge of each frame. Poloidal velocity vectors (top) and contours of toroidal velocity (bottom) are plotted at different times. Also plotted are the fast magnetosonic surface (long dashed line), the Alfvén surface (dashed line), and slow magnetosonic surface (dot-dashed line). This figure is reproduced with kind permission of the original authors and the AAS.

obtaining solutions with periodic structures, not unlike Ouyed & Pudritz (1997b). In the case of sinusoidal perturbations, they find a clear dependence between the “knot” spacing and the perturbation period, but recognise that the spacing between their episodic ejections is too small to explain observations.

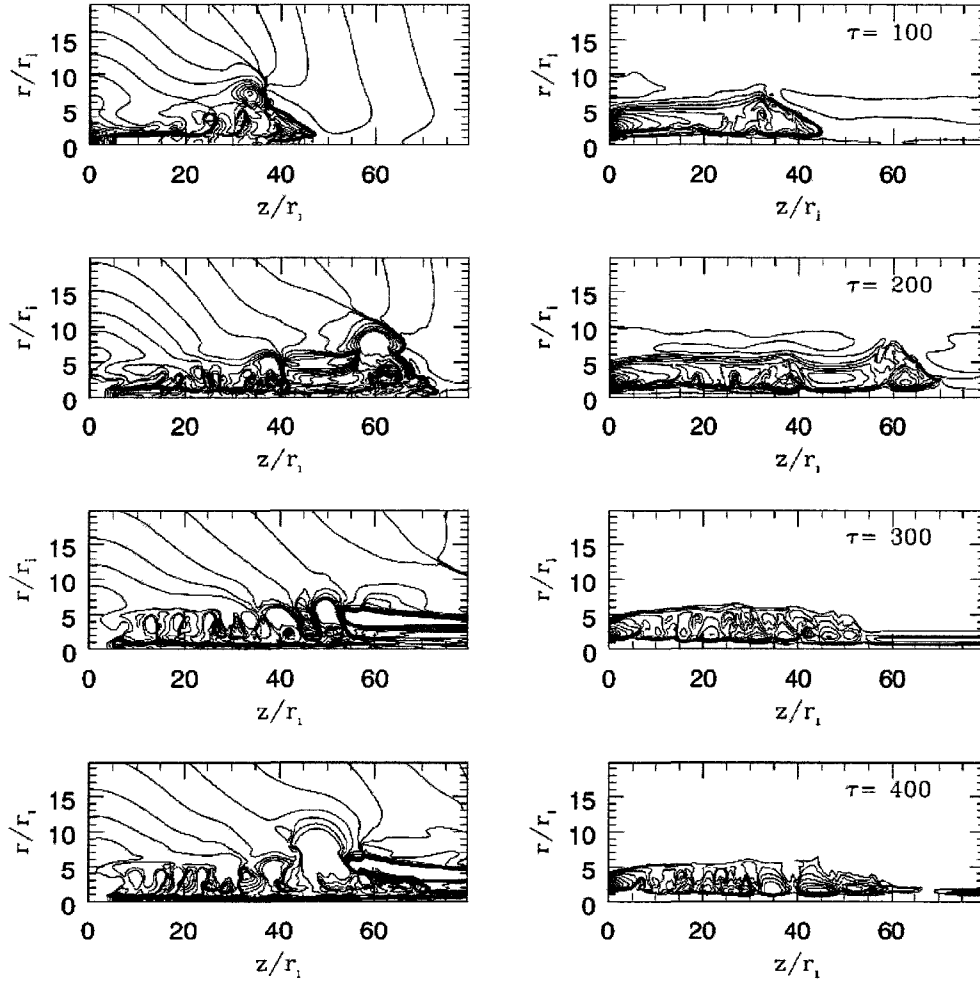


Figure 1.5 Results from “Numerical simulations of astrophysical jets from Keplerian disks. II. Episodic outflows” (Ouyed & Pudritz 1997b; Figure 2) showing episodic knot-like features. Twenty logarithmically spaced contours of density (left) and twenty linearly spaced contours of the toroidal magnetic field (right) are plotted at four different times. The disc as a boundary condition is on the left-hand side of each frame. This figure is reproduced with kind permission of the original authors and the AAS.

Also following Ouyed & Pudritz (1997a), Fendt & Čemeljić (2002) extend models of magnetic winds from Keplerian discs by applying the equations of *resistive* MHD (*i.e.*, it is no longer assumed that the fluid is a perfect conductor). Through the use of a constant

turbulent magnetic diffusivity, Fendt & Čemeljić find that a finite resistivity generally decreases the jet propagation speed and the collimation of the magnetic field. They also find evidence for a critical value of the diffusivity, beyond which the bulk outflow is radial rather than collimated.

Extending the study of Ouyed & Pudritz (1999), Pudritz *et al.* (2006) systematically investigate different profiles for the initial magnetic field distribution (*i.e.*, different mass load distributions), finding the radial distribution of the mass load has an effect on both the collimation and rotation profile of the jet, and concluding that hydromagnetic winds can explain both wide-angle and highly collimated outflows. More specifically, steeply declining mass loads collimate to cylinders, while gradually declining mass loads result in wide-angle winds. Fendt (2006) perform a similar and nearly contemporaneous study, but includes a magnetic diffusivity and explores a larger parameter space through variation in the total magnetic field strength and mass flux. The results for magnetic field distribution are in general agreement with Pudritz *et al.* (2006), and he additionally finds evidence that the terminal jet speed scales with magnetic field strength.

Ustyugova *et al.* (1999) present jet simulations using a steeply declining split-monopole magnetic field configuration, finding solutions which are stationary and poorly collimated, confirmed by the results of Pudritz *et al.* (2006). Importantly, Ustyugova *et al.* also employ partially time-dependent boundary conditions for the disc, allowing the inflow velocity, as well as the radial and toroidal components of the field, to vary with time, in contrast to the fixed in time boundary conditions of Ouyed & Pudritz and related studies.

These boundary conditions are adopted and generalised by Krasnopolsky *et al.* (1999, 2003), who perform simulations of steady-state, cold, and collimated ideal MHD jets. Their boundary conditions allow both the radial and toroidal components of the magnetic field and velocity to respond to conditions in the atmosphere above the disc. Similar to Ouyed & Pudritz, these authors find their results are insensitive to changes in the density or velocity at the disc surface, so long as their product ($\propto \eta$, the mass load) is constant. As measured by the ratio of Poynting to kinetic energy flux, they find that far from the disc, $\sim 60\text{--}80\%$ of the magnetic energy extracted from the disc has been converted to kinetic energy of the wind.

Anderson *et al.* (2005) expand upon the results of Krasnopolsky *et al.* by performing simulations across a wide range of mass loads (through variation in the injection speed at the disc surface). They find that high mass loads increases collimation, but lead to unsteady winds, while low mass loads result in steady-state solutions. This is opposite to the trend for mass load found in Ouyed & Pudritz (1999), and the authors postulate this could be due to the differences in the boundary conditions in the two studies. Whereas Anderson *et al.* (2005) use a disc boundary which can respond to conditions in the atmosphere above it, Ouyed & Pudritz (1999) use a time-independent boundary which appears to be formally overspecified (for a discussion, see Appendix B of Porth & Fendt 2010). Anderson *et al.* also find that above some critical mass load unsteadiness is unavoidable, likely because the field is too weak to accelerate the mass efficiently. They also discover that the terminal speed along a given field line is $\propto \dot{M}_w^{-1/3}$ (where \dot{M}_w is the mass load), in agreement with analytical radially self-similar models (*e.g.*, Michel 1969).

Fendt & Elstner (2000) take a slightly different approach relative to the other studies discussed here by simulating a two-component magnetic field in ideal MHD, consisting of a stellar-type dipole and a stellar wind component. They find the dipole field is disrupted, forming a disc wind, while a second separate component forms due to the stellar wind. There is a clear boundary between the two components, a result of oppositely directed magnetic fields in the disc and stellar wind components.

As a follow-up to Fendt & Elstner (2000), Fendt (2009) simulates two-component outflows, including a magnetic diffusivity. Although the value of the magnetic diffusivity is small relative to Fendt & Čemeljić (2002), physical magnetic reconnection is still permitted. Indeed, “strong flares” are observed in the simulations, resulting in sudden, transient changes in jet mass flux and velocity by factors of a few. In addition, Fendt finds that a strong disc wind is required to combat the radial character of the stellar wind and maintain collimation.

Following a different approach, the work of Gracia *et al.* (2006), Matsakos *et al.* (2008, 2009), and Stute *et al.* (2008, 2010) take as initial conditions for their simulations analytical self-similar models which already include a jet in a nearly steady-state. Additionally, they do not simultaneously include the disc as a boundary condition and large simulation boxes, but rather begin the computational domain slightly above the disc surface to avoid numerical issues near the equatorial plane. In all cases, the steady-state models relax to a modified stationary state, which is usually quite similar to the original analytical solution. By producing synthetic forbidden emission maps, Stute *et al.* (2010)

demonstrate for these models that a finite outer launching radius is necessary in order to agree with observed values of protostellar jet widths.

To date, there have only been a few 3-D studies of jets launched from discs as a boundary condition. For instance, Ouyed, Clarke, & Pudritz (2003) present 3-D simulations with initial conditions derived from Ouyed & Pudritz (1997b), finding that the launching mechanism carries over from axisymmetric simulations. They also find that the jet, while subject to Kelvin-Helmholtz instabilities, maintains long-term stability with help from a “backbone” of poloidal magnetic field along the axis of the jet, and by a self-limiting of jet velocities to trans-Alfvénic speeds. This remains true even after introducing perturbations at the disc surface (Figure 1.6).

Anderson *et al.* (2006) have also published 3-D simulations, this time based on the axisymmetric studies of Anderson *et al.* (2005). In this study, an attempt is made to drive the outflow unstable by unevenly distributing the mass load at the disc surface, but the authors instead find that the jet settles into a new, asymmetric steady-state. Similar to Ouyed, Clarke, & Pudritz (2003), a concentration of poloidal field lines near the jet axis appears to help maintain stability.

Finally, Staff *et al.* (2010) begin with the initial conditions of Ouyed, Clarke, & Pudritz (2003) and perform 3-D simulations with the magnetic field profiles of Ouyed & Pudritz (1997a) and BP82. Calculating the synthetic forbidden emission of [OI], they find the Ouyed & Pudritz-type field configuration produces results which are in better agreement with observations than the BP82 configuration. They also find jets with speeds

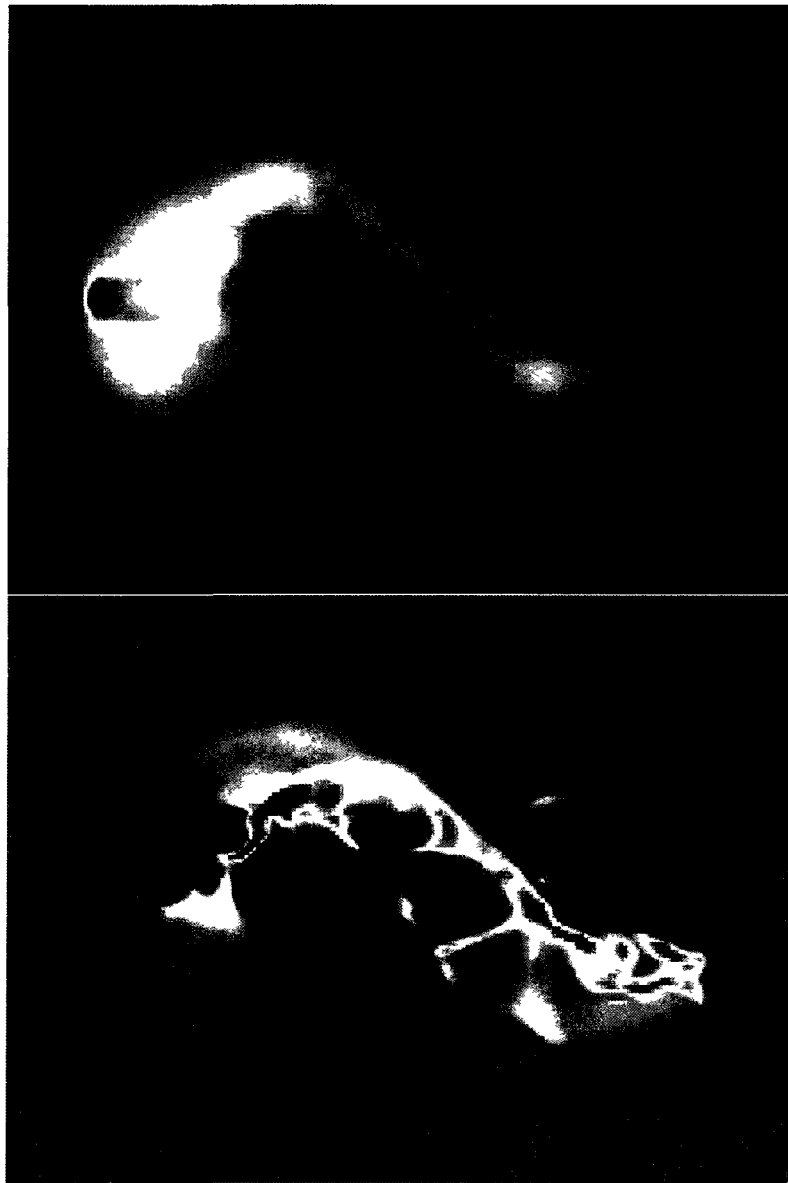


Figure 1.6 Results from one of the 3-D simulations of “Three-dimensional simulations of jets from Keplerian disks: self-regulatory stability” (Ouyed, Clarke, & Pudritz 2003; Figure 3). Shown are false colour representations of $\int \rho dl$ (top) and $\int (\nabla \cdot \vec{v}) dl$ (bottom). The disk is on the left-hand side of the image (not shown), and the jet propagates from left to right. This figure is reproduced with kind permission of the original authors and the AAS.

up to 400 km s^{-1} , and jet widths of $\leq 20 \text{ AU}$. More importantly though, a strong rotation signature is still present in their synthetic observations, despite time variability and perturbations at the disc surface.

Based on the studies discussed above, the magneto-centrifugal wind launching mechanism is robust. Several different groups have found that jets are launched magneto-centrifugally regardless of the magnetic field profile, the specifics of the mass loading profile, the details of the boundary conditions, or the inclusion of additional physics. Furthermore, jets produced with the magneto-centrifugal mechanism are stable to perturbations in both 2-D and 3-D. It is for these reasons, among others, that this mechanism is currently regarded as the most credible model for explaining not only protostellar outflows, but jets in many different astrophysical settings.

For the simulations which have been scaled to physical units, Table 1.2 summarises results which can be compared directly with observations. While properties such as jet speeds and mass fluxes overlap at least partially with observed characteristics of protostellar jets (Table 1.1), the maximum simulated extent of 100 AU (Anderson *et al.* 2005) is orders of magnitude smaller than the observed sizes of these objects.

The disconnect between scale lengths of observations and simulations prevents a number of outstanding questions from being answered. For example, can the magneto-centrifugal mechanism, by itself, produce jets which agree with observations on large-scales? What properties will these jets have? Are they capable of propagating to the lengths of giant HH outflows? Do the knots produced by some small-scale simulations

| | |
|---|---------------------|
| poloidal velocity (km s^{-1}) | 35 – 1300 |
| toroidal velocity (km s^{-1}) | $\lesssim 50$ |
| mass fluxes ($M_{\odot}\text{yr}^{-1}$) | $10^{-8} - 10^{-5}$ |
| max. physical extent (AU) | 1 – 100 |
| simulation lifetimes (yr) | 1 – 100 |

Table 1.2 Several properties from simulations of protostellar jets launched from a disc as a boundary condition.

References. — Ouyed & Pudritz (1997a); Ustyugova *et al.* (1999); Anderson *et al.* (2005); Fendt (2009); Staff *et al.* (2010).

evolve to form the clumpy structures observed at much larger scales? While on small-scales, the conditions at the accretion disc have clear relationships with the properties of the jet. On large scales, how do the observed properties of jets, such as mass flux or proper motion, relate to the conditions at the surface of the accretion disc? For the simulations discussed above, the jet has long moved off the grid and the ambient medium surrounding the jet has long been pushed completely off the computational domain. In reality, the jet is directly influenced by a confining medium. Thus, none of these simulations can address what effect the ambient medium has on jets launched by the magneto-centrifugal mechanism.

1.4 This work

Evidently, there is a disparity between observations of jets which stretch for $\geq 10^4$ AU, and simulations with a maximum extent of only 100 AU. It is then difficult to reconcile the magneto-centrifugal model for jet launching with observations when the maximum

extent of simulations are only a few times larger than the highest spatial resolution currently attainable (~ 14 AU for the Taurus Auriga complex; Ray *et al.* 2007). To further put this into context, Figure 1.7 shows false colour images of protostellar jets with a scale of 1000 AU indicated in the bottom left of each panel. In the cases of HH 34 and HH 47, 100 AU barely registers as a single resolution element, and very little information is available on these scales. In order to establish whether the magneto-centrifugal model can produce realistic protostellar jets, we need either observations which resolve down to the AU scale, or simulations which include both the launching mechanism and the large observational scale structure.

In this work, I aim to do the latter by presenting axisymmetric, ideal, time-dependent MHD simulations of protostellar jets, simultaneously including both the launching mechanism at sub-AU scales and observable scales of thousands of AU. By placing an emphasis on quantities which are directly comparable to current observations, I attempt to determine if the magneto-centrifugal jet launching mechanism is suitable for producing observed protostellar jets.

To make these simulations possible, I employ the new adaptive mesh refinement (AMR) MHD fluid code AZEuS. The development and testing of AZEuS constitutes a significant portion of this work, and in Chapter 2 I describe how we adapt the AMR scheme of Berger & Colella (1989) for use with the fully staggered-mesh of *ZEUS-3D* (Clarke 1996, 2010).

At the outset of this project, a purely 3-D, hydrodynamical, and Cartesian AMR prototype of AZEuS had been developed by Sasha Men'shchikov, then a post-doctoral

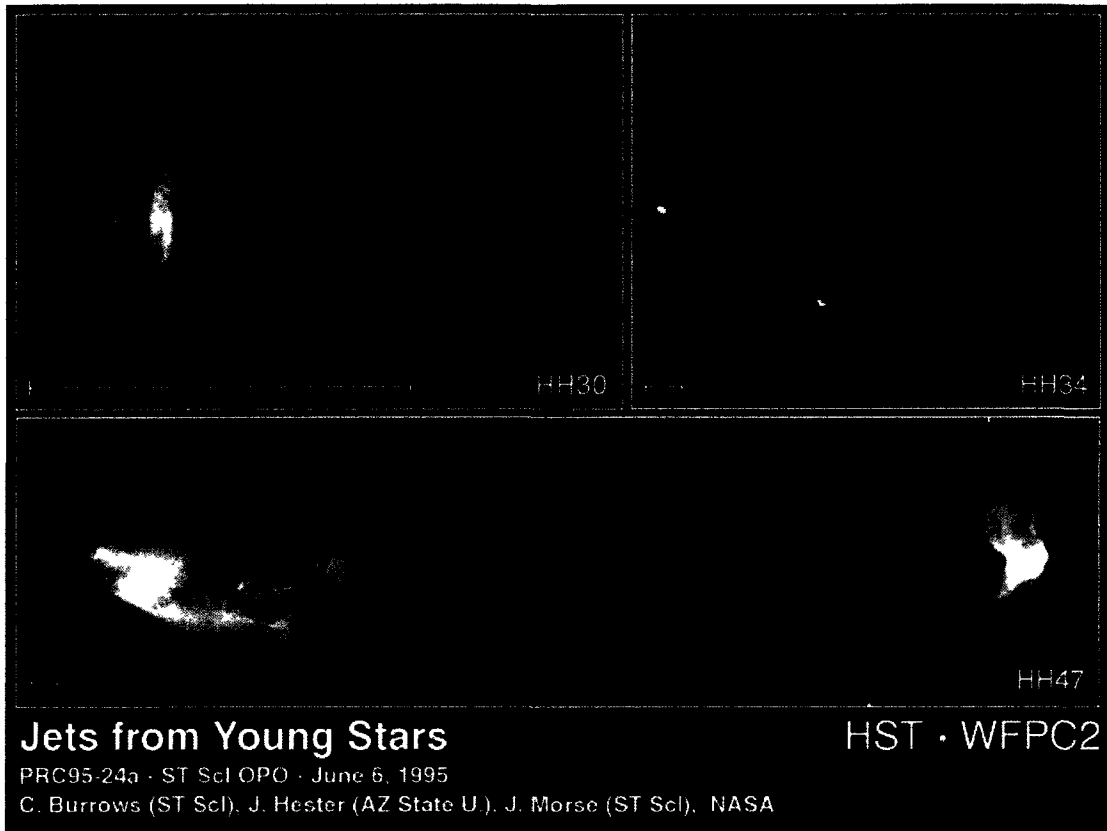


Figure 1.7 False colour images of the HH 30 (top left), HH 34 (top right), and HH 47 jets (bottom) taken with the Hubble space telescope. HH 47 exhibits clear non-axisymmetric behaviour while HH 30 and HH34 appear more axisymmetric. The images were taken with WFPC2 in visible light, and the scales in the bottom left of each panel correspond to 1000 AU. Top left credit: J. Morse/STScI, and NASA. Top right credit: J. Hester (Arizona State University), the WFPC 2 Investigation Definition Team, and NASA. Bottom credit: C. Burrows (STScI & ESA), the WFPC 2 Investigation Definition Team, and NASA.

fellow at Saint Mary's. Since his departure, I was responsible for completing the development of AZEuS which included geometrical symmetries (1-D, 2-D), curvilinear coordinates (cylindrical and spherical polar coordinates), magnetic fields (and the preservation of the solenoidal condition), higher-order conservative prolongation schemes (*i.e.*, interpolation), and the treatment of physical boundary conditions. The *ZEUS-3D* portion of

AZEuS is equivalent to the version currently developed and maintained by David Clarke (<http://www.ica.smu.ca/zeus3d>). With regards to both *ZEUS-3D* and AMR modules, I was also responsible for OpenMP shared-memory parallelisation and general performance tuning, resulting in an increase in serial performance of $\sim 20\%$, and a parallel speed-up factor of 12.5 on 16 CPUs. To the best of my knowledge, AZEuS is the only *fully*-staggered mesh (*i.e.*, both magnetic fields and momenta are located at face centres) AMR-MHD code in use in astrophysics.

In performing these simulations, I have made a number of physical assumptions which simplify our models, making them tractable for the large computational domains and long simulation run times we use. Here, I perform a “reality check” to examine whether or not these assumptions were valid in the first place. The major assumptions I discuss here are 1) the ideal MHD approximation, 2) neglecting self-gravity of the fluid, and 3) cylindrical axisymmetry.

The ideal MHD fluid approximation is the simplest single-fluid model available for studying a conducting fluid, and to check its validity, we start by examining the applicability of the fluid model. This requires the mean free path of the particles, δl , to be much less than the characteristic length scale of interest, L :

$$\delta l \ll L. \tag{1.8}$$

For particles with a Maxwell-Boltzmann distribution of velocities, the mean free path can be written as

$$\delta l = \frac{1}{\sqrt{2}n\sigma}, \quad (1.9)$$

where n is the number density of particles, and $\sigma = \pi r^2$ is the cross sectional area of collision (Baierlein 1999; p. 376). Using a characteristic value for the density in protostellar jets ($n \sim 10^{11} \text{ m}^{-3}$; McKee & Ostriker 2007), along with five times the Bohr radius ($5r_{\text{B}} = 2.6 \times 10^{-10} \text{ m}$) in the cross-sectional area¹, I calculate a mean free path of $l \simeq 3 \times 10^7 \text{ m}$. Taking as the characteristic length scale the size of the smallest resolution element from my simulations, $L = \Delta x_{\text{min}} \simeq 10^9 \text{ m}$, then $\delta l \ll L$, as desired.

Next, in order for the MHD approximation to be considered valid, the fluid must be sufficiently magnetised for the fields to couple to the particles. Equivalently, for the approximation to apply, the ion gyro radius

$$r_{\text{g}} = \frac{mv}{qB} \quad (1.10)$$

(also known as the Larmor radius) must be much smaller than the characteristic length scale. In this expression, m is the mass of an ionised particle, v is the velocity of these particles, q is the electric charge, and B is the strength of the local magnetic field. Using the maximum velocities measured in protostellar jets ($v_{\text{max}} \simeq 5 \times 10^5 \text{ m s}^{-1}$; Table 1.1), a magnetic field strength of $B \sim 10^{-8} \text{ T}$ (Vallée 2003), and a proton as the particle, the gyro radius is then $r_{\text{g}} \simeq 5 \times 10^5 \text{ m} \ll L = \Delta x_{\text{min}}$.

¹A value of $5r_{\text{B}}$ is used to account for the increase in cross-sectional area due to charged particles and the resulting Coulomb force.

Finally, for the MHD approximation to be considered ideal, magnetic diffusion must be completely negligible (*i.e.*, the electrical conductivity $\sigma \rightarrow \infty$). This can be expressed through the magnetic Reynolds number:

$$R_m = \frac{vL}{\eta}, \quad (1.11)$$

where η is the magnetic diffusivity. A value of the magnetic Reynolds number much larger than unity indicates magnetic diffusion is unimportant. Following Fendt & Čemeljić (2002), for a fully ionised hydrogen gas, the magnetic diffusivity parallel to the field can be expressed as

$$\eta \sim r_e c \left(\frac{v_{\text{th}}}{c} \right)^{-3}, \quad (1.12)$$

where r_e is the classical electron radius, $v_{\text{th}} = \sqrt{k_B T / m_e}$ is the thermal speed of the electrons, c is the speed of light, T is the gas temperature, k_B is the Boltzmann constant, and m_e is the electron mass. Again using the smallest resolution element for the characteristic length, a velocity of $5 \times 10^5 \text{ m s}^{-1}$, and a gas temperature of 100 K, I calculate a magnetic Reynolds number of $R_m \simeq 10^9 \gg 1$.

The magnetic diffusivity perpendicular to the field will, in general, be different than along the field. However, for such large magnetic Reynolds numbers, these anisotropic effects are negligible and only the diffusivity parallel to the field needs to be considered.

While the inclusion of self-gravity is important for studies of molecular cloud and core collapse, in our relatively small-scale simulations it is negligible. This can be demonstrated

by calculating the free-fall time of our simulated “core”:

$$t_{\text{ff}} = \left(\frac{3\pi}{32G\langle\rho\rangle} \right)^{1/2}, \quad (1.13)$$

where $\langle\rho\rangle$ is the mean density (Truelove *et al.* 1998).

This mean density is calculated by integrating our initial density profile over a sphere of radius R_{max} , where R_{max} is the maximum extent of our computational domain, and then dividing the result by the volume of a sphere with the same radius. Using a hydrostatic profile plus a density floor:

$$\rho(R) = \rho_i R^{-1/(\gamma-1)} + 10^{-6} \rho_i, \quad (1.14)$$

where r_i is the scaling length, ρ_i is the density at r_i , $\gamma = 5/3$ is the ratio of specific heats, and $R = \sqrt{r^2 + z^2}$ is the spherical radius. Integrating over a sphere, the mean density is given by

$$\langle\rho\rangle = \frac{1}{\frac{4}{3}\pi R_{\text{max}}^3} \int_V \rho(R) R^2 \sin\theta \, dR \, d\theta \, d\phi = \frac{3}{R_{\text{max}}^3} \int_0^{R_{\text{max}}} \rho(R) R^2 \, dR. \quad (1.15)$$

For a maximum extent of $R_{\text{max}} = z_{\text{max}} = 4096$ AU, I calculate a mean density of $\langle\rho\rangle \simeq 5 \times 10^{-15}$ kg m⁻³. Substituting into Equation (1.13), I find a free-fall time of $t_{\text{ff}} \simeq 3 \times 10^4$ yr, *much* longer than our maximum simulation time of 100 yr. Even then, the magnetic and pressure forces in our simulations act on significantly smaller timescales than 100 yr, further justifying neglecting self-gravity of the fluid.

The third major assumption I have made in this work is that of axisymmetry. For cylindrical coordinates, this approach assumes that all variables are symmetric and all derivatives are zero in the φ -direction ($\partial/\partial\varphi = 0$). Unlike pure 2-D, it does allow for the φ -components to take on non-zero values and affect the dynamics of the simulation. This simplifying assumption is justified so long as the physical phenomena we are trying to model also exhibits axisymmetric behaviour. HH 34 in the Orion nebula is an excellent example of an axisymmetric protostellar jet, showing essentially only axisymmetric structure along the visible jet (Figure 1.1, 1.7). Although there are HH objects which show clear non-axisymmetric structure (*e.g.*, HH 47, Figure 1.7; Heathcote *et al.* 1996), I focus here on astrophysical examples which do show a high degree of axisymmetry (*e.g.*, HH 30, HH 111; Ray *et al.* 1996, Reipurth *et al.* 1997a), and demonstrate that axisymmetric models are relevant. Indeed, to perform fully 3-D simulations on the scale of the 2-D models presented here, even with AMR, would require computing resources *far* beyond those which we have access to.

In addition, I have assumed in this work that radiative effects are not important. However, protostellar jets are clearly emission line objects (*e.g.*, Figures 1.1 and 1.7) and, as such, ignoring radiation is not necessarily a reasonable assumption. Indeed, radiative cooling immediately behind a shock can have significant consequences on conditions in the jet (Reipurth & Bally 2001), in particular, on the ionisation fraction and temperature. Although I understand the importance of these effects, they are not included here due to the additional complexity and computational demands associated with calculating line

cooling, and radiative timescales which can dominate the other timescales in the problem (*e.g.*, Teşileanu *et al.* 2008).

An outline of this thesis is as follows. Chapter 2 discusses the details of the implementation of AMR on the fully-staggered mesh of AZEuS. In Chapter 3, I present the first results of the application of AZEuS to studies of protostellar jets. These results are also the first simulations to include the jet launching mechanism and length scales $> 10^3$ AU simultaneously.

In Chapter 4, I discuss further aspects of the jet simulations, and expand the discussion on comparing simulations with observations. The jet launching mechanism and the generation of “knot”-like structures in the simulations is also addressed.

Finally, Chapter 5 summarises the major findings, and comments on their implications for both our current understanding of protostellar jets and future simulations.

Chapter 2

AZEuS: An Adaptive Zone Eulerian Scheme¹

A new adaptive mesh refinement (AMR) version of the *ZEUS-3D* astrophysical magnetohydrodynamical (MHD) fluid code, AZEuS, is described. The AMR module in AZEuS has been completely adapted to the staggered mesh that characterises the *ZEUS-3D* family of codes, on which scalar quantities are zone-centred and vector components are face-centred. In addition, for applications using static grids, it is necessary to use higher-order interpolations for prolongation to minimise the errors caused by waves crossing from a grid of one resolution to another. Finally, solutions to test problems in 1-, 2-, and 3-dimensions in both Cartesian and spherical coordinates are presented.

2.1 Introduction

High-resolution, multidimensional simulations have become indispensable for many complex problems in astrophysics, particularly those involving (magneto-)fluid dynamics. One of the most important innovations in this area has been the use of dynamic and variable resolution techniques. Adaptive mesh refinement (AMR), pioneered in the context

¹The contents of this chapter have been submitted for publication to The Astrophysical Journal Supplement Series.

of the fluid equations by Berger & Oliger (1984) and Berger & Colella (1989; BC89), is one such approach.

With AMR, a hierarchy of grids is used to provide high numerical resolution when and where the physics requires it, leaving as much of the volume at lower resolution as possible to minimise computational effort. This makes AMR an efficient means of studying problems with a very large spatial dynamic range (*e.g.*, star formation, galaxy evolution), as borne out by the large number of codes which employ it: *ORION* (Klein 1999), *FLASH* (Fryxell *et al.* 2000), *RIEMANN* (Balsara 2001), *RAMSES* (Fromang *et al.* 2006), *PLUTO* (Mignone *et al.* 2007), *NIRVANA* (Ziegler 2008), *AstroBEAR* (Cunningham *et al.* 2009), and *ENZO* (Collins *et al.* 2010) to name several.

Virtually all AMR fluid codes to date are based on a zone-centred grid, with all hydrodynamical variables (density, energy, and momentum components) taken to be located at the centres of their respective zones. Indeed, AMR was originally designed specifically for zone-centred schemes. Magnetohydrodynamic (MHD) solvers are designed with either zone-centred or face-centred magnetic field components, depending in part on the mechanism used to preserve the solenoidal condition. One scheme that has enjoyed somewhat of a renaissance of late is Constrained Transport (CT; Evans & Hawley 1988), which places magnetic field components at the centres of the zone-faces to which they are normal. The staggered mesh introduced in such a scheme has to be specifically accounted for in the AMR modules and in such a way that $\nabla \cdot \vec{B}$ remains zero everywhere—including within the boundaries—to machine round-off error.

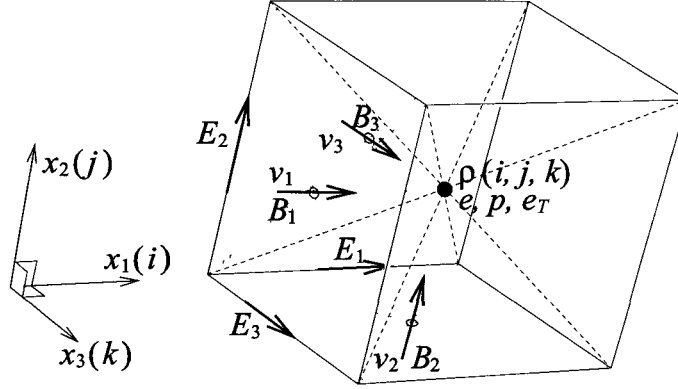


Figure 2.1 On a fully-staggered grid, scalars (ρ , e_T , e , p) are zone-centred, primitive vectors (\vec{v} , \vec{B}) are face-centred, and derived vectors ($\vec{E} = -\vec{v} \times \vec{B}$, $\vec{J} = \nabla \times \vec{B}$) are edge-centred.

The only astrophysical fluids code in wide use that employs a fully staggered grid, where the momentum components are also face-centred, are the *ZEUS-3D* family of codes (Figure 2.1). While concerns have been expressed over the suitability of its MHD algorithms in certain pedagogical 1-D test problems (*e.g.*, Falle 2002), the fact remains that in one form or another, *ZEUS-3D* is among the best tested, documented, and widely-used fluid codes in astrophysics (Stone & Norman 1992a,b; Stone, Mihalas, & Norman 1992; Clarke 1996, 2007, 2010; Hayes *et al.* 2006), and a proper merger with AMR is warranted. To do this, AMR has to be modified for a fully staggered grid, including the proper treatment of face-centred magnetic fields and face-centred momenta.

In this paper, we introduce the newest member of the *ZEUS-3D* family of codes, AZEuS, whose “maiden simulations” have already appeared in Ramsey & Clarke (2011). AZEuS is a block-structured AMR version of *ZEUS-3D* (Clarke 1996, 2010) which preserves the modularity and structure of the underlying *ZEUS-3D* module. The AMR scheme of

BC89 including the changes described in Bell *et al.* (1994) are modified for a fully-staggered grid, with additional modifications made to the prolongation procedure to allow for smooth passage of all types of waves between adjacent grids of differing resolution. AZEuS is currently capable of ideal MHD in 1-, 1.5-, 2-, 2.5-, and 3-D in Cartesian, cylindrical, and spherical polar coordinates using both dynamic and static grids, and with a full suite of physical boundary conditions. As with all *ZEUS-3D*-type codes, additional physics modules (*e.g.*, gravity, viscosity, radiation, *etc.*) can be easily added.

This paper does not attempt to give a full recount of the basic methodology in either AMR or *ZEUS-3D*, but focuses instead on the modifications to AMR (not so much to *ZEUS-3D*) necessary for their merger. Thus, the reader should be familiar with BC89 and Clarke (1996, 2010). In Section 2.2, we list the MHD equations solved by AZEuS, and define our conventions and notation. In Sections 2.3 and 2.4, we enumerate the modifications necessary for restriction and prolongation on a staggered grid, as well as outline the interpolation schemes used to allow the smooth passage of waves across grid boundaries. Section 2.5 focuses on boundary conditions, while in Section 2.6 we discuss how grids are created and how the proper nesting criterion must be modified for a fully-staggered grid. Several of the 1-D, 2-D, and 3-D test problems used to validate AZEuS are given in Section 2.7, followed by a quick summary in Section 2.8. Discussion of curvilinear coordinates, use of the vector potential, and a schematic overview of the code are relegated to the appendices.

2.2 Preamble

2.2.1 Underlying numerical method

AZEUS solves the following equations of ideal MHD (with the artificial viscosity and gravity terms included):

$$\frac{\partial \rho}{\partial t} + \nabla \cdot (\rho \vec{v}) = 0, \quad (2.1)$$

$$\frac{\partial \vec{s}}{\partial t} + \nabla \cdot (\vec{s} \vec{v}) = -\nabla(p + p_B) + \nabla \cdot (\vec{B} \vec{B} - \mathbf{Q}) - \rho \nabla \phi, \quad (2.2)$$

$$\frac{\partial \vec{B}}{\partial t} + \nabla \times \vec{E} = 0, \quad (2.3)$$

$$\frac{\partial e}{\partial t} + \nabla \cdot (e \vec{v}) = -p \nabla \cdot \vec{v} - \mathbf{Q} : \nabla \vec{v}, \quad (2.4)$$

$$\frac{\partial e_T}{\partial t} + \nabla \cdot ((e_T - p_B) \vec{v} + \vec{E} \times \vec{B} + \mathbf{Q} \cdot \vec{v}) = 0, \quad (2.5)$$

where ρ is the mass density, \vec{v} is the velocity, $\vec{s} = \rho \vec{v}$ is the momentum density, p is the thermal pressure, \vec{B} is the magnetic induction², $p_B = B^2/2$ is the magnetic pressure, \mathbf{Q} is the von Neumann-Richtmyer artificial viscous stress tensor (von Neumann & Richtmyer 1950; Clarke 2010), ϕ is the gravitational potential and satisfies the Poisson equation ($\nabla^2 \phi = 4\pi G \rho$), $\vec{E} = -\vec{v} \times \vec{B}$ is the induced electric field, e is the internal energy density, and $e_T = e + \frac{1}{2} \rho v^2 + p_B + \rho \phi$ is the total energy density. This set of equations is closed by the ideal gas law, $p = (\gamma - 1)e$, where γ is the ratio of specific heats. Figure 2.1 shows the locations of most of these variables on a fully-staggered grid. Other physics terms often found in *ZEUS-3D* codes such as a second fluid, physical viscosity, radiation, *etc.*, have yet to be implemented.

²in units where $\mu_0 = 1$

AZEuS inherits the operator-split methodology of *ZEUS-3D*, wherein the terms on the RHS of equations (2.1)–(2.5) are treated in a *source step* while those on the LHS are accounted for in a separate *transport* and *inductive step*. As such, the algorithm is not strictly conservative. However, based as it is on the version of *ZEUS-3D* described by Clarke (2010), AZEuS can solve either the internal energy equation or the total energy equation, where the latter choice does ensure conservation of total energy to machine round-off error, but at the cost of non-positive-definite thermal pressure. Should positive definite pressures be paramount, the internal energy equation offers a viable option with, in most cases, total energy conserved to within 1% or less (see Clarke 2010 for further discussion).

To accommodate the interpolation schemes, two boundary zones must be specified at the edges of all grids. On a staggered grid, all zone-centred quantities have just the two boundary values, while face-centred quantities have two boundary values plus a value that lies on the face separating the “active zones” from the “boundary zones”, henceforth referred to as the “skin” of the grid (Figure 2.2). As we shall see, skin values for the magnetic field are treated just like active zones, while the momenta on the skin are treated somewhere in between active and boundary values; the difference attributed to the conservation properties of these two quantities.

2.2.2 Conventions and Notation

We adopt the following conventions and notation throughout this paper:

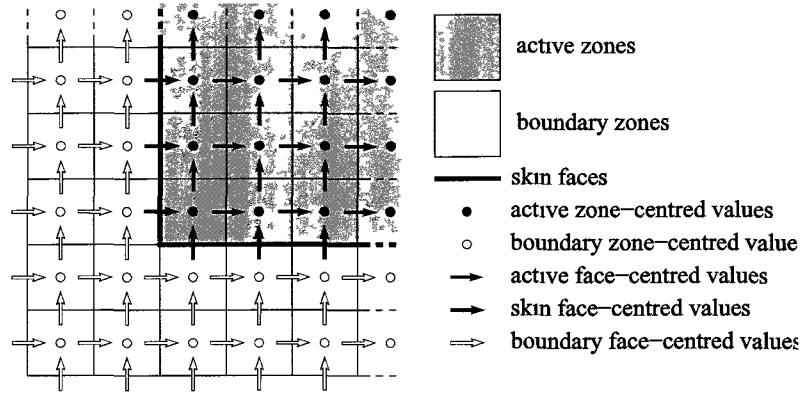


Figure 2.2 On a fully-staggered grid, all variables have two boundary values. In addition, for each direction, one component of a face-centred vector and two components of an edge-centred vector have one skin value.

1. Quantities in coarse and fine zones are denoted with upper and lower cases respectively: *e.g.*, $Q(I, J, K)$, $q(i, j, k)$. Fluxes for a quantity Q (q) are denoted $F_{m,Q}$ ($f_{m,q}$), where $m = 1, 2$, or 3 indicates the vector direction.
2. Unless otherwise indicated, a “coarse” grid or zone is considered to be at level l , while its daughter “fine” grid or zone is at level $l + 1$. The base and coarsest grid, which covers the entire domain, is at level $l = 1$. Refinement ratios, ν , between level l and $l + 1$ must be a power of 2 and the same in all directions.
3. Grid volumes, areas, lengths and time steps are ΔV , ΔA_m , Δx_m , and Δt for a coarse grid, and δV , δA_m , δx_m , and δt for a fine grid.
4. Indices (i, j, k) correspond to a fine zone at the (left, bottom, back) of a coarse zone with indices (I, J, K) . The zone-centre of a particular fine zone within a coarse zone

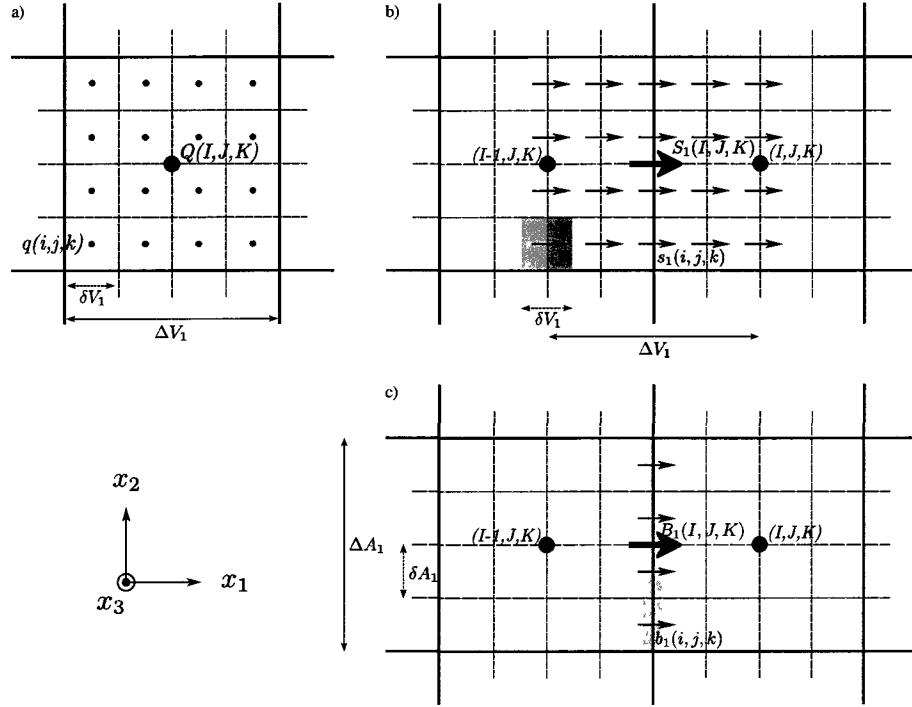


Figure 2.3 The regions of influence (ROI) (shaded) for: (a) zone-centred variables, (b) face-centred and volume-conserved variables, and (c) face-centred and area-conserved variables. A refinement ratio of $\nu = 4$ is shown.

is designated $(i + \alpha, j + \beta, k + \eta)$, where $\alpha, \beta, \eta = 0, 1, \dots, \nu - 1$. For the 1-face-centre of a fine zone, $\alpha = 0, 1, \dots, \nu$ while $\beta, \eta = 0, 1, \dots, \nu - 1$, etc.

- Similarly, grid positions for the coarse grid use upper case indices [e.g., $x_1(I)$], while grid positions for the fine grid use lower-case indices [e.g., $x_1(i)$].
- The current time step for the coarse grid is indicated by the upper case superscript N , while the current fine time step is indicated by the lower case superscript n .

Typically, $n = \nu N$. To designate a fine time step within a coarse time step, we use $n + \tau$, where $\tau = 0, 1, \dots, \nu$.

7. The *region of influence* (ROI) of a variable is defined as the area or volume over which that quantity is conserved. For zone-centred scalars on the coarse grid, this is the volume $\Delta V(I, J, K)$ (Figure 2.3a). For face-centred but volume-conserved quantities (*e.g.*, S_1), the ROI is the *staggered* volume [*e.g.*, $\frac{1}{2}(\Delta V(I, J, K) + \Delta V(I - 1, J, K))$] (Figure 2.3b). Finally, for face-centred but area-conserved quantities (*e.g.*, B_1), the ROI is the area of the face at which the vector component is centred [*e.g.*, $\Delta A_1(I, J, K)$] (Figure 2.3c).

Finally, while AZEuS is written in the covariant fashion of *ZEUS-2D* (Stone & Norman 1992a), our discussion is given in terms of Cartesian-like components with uniform zone sizes within each grid for simplicity. As such, $\Delta V/\delta V = \nu^3$, $\Delta A_m/\delta A_m = \nu^2$, $\Delta x_m/\delta x_m = \nu$, and $\Delta t/\delta t = \nu$. Some of the modifications necessary for curvilinear coordinates are given in Appendix 2.A.

2.3 Restriction

Restriction is the process by which data on the coarse grid are replaced by an average of data from an overlying fine grid. This must be done in a fashion that locally preserves all conservation laws and the solenoidal condition to within machine round-off error. Two types of restriction are considered: the conservative overwrite of coarse values with ROIs which are entirely covered by ROIs of overlying fine zones, and flux corrections to coarse

zones (sometimes called “refluxing”) with ROIs which are adjacent to, or partially covered by, the ROIs of fine zones.

2.3.1 Conservative Overwrite

At the end of a coarse time step, fine and coarse grids are synchronised by overwriting the coarse grid with “better” values from overlying fine grids. Because of the different ROIs on a staggered mesh, the specifics of the overwriting procedure depend on which variable is being overwritten. For zone-centred, volume-conserved quantities (*e.g.*, ρ , e , e_T), the procedure is the same as in BC89:

$$Q(I, J, K) = \frac{1}{\nu^3} \sum_{\alpha, \beta, \eta=0}^{\nu-1} q(i + \alpha, j + \beta, k + \eta), \quad (2.6)$$

which, by inspection, can be seen to conserve the quantity locally to within machine round-off error.

For face-centred, volume-conserved quantities such as the momentum density whose ROIs are completely covered by the ROIs of overlying fine zones, we have:

$$S_1(I, J, K) = \frac{1}{\nu^3} \sum_{\alpha=-\nu/2}^{\nu/2} \sum_{\beta, \eta=0}^{\nu-1} \mathcal{G}(\alpha) s_1(i + \alpha, j + \beta, k + \eta), \quad (2.7)$$

$$\text{where } \mathcal{G}(\alpha) = \begin{cases} 1/2 & \text{if } \alpha = \pm \nu/2 \\ 1 & \text{otherwise,} \end{cases} \quad (2.8)$$

for the 1-component of the momentum. The factor $\mathcal{G}(\alpha)$ takes into account that only half of the ROIs of the fine momenta at $\alpha = -\nu/2, \nu/2$ cover the ROI of coarse momentum (Figure 2.3b).

Coarse momenta with ROIs partially covered by a fine grid are co-spatial with the skin of the overlying fine grid. As skin values of momenta are considered to be boundary values (since one of the fluxes is completely determined from within the boundary), they are not taken to be more reliable than the underlying coarse values (whose fluxes are determined exclusively by interior zones), and thus the coarse values are not overwritten by the fine grid values. Instead, coarse momenta cospatial with a fine grid skin are considered to be adjacent to the fine grid and, as such, are subject to the “flux-correction” step described in the next subsection.

For magnetic fields, the conserved quantity is the magnetic flux ($\int \vec{B} \cdot d\vec{A}$). Thus, coarse values of B_1 are overwritten using:

$$B_1(I, J, K) = \frac{1}{\nu^2} \sum_{\beta, \eta = 0}^{\nu-1} b_1(i, j + \beta, k + \eta), \quad (2.9)$$

where the sum is over all fine ROIs (areas of 1-faces) that cover the coarse ROI. One can easily show that overwritten values of \vec{B} will still satisfy the solenoidal condition—even when combined with values of \vec{B} that are not overwritten—so long as the overlying values of \vec{b} are divergence-free and adjacent values of \vec{B} are properly “refluxed” (Section 2.3.2). In addition, since \vec{B} is an area-conserved quantity, there is never partial coverage of ROIs as there is with the momenta, and thus no analogue of $\mathcal{G}(\alpha)$ (equation 2.8) is necessary for the magnetic fields.

A straightforward permutation of indices gives the analogous expressions for the other components of momentum and magnetic field.

2.3.2 Flux Corrections

A coarse zone adjacent to but not covered by a fine grid shares a face with the fine grid. In order that local mass, momentum, and magnetic flux remain conserved to within machine round-off error, the coarse and fine zones must agree on the fluxes passing across their common face. This is accomplished by keeping track of all coarse fluxes passing across the skin of a contained fine grid, and then subtracting from these the fine fluxes computed during the MHD updates of the fine grids. These “flux corrections” are then subtracted from the coarse zones adjacent to the fine grid during the so-called “refluxing step”, effectively replacing the coarse fluxes with the fine fluxes along their common face.

For zone-centred, volume-conservative quantities this procedure follows BC89. Thus, for transport in the 1-direction, we have for the flux-corrected quantity, \tilde{Q} :

$$\tilde{Q}^{N+1}(I, J, K) = Q^{N+1}(I, J, K) - \frac{1}{\Delta V(I, J, K)} \left(F_{1,Q}^{N+\frac{1}{2}}(I, J, K) - \sum_{\beta, \eta, \tau=0}^{\nu-1} f_{1,q}^{n+\tau+\frac{1}{2}}(i, j + \beta, k + \eta) \right), \quad (2.10)$$

where the quantities in large brackets are the flux corrections. For the purpose of illustration, the coarse zone (I, J, K) is taken to be immediately to the right (increasing I) of a fine grid. $F_{1,Q}^{N+1/2}$ is the time-centred 1-flux of Q (with units $Q\mathcal{V}\Delta A\Delta t$, where \mathcal{V} is

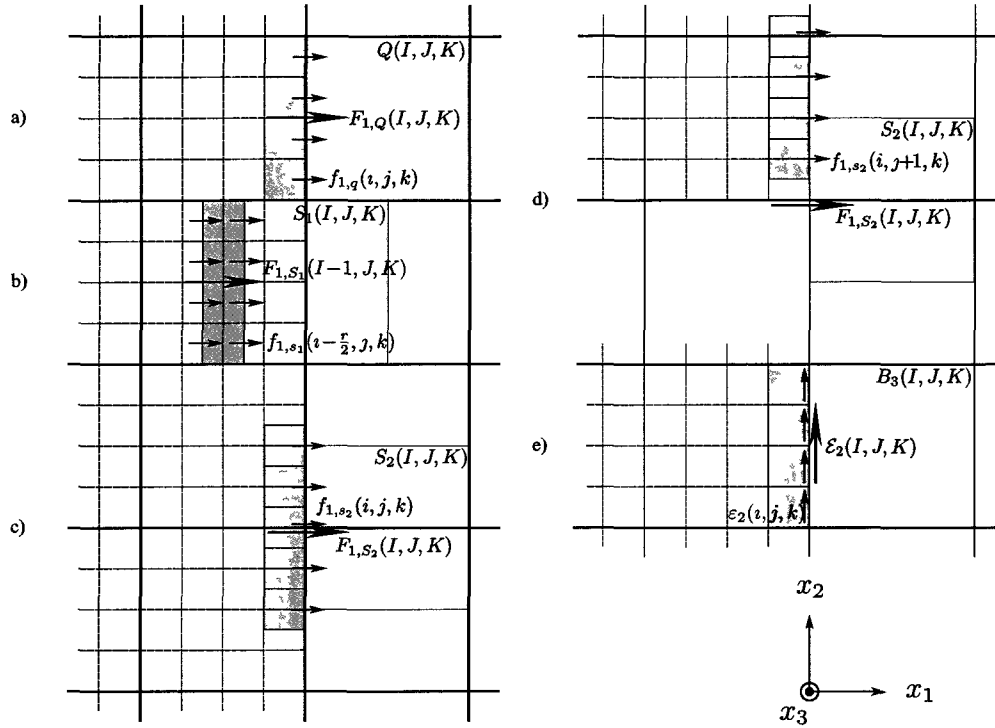


Figure 2.4 The different cases for flux corrections on a staggered grid, including: (a) zone-centred quantities; (b, c, and d) the three different cases for face-centred, volume-conserved momenta; and (e) area-conserved magnetic field corrections via the EMFs. Note that in this figure, all arrows correspond to components of fluxes or EMFs.

the coarse velocity)³ passing across the 1-face co-spatial with the skin of the fine grid, while $f_{1,q}^{n+\tau+1/2}$ are the corresponding fine fluxes (with units $qv\delta A\delta t$, where v is the fine velocity; Figure 2.4a). Note the sum over τ reflecting the fact there are several fine time steps (typically ν of them) within a single coarse time step.

When flux correcting the face-centred, volume-conserved momenta, we must depart from BC89 as there arise three different situations that must be dealt with explicitly.

First, when a component of momentum is normal to and straddling the boundary of a

³Strictly speaking, this is not a flux because of the factor Δt . However, for the purposes of accounting, we find it advantageous to define the fluxes with the time steps embedded.

fine grid, its ROI is only halfway inside the fine grid. Consider the coarse ROI of S_1 straddling the right boundary of a fine grid (Figure 2.4b). In this case, the flux correction takes the form:

$$\begin{aligned} \tilde{S}_1^{N+1}(I, J, K) = S_1^{N+1}(I, J, K) - \frac{1}{\Delta V(I, J, K)} & \left(F_{1,S_1}^{N+\frac{1}{2}}(I-1, J, K) \right. \\ & - \frac{1}{2} \sum_{\beta, \eta, \tau=0}^{\nu-1} \left(f_{1,s_1}^{n+\tau+\frac{1}{2}}(i - \frac{\nu}{2} - 1, j + \beta, k + \eta) \right. \\ & \left. \left. + f_{1,s_1}^{n+\tau+\frac{1}{2}}(i - \frac{\nu}{2}, j + \beta, k + \eta) \right) \right). \end{aligned} \quad (2.11)$$

Note that in the 1-direction, the coarse and fine momenta pass through the same face, but the fluxes do not. Thus, an average of the fine fluxes at $i - \nu/2 - 1$ and $i - \nu/2$ is needed to properly centre the fine fluxes, and to ensure local conservation of momentum flux.

Second, when a component of momentum lies adjacent to a fine grid and its direction is parallel to the fine grid boundary, its ROI is entirely outside the fine grid just as for a zone-centred quantity. For example, consider the 1-flux correction for the ROI of S_2 lying to the right of a fine grid (Figure 2.4c). The flux correction here is given by:

$$\begin{aligned} \tilde{S}_2^{N+1}(I, J, K) = S_2^{N+1}(I, J, K) - \frac{1}{\Delta V(I, J, K)} & \left(F_{1,S_2}^{N+\frac{1}{2}}(I, J, K) \right. \\ & \left. - \sum_{\beta=-\nu/2}^{\nu/2} \sum_{\eta, \tau=0}^{\nu-1} \mathcal{G}(\beta) f_{1,s_2}^{n+\tau+\frac{1}{2}}(i, j + \beta, k + \eta) \right). \end{aligned} \quad (2.12)$$

The factor $\mathcal{G}(\beta)$ (equation 2.8) ensures that only half of the fine 1-fluxes of the fine ROIs at $\beta = \pm\nu/2$ are included, as a quick glance at Figure 2.4c will verify.

The third case is similar to the second, with the coarse ROI also straddling a boundary in another direction (*i.e.*, at a corner of the fine grid; Figure 2.4d). Consider again the ROI of S_2 to the right of a fine grid that is also straddling a boundary in the 2-direction. The flux correction in this case is:

$$\begin{aligned} \tilde{S}_2^{N+1}(I, J, K) = S_2^{N+1}(I, J, K) - \frac{1}{\Delta V(I, J, K)} & \left(\frac{\nu - 1}{2\nu} F_{1, S_2}^{N+\frac{1}{2}}(I, J, K) \right. \\ & \left. - \sum_{\beta=1}^{\nu/2} \sum_{\eta, \tau=0}^{\nu-1} \mathcal{G}(\beta) f_{1, s_2}^{n+\tau+\frac{1}{2}}(i, j + \beta, k + \eta) \right), \end{aligned} \quad (2.13)$$

where the fraction $(\nu - 1)/2\nu$ is the *area filling ratio* between the fine to coarse fluxes. For example, for $\nu = 4$, $(\nu - 1)/2\nu = 3/8$ (Figure 2.4d), and 3/8 of the coarse flux must be replaced with the overlapping fine fluxes. Note that $f_{1, s_2}(i, j, k)$ does not contribute to the fine fluxes that replace part of the coarse flux since it is determined, in part, by values from the boundary region of the fine grid, and thus not taken as reliable enough to replace part of the coarse flux determined exclusively from active zones of the coarse grid.

For the magnetic field components, the operator in the evolution equation (equation 2.3) is the curl, and not the divergence of the hydrodynamical variables. Thus, \vec{B} is a surface conserved quantity (rather than volume-conserved) and, as such, we make adjustments to the EMFs instead of the fluxes; otherwise the procedure is the same. Consider the coarse ROI of B_3 immediately to the right of a fine grid (Figure 2.4e). Following

Balsara (2001), we have:

$$\tilde{B}_3^{N+1}(I, J, K) = B_3^{N+1}(I, J, K) + \frac{1}{\Delta A_3(I, J, K)} \left(\mathcal{E}_2^{N+\frac{1}{2}}(I, J, K) - \sum_{\beta, \tau=0}^{\nu-1} \varepsilon_2^{n+\tau+\frac{1}{2}}(i, j + \beta, k) \right), \quad (2.14)$$

where $\mathcal{E}_2^{N+1/2}(I, J, K) = E_2 \Delta x_2 \Delta t$ is the time-centred coarse 2-EMF⁴ (“electro-motive force”) located along the 2-edge, and where $\varepsilon_2^{n+\tau+1/2}(i, j + \beta, k)$ is the time-centred fine 2-EMF, located along the same 2-edge as the coarse 2-EMF. Here, the quantity in large brackets are the “EMF corrections”, analogous to the flux corrections for the hydrodynamical variables. In *ZEUS-3D*, the EMFs can be evaluated using various algorithms. In our case, we use the Consistent Method of Characteristics (CMoC) described by Clarke (1996).

Because the magnetic field is an area-conserved quantity, there is no situation where the coarse ROI of a magnetic field component is partially covered by fine ROIs as can happen for the volume-conserved, face-centred momentum. Thus, equation (2.14) and its permutations are sufficient to cover all EMF corrections for all field components in all directions. Note, for example, there are no corrections to be made in the 1-direction for the 1-field, again because of the surface conservative nature of the magnetic field.

Further, induction of magnetic field components penetrating the skin of a fine grid is affected by EMFs computed from quantities taken entirely from within the active portion of the grid. This is in contrast to a momentum component penetrating the skin, half of

⁴Similar to the hydrodynamical fluxes, we define the EMFs with the factor Δt embedded to simplify the accounting.

whose fluxes are computed from boundary values. Thus, we take the skin values of the EMFs and the magnetic components they induce to be just as reliable as those evaluated from within the grid, and it is appropriate to restrict the coarse magnetic field values on the skin of a fine grid with the overlying fine values (*e.g.*, equation 2.9).

Finally, expressions for flux corrections to coarse zones which are to the left of a fine grid (decreasing I) are derived by simply adding 1 to the first index of $F_{1,Q}$ or \mathcal{E}_i , adding ν to the first index of $f_{1,Q}$ or ε_i , and changing the sign of the correction terms in equations (2.10)–(2.14). Flux correction equations for coarse zones at the front or back (increasing or decreasing J), and top or bottom (increasing or decreasing K) of fine grids can be obtained by a suitable permutation of indices and subscripts.

2.4 Prolongation

Prolongation is the process by which fine grid zones are filled using the best information available. This could either be by interpolating values from the underlying coarse grid in a way to ensure local conservation and local monotonicity, or taking them from adjacent or overlapping fine grids. As with restriction, prolongation can be divided into two types. First, when a fine grid is created or extended, the new fine zones must be filled. Second, at the beginning of a fine grid time step, fine boundary zones must be set. Both types require interpolation methods, some of which have been introduced here specifically for static grid refinement.

2.4.1 Spatial interpolation

In an effort to minimise the errors caused by waves travelling across boundaries between fine and coarse grids, we have introduced higher-order interpolation schemes (*e.g.*, piecewise parabolic interpolation, PPI, Colella & Woodward 1984; CW84) to the prolongation step. This improves the results for adaptive refinement, and has proven important for static refinement where strong waves are required to cross grid boundaries. By design, these interpolation schemes honour conservation laws and monotonicity.

In all cases and for all variables, we begin by estimating the interface values $Q_{L,R}(I)$ from cubic fits to the coarse grid data (Section 1 of CW84) without the monotonisation or steepening steps. Now, to fit a parabolic interpolation function, $q_1^*(x)$, across the coarse ROI for zone I , we need three constraints. Two come from requiring that $q_1^*(x)$ passes through $Q_{L,R}(I)$, while the third comes from requiring that the zone-average value $Q(I, J, K)$ times the zone volume equal the volume integral of $q_1^*(x)$. For the original PPI scheme, this final constraint is written as:

$$Q(I, J, K)\Delta x_1(I) = \int_{\Delta x} q_1^*(x)dx.$$

For our purposes, we need to interpolate fine zone *averages* from the coarse ones and, as such, the conserved quantity is the *Riemann sum* and not the integral. Thus, in the 1-direction, our final constraint is:

$$Q(I, J, K)\Delta x_1(I) = \sum_{\alpha=0}^{\nu-1} q_1^*(i + \alpha, j, k) \delta x_1(i) \quad (2.15)$$

$$\Rightarrow Q(I, J, K) = \frac{1}{\nu} \sum_{\alpha=0}^{\nu-1} q_1^*(i + \alpha, j, k) \quad (2.16)$$

for constant Δx , δx . With this, our parabolic interpolation function is (*c.f.*, equation 1.4 in CW84):

$$q_1^*(i + \alpha) = Q_L(I) + \zeta(Q_R(I) - Q_L(I) - \mathcal{H}_1(1 - \zeta)), \quad (2.17)$$

where:

$$\begin{aligned} \zeta &= \frac{x_1(i + \alpha) - x_1(I)}{\Delta x_1(I)}; \\ \mathcal{H}_1 &= \frac{1}{f_2(\nu) - f_1(\nu)} \left(Q(I, J, K) - Q_L(I) - f_1(\nu)(Q_R(I) - Q_L(I)) \right); \\ f_1(\nu) &= \frac{1}{2\nu^2} \sum_{\xi=1}^{\nu} (2\xi - 1); \quad f_2(\nu) = \frac{1}{4\nu^3} \sum_{\xi=1}^{\nu} (2\xi - 1)^2. \end{aligned} \quad (2.18)$$

With $q_1^*(i + \alpha)$ determined, we set the differences between the fine and coarse zones:

$$\delta q_1(i + \alpha) = q_1^*(i + \alpha) - Q(I, J, K). \quad (2.19)$$

For zone-centred quantities, we determine the fine-zone differences in the manner of equation (2.19) in each of the three directions, and set the interpolated fine zone averages to be:

$$q(i + \alpha, j + \beta, k + \eta) = Q(I, J, K) + \delta q_1(i + \alpha) + \delta q_2(j + \beta) + \delta q_3(k + \eta). \quad (2.20)$$

Given equation (2.16) and analogous expressions in the 2- and 3-directions, it is easy to show that this prescription is conservative; that is,

$$Q(I, J, K) = \frac{1}{\nu^3} \sum_{\alpha, \beta, \eta=0}^{\nu-1} q(i + \alpha, j + \beta, k + \eta), \quad (2.21)$$

for uniform grids ($\Delta V = \nu^3 \delta V$).

For face-centred quantities, we determine the fine-zone differences in the manner of equation (2.19) in each of the two orthogonal directions (*e.g.*, in the 2- and 3-directions for S_1), and set the interpolated fine zone averages along each coarse face to be:

$$s_1(i, j + \beta, k + \eta) = S_1(I, J, K) + \delta s_{1,2}(j + \beta) + \delta s_{1,3}(k + \eta). \quad (2.22)$$

Exactly the same procedure is used to interpolate B_1 across each coarse 1-face. As with the zone-centred quantities, it is easy to show that this procedure conserves momentum (magnetic) flux on the face:

$$S_1(I, J, K) = \frac{1}{\nu^2} \sum_{\beta, \eta=0}^{\nu-1} s_1(i, j + \beta, k + \eta). \quad (2.23)$$

The next step is to interpolate the face-centred quantities into the interior of the zone, and it is here where the procedure for momentum and magnetic components diverge.

For the volume-conserved momenta, we perform a linear interpolation between the fine momenta on opposing coarse faces. For example, between $s_1(i, j + \beta, k + \eta)$ and

$s_1(i + \nu, j + \beta, k + \eta)$ we set:

$$s_1(i + \alpha, j + \beta, k + \eta) = (1 - \zeta) s_1(i, j + \beta, k + \eta) + \zeta s_1(i + \nu, j + \beta, k + \eta), \quad (2.24)$$

where $\alpha = 1, \dots, \nu - 1$ and $\zeta = \alpha \delta x / \Delta x$. This prescription guarantees that over a *zone-centred volume*, the prolongation of the 1-momentum is conservative. The fact that conservation is over the zone-centred volume and not specifically the 1-momentum ROI is required for equations (2.23) and (2.24) to be consistent with the restriction procedure of equation (2.11).

For the area-conserved magnetic fields, a simple linear interpolation between opposing coarse faces does not preserve the solenoidal condition. Thus, we turn to a generalised, directionally unsplit version of the algorithm described by Li & Li (2004) in which $\nabla \cdot \vec{b} = 0$ so long as $\nabla \cdot \vec{B} = 0$ holds on the underlying coarse grid.

In this approach, we take the coarse and recently interpolated fine values of magnetic field (equation 2.22), and apply the solenoidal condition to determine “intermediate” coarse field values (*e.g.*, B_1^* ; Figure 2.5), which are cospatial with fine zone faces. For example, the intermediate values for B_1 are given by:

$$B_1^*(i + \alpha + 1) = B_1^*(i + \alpha) - \delta x_1(i + \alpha) \left(\frac{b_{2,1}^*(i + \alpha, j + \nu, k) - b_{2,1}^*(i + \alpha, j, k)}{\Delta x_2(J)} + \frac{b_{3,1}^*(i + \alpha, j, k + \nu) - b_{3,1}^*(i + \alpha, j, k)}{\Delta x_3(K)} \right), \quad (2.25)$$

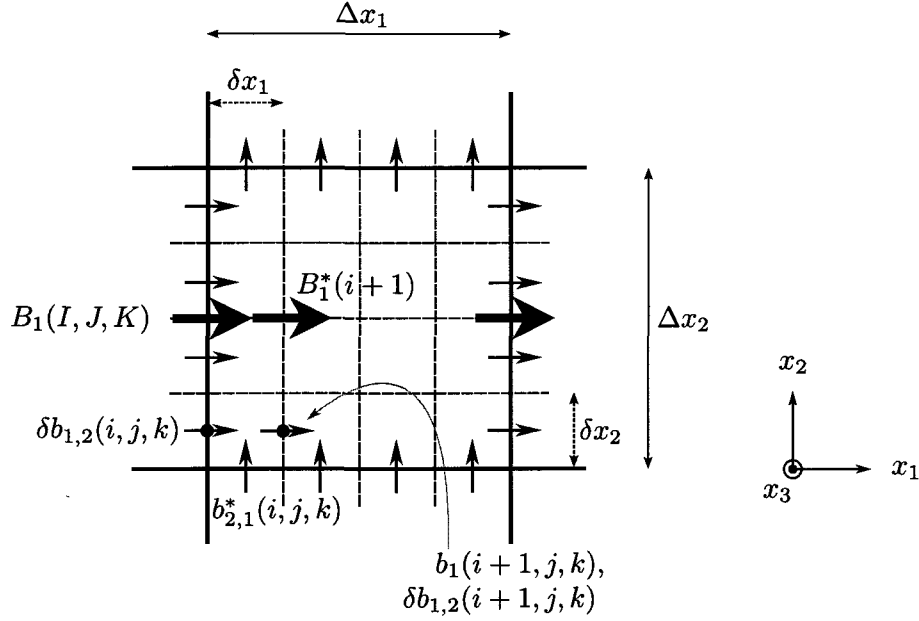


Figure 2.5 Schematic representation of the directionally unsplit Li & Li algorithm for calculating fine values of \bar{b} between coarse grid faces when $\nu = 4$.

where:

$$\begin{aligned}
 b_{2,1}^*(i + \alpha, j, k) &= \frac{1}{\nu} \sum_{\eta=0}^{\nu-1} b_2(i + \alpha, j, k + \eta), \\
 b_{3,1}^*(i + \alpha, j, k) &= \frac{1}{\nu} \sum_{\beta=0}^{\nu-1} b_3(i + \alpha, j + \beta, k); \\
 B_1^*(i + 0) &= B_1(I, J, K),
 \end{aligned} \tag{2.26}$$

and $0 \leq \alpha \leq \nu - 2$. Given $B_1^*(i + \alpha + 1)$, and the differences between fine and coarse values at the coarse faces ($\delta b_{1,l}$, $l = 2, 3$; equation 2.19), we then calculate the fine magnetic fields

at $i + \alpha + 1$:

$$\begin{aligned} b_1(i + \alpha + 1, j + \beta, k + \eta) = & B_1^*(i + \alpha + 1) + \delta b_{1,2}(i + \alpha + 1, j + \beta, k) \\ & + \delta b_{1,3}(i + \alpha + 1, j, k + \eta), \end{aligned} \quad (2.27)$$

where:

$$\begin{aligned} \delta b_{1,2}(i + \alpha, j + \beta, k) = & (1 - \zeta) \delta b_{1,2}(i, j + \beta, k) + \zeta \delta b_{1,2}(i + \nu, j + \beta, k), \\ \delta b_{1,3}(i + \alpha, j, k + \eta) = & (1 - \zeta) \delta b_{1,3}(i, j, k + \eta) + \zeta \delta b_{1,3}(i + \nu, j, k + \eta), \end{aligned} \quad (2.28)$$

and $\zeta = \alpha \delta x / \Delta x$.

Proceeding incrementally from $i + 1$ to $i + \nu - 1$ provides all of the values of $b_1(i, j, k)$ between the coarse faces (I, J, K) and $(I + 1, J, K)$. Values for the other magnetic field components are given by a straightforward permutation of indices.

Finally, we offer a note on the use of vector potentials. Igumenshchev & Narayan (2002) have demonstrated that the vector potential, \vec{A} , may be used in the CT algorithm (Evans & Hawley 1988) instead of the magnetic field with results identical to machine round-off error. Thus, one may be tempted to adopt this approach so that prolongation methods simpler than the Li & Li algorithm may be used on \vec{A} as a way to guarantee that the fine grid satisfies the solenoidal condition. Reasons for *not* taking this approach are given in Appendix 2.B.

2.4.2 Temporal interpolation

Fine grids require prolonged boundary values at the beginning of each fine time step, and thus we also need to perform temporal interpolations on the coarse values. Following BC89, we perform a linear interpolation on the coarse hydrodynamic variables in time, and then spatially interpolate them as described above to obtain the necessary boundary information for each fine time step.

For the magnetic fields, the fine components penetrating the skins of the fine grid are retained; only those values completely within the boundary region need to be prolonged from the coarse grid. Temporal interpolations cannot be performed directly on the coarse magnetic field components without violating the solenoidal condition. Instead, we perform a linear interpolation on the coarse EMFs in time, replacing those coincident with the skin of the fine grid with spatial and temporal sums of the overlying fine values. Thus and for example, we set

$$\mathcal{E}_2^{N+\psi}(I, J, K) = \sum_{\tau=0}^{\tau'} \sum_{\beta=0}^{\nu-1} \varepsilon_2^{n+\tau+\frac{1}{2}}(i, j + \beta, k), \quad (2.29)$$

where $\psi = (2\tau' + 1)/2\nu$, and where $0 \leq \tau' \leq \nu - 2$ designates the last completed fine time step. Equation (2.29) gives the properly time-centred values for \mathcal{E}_2 necessary to update the coarse magnetic field components from the coarse time step N to the end of each fine time step contained within the single coarse time step, except for the final one. In turn, the coarse fields are interpolated spatially as described above to obtain the necessary fine magnetic boundary values.

2.4.3 Monotonicity

We have found it necessary to maintain a certain monotonicity in our prolongations. Failure to do so can lead to negative pressures (even when solving the internal energy equation) and violations of the CFL condition. For example, if the current time step is governed by the sound speed, and the prolongation process leads to an interpolated density less than the surrounding zones, the sound speed in a fine zone could be greater than that which was used in determining the CFL time step, possibly leading to numerical oscillations and loss of stability.

Sequentially stringing together two (or three) 1-D PPIs as we do for prolongation of zone-centred quantities (*e.g.*, equation 2.20) can lead to non-monotonic behaviour even if each 1-D interpolation is separately monotonic. If a PPI-determined value $q(i + \alpha, j + \beta, k + \eta)$ is found to lie outside the range set by neighbouring coarse zones:

$$\left. \begin{aligned} Q_{\min} &= \min (Q(I + \Gamma, J + \Lambda, K + \Upsilon)); \\ Q_{\max} &= \max (Q(I + \Gamma, J + \Lambda, K + \Upsilon)), \end{aligned} \right\} -1 \leq \Gamma, \Lambda, \Upsilon \leq +1,$$

then we “fall back” to piece-wise linear interpolations (PLI; van Leer 1977). In rare cases where the PLI-determined value is also non-monotonic (possible only in 3-D), we revert to piece-wise constant interpolations (PCI, *a.k.a.* “direct injection” or “donor cell”):

$$q(i + \alpha, j + \beta, k + \eta) = Q(I, J, K).$$

Where PPI yields non-monotonic results, we note that transmission of strong waves across changes in resolution (*e.g.*, static grids) is significantly improved if one first tries PLI rather than falling back directly to PCI or limiting the interpolated value to lie between Q_{\min} and Q_{\max} .

2.5 Boundary conditions

Boundary conditions are applied directly to the hydrodynamical variables (ρ , e , \vec{v}) and indirectly to the magnetic field via the EMFs. Attempting to apply boundary conditions directly to \vec{B} often generates monopoles in the boundary regions, which can have disastrous effects on the dynamics in the active grid.

In addition to the usual boundary conditions applied by the *ZEUS-3D* module during each MHD cycle, the AMR module must also set boundary conditions on two occasions. After restriction and before prolongation, boundary values are set on the coarse grid. Then, after prolongation and before the *ZEUS-3D* module is called for the next MHD cycle; boundary values for the fine grid are set using the results of the prolongation step. These additional applications of boundary conditions are necessary to maintain the imposed physical boundaries after restriction and prolongation have altered some of the values on the active grid, and to reconcile boundaries of grids that may be contained within or adjacent to other grids, henceforth referred to as *adjacent boundaries*.

Because of their nature, physical boundaries (inflow, outflow, reflecting; those traditionally applied by single-grid MHD codes), and adjacent boundaries must be treated differently, and each is discussed in turn.

2.5.1 Physical Boundaries

Generally, a fine grid is completely embedded within a coarse grid. The single exception is when both grids share a physical boundary and two items of note must be borne in mind when adapting the physical boundary condition routines in *ZEUS-3D* to *AZEuS*.

First, since each grid has only two boundary zones, only part of the coarse boundary region is covered by fine boundary zones. Thus, coarse boundary zones cannot be included in the restriction step; a particular concern when setting magnetic boundary conditions. In *AZEuS*, we extend the EMF correction scheme of Section 2.3.2 by retaining *three* layers of transverse EMF corrections, and *two* layers of longitudinal EMF corrections⁵, including the skin layer plus two additional layers interior and adjacent to the skin. Immediately before the restriction step, physical boundary conditions are applied to the EMF corrections, which are then used to update the boundary values of the magnetic field components in the coarse grid according to equation (2.14). Done in this fashion, there is no risk of introducing monopoles to the coarse boundary zones during the restriction step when two or more grids overlap a physical boundary.

Second, not handled properly, inflow boundary conditions can introduce unexpected violations of conservation laws which can cause unwanted discontinuities in the boundary. In particular, if a boundary variable is to be set according to an analytical function of the coordinates, that variable should be set to the *zone average* of that function, and not simply to the function value at the location of the variable. While this is good advice for a single grid application, it is critical for AMR.

⁵*e.g.*, the transverse (longitudinal) EMFs for the 1-boundary are ε_2 and ε_3 (ε_1).

Similarly, for the fine zones,

$$m(j) = \frac{\delta r \delta z}{(r - \frac{1}{2}\delta r)^{1/2}}; \quad m(j+1) = \frac{\delta r \delta z}{(r + \frac{1}{2}\delta r)^{1/2}}.$$

Adding the masses in the four fine zones contained by the coarse zone, we find:

$$2(m(j) + m(j+1)) = m(J) \left(1 + \frac{3}{32} \left(\frac{\delta r}{r} \right)^2 + \dots \right) > m(J),$$

and the physical boundary conditions violate mass conservation.

Instead, $\rho(J)$ should be set to the *zone average*, determined by:

$$\rho(J) = \frac{m(J)}{\Delta V(J)}$$

where the mass function, $m(J)$, is given by:

$$m(J) = \int_{\Delta V(J)} \rho(r) dV, \quad (2.31)$$

where $\rho(r)$ is the given density profile (*e.g.*, equation 2.30). Similar expressions apply for $m(j)$, and $m(j+1)$. Done in this fashion, it is easy to show that

$$\rho(J)\Delta V(J) = 2(\rho(j+1)\delta V(j+1) + \rho(j)\delta V(j)),$$

and both grids agree on the mass contained with coarse boundary zone J to within machine round-off error. With a little bit of algebra, this can be confirmed analytically for the

specific case of equation (2.30). For more complicated profiles, a numerical integrator can be employed to perform the necessary integrations in equation (2.31).

2.5.2 Adjacent Boundaries

Unlike Godunov methods which typically require a single application of boundary conditions at the end of each MHD cycle, the operator-split nature of *ZEUS-3D* requires boundary conditions to be set several times. For physical boundaries, this is not an issue; physical boundary conditions may be set whenever needed based on data from a single grid. However, adjacent boundaries pose a unique challenge in *AZEuS* since the *ZEUS-3D* module is aware only of the grid being updated, and other grids cannot be accessed in the middle of an MHD cycle to update these boundaries.

We have introduced into *AZEuS* the concept of “self-computing” boundary conditions for adjacent boundaries. In this approach, boundary zones are set at the beginning of each time step using the best information available (either from an adjacent grid of the same resolution, or from the prolongation of an underlying coarse grid possibly interpolated in time), and then the full set of operator-split MHD equations are applied to both the boundary and active zones; no adjacent boundary zones are reset to any pre-determined quantity inside a single MHD time step.

Of course, assumptions about missing data beyond the outermost edge of the grid must be made, and “pollution” from these missing data necessarily propagates inward. For example, consider the left 1-boundary where $v_1(i = 1)$ and $v_1(i = 2)$ represent the boundary values of v_1 , $v_1(i = 3)$ the skin value (treated as a boundary value), and $v_1(i = 4)$

the first active value. The pressure gradient at $v_1(i = 1)$ is proportional to $p(i = 1) - p(i = 0)$, yet $p(i = 0)$ is completely unknown [$p(i = 1)$ and $p(i = 2)$ are the only boundary values available]. The best we can do for a missing datum such as this is to extrapolate assuming a zero-gradient, in which case $p(i = 0) = p(i = 1)$ and no pressure gradient is applied to $v_1(i = 1)$. In this manner, $v_1(i = 1)$ is polluted by the missing datum at the very beginning of the source step.

Additional steps inside a single MHD cycle include the application of artificial viscosity, adiabatic expansion/compression for the internal energy equation, the transport steps, and the induction step. All but the latter contribute to propagating pollution from missing data toward the active portion of the grid. Ideally, one would carry enough boundary zones to prevent pollution from reaching the active grid within a single MHD step, so that the AMR module (with knowledge of all grids) can reset all boundary values to new and unpolluted values before their effects ever reach the active zones. However, for van Leer (1977) interpolation in the transport step and within a single MHD cycle, pollution from missing data reaches the skin and first active zone-centre on the grid, as well as the first active face and second active zone-centre if the local velocity points away from the boundary (true regardless of which energy equation is used). Thus, to completely prevent pollution from reaching the active grid, we would have to double the number of boundary zones from two to four.

We have investigated this effect thoroughly and have found no test problem that demonstrates anything but the slightest quantitative effect from pollution by missing data at adjacent boundaries between fine and coarse grids. For adjacent boundaries between

grids of like resolution, we have elected to force these grids to overlap (for reasons explained in Section 2.6) by an amount sufficient to eliminate the problem of missing data pollution altogether.

Finally, self-computed boundary zones are included in the calculation of the Courant-limited time step. For an operator-split code such as AZEuS, this step is critical in minimising transmission errors when waves of any significant amplitude cross adjacent boundaries.

2.6 Grid creation and adaptation

Creation or modification of adaptive grids in AZEuS proceeds in a manner similar to Bell *et al.* (1994) including the suggestions of Berger & Rigoutsos (1991), with two important differences. First, we have had to modify the proper nesting criterion of BC89 by increasing from one to three the number of zones at level $l - 1$ separating an active zone at level l from level $l - 2$. This is because prolongation of boundary values for level l from level $l - 1$ requires one zone from level $l - 1$ beyond the edge of a grid at level l , plus two additional zones at level $l - 1$ on either side to satisfy the five-zone molecule needed by PPI.

Second, BC89 allow grids of the same resolution to abut without overlapping, whereas we have found it advantageous for at least two reasons to extend abutting grids so that they overlap by a minimum of one coarse zone (Figure 2.7). For one, since the momenta penetrating a grid skin are no more reliable than boundary values, two abutting grids would, in general, disagree on the values of the momentum penetrating their common skin.

This turns out to pose an intolerable ambiguity in the solution. Second, the problem of pollution propagating from missing data onto the active grid (Section 2.5.2) is completely averted by overlapping two abutting grids by one coarse zone.

By forcing abutting grids to overlap, there is always a clear choice of which value to use at a given location. Where the boundary and skin values of one grid overlap the active zone values of another, the active zone values prevail, and are used by the other grid for its boundary values.

Grids which are abutting at the end of the grid generation and modification process, but before they are prolonged, are made to overlap by one coarse zone. Numerous situations arise in which more than one grid may overlap at the same location (*e.g.*, the test problems in sections 2.7.2 and 2.7.2), and this can result in overlaps which are greater than one coarse zone. Further, the possibility of a complex distribution of AMR grids opens up a whole host of pedagogical cases which one must consider, particularly when looking to maintain the solenoidal condition. During the development of AZEuS, we have carefully examined each case involving multiple levels with numerous grids overlapping each other, to ensure that where grids overlap, they all agree on the flow variables and all conservation laws are preserved to machine round-off error.

Note that mismatched momentum and velocity components can be more insidious than one might at first imagine. With mismatched velocities, CMoC will generate mismatching EMFs on the two grids, and this can lead to monopoles. Even if such monopoles are restricted entirely to the boundary zones, their unphysical forces can affect neighbouring active zones whose effects propagate rapidly throughout the grid. Preserving

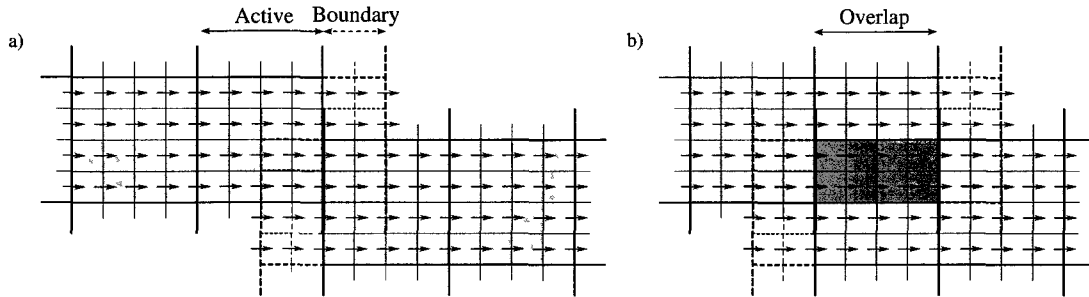


Figure 2.7 Two grids that originally abut (panel a) are made to overlap by at least one coarse zone (panel b).

agreement between overlapping zones including boundary zones to machine round-off is, therefore, of paramount importance.

2.7 Numerical Tests

We have verified AZEuS against a number of standard test problems, some of which are presented in this section. Further results will be posted to <http://www.ica.smu.ca/azeus>, as they become available. Additional and similar test problems for *ZEUS-3D* (without AMR) are found in Clarke (2010) and on-line at <http://www.ica.smu.ca/zeus3d>.

2.7.1 1-D shock tubes

While most AMR applications rely exclusively on dynamic grids, certain applications, particularly those which exhibit some degree of self-similarity, can benefit enormously from the use of a base of nested, static grids (*e.g.*, Ramsey & Clarke 2011). As such solutions evolve, waves of all types—including strong shocks—must pass sequentially from one grid

to another, and it is here where our higher order prolongation algorithms for adjacent boundaries are critical.

AZEuS has been tested with all 1-D shock tube problems from Ryu & Jones (1995; RJ95) for both static and dynamic grids, and we show the results from two to highlight these features of the code. Both tests use the total energy equation with $\gamma = 5/3$, $\mathcal{C} = 0.75$ (Courant number), and artificial viscosity parameters $q_{\text{con}} = 1.0$ and $q_{\text{lin}} = 0.2$.

For static grids, Figure 2.8 shows two solutions for ρ , e_T , v_2 , and B_2 from problem (4a) of RJ95 over a domain of $x_1 \in [-0.5, 2.5]$ (three times larger than RJ95) for a time $t = 0.45$ (three times longer). The initial discontinuity is placed at $x_1 = 0.5$, with the left and right states given in the figure caption. The left panels show the domain resolved with 1200 zones and no AMR, while the central panels show the AMR solution with a base resolution of 600 zones and fine static grids with a refinement ratio of 2 placed at $x_1 \in [-0.2, 0.1]$ and $x_1 \in [0.7, 1.245]$ (grey). These locations allow all the physical features, with the exception of the sluggish slow rarefaction, to suffer at least one change in resolution. The right panels show the percent differences between the two solutions.

Discounting all zones trapped within a discontinuity (which, even without AMR, are already in error by as much as 100% since discontinuities are supposed to be infinitely sharp), the maximum error one can attribute to the use of static grids in any of the variables is less than 1%. As further evidence of the ability of AZEuS to pass waves of all types across adjacent boundaries, Ramsey & Clarke (2011) find almost no sign of reflection, refraction, or distortion of any type of wave across any of the static

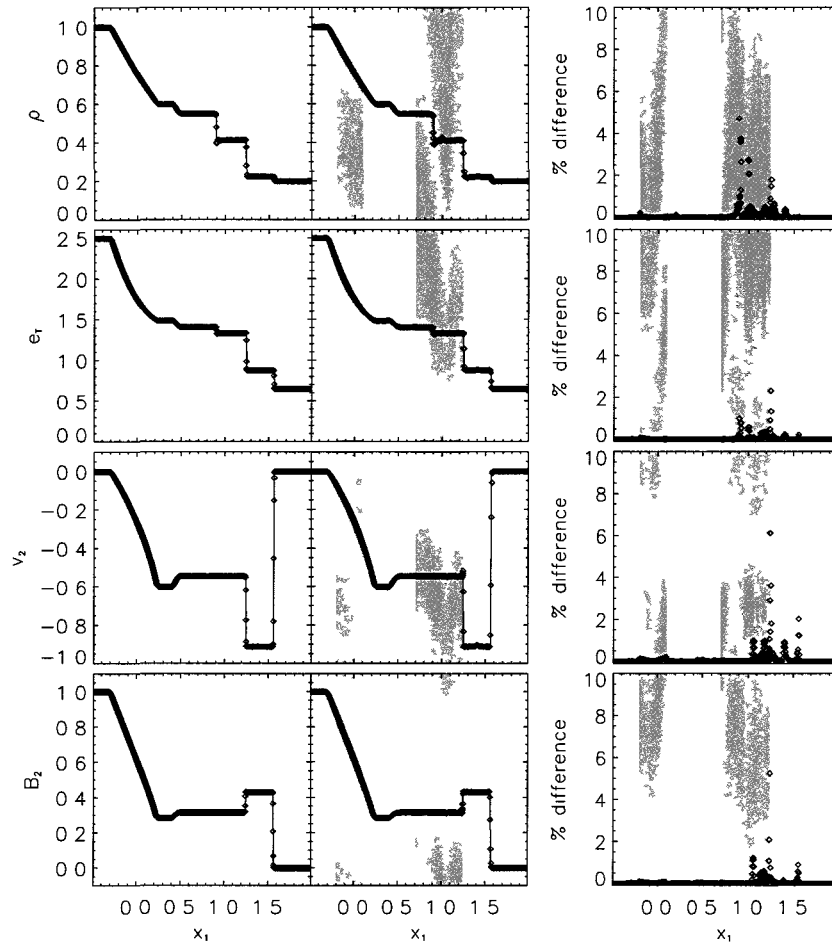


Figure 2.8 Static grid solution to problem (4a) of RJ95 at time $t = 0.45$. The initial left and right states are $(\rho, v_1, v_2, v_3, B_2, B_3, p) = (1, 0, 0, 0, 1, 0, 1)$ and $(0.2, 0, 0, 0, 0, 0, 0.1)$, with $B_1 = 1$. From left to right, the physical features are: (1) fast rarefaction, (2) slow rarefaction, (3) contact discontinuity, (4) slow shock, and (5) “switch-on” shock. *Left panels*: uniform “fine” grid solution; *middle panels*: same solution with two fine, static grids (gray) overlying the coarse grid; *right panel*: percent difference between the uniform and static grid solutions. Solid lines are the analytical solutions from the Riemann solver described in RJ95.

grid boundaries in their 2-D axisymmetric simulations of protostellar jets in cylindrical coordinates.

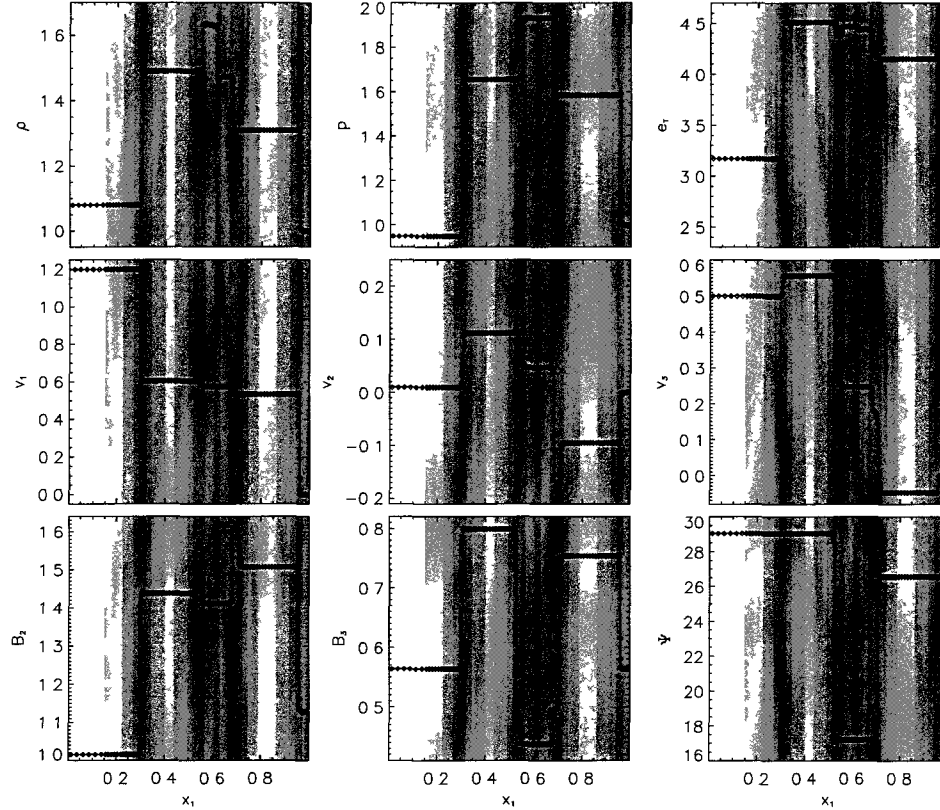


Figure 2.9 AZEuS solution to problem (2a) of RJ95 at $t = 0.20$. The initial left and right states are $(\rho, v_1, v_2, v_3, B_2, B_3, p) = (1.08, 1.2, 0.01, 0.5, 3.6/\sqrt{4\pi}, 2/\sqrt{4\pi}, 0.95)$ and $(1, 0, 0, 0, 4/\sqrt{4\pi}, 2/\sqrt{4\pi}, 1)$, with $B_1 = 2/\sqrt{4\pi}$. The physical features, from left to right, are: (1) fast shock, (2) rotational discontinuity, (3) slow shock, (4) contact discontinuity, (5) slow shock, (6) rotational discontinuity, and (7) fast shock. Shaded regions indicate the location of finer grids, with the level of shading indicating the level of refinement. $\Psi = \tan^{-1}(B_3/B_2)$ is the angle between the transverse field components. The solid lines are the analytical solution from the Riemann solver described in RJ95.

For dynamic grids, Figure 2.9 illustrates the results of test problem (2a) of RJ95.

We employ four levels of refinement (sequentially darker shades of grey) above the base grid with a resolution of 40 zones over the domain $x_1 \in [0.0, 1.0]$. The initial discontinuity is located at $x_1 = 0.5$, with the left and right states given in the figure caption. To

track the developing features, refinements are based on three criteria (Khokhlov 1998): contact discontinuities (CD), shocks, and gradients in certain variables, each requiring a threshold value to be set above which a zone is flagged for refinement. Here, we set parameters `tolcd` = `tolshk` = 0.1 for CDs and shocks, respectively, and check v_2 for gradients above `tolgrad` = 0.1. For this problem, the gradient detector is needed to refine both the discontinuity of the initial conditions as well as rotational discontinuities ($x_1 \simeq 0.53$ and $x_1 \simeq 0.71$ in Figure 2.9), neither of which are detectable as a CD or shock.

Additional parameters used to obtain this solution include `kcheck` = 5 (the number of cycles between successive grid modifications), `geffcy` = 0.95 (the minimum allowed grid efficiency, defined as the ratio of zones flagged for refinement to the number of zones actually present in a new grid), and `ibuff` = 2 (the number of buffer zones added around flagged zones).

2.7.2 2-D tests

MHD Blast

The MHD blast problem of Londrillo & Del Zanna (2000) and Gardiner & Stone (2005) has proven to be a very valuable test of our AMR algorithms and for rooting out problems in the code. It is also a good test of directional biases and the ability of a code to handle the evolution of strong MHD waves. We initialise the problem in the same manner as Clarke (2010) with domain $x \in [-0.5, 0.5], y \in [-0.5, 0.5]$ and $(\rho, \vec{v}, B_1, B_2, B_3) = (1, 0, 5\sqrt{2}, 5\sqrt{2}, 0)$ everywhere. Within radius $r = 0.125$ of the origin, we set the gas pressure to $p = 100$, and $p = 1$ elsewhere.

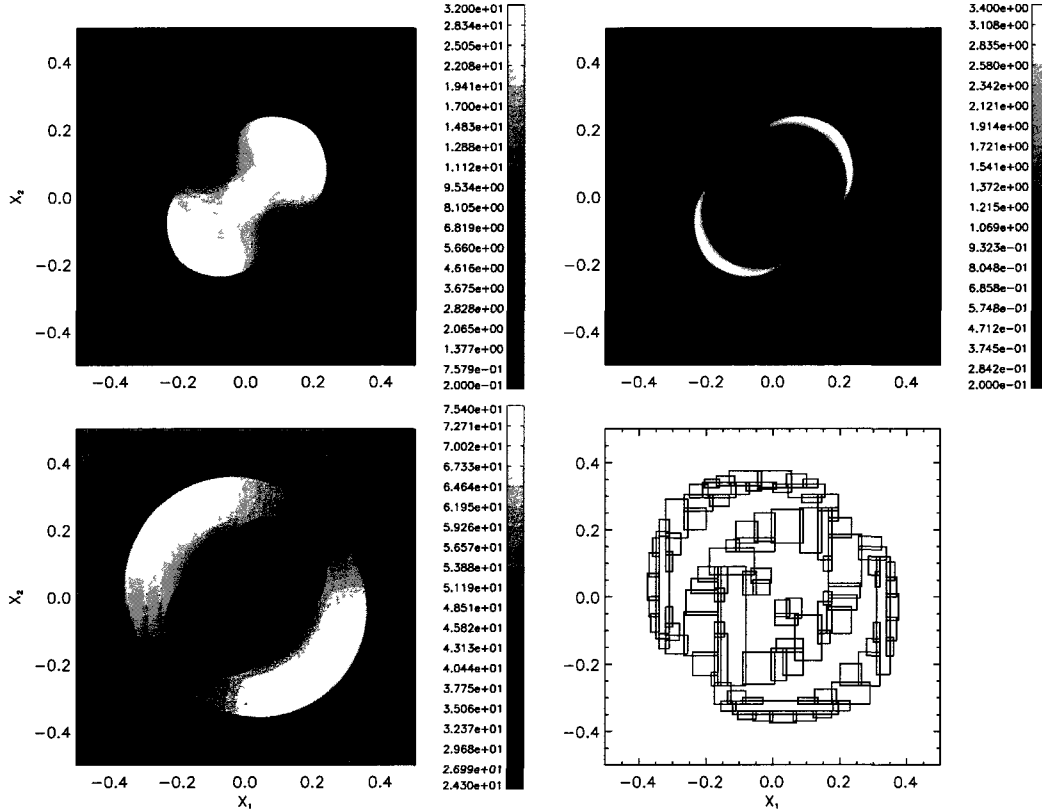


Figure 2.10 AZEuS solution for the 2-D MHD blast problem at $t = 0.02$ using 2 levels of refinement. *Top left:* gas pressure; *bottom left:* magnetic pressure ($p_B = |B|^2/2$); *top right:* gas density; and *bottom right:* distribution of AMR grids at $t = 0.02$.

Figure 2.10 presents our results for the 2-D blast problem at $t = 0.02$ for a base grid of 200^2 zones, and one additional level of refinement with ratio $\nu = 2$. For this test, we have purposely chosen a high grid efficiency of $\text{geffcy} = 0.92$ to strenuously test the ability of AZEuS to handle a large number of grids in a complicated pattern and refine on features which are not preferentially aligned with a coordinate axis. Typically, a lower value for the grid efficiency is used (*e.g.*, $\text{geffcy} \simeq 0.7$) to try and balance minimising

| | AMR | | Uniform, 200 ² | | Uniform, 400 ² | |
|--------|-------|------|---------------------------|------|---------------------------|------|
| | Min | Max | Min | Max | Min | Max |
| ρ | 0.201 | 3.36 | 0.200 | 3.22 | 0.189 | 3.40 |
| p | 0.737 | 32.3 | 0.771 | 32.0 | 0.714 | 32.1 |
| p_B | 24.2 | 75.7 | 24.9 | 76.0 | 23.6 | 75.6 |

Table 2.1 Extrema for density, ρ , gas pressure, p , and magnetic pressure, p_B , in AMR and uniform grid solutions of the 2-D MHD blast problem at $t = 0.02$.

the number of refined zones with the overhead associated with managing an increasing number of small grids.

Evidently, AZEuS is able to follow the blast wave closely, regardless of its orientation. Table 2.1 compares the extrema of the plotted variables between the AMR calculation and uniform grid solutions with 200² and 400² zones. With the exception of the density, which exhibits differences between the uniform 200² and AMR solutions of $\lesssim 0.5\%$, the uniform grid results bracket the AMR solution.

For this test, we set `tolshk` = `tolcd` = 0.2, and apply `tolgrad` = 0.2 to e_T . While the gradient detector is useful in refining the initial pressure jump, most ($\sim 99.9\%$) of the zones flagged for refinement soon thereafter are detected by the CD and shock detectors. Additional parameter settings include `kcheck` = 10, `ibuff` = 3, $\gamma = 5/3$, `C` = 0.5, `qcon` = 1.0, and `qlin` = 0.1. All boundaries are set to outflow conditions.

Orszag-Tang MHD vortex

The 2-D vortex problem of Orszag & Tang (1979) has become a standard test for astrophysical MHD codes, and as it has not previously been performed using our version of *ZEUS-3D*, we present both non-AMR and AMR results here. It is important to note

that the same code was used to produce both sets of results: AZEuS is designed to be modular, and by deselecting the ‘AMR’ option at the precompilation step, the code reverts to ZEUS-3D.

For this test, we follow Stone *et al.* (2008) by initialising a periodic, Cartesian box of size $x, y \in [0, 1]$ with initially constant pressure and density, $P = 5/12\pi$ and $\rho = \gamma P = 25/36\pi$, for $\gamma = 5/3$. The velocity is initialised to $(v_x, v_y, v_z) = (-\sin(2\pi y), \sin(2\pi x), 0)$, and the magnetic field is set through the vector potential $A_z = (B_0/4\pi)\cos(4\pi x) + (B_0/2\pi)\cos(2\pi y)$, where $B_0 = 1/\sqrt{4\pi}$.

The results for uniform grids with 256^2 and 512^2 zones at $t = 1/2$, as well as the AMR results for a base grid of 128^2 zones and 2 levels of refinement (effective resolution of 512^2 zones), are presented in Figure 2.11. The bottom right panel shows the distribution of AMR grids at $t = 1/2$. For clarity, we have only plotted the grids at level 3 (*i.e.*, 2 levels higher resolution than the base grid). Even then, the filling factor of level $l = 2$ grids at this time is $\gtrsim 95\%$. Examining the first three panels of Figure 2.11 closely, features are noticeably sharper in the 512^2 solution relative to the 256^2 results, while the AMR and 512^2 solutions are indistinguishable.

Figure 2.12 shows slices of the gas pressure as a function of x at $t = 1/2$ and $y = 0.4277$, which once again demonstrate that the AMR and 512^2 uniform grid solutions are virtually identical. Quantitatively, these solutions compare favourably with those from higher-order codes such as ATHENA, with the discontinuities in the AZEuS solutions being slightly broader.

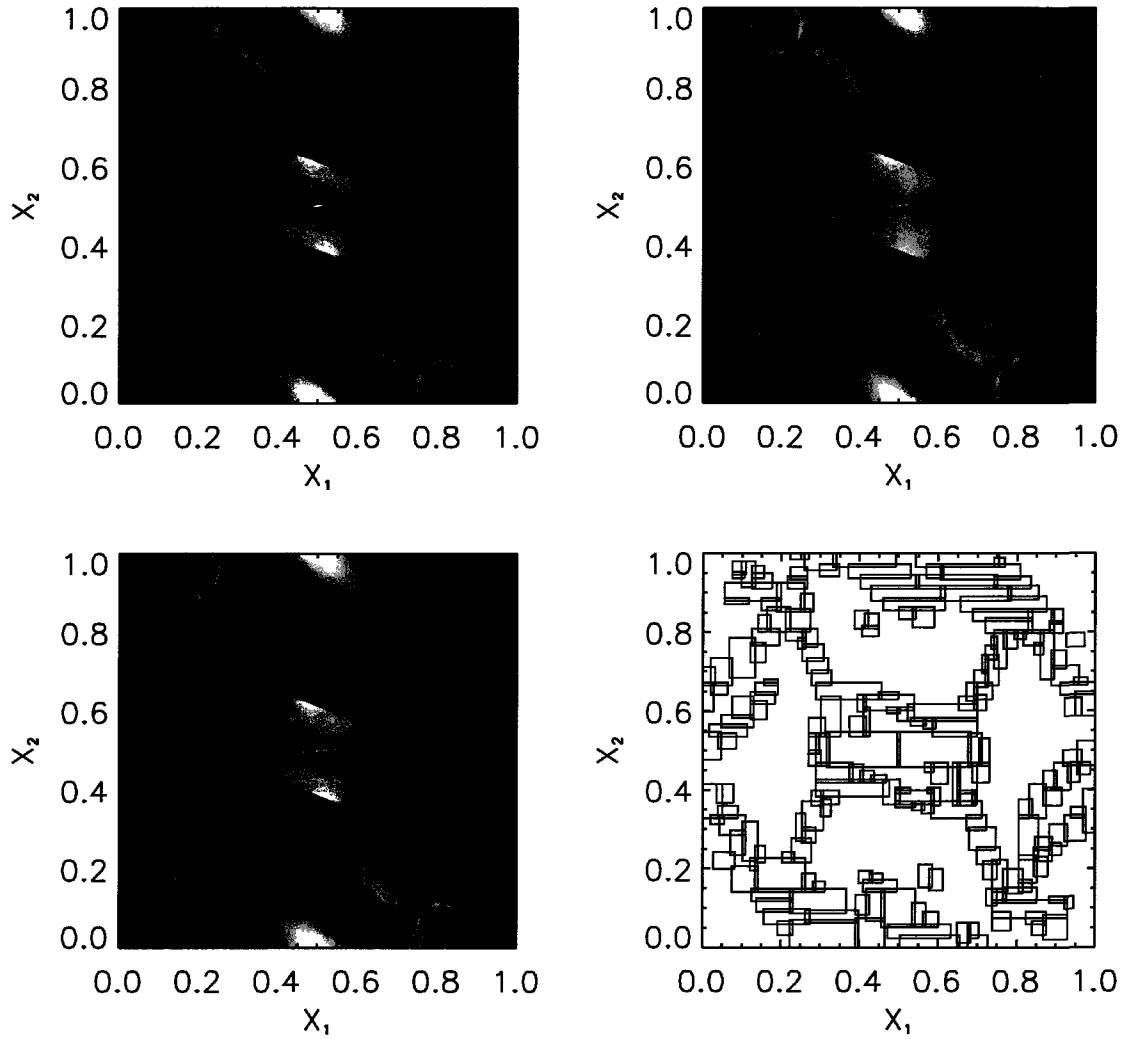


Figure 2.11 Uniform and adaptive grid solutions for the Orszag-Tang MHD vortex at $t = 1/2$. Plotted are 20 evenly spaced contours of the gas pressure with range $[0.03, 0.50]$. *Top left*: uniform grid solution with 256^2 zones; *top right*: uniform grid solution with 512^2 zones; *bottom left*: AMR solution with a base grid resolution of 128^2 and 2 levels of refinement; and *bottom right*: distribution of grids at level 3 in the AMR solution.

For this problem, we set $\mathcal{C} = 0.5$, $q_{\text{con}} = 1.0$, and $q_{\text{lin}} = 0.1$ for both uniform and adaptive grids. For the AMR results, $k_{\text{check}} = 10$, $g_{\text{effcy}} = 0.9$, $i_{\text{buff}} = 2$, and $\text{tolshk} = 0.2$. Neither the CD nor gradient detector were engaged.

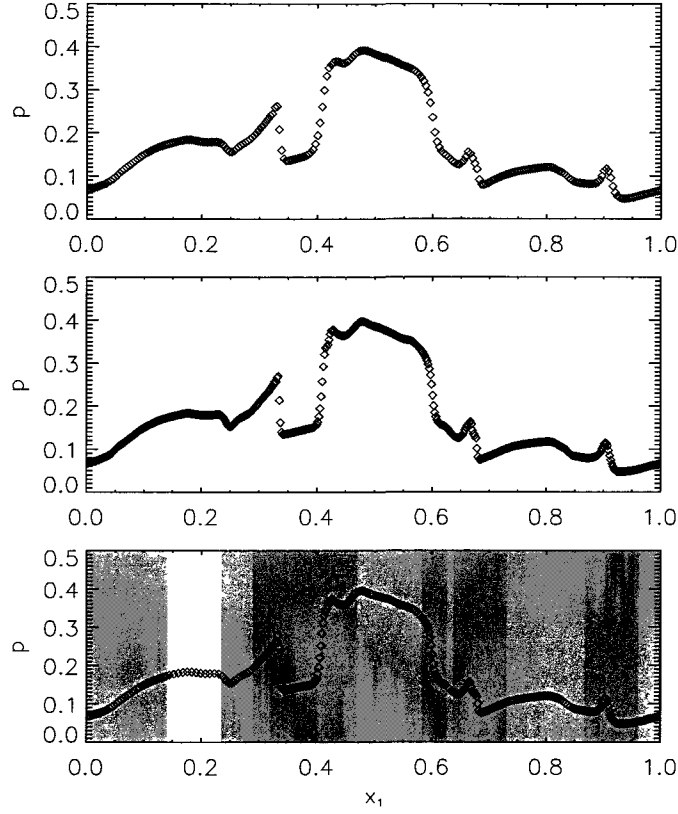


Figure 2.12 1-D slices of the gas pressure at $t = 1/2$ and $y = 0.4277$ in the Orszag-Tang MHD vortex problem. From top to bottom, uniform 256^2 grid, uniform 512^2 grid, AMR solution with 2 levels of refinement and an effective resolution of 512^2 zones.

Magnetised accretion torus

This test is based on the simulations of Hawley (2000) and Mignone *et al.* (2007) for a magnetised, constant angular momentum torus in axisymmetric spherical (r, ϑ) coordinates, and highlights the use of curvilinear coordinates in AZEuS.

The torus structure is described by the equilibrium condition:

$$\frac{\gamma p}{(\gamma - 1)\rho} = C - \phi - \frac{1}{2} \frac{l_{\text{Kep}}^2}{r^2 \sin^2 \vartheta}, \quad (2.32)$$

where C is a constant of integration, $\phi = -1/(r-1)$ is the pseudo-Newtonian gravitational potential, and l_{Kep} is the Keplerian angular momentum at the pressure maximum. The pressure p is initially related to the density via the polytropic relation, $p = \kappa\rho^\gamma$, with $\gamma = 5/3$. By specifying the location of the pressure maximum ($r_{\text{max}} = 4.7$) and the inner edge of the torus ($r_{\text{min}} = 3$), we can determine the value of C and the (hydrodynamic) structure of the torus.

A poloidal magnetic field is initialised in the torus from the φ -component of the vector potential:

$$A_\varphi = \frac{B_0}{\rho_m} \min(\rho(r, \vartheta) - \rho_c, 0),$$

where $B_0^2 = 2\kappa\rho_m^\gamma/\beta_m$, β_m and ρ_m are, respectively, the plasma-beta and density at r_{max} , κ is determined by equation (2.32) evaluated at r_{max} , and $\rho_c = \rho_m/2$ determines the surface of the last vector equipotential. For the simulations presented here, $\beta_m = 350$ and $\rho_m = 10$. The toroidal velocity (v_φ) in the torus is initialised to the local Keplerian speed, while the poloidal velocity is set to zero everywhere.

Outside the torus, the magnetic field is zero and we initialise a hydrostatic atmosphere with density and temperature contrasts of $\rho_{\text{atm}}/\rho_m = 10^{-4}$ and $T_{\text{atm}}/T_m = 100$, respectively, where T_m is the temperature at r_{max} .

The domain of the grid is $r \in [1.5, 20]$ and $\vartheta \in [0, \pi/2]$. We impose reflecting boundary conditions suitable for a rotation axis at $\vartheta = 0$, reflecting/conducting boundary conditions at the equatorial plane ($\vartheta = \pi/2$), and outflow boundary conditions at $r = 20$. At $r = r_{\text{in}} = 1.5$, we impose ‘‘sink’’ boundary conditions in an attempt to absorb any material reaching the inner boundary. This involves maintaining the density and pressure

at their initial values, and setting $v_r = v_\vartheta = v_\varphi = 0$ within the boundary. On the inner skin ($r = r_{\text{in}}$), v_r is set to the minimum of zero and a linear extrapolation from the grid. Finally, outflow boundary conditions are applied to the EMFs:

$$\begin{aligned}\mathcal{E}_1(r < r_{\text{in}}) &= \mathcal{E}_1(2r_{\text{in}} - r); \\ \mathcal{E}_2(r < r_{\text{in}}) &= 2\mathcal{E}_2(r_{\text{in}}) - \mathcal{E}_2(2r_{\text{in}} - r); \\ \mathcal{E}_3(r < r_{\text{in}}) &= 2\mathcal{E}_3(r_{\text{in}}) - \mathcal{E}_3(2r_{\text{in}} - r).\end{aligned}\tag{2.33}$$

Values of $\mathcal{E}_2(r_{\text{in}})$ and $\mathcal{E}_3(r_{\text{in}})$ are determined by the CMoC algorithm in AZEuS.

Both the uniform grid and AMR solutions are presented here. For the single grid calculation, we use 592 uniform radial zones and 256 uniform meridional zones. For the AMR solution, we use a base grid of 296×128 zones, and allow one level of refinement with a refinement ratio $\nu = 2$, giving the same effective resolution as the uniform grid calculation.

For both calculations, $\mathcal{C} = 0.5$, $\text{qcon} = 1.0$, and $\text{qlin} = 0.1$. For AMR, $\text{kcheck} = 50$, $\text{geffcy} = 0.8$, $\text{ibuff} = 2$, $\text{tolshk} = \text{tolcd} = 0.2$, and $\text{tolgrad} = 0.2$ is applied to B_ϑ . We use the gradient detector to refine on the initial magnetic field configuration (contained entirely within the torus), and the complex field structure that develops later on from the magneto-rotational instability (MRI; Balbus & Hawley 1991), since neither are well-tracked by the shock and CD detectors.

Following Hawley (2000), we enforce a density floor of $10^{-3}\rho(r_{\text{in}})$ to prevent the time step from becoming prohibitively small, and we use the internal energy equation to avoid

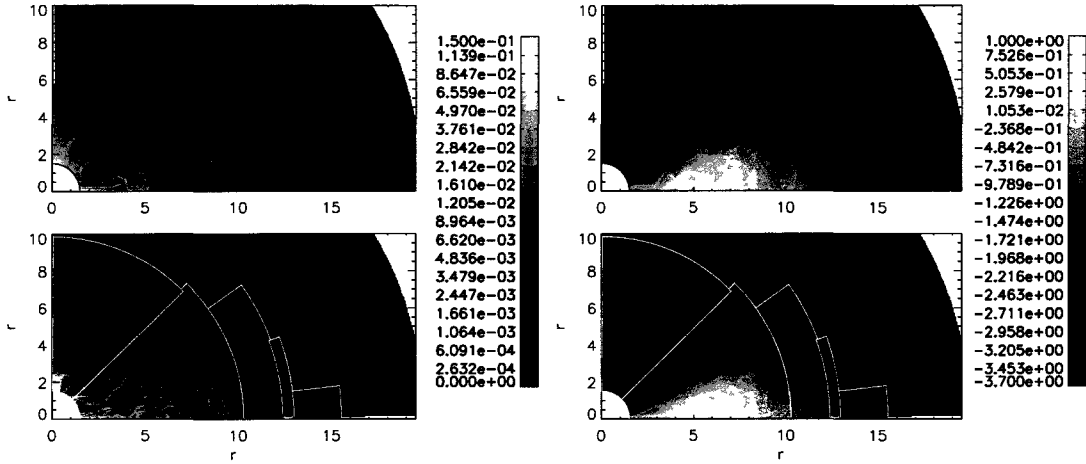


Figure 2.13 The “beard of AZEuS”: Results of MHD accretion torus simulations in (r, ϑ) coordinates at $t = 300$, where the vertical axis is the rotation axis. Plotted are contours of poloidal magnetic field (left) and logarithmic density (right). Top panels are for the uniform grid, bottom panels the AMR solution with one level of refinement. Borders of the adaptive grids are shown with black lines.

negative pressures. Unlike Hawley (2000), we do not introduce any perturbations on the initial conditions, which slows but does not prevent the onset of MRI.

Figure 2.13 presents the results of our simulations at $t = 300$. Evidently and very much unlike the Orszag-Tang vortex, the AMR and uniform grid solutions are visually different, even though they have the same effective resolution. For a pseudo-turbulent, “irreversible” problem such as this, small differences between values in the coarse and fine grids grow exponentially during the simulation, and lead to visually different solutions. This is quite unlike the behaviour of a “reversible” problem such as the Orszag-Tang vortex, for which small fluctuations grow at worse linearly in time, and never manifest as visual differences in the plots. On the other hand, integrated quantities tend to be in better agreement than their detailed distributions. For example, between the uniform grid

and AMR solutions, the integrated mass and kinetic energy at $t = 300$ differ by only 1.1% and 3.5% respectively. Furthermore, our results are qualitatively similar to Mignone *et al.* (2007); Figure 2.13 could easily fit in with their Figure 8 for different Riemann solvers and interpolation schemes.

2.7.3 A 3-D test: self-gravitational hydrodynamical collapse

The last test is the self-gravitational hydrodynamical collapse calculation first presented by Truelove *et al.* (1997) and Truelove *et al.* (1998; T98). At the time of this writing, self-gravity has not been fully implemented in AZEuS, and so we use the successive over-relaxation (SOR) method (Press *et al.* 1992) as an easy-to-program, albeit slow, stop-gap measure. Since SOR is incompatible with periodic boundary conditions, we apply inflow boundary conditions instead. This results in some subtle differences from T98, which we discuss below.

A rotating, uniform cloud of mass $M = 1M_{\odot}$ and radius $R = 5 \times 10^{16}$ cm is initialised in the centre of a 3-D Cartesian box with side length $4R$. We use a nearly isothermal equation of state ($p = \kappa\rho^{\gamma}$, $\gamma = 1.001$), initially uniform rotation $\Omega = 7.14 \times 10^{-13}$ rad s^{-1} with angular momentum axis in the positive x_3 -direction, and energy ratios of

$$\alpha = \frac{5}{2} \left(\frac{3}{4\pi\rho_0 M^2} \right)^{1/3} \frac{c_s^2}{G} = 0.16 \quad \text{and} \quad \beta_{\Omega} = \frac{1}{4\pi} \frac{\Omega^2}{G\rho_0} = 0.26, \quad (2.34)$$

where ρ_0 is the initial density of the uniform cloud (T98). The remainder of the computational volume is initialised with uniform density and pressure given by $\rho_{\text{atm}} = 100\rho_{\text{cloud}}$ and $p_{\text{atm}} = 10p_{\text{cloud}}$. Upon the initial uniform density distribution, we apply an azimuthal

$m = 2$ perturbation of the form $\rho_{\text{cloud}}(1 + A \cos(2\varphi))$, where $A = 10\%$ is the perturbation amplitude and φ is the azimuthal angle relative to the cloud centre.

Following T98, we set the coarsest grid to 32^3 zones, or eight zones per cloud radius. We immediately add 1 level of refinement by flagging all zones which have density $\rho > \rho_{\text{cloud}}$ (for a refinement ratio of 4, this gives 32 zones per cloud radius). Beyond this, we enforce the so-called “Truelove criterion”:

$$J = \frac{\Delta x}{\lambda_J} = \Delta x \left(\frac{G\rho}{\pi c_s^2} \right)^{1/2} < J_{\text{max}}, \quad (2.35)$$

refining zones which have Jeans numbers J larger than critical value $J_{\text{max}} = 0.25$. Additional run-time parameters for this test include $\mathcal{C} = 0.33$, $\text{qcon} = 1.0$, $\text{qlin} = 0.1$, $\text{kcheck} = 20$, $\text{geffcy} = 0.7$, $\text{ibuff} = 2$, and refinement ratio $\nu = 4$.

Figure 2.14 shows our results at $t = 0.598133 = 1.215t_{\text{ff}}$. At this time, there are seven levels of refinement above the base grid and, in the terminology of T98, our highest resolution grids correspond to R_{131072} . Our maximum density at this time is $\log \rho_{\text{max}} = -8.8767$, with density measured in g cm^{-3} , an increase over ρ_0 of more than 8.5 orders of magnitude. While our simulation collapses more quickly than T98 and our Figure 2.14 does not correspond exactly with their Figures 12 and 13, we actually reach a higher maximum density.

The differences between our results and T98 are most likely caused by the differing boundary conditions (ours inflow, theirs periodic). Indeed, T98 allude to this possibility, suggesting that non-periodic boundary conditions could slightly increase the rate of collapse, which we observe.

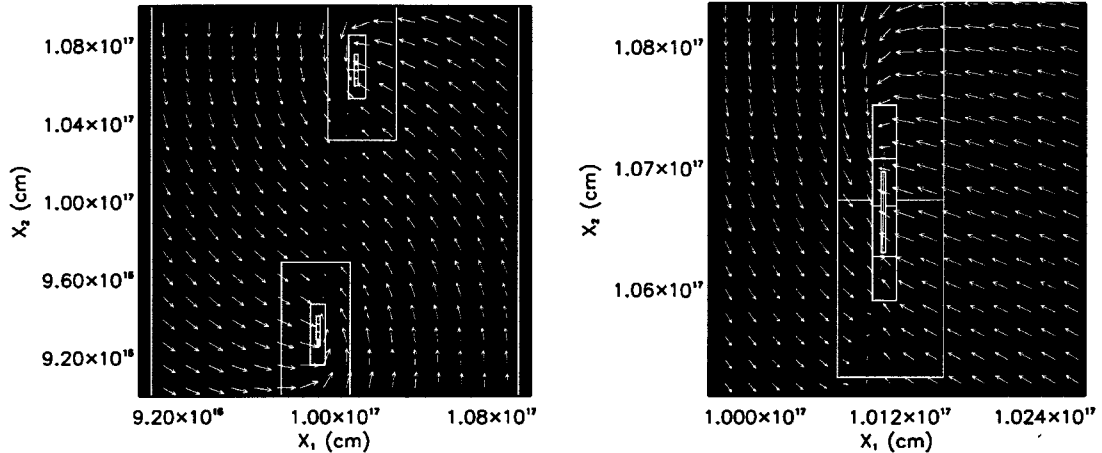


Figure 2.14 AZEuS results for the Truelove problem with a 10% amplitude perturbation at $t = 0.598133 = 1.215t_{\text{ff}}$, where t_{ff} is the free-fall time. *Left*: Equatorial x_1 - x_2 slice of logarithmic density with velocity vectors over-plotted. The highest resolution shown here is R_{8192} . *Right*: Equatorial x_1 - x_2 slice of logarithmic density of the upper fragment. The highest resolution in this plot is R_{32768} ; there is one additional level of refinement not shown. Black lines denote the borders of AMR grids and the units of density are g cm^{-3} . For each panel, 20 evenly spaced contours are plotted with ranges $\log \rho = [-16.10, -9.905]$ (left) and $[-14.30, -9.604]$ (right).

2.8 Summary

We have described a method for block-based AMR on a fully-staggered mesh, and implemented this method in a new version of *ZEUS-3D* called *AZEuS*. In addition to describing the modifications required to AMR to account for the fully staggered grid, we also describe higher order interpolation methods for the prolongation step which we found necessary to allow for static grids. Static grids are important for problems which, at first order, have a self-similar character and expand over the course of the simulation to ever larger scale lengths. Such a simulation by *AZEuS* has already appeared in the literature (Ramsey & Clarke 2011), which showcases the ability of the code to transmit waves of

all types and strengths across grid boundaries, and to do so in cylindrical coordinates. The higher-order prolongation operator is designed to maintain the conservation of all important physical quantities such as mass, momentum, energy, and magnetic flux.

Numerous test problems were also presented in 1-, 2-, and 3-D, and in both Cartesian and spherical polar coordinates. These tests demonstrate the ability of the code to produce essentially identical results in “reversible” (non-turbulent) problems whether using a single grid or AMR, and give an example of the differences that can occur in “irreversible” (turbulent) problems as minute differences caused by the insertion or deletion of a grid amplify.

Finally, the AZEuS website <http://www.ica.smu.ca/azeus> was introduced on which test problems and simulations will be posted as they become available, and from which the code can be downloaded in the near future.

2.A Curvilinear Coordinates

Like other codes in the *ZEUS-3D* family, AZEuS uses the “covariant” (coordinate independent) form of the MHD equations (Stone & Norman 1992a). Supported geometries in AZEuS include Cartesian (x, y, z) , cylindrical (z, r, φ) , and spherical polar (r, ϑ, φ) coordinates while other orthogonal curvilinear coordinate systems may be easily implemented as needed. For simplicity, the equations presented in the main body of the paper were all written assuming Cartesian-like coordinates. In this appendix, we show how these may be rewritten in a covariant fashion.

| (x_1, x_2, x_3) | $g_{12}(j)$ | $g_{13}(k)$ | $g_{23}(k)$ | $g_{21}(i)$ | $g_{31}(i)$ | $g_{32}(j)$ |
|---------------------------|-------------|-------------|-------------|-------------|-------------|---------------|
| (x, y, z) | 1 | 1 | 1 | 1 | 1 | 1 |
| (z, r, φ) | 1 | 1 | 1 | 1 | 1 | $x_2(j)$ |
| (r, ϑ, φ) | 1 | 1 | 1 | $x_1(i)$ | $x_1(i)$ | $\sin x_2(j)$ |

Table 2.2 The metric scaling factors in AZEuS for Cartesian, cylindrical, and spherical polar coordinates.

The distance differential in an orthogonal coordinate system, (x_1, x_2, x_3) , is given by:

$$ds^2 = g_1^2 dx_1^2 + g_2^2 dx_2^2 + g_3^2 dx_3^2, \quad (2.36)$$

where g_i , $i = 1, 2, 3$, are the usual metric scaling factors and all are functions of the coordinates. If the scaling factors are separable and independent of their own direction, we can write:

$$\begin{aligned} g_1 &= g_1(j, k) = g_{12}(j) g_{13}(k); \\ g_2 &= g_2(k, i) = g_{23}(k) g_{21}(i); \\ g_3 &= g_3(i, j) = g_{31}(i) g_{32}(j). \end{aligned} \quad (2.37)$$

For Cartesian, cylindrical, and spherical polar coordinates, these factors are given in Table 2.2.

Face areas and zone volumes important for the calculation of fluxes and conserved quantities are written as:

$$\begin{aligned}
\delta A_1(i, j, k) &= \int_{x_2(j)}^{x_2(j+1)} \int_{x_3(k)}^{x_3(k+1)} g_{21}(i) g_{31}(i) g_{32}(j') dx'_2 dx'_3 \\
&= g_{21}(i) g_{31}(i) \int_{x_2(j)}^{x_2(j+1)} g_{32}(j') dx'_2 \int_{x_3(k)}^{x_3(k+1)} dx'_3 \\
&\equiv g_{21}(i) g_{31}(i) \delta A_{12}(j) \delta A_{13}(k),
\end{aligned} \tag{2.38}$$

$$\begin{aligned}
\delta A_2(i, j, k) &= \int_{x_3(k)}^{x_3(k+1)} \int_{x_1(i)}^{x_1(i+1)} g_{31}(i') g_{32}(j) dx'_3 dx'_1 \\
&= g_{32}(j) \int_{x_3(k)}^{x_3(k+1)} dx'_3 \int_{x_1(i)}^{x_1(i+1)} g_{31}(i') dx'_1 \\
&\equiv g_{32}(j) \delta A_{23}(k) \delta A_{21}(i),
\end{aligned} \tag{2.39}$$

$$\begin{aligned}
\delta A_3(i, j, k) &= \int_{x_1(i)}^{x_1(i+1)} \int_{x_2(j)}^{x_2(j+1)} g_{21}(i') dx'_1 dx'_2 \\
&= \int_{x_1(i)}^{x_1(i+1)} g_{21}(i') dx'_1 \int_{x_2(j)}^{x_2(j+1)} dx'_2 \\
&\equiv \delta A_{31}(i) \delta A_{32}(j).
\end{aligned} \tag{2.40}$$

$$\begin{aligned}
\delta V(i, j, k) &= \int_{x_1(i)}^{x_1(i+1)} \int_{x_2(j)}^{x_2(j+1)} \int_{x_3(k)}^{x_3(k+1)} g_{21}(i') g_{31}(i') g_{32}(j') dx'_1 dx'_2 dx'_3 \\
&= \int_{x_1(i)}^{x_1(i+1)} g_{21}(i') g_{31}(i') dx'_1 \int_{x_2(j)}^{x_2(j+1)} g_{32}(j') dx'_2 \int_{x_3(k)}^{x_3(k+1)} dx'_3
\end{aligned} \tag{2.41}$$

$$\begin{aligned}
&\equiv \int_{x_1(i)}^{x_1(i+1)} dV'_1 \int_{x_2(j)}^{x_2(j+1)} dV'_2 \int_{x_3(k)}^{x_3(k+1)} dV'_3 \\
&\equiv \delta V_1(i) \delta V_2(j) \delta V_3(k),
\end{aligned} \tag{2.42}$$

where metric scaling factors equal to 1 in Table 2.2 have been and will continue to be dropped.

Finally, *ZEUS-3D* has traditionally defined the momentum densities, \vec{s} , as:

$$\begin{aligned}
 s_1(i, j, k) &= \rho(i - \frac{1}{2}, j, k) v_1(i, j, k); \\
 s_2(i, j, k) &= g_{21}(i) \rho(i, j - \frac{1}{2}, k) v_2(i, j, k); \\
 s_3(i, j, k) &= g_{31}(i) g_{32}(j) \rho(i, j, k - \frac{1}{2}) v_3(i, j, k),
 \end{aligned} \tag{2.43}$$

where the half indices in the density indicate two-point averages. Defining the momentum components with the metric scaling factors simplifies the momentum equation somewhat by eliminating all “Coriolis-like” fictitious forces, leaving only the “centrifugal-like” terms.

2.A.1 Restriction

Conservative Overwrite

When applying the conservative overwriting procedure on a curvilinear grid, the equations of Section 2.3.1 must be modified to account for the non-constant volumes of zones. For example, equation (2.6) for zone-centred quantities becomes:

$$\begin{aligned}
 Q(I, J, K) \Delta V_1(I) \Delta V_2(J) \Delta V_3(K) &= \sum_{\alpha, \beta, \eta=0}^{\nu-1} q(i + \alpha, j + \beta, k + \eta) \\
 &\times \delta V_1(i + \alpha) \delta V_2(j + \beta) \delta V_3(k + \eta),
 \end{aligned} \tag{2.44}$$

and equation (2.7) for face-centred momenta generalises to:

$$S_1(I, J, K) \Delta V_1(I) \Delta V_2(J) \Delta V_3(K) = \sum_{\alpha=-\nu/2}^{\nu/2} \sum_{\beta, \eta=0}^{\nu-1} \mathcal{G}'(\alpha) s_1(i + \alpha, j + \beta, k + \eta) \quad (2.45)$$

$$\times \delta V_1(i + \alpha) \delta V_2(j + \beta) \delta V_3(k + \eta),$$

where:

$$\mathcal{G}'(\alpha) = \begin{cases} w_{1,R}(i + \alpha) & \text{if } \alpha = -\nu/2; \\ w_{1,L}(i + \alpha) & \text{if } \alpha = +\nu/2; \\ 1 & \text{otherwise,} \end{cases} \quad (2.46)$$

and where:

$$w_{1,L}(i) = \frac{1}{\delta V_1(i)} \int_{x_1(i-1/2)}^{x_1(i)} dV_1; \quad w_{1,R}(i) = \frac{1}{\delta V_1(i)} \int_{x_1(i)}^{x_1(i+1/2)} dV_1. \quad (2.47)$$

While it is still true that the fine zones at $\alpha = \pm\nu/2$ are halfway outside the coarse ROI in *position* space (Figure 2.3b), this is not generally true in volume space. As an example, consider spherical coordinates where the 1-volume differential is $dV_1(i) = g_{21}(i)g_{31}(i) dx_1(i) = x_1^2(i) dx_1(i)$. Clearly, $dV_1(i)$ in spherical coordinates is not a linear function of position, and it cannot be assumed that exactly 1/2 of the fine momentum volume is outside the coarse ROI. To correct for this, we calculate the ratio of the *half*-volume inside the coarse ROI to the actual volume element (equation 2.47), which is then used as a weighting factor in $\mathcal{G}'(\alpha)$. For reasonable grid parameters, these weighting factors are

small corrections (< a few %) relative to the Cartesian factor of 1/2, but nonetheless are included for accuracy.

Suitable expressions for the 2-direction are obtained by a permutation of indices. No corrections are necessary for the 3-direction, since $dV_3(k) = dx_3(k)$ for the curvilinear coordinates discussed here.

For the magnetic fields, equation (2.9) changes to account for non-uniform areas:

$$B_1(I, J, K) \Delta A_1(I, J, K) = \sum_{\beta, \eta=0}^{\nu-1} b_1(i, j + \beta, k + \eta) \delta A_1(i, j + \beta, k + \eta). \quad (2.48)$$

Flux Corrections

Fluxes and EMFs as stored by *ZEUS-3D* already include the appropriate area and length elements, so the required changes for flux corrections in curvilinear coordinates are not substantial. As with the conservative overwrite, the corrections need to be adjusted by replacing occurrences of \mathcal{G} (equation 2.8) with \mathcal{G}' (equation 2.46). Similar to equation (2.45), equation (2.11) for the flux corrections of momentum components normal to the boundary must also be modified to account for non-constant volumes:

$$\begin{aligned} \tilde{S}_1^{N+1}(I, J, K) = & S_1^{N+1}(I, J, K) - \frac{1}{\Delta V(I, J, K)} \left(F_{1, s_1}^{N+\frac{1}{2}}(I-1, J, K) \right. \\ & - \sum_{\beta, \eta, \tau=0}^{\nu-1} \left(w_{1, R} \left(i - \frac{\nu}{2} \right) f_{1, s_1}^{n+\tau+\frac{1}{2}} \left(i - \frac{\nu}{2} - 1, j + \beta, k + \eta \right) \right. \\ & \left. \left. + w_{1, L} \left(i - \frac{\nu}{2} \right) f_{1, s_1}^{n+\tau+\frac{1}{2}} \left(i - \frac{\nu}{2}, j + \beta, k + \eta \right) \right) \right). \end{aligned} \quad (2.49)$$

By the same argument, equation (2.13) for coarse momenta with components parallel to a grid boundary also needs to be modified, as the original factor of $(\nu - 1)/2\nu \equiv \mathcal{R}$ is not correct for curvilinear coordinates:

$$\begin{aligned} \tilde{S}_2^{N+1}(I, J, K) = S_2^{N+1}(I, J, K) - \frac{1}{\Delta V(I, J, K)} & \left(\mathcal{L}(J, \nu) F_{1, S_2}^{N+\frac{1}{2}}(I, J, K) \right. \\ & \left. - \sum_{\beta=1}^{\nu/2} \sum_{\eta, \tau=0}^{\nu-1} \mathcal{G}'(\beta) f_{1, S_2}^{n+\tau+\frac{1}{2}}(i, j + \beta, k + \eta) \right). \end{aligned} \quad (2.50)$$

Here, $\mathcal{L}(J, \nu) = W_{2,L}(J, \nu)$ if $S_2(I, J, K)$ is at the upper edge of the fine grid (high j), and $\mathcal{L}(J, \nu) = W_{2,R}(J, \nu)$ if $S_2(I, J, K)$ is at the lower edge of the fine grid (low j), with:

$$\begin{aligned} W_{2,L}(J, \nu) &= \frac{1}{\Delta V_2(J)} \int_{x_2(J-1/2)}^{x_2(J-1/2+\mathcal{R})} dV_2; \\ W_{2,R}(J, \nu) &= \frac{1}{\Delta V_2(J)} \int_{x_2(J+1/2-\mathcal{R})}^{x_2(J+1/2)} dV_2. \end{aligned}$$

Like the function \mathcal{G}' , \mathcal{L} accounts for the portion of the coarse zone flux in volume space which is being replaced by fine fluxes. As before, expressions for the 2-direction are obtained by a suitable permutations of indices.

2.A.2 Prolongation

The changes required for prolongation on curvilinear grids deal entirely with making the interpolations conservative for curvilinear volumes and areas. In the case of 1-D PPI,

equation (2.16) summarising the conservation constraint is modified to:

$$Q(I, J, K)\Delta V_1(I) = \sum_{\alpha=0}^{\nu-1} q(i + \alpha, j, k)\delta V_1(i), \quad (2.51)$$

which then affects the rest of the scheme (equations 2.17 and 2.18):

$$q_1^*(i + \alpha) = Q_L(I) + \zeta \left(Q_R(I) - Q_L(I) - \mathcal{H}'_1(1 - \zeta) \right), \quad (2.52)$$

where:

$$\begin{aligned} \mathcal{H}'_1 &= \frac{1}{f'_2(\nu, i) - f'_1(\nu, i)} \left(\Delta V_1(I) (Q(I, J, K) - Q_L(I)) \right. \\ &\quad \left. - f'_1(\nu, i) (Q_R(I) - Q_L(I)) \right); \\ f'_1(\nu, i) &= \frac{1}{2\nu} \sum_{\xi=1}^{\nu} (2\xi - 1) \delta V_1(i + \xi - 1); \\ f'_2(\nu, i) &= \frac{1}{4\nu^2} \sum_{\xi=1}^{\nu} (2\xi - 1)^2 \delta V_1(i + \xi - 1), \end{aligned}$$

and where:

$$\zeta = \frac{x_1(i + \alpha) - x_1(I)}{\Delta x_1(I)}.$$

As for PLI, the original 1-D scheme in the 1-direction takes the form (van Leer 1977):

$$q_1^*(i + \alpha) = Q(I) + (2\zeta - 1) \Delta Q', \quad (2.53)$$

where:

$$\Delta Q' = \begin{cases} \frac{\Delta Q_R \Delta Q_L}{\Delta Q_R + \Delta Q_L} & \text{if } \Delta Q_R \Delta Q_L > 0; \\ 0, & \text{otherwise,} \end{cases}$$

and where:

$$\Delta Q_R = Q(I+1) - Q(I); \quad \Delta Q_L = Q(I) - Q(I-1).$$

Equation (2.53) will not generally conserve mass, momentum, or magnetic flux on a curvilinear grid. To correct this, we relax the constraint that the linear interpolation profile must pass through $Q(I)$ at the zone-centre. This releases one degree of freedom that can then be used with equation (2.51), resulting in:

$$q_1^*(i + \alpha) = Q(I) + \Delta Q' \left(2\zeta - 1 - \frac{1}{\Delta V_1(I)} f_3'(\nu, i) \right), \quad (2.54)$$

where:

$$f_3'(\nu, i) = \frac{1}{\nu} \sum_{\xi=1}^{\nu} ((2\xi - 1) - \nu) \delta V_1(i + \xi - 1).$$

The additional term in equation (2.54) can be viewed as either a shift in the zone-centred intercept, or as choosing a modified value of ζ corresponding to the volume-centred rather than the spatial-centred coordinate.

Unfortunately, this “shift” can push $q_1^*(i + \alpha)$ beyond neighbouring values of $Q(I)$ at the edges of the interpolation profile, resulting in a loss of monotonicity. However, since

$\zeta = 0$ or 1 at the left or right side of the interpolation profile, we can write:

$$\begin{aligned} \Delta Q'_L &= Q(I) - q_1^*(i + \alpha) = \Delta Q'(1 + \mathcal{K}'_1) \\ \text{or } \Delta Q'_R &= q_1^*(i + \alpha) - Q(I) = \Delta Q'(1 - \mathcal{K}'_1), \end{aligned} \quad (2.55)$$

where $\mathcal{K}'_1 = f'_3(\nu, i) / \Delta V_1(I)$. If we limit the slope of the interpolation profile to:

$$\Delta Q'' = \begin{cases} \text{sign}(\Delta Q') |\Delta Q_L| / (1 + \mathcal{K}'_1) & \text{if } |\Delta Q'_L| > |\Delta Q_L| \\ \text{sign}(\Delta Q') |\Delta Q_R| / (1 - \mathcal{K}'_1) & \text{if } |\Delta Q'_R| > |\Delta Q_R| \\ \Delta Q' & \text{otherwise,} \end{cases} \quad (2.56)$$

and, because of the properties of the PLI slope $\Delta Q'$, the first two cases of equation (2.56) will never occur simultaneously. Thus, the equation for conservative, monotonic, 1-D PLI in curvilinear coordinates is:

$$q_1^*(i + \alpha) = Q(I) + \Delta Q''((2\zeta - 1) - \mathcal{K}'_1). \quad (2.57)$$

The previous discussion applies to interpolation of momenta in the directions perpendicular to the component normal (*e.g.*, s_1 in the 2- and 3-directions). The covariant

procedure for linear interpolation in between coarse faces (*e.g.*, s_1 in the 1-direction; equation 2.24) is as follows:

$$s_1(i + \alpha, j + \beta, k + \eta) \delta V_1(i + \alpha) = (1 - \zeta) s_1(i, j + \beta, k + \eta) \delta V_1(i) + \zeta s_1(i + \nu, j + \beta, k + \eta) \delta V_1(i + \nu). \quad (2.58)$$

Finally, the generalised Li & Li (2004) algorithm is adapted to curvilinear coordinates simply by replacing \vec{B} (and \vec{b}) in equations (2.25)–(2.28) with the magnetic “flux functions”:

$$\vec{\Psi} = (\Psi_1, \Psi_2, \Psi_3) = \left(g_{21} g_{31} \frac{\Delta V_2}{\Delta x_2} B_1, g_{31} g_{32} B_2, g_{21} B_3 \right). \quad (2.59)$$

With this modification, the solenoidal condition can be written in “Cartesian-like” form, regardless of the geometry:

$$\nabla \cdot \vec{\Psi} = \frac{\partial \Psi_1}{\partial x_1} + \frac{\partial \Psi_2}{\partial x_2} + \frac{\partial \Psi_3}{\partial x_3} = 0,$$

and the prolongation of magnetic fields in curvilinear coordinates proceeds exactly as described in Section 2.4.1.

2.B The Vector Potential

Writing $\vec{B} = \nabla \times \vec{A}$ and assuming 3-symmetry with an appropriate gauge, one can easily show from the induction equation (equation 2.3) that A_3 obeys an “advection

equation”:

$$\frac{\partial A_3}{\partial t} + \vec{v} \cdot \nabla A_3 = 0, \quad (2.60)$$

from which the poloidal components of the magnetic field are given by:

$$B_1 = \frac{\partial A_3}{\partial x_2}; \quad B_2 = -\frac{\partial A_3}{\partial x_1}. \quad (2.61)$$

Further, one can show that B_3 is given by:

$$\frac{\partial B_3}{\partial t} + \nabla \cdot (B_3 \vec{v}) = \vec{B} \cdot \nabla v_3. \quad (2.62)$$

Since equation (2.62) has exactly the same form as the internal energy equation (equation 2.4), and since equation (2.60) is a simple induction equation, the induction step in the original *ZEUS-3D* code (zeus04; Clarke 1988) was based on solving these equations using the hydrodynamical algorithms already in the code, and then calculating B_1 , B_2 from equations (2.61). Evidently, the solenoid condition is *strictly* satisfied. Regardless of the initial magnetic field configuration, it is easy to show that a face-centred \vec{B} and a corner-centred (edge-centred in 3-D) A_3 guarantees $\nabla \cdot \vec{B} = 0$ everywhere and at all times to machine round-off error.

However, Clarke (1988) points out that a second-order accurate A_3 means first order accurate poloidal magnetic field components and a *zeroth-order* accurate current density J_3 (each differentiation reduces the order of accuracy by one), and this was found to have catastrophic consequences in computing the $\vec{J} \times \vec{B}$ source terms in the momentum equation (equation 2.2). Thus, the vector potential algorithm in zeus04 was abandoned,

and the first publicly released version of *ZEUS-2D* (Stone & Norman 1992a,b), and later *ZEUS-3D* (Clarke 1996), were based on the CT algorithm of Evans & Hawley (1988) in which the magnetic fields are updated directly. Note that the CT scheme *conditionally* satisfies the solenoidal condition, requiring that the magnetic field be initialised such that $\nabla \cdot \vec{B} = 0$.

Still, the failure of the vector potential algorithm in *zeus04* is not a complete indictment of \vec{A} for use in numerical MHD algorithms. Indeed, Londrillo & Del Zanna (2000) and Igumenshchev & Narayan (2002) have successfully demonstrated the use of \vec{A} as the primary magnetic variable in their MHD codes. By substituting $\vec{B} = \nabla \times \vec{A}$ into equation (2.3) and with an appropriate gauge, we can write:

$$\frac{\partial \vec{A}}{\partial t} = \vec{v} \times \vec{B} = \vec{\mathcal{E}}. \quad (2.63)$$

Thus, CT can be used as originally designed in which $\nabla \times \vec{\mathcal{E}}$ is used to update \vec{B} , or easily modified to use $\vec{\mathcal{E}}$ to update \vec{A} directly, then update \vec{B} by taking a curl of the time derivative of \vec{A} . Either way, a curl must be taken and the algorithms are interchangeable to machine round-off error. Note that the algorithms used by Londrillo & Del Zanna (2000) and Igumenshchev & Narayan (2002) are very different from the failed algorithm described for *zeus04*.

Based on this observation, early versions of *AZEUS* used the vector potential as the primary magnetic variable so that prolongation could be accomplished by interpolating \vec{A} (rather than \vec{B}), thus guaranteeing preservation of the solenoidal condition on a newly-created fine grid. Furthermore, because the vector potential conserves magnetic flux via a

path integral ($\oint \vec{A} \cdot d\vec{l} = \int \vec{B} \cdot d\vec{\sigma}$), by restricting on the vector potentials directly and then calculating \vec{B} everywhere, no EMF corrections are required. This approach, however, was found to be unsatisfactory since the parabolic interpolation function generated by PPI on \vec{A} produces linear profiles for \vec{B} and piecewise-constant profiles for \vec{J} , recovering the problem that doomed the original `zeus04` algorithm.

In addition, having to match gauges on overlapping grids poses a significant problem, and one that we never solved. In order to arrive at equation (2.63), one implicitly assumes a specific gauge. For a single grid, this is not a problem since there is never a need to specify this gauge. For multiple grids, however, each grid may have its own gauge (especially for grids whose origins are not coincident) and leaving them unspecified gives rise to discontinuities in the magnetic field components perpendicular to adjacent boundary normals. While a solution to this problem likely exists, we abandoned vector potentials in AZEuS before finding one simply because of the insurmountable problem of the lack of accuracy in the current densities.

As an illustration, Figure 2.15 shows early results of the simulations in Ramsey & Clarke (2011) in which the vector potential is used as the primary magnetic variable. The left panel shows the solution immediately before a grid modification, and the right panel the solution a few time steps after, where the fine grid was extended from $x_1 = 160$ to $x_1 = 166$. The errors committed by the piecewise constant current densities take a while to dissipate and, in this particular example, result in particularly egregious defects in the velocity divergence distribution within the new portion of the grid. Conversely, the Li &

Li (2004) algorithm we currently employ renders adjacent boundaries virtually invisible in the distributions of all variables.

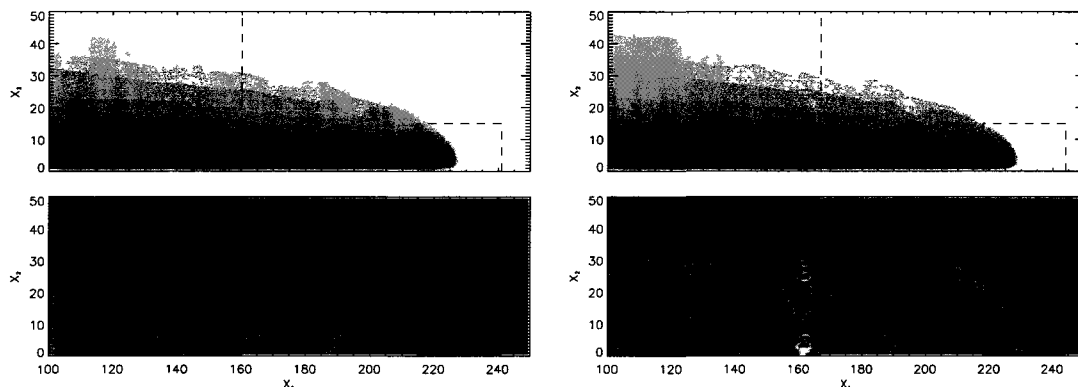


Figure 2.15 The effects of differencing a parabolic interpolation of \vec{A} twice to calculate $\vec{J} \times \vec{B}$ forces. Left panel: the solution immediately before a grid adaptation step. Right panel: the solution a few time steps after. Plotted are 20 evenly spaced contours of the toroidal magnetic field (top) and velocity divergence (bottom) with ranges $B_\phi = [-0.035, 0.0]$ and $\nabla \cdot \vec{v} = [-0.15, 0.15]$, respectively.

2.C Schematic overview of the AMR module

This appendix is designed mainly for programmers and those who may wish to use and/or modify AZEuS. It is meant as an overview to illustrate how the main ideas covered in this paper have been implemented in the code.

Step 0. **Initialise** computational domain and all variables for the current run.

Set level `lv1 = 1`, `ntogo(lv1) = 1`.

MAIN LOOP:

Step 1. **For** level `lv1`, call `REGRID(lv1)` if `kcheck` cycles have transpired at level `lv1` since the last call to `REGRID`, or if `t = 0`.

For `l = maxlevel - 1, lv1, -1`:

Step 1a. Flag existing grids at level `l` for refinement based on one or more physical criteria. Add `ibuff` buffer zones around flagged points.

Step 1b. Create grids around flagged points based on `geffcy`.

Step 1c. Check for proper nesting on all new/modified grids; fix grids which are not properly nested via bisection.

Step 1d. If any new/modified grids are abutting, make them overlapping instead.

End For

For `l = lv1 + 1, maxlevel`:

Step 1e. Fill new/modified grids with values either from old grids at level `l` or interpolated from coarse grids at level `l - 1`.

Step 1f. Remove old grids which are no longer in use.

End For

Step 2. **For** level `lv1`, call `ADVANCE(lv1, dt)`.

Step 2a. **For** all grids at level `lv1`, fill boundary zones either from overlapping grids at the same level, or interpolate values from coarse grids at level `lv1 - 1` (unless `lv1 = 1`, in which case use physical boundary values).

For each grid m at level $lv1$:

Step 2b. Advance grid m by time step dt with *ZEUS-3D*.

Step 2c. Save fluxes/EMFs along the edges of grid m for flux corrections later.

End For

Step 3. One time step at level $lv1$ is complete; check for levels $> lv1$.

Set $ntogo(lv1) = ntogo(lv1) - 1$.

Step 3a. **If** $lv1 < maxlevel$ then:

Set $lv1 = lv1 + 1$.

Set $ntogo(lv1) = nu$, where nu is the refinement ratio.

Set $dt = dt / ntogo(lv1)$.

Go to the beginning of the main loop.

End If

Step 3b. **If** $ntogo(lv1) > 0$ then **go to** the top of the main loop,

Else Set $lv1 = lv1 - 1$.

Step 4. **For** level $lv1$, call *UPDATE*($lv1$).

For each grid m at level $lv1$:

Step 4a. Flux correct each grid m with fluxes from grids at level $lv1 + 1$, if any.

Step 4b. Overwrite zones on grid m with overlying zones at level $lv1 + 1$, if any.

Step 4c. Update any physical (non-periodic) boundary values which depend on zones which were just flux corrected or overwritten.

End For

If $lv1 > 1$, go to Step 3b.

Step 5. One entire AMR cycle is complete. Reconcile time steps across all grids and levels.

Step 6. Perform any required input/output.

Step 7. **If** $t < tlimit$, **go to** the top of the main loop, **else** exit.

Chapter 3

Simulating protostellar jets simultaneously at launching and observational scales¹

We present the first 2.5-D MHD simulations of protostellar jets that include both the region in which the jet is launched magnetocentrifugally at scale lengths < 0.1 AU, and where the propagating jet is observed at scale lengths $> 10^3$ AU. These simulations, performed with the new AMR-MHD code AZEuS, reveal interesting relationships between conditions at the disc surface, such as the magnetic field strength, and direct observables such as proper motion, jet rotation, jet radius, and mass flux. By comparing these quantities with observed values, we present direct numerical evidence that the magnetocentrifugal launching mechanism is capable, by itself, of launching realistic protostellar jets.

3.1 Introduction

Jets and outflows from protostellar objects are fundamental aspects of the current star formation paradigm, and are observed anywhere star formation is ongoing. The mechanism proposed by Blandford & Payne (1982), in which jets are launched from accretion

¹The contents of this chapter originally appeared as Ramsey, J.P., & Clarke, D.A., 2011, *The Astrophysical Journal*, 728, L11.

discs by gravitational, magnetic, and centrifugal forces, has been extensively studied numerically (*e.g.*, Uchida & Shibata 1985; Meier *et al.* 1997; Ouyed & Pudritz 1997a,b, 1999; Krasnopolsky *et al.* 1999; Vitorino *et al.* 2002; von Rekowski *et al.* 2003; Ouyed, Clarke, & Pudritz 2003; Porth & Fendt 2010; Staff *et al.* 2010). By treating the accretion disc as a boundary condition (*e.g.*, Ustyugova *et al.* 1995), one can study jet dynamics independently of the disc (*e.g.*, Pudritz *et al.* 2007) though, in order to resolve the launching mechanism, numerical simulations have not followed the jet beyond 100 AU (*e.g.*, Anderson *et al.* 2005).

In stark contrast, protostellar jets are $\gtrsim 10^4$ AU long (Bally, Reipurth, & Davis 2007), and only recently have observations reached within 100 AU of the source (*e.g.*, Hartigan, Edwards, & Pierson 2004; Coffey *et al.* 2008). This large scale difference between observations and simulations makes direct comparisons difficult and, in this work, we aim to close this gap. We present axisymmetric (2.5-D) simulations of protostellar jets launched from the inner AU of a Keplerian disc, and follow the jet well into the observational domain (2500 AU). These calculations allows us to address the efficacy of the magnetocentrifugal mechanism, and to relate conditions near the disc with directly observable properties of the jet.

The simulations presented herein are performed with an adaptive mesh refinement (AMR) version of *ZEUS-3D* (Clarke 1996, 2010) called AZEuS (Adaptive Zone Eulerian Scheme). The *ZEUS-3D* family of codes are among the best tested, documented, and most widely used astrophysical MHD codes available, though this is the first attempt to

couple *ZEUS-3D* with AMR². We have implemented the block-based method of AMR detailed in Berger & Colella (1989) and Bell *et al.* (1994). Significant effort was spent minimising errors caused by passing waves across grid boundaries, which is of particular importance to this work. A full description of the code and the changes required for AMR on a fully-staggered mesh will appear in Ramsey & Clarke (in preparation).

3.2 Initialisation

Observationally, the inner radius of a protostellar accretion disc, r_i , is between 3–5 R_* (Calvet *et al.* 2000) and, for a typical T Tauri star ($M = 0.5 M_\odot$, $R_* = 2.5 R_\odot$), $r_i = 0.05$ AU. Thus, following Ouyed & Pudritz (1997a), we initialise a hydrostatic, force-free atmosphere surrounding a $0.5 M_\odot$ protostar coupled to a rotating disc with $r_i = 0.05$ AU. However, unlike Ouyed & Pudritz we use an adiabatic equation of state that conserves energy across shocks rather than an isentropic polytropic equation of state, as the distinction becomes important for supermagnetosonic flow (Ouyed, Clarke, & Pudritz 2003).

We solve the equations of ideal MHD³ ($\gamma = 5/3$) over a total domain of $4096 \text{ AU} \times 256 \text{ AU}$. To span the desired length scales, nine nested, static grids (refinement ratio 2) are initialised each with an aspect ratio of 4:1 (16:1 for the coarsest grid only) and bottom left corner at the origin. Our finest grid has a domain $4 \text{ AU} \times 1 \text{ AU}$ and a resolution $\Delta z = r_i/8 = 0.00625 \text{ AU}$ which we find sufficient to resolve the launching mechanism.

²*ENZO*, a hybrid N-body Eulerian code (O’Shea *et al.* 2004), links AMR with the *hydrodynamical* portion of *ZEUS-2D*.

³*AZEUS* solves either the total or internal energy equation. We chose the latter because positive-definite pressures trump strict conservation of energy in these simulations; see Clarke (2010).

Thus, the effective resolution for the entire domain is > 26 billion zones. The simulation highlighted in §3.3 was run to $t = 100$ yr with an average time step in the finest grid of ~ 3 minutes and thus ~ 18 million time steps.

During the simulations, a thin region of low velocity and high poloidal magnetic field, $B_p = \sqrt{B_z^2 + B_r^2}$, develops along the symmetry axis, the edge of which is defined by a large gradient in the toroidal magnetic field, $\partial_r B_\varphi$. Insufficient resolution of $\partial_r B_\varphi$ can lead to numerical instabilities, and grids are added dynamically whenever this gradient is resolved by fewer than five zones.

3.2.1 The atmosphere

The atmosphere is initialised in hydrostatic equilibrium (HSE; $v_z = v_r = v_\varphi = 0$). Because the LHS of the equation governing HSE,

$$\nabla p + \rho \nabla \phi = 0, \quad (3.1)$$

is not a perfect gradient, differencing it directly on a staggered-mesh can commit sufficient truncation error to render the atmosphere numerically unstable. Thus, we replace $\nabla \phi$ with the corresponding poloidal gravitational acceleration vector,

$$\vec{g} = -\frac{1}{\rho_h} \nabla p_h, \quad (3.2)$$

where ρ_h and p_h are the hydrostatic density and pressure given by:

$$\rho_h = \rho_i \left(\frac{r_i}{\sqrt{r^2 + z^2}} \right)^{\frac{1}{\gamma-1}} \quad \text{and} \quad p_h = \frac{p_i}{\gamma} \left(\frac{\rho_h}{\rho_i} \right)^\gamma. \quad (3.3)$$

Here, ρ_i and p_i are the initial density and pressure at r_i and $p \propto \rho^\gamma$ is assumed throughout the atmosphere at $t = 0$. In this way, differencing equation (3.1) maintains HSE to within machine round-off error *indefinitely*.

However, equations (3.3) as given are singular at the origin where truncation errors are significant regardless of resolution. These errors can launch a supersonic, narrow jet from the origin destroying the integrity of the simulation. To overcome this problem, we replace the point mass at the origin with a uniform sphere of the same mass and a radius R_0 , thus modifying the first of equations (3.3) to:

$$\left(\frac{\rho_h}{\rho_i} \right)^{\gamma-1} = \begin{cases} \frac{r_i}{\sqrt{r^2 + z^2}}, & r^2 + z^2 \geq R_0^2; \\ \frac{r_i}{R_0} \frac{3R_0^2 - r^2 - z^2}{2R_0^2}, & r^2 + z^2 < R_0^2. \end{cases} \quad (3.4)$$

If R_0 is sufficiently resolved (*e.g.*, four zones), the numerical jet is eliminated. The resulting “smoothed potential” is superior to a “softened potential” since the former has no measurable effects beyond R_0 . Here, we use $R_0 = r_i$.

The atmosphere is initialised with the force-free magnetic field used by Ouyed & Pudritz (1997a):

$$A_\varphi = \frac{B_i}{\sqrt{2 - \sqrt{2}}} \frac{\sqrt{r^2 + (z + z_d)^2} - (z + z_d)}{r}; \quad (3.5)$$

$$B_z = \frac{1}{r} \frac{\partial(rA_\varphi)}{\partial r}, \quad B_r = -\frac{\partial A_\varphi}{\partial z}, \quad B_\varphi = 0,$$

where A_φ is the vector potential, z_d is the disc thickness (set to r_i), and B_i is the magnetic field strength at r_i , given by:

$$B_i = \sqrt{\frac{8\pi p_i}{\beta_i}}. \quad (3.6)$$

Here, p_i and β_i (plasma beta at r_i) are free parameters.

Finally, to ensure the declining density and magnetic field profiles do not fall below observational limits, we add floor values $\rho_{\text{floor}} \sim 10^{-6}\rho_i$ and $B_{z,\text{floor}} \sim 10^{-5}B_i$ (c.f. Bergin & Tafalla 2007, Vallée 2003) to equations (3.4) and (3.5). By imposing HSE and the adiabatic gas law at $t = 0$, a floor value on ρ imposes effective floor values on \vec{g} and p as well.

3.2.2 Boundary Conditions

In the accretion disc ($z \leq 0$, $r \geq r_i$), $v_\varphi = v_K = \sqrt{GM_*/r}$, the Keplerian speed, and $v_z = \zeta v_K = 10^{-3}v_K$ is an “evaporation speed” at the disc surface. The disc and atmosphere are initially in pressure balance with a density contrast $\eta = \rho_{\text{disc}}/\rho_{\text{atm}} = 100$, while \vec{B} is initialised using equations (3.5).

Following Krasnopolsky *et al.* (1999), ρ , p , and v_z are held constant, $v_r = v_z B_r / B_z$, $v_\varphi = v_K + v_z B_\varphi / B_z$, $E_z(-z) = E_z(z)$ (where $\vec{E} = \vec{v} \times \vec{B}$ is the induced electric field), $E_r(0) = v_K B_z(0)$, $E_r(-z) = 2E_r(0) - E_r(z)$, $E_\varphi(0) = 0$, and $E_\varphi(-z) = -E_\varphi(z)$. Since v_z is sub-slow, these conditions are formally over-determined and p should probably be allowed to float. Indeed, we allowed p to be determined self-consistently in test simulations, and found only minor quantitative differences in the jet since the pressure gradient is only about 1% of the net Lorentz force at the disc surface. However, allowing p to float in the boundary caused undue high temperatures in the disc, and thus small time steps. Therefore, the simulation proceeds more rapidly but otherwise virtually unchanged when p is maintained at its initial value.

Inside r_i ($z \leq 0$), we apply reflecting, conducting boundary conditions ($\vec{J} = \nabla \times \vec{B} \neq 0$). Thus, ρ , p , and \vec{v} are reflected across $z = 0$, and magnetic boundary conditions are set according to $E_z(-z) = -E_z(z)$, $E_r(-z) = E_r(z)$, and $E_\varphi(-z) = E_\varphi(z)$. At $z = 0$, E_r and E_φ are evolved using the full MHD equations.

Finally, we use reflecting boundary conditions along the $r = 0$ symmetry axis, and outflow conditions along the outermost r and z boundaries.

3.2.3 Scaling Relations

From equation (3.1) and the adiabatic gas law, one can show:

$$c_s^2 = \gamma \frac{p}{\rho} = (\gamma - 1) \frac{GM_*}{R} = (\gamma - 1) v_K^2, \quad (3.7)$$

where R is the spherical polar radius. From equations (3.6), (3.7), and the ideal gas law ($p = \rho kT / \langle m \rangle$, where $\langle m \rangle$ is half a proton mass), we derive the following scaling relations to convert from unitless to physical quantities:

$$p_i = (160 \text{ dyne cm}^{-2}) \left(\frac{\beta_i}{40} \right) \left(\frac{B_i}{10 \text{ G}} \right)^2; \quad (3.8)$$

$$\frac{\rho_i}{\langle m \rangle} = (5.4 \times 10^{12} \text{ cm}^{-3}) \left(\frac{\beta_i}{40} \right) \left(\frac{B_i}{10 \text{ G}} \right)^2 \left(\frac{r_i}{0.05 \text{ AU}} \right) \left(\frac{0.5 M_\odot}{M_*} \right); \quad (3.9)$$

$$T_i = (2.2 \times 10^5 \text{ K}) \left(\frac{0.05 \text{ AU}}{r_i} \right) \left(\frac{M_*}{0.5 M_\odot} \right); \quad (3.10)$$

$$c_{s,i} = (77 \text{ km s}^{-1}) \left(\frac{0.05 \text{ AU}}{r_i} \right)^{1/2} \left(\frac{M_*}{0.5 M_\odot} \right)^{1/2}; \quad (3.11)$$

$$\tau_i = \frac{r_i}{c_{s,i}} = (9.7 \times 10^4 \text{ s}) \left(\frac{r_i}{0.05 \text{ AU}} \right)^{3/2} \left(\frac{0.5 M_\odot}{M_*} \right)^{1/2}, \quad (3.12)$$

for $\gamma = 5/3$. Note that β_i is the only free parameter varied in this work.

3.3 Results for $\beta_i = 40$

Figure 3.1 depicts a jet with $\beta_i = 40$ at $t \simeq 100$ yr from the highest resolution grid near the disc surface (bottom panel) to the coarsest grid in which the jet has reached a length of just under 2500 AU (top panel)⁴. A few features worth noting include:

- When $\theta < 60^\circ$ (angle between \vec{B}_p and disc surface), Blandford & Payne (1982) show that cold gas near the disc is launched into a collimated outflow. Here, $\theta < 60^\circ$ for all $r > r_i$, but significant outflow is limited to inside the point where the slow surface intersects the disc ($r_{j,d} \sim 30 \text{ AU} = \text{jet radius at the disc}$; second panel

⁴Time-lapse animations are available at <http://www.ica.smu.ca/zeus3d/rc10/>.

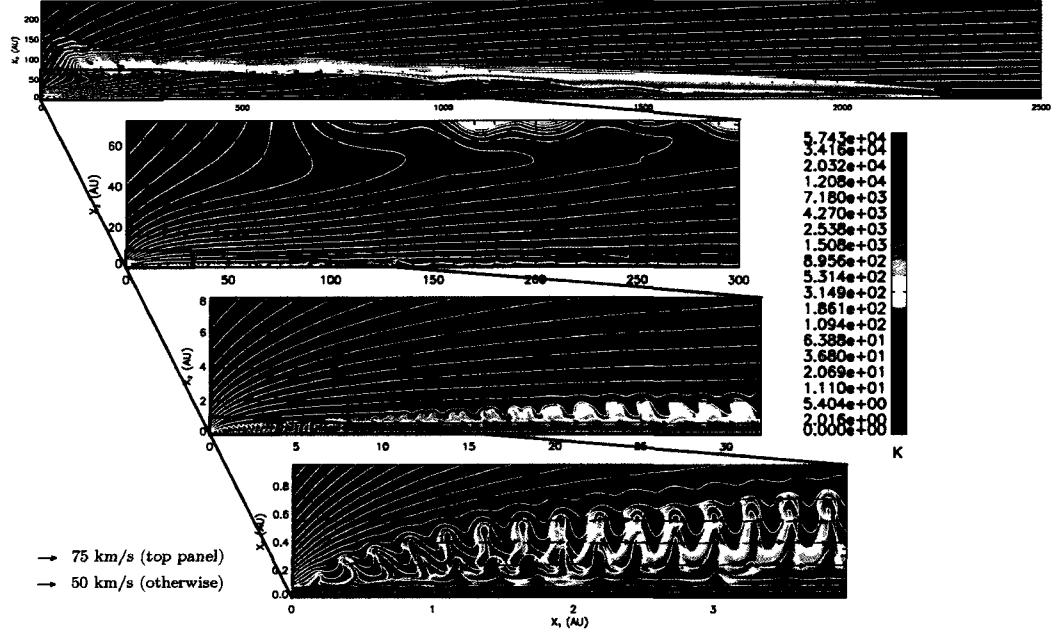


Figure 3.1 Nested images of a $\beta_i = 40$ jet at $t = 100$ yr. Colours indicate temperature, white contours magnetic field lines, maroon contours the slow surface, and arrows the velocity. Dashed lines denote grid boundaries, and $x_1 = z$, $x_2 = r$.

from top). Below $r_{j,d}$, cold disc material has moved onto the grid and accelerated into the outflow. Above $r_{j,d}$, the weak magnetic field has yet to drive enough disc material onto the grid to displace the hot atmosphere, and outflow is stifled. While $r_{j,d}$ gradually increases with time, the majority of mass flux *originating from the disc* is driven within $r_i < r < 10 r_i$ (0.5 AU; bottom panel).

- Jet material becomes super-fast ($M_f \lesssim 5$) within a few AU of the disc, and the boundary between jet and entrained ambient material is defined by a steep temperature gradient (contact discontinuity; second panel). Portions of the original

atmosphere, which remain virtually stationary throughout the simulation, are still visible above and ahead of the bow shock (top panel).

- At large distances from the disc ($\gtrsim 500$ AU; top panel), the dynamics of the jet become dominated by B_φ , and the jet is led by an essentially ballistic, magnetic “nose-cone” with a Mach number of ~ 10 (*e.g.*, Clarke, Norman, & Burns 1986). Still, B_φ is a small fraction (10^{-3}) of B_i , consistent with Hartigan *et al.* (2007).
- The knots dominating the bottom panel (*c.f.*, Ouyed & Pudritz 1997b) are produced by the nearly harmonic oscillation of \vec{B}_p in $r_i < r < 2r_i$, whereby θ fluctuates between 55° and 65° with a period $\sim 30 \tau_i$. These oscillations result from the interplay between in-falling material along the symmetry axis, and under/over pressurisation near the central mass. The knots are denser and hotter than their surroundings, and bound by magnetic field loops. They occupy a region within ~ 2 AU of the symmetry axis, and gradually merge to form a continuous and narrow column of hot, magnetised material⁵ (third panel). As such, they are unlikely to be the origin of the much larger-scale knots observed in some jets (*e.g.*, HH111; Raga *et al.* 2002).

Further details of this and other simulations of protostellar jets are left to a future paper, and we focus here on a few properties directly comparable with observations.

⁵The knots are resolved by 10–20 zones when they merge, and thus their merger is unlikely related to the ever-decreasing resolution of the nested grids.

| | |
|---|----------------------|
| proper motion (km s^{-1}) | 100 – 200 (500 max.) |
| rotational velocity (km s^{-1}) | $(5 - 25) \pm 5$ |
| FWHM jet width (AU) | 30 – 80 (at 200 AU) |
| mass-loss rate ($10^{-6} M_{\odot} \text{yr}^{-1}$) | 0.01 – 1 |

Table 3.1 Selected observational characteristics of protostellar jets. References: Reipurth & Bally (2001), Ray *et al.* (2007), McKee & Ostriker (2007).

3.4 Comparing simulations and observations

Table 3.1 summarises a few observational characteristics of protostellar jets. To connect these attributes to conditions in the launching region, we have performed a small parameter survey in β_i , and made numerical measurements of the quantities in Table 3.1. Variation of other parameters (such as ζ and ρ_i) is left to future work.

Note that β_i is the initial value of the plasma beta at r_i , and not the average β in the jet. Indeed, Fig. 3.2a demonstrates that at very early time, $\langle\beta\rangle = 8\pi\langle p\rangle/\langle B^2\rangle \lesssim \beta_i/5$, where $B^2 = B_p^2 + B_\varphi^2$, and where the average is taken over zones that exceed a certain threshold v_z so that only out-flowing jet material is considered. Thus, the magnetic field within the jet is stronger than β_i would suggest. Initially, $\langle\beta\rangle$ is dictated by B_p , but becomes dominated by B_φ within $\lesssim 10$ yr after launch. As time progresses, $\langle\beta\rangle$ gradually increases but never rises above unity (at least for $t < 100$ yr), even for $\beta_i \gg 1$. Still, one might speculate from Fig. 3.2a that with sufficient time, $\langle\beta\rangle \rightarrow 1$ regardless of β_i .

3.4.1 Proper motion

For $t \gtrsim 10$ yr, the velocity of the tip of the jet, v_{jet} , is nearly constant and, from Fig. 3.2b and Table 3.2, we find $v_{\text{jet}} \propto B_i^{0.44 \pm 0.01}$.

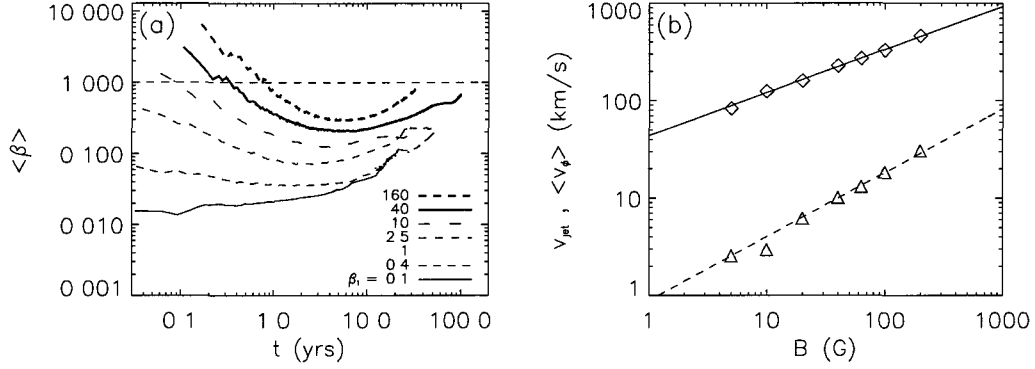


Figure 3.2 (a) $\langle \beta \rangle$ as a function of time for different β_1 . (b) v_{jet} (diamonds) and $\langle v_{\phi} \rangle$ (triangles) of each jet as a function of B_1 . Best fit power-law coefficients for these data are $\alpha = 0.44 \pm 0.01$ (v_{jet} , solid line) and 0.66 ± 0.01 ($\langle v_{\phi} \rangle$, dashed line).

To understand this result physically, we begin with the magnetic forces:

$$\begin{aligned}
 F_{\parallel} &= -\frac{B_{\phi}}{r} \nabla_{\parallel} (r B_{\phi}); \\
 F_{\phi} &= \frac{B_p}{r} \nabla_{\parallel} (r B_{\phi}); \\
 F_{\perp} &= -\frac{B_{\phi}}{r} \nabla_{\perp} (r B_{\phi}) + J_{\phi} B_p,
 \end{aligned} \tag{3.13}$$

(e.g., Ferreira 1997; Zanni *et al.* 2007) where $\nabla_{\parallel}, \nabla_{\perp}$ are the gradients parallel and perpendicular to \vec{B}_p . For a given field line, a stronger B_p at its “footprint” in the disc ($r = r_0$) generates a stronger B_{ϕ} which leads to stronger gradients in $r B_{\phi}$ and thus, from equations (3.13), greater magnetic forces to accelerate the flow. In practice, we find that most of the acceleration occurs before the fast point (and not the Alfvén point) located at $r = r_f$, where r_f is a weak function of the field strength at the footprint and thus of B_1 .

Following Spruit (1996), one can show that as a function of the “fast moment arm” ($\xi \equiv r_f/r_0$), the poloidal velocity at the fast point is:

$$v_{p,f} = \sqrt{a_{p,f} v_{K,0}} \left(\xi^2 + \frac{2}{\xi} - 3 \right)^{1/4} \propto \sqrt{B_i} \quad (3.14)$$

since $a_{p,f}$, the poloidal Alfvén speed at the fast point, is roughly proportional to B_i . $v_{K,0} = \sqrt{GM_*/r_0}$ is the Keplerian speed at the footprint of the field line. We note that measured values of $v_{p,f}$ in our simulations vary as $B_i^{0.5}$ and agree with equation (3.14) to within 1% so long as the fluid is in approximate steady-state⁶.

After the poloidal force given by equations (3.13) decreases to 1% of its maximum value (\gtrsim a few r_f), v_p still follows a power law in B_i with index 0.52 ± 0.04 and essentially unchanged from equation (3.14). Nearer the head of the jet where steady state is no longer valid, we find $\langle v_p \rangle \propto B_i^{0.45 \pm 0.02}$ (where the momentum-weighted average is taken across the jet radius), only slightly shallower than equation (3.14). Thus, while the conditions in the jet have changed, some memory of the steady-state conditions at r_f persists.

Finally, v_{jet} (Fig. 3.2b and Table 3.2) is within $\sim 10\%$ of $\langle v_p \rangle$ near the bow shock and maintains the same power-law dependence on B_i . Thus, these jets are essentially ballistic, where the observed jet speed $v_{\text{jet}} \propto B_i^{0.44 \pm 0.01}$. In short, all measures of jet speed increase with B_i , a trend that agrees with Anderson *et al.* (2005) who find for much less evolved jets, $v_p \propto B_i^{1/3}$.

⁶Indeed, all four steady-state functions from Spruit (1996) remain constant in our simulations to within $\lesssim 5\%$ along steady-state field lines, which we take as validation of our numerical methods.

| β_i | 160 | 40 | 10 | 2.5 | 1.0 | 0.4 | 0.1 | |
|--|------|-----|-----|------|------|------|------|-----------------|
| B_i (G) | 5 | 10 | 20 | 40 | 63.2 | 100 | 200 | α |
| v_{jet} (km s ⁻¹) | 84 | 125 | 161 | 230 | 270 | 330 | 460 | 0.44 ± 0.01 |
| $\langle v_\varphi \rangle$ (km s ⁻¹) | 2.6 | 3.0 | 6.2 | 10.1 | 13.1 | 18.4 | 31 | 0.66 ± 0.01 |
| $2 r_{\text{jet}}$ (AU) | 21 | 40 | 60 | 85 | 94 | 104 | 130 | 0.35 ± 0.04 |
| \dot{M}_{jet} ($10^{-6} M_\odot \text{ yr}^{-1}$) | 0.44 | 1.9 | 2.8 | 4.2 | 6.9 | 10.1 | 17.9 | 0.92 ± 0.09 |

Table 3.2 Simulation “observables” v_{jet} and $\langle v_\varphi \rangle$ are asymptotic values while r_{jet} and \dot{M}_{jet} are measured at $z = 200$ AU and $t = 20$ yr. Uncertainties in α are from the fitting procedure.

3.4.2 Toroidal velocity

Figure 3.2b and Table 3.2 show v_φ averaged over time and the jet volume for $z \geq 100$ AU as a function of B_i . Like v_{jet} , v_φ asymptotes to a constant value. The region inside 100 AU is ignored because the torsion Alfvén wave at low z has a non-negligible v_φ , is not part of the jet, and skews our results. By fitting a power law to these data, we find $\langle v_\varphi \rangle \propto B_i^{0.66 \pm 0.01}$.

Unlike v_{jet} , we have not uncovered a rationale for this power law, yet it seems plausible one must exist given the tightness of fit. Eliminating B_i from the power laws for $\langle v_\varphi \rangle$ and v_{jet} , we find that $\langle v_\varphi \rangle \propto v_{\text{jet}}^{1.50 \pm 0.06}$. To render this a useful observational tool, further work is needed to quantify the effects of other initial conditions such as ζ and ρ_i on both the power law index and the proportionality constant, as well as the effect our simplified disc model may have on conditions in the jet at observational length scales.

3.4.3 Jet radius and mass flux

The jet radius, r_{jet} , is defined by the contact discontinuity (steep temperature gradient in the second panel of Fig. 3.1) between shocked jet and shocked ambient material, which in turn is determined by where the radial jet ram pressure balances all external forces. Since ram pressure increases with v_p , r_{jet} should increase with B_i , just as observed in Table 3.2. At any given time, we find that r_{jet} varies with B_i as a reasonable power law though, unlike v_{jet} or $\langle v_\varphi \rangle$, the power index is not constant and decreases slowly in time, while r_{jet} itself increases in time, though at an ever-slowing rate.

The mass flux transported by the jet, \dot{M}_{jet} , consists of material from both the disc and the atmosphere. Unlike previous simulations where jets are typically evolved long after the leading bow shock has left the grid, no part of any bow shock in our simulations reaches the boundary of the coarsest grid. Thus, each jet continues to entrain material from the atmosphere throughout the simulation at a rate that has a strong dependence on B_i , as seen in Table 3.2. Indeed we find that \dot{M}_{jet} varies with B_i as a reasonable power law, with the power index decreasing slowly in time. As the atmosphere is depleted, the mass flux contribution from the disc (which, by design, is independent of B_i) becomes more important and the dependence of \dot{M}_{jet} on B_i diminishes.

3.5 Discussion

We have presented the first MHD simulations of protostellar jets that start from a well-resolved launching region ($\Delta z_{\text{min}} = 0.00625$ AU) and continue well into the observational domain (2500 AU). On the AU scale, each jet shows the characteristic and

near steady-state knotty behaviour first reported by Ouyed & Pudritz (1997b), though the origin of our knots is quite different. On the 1000 AU scale, each jet develops into a ballistic, supersonic ($8 \lesssim M \lesssim 11$) outflow led by a magnetically confined “nose-cone” (Clarke, Norman, & Burns 1986) and a narrow bow shock, consistent with what is normally observed.

On comparing Tables 3.1 and 3.2, our simulations comfortably contain virtually all observed protostellar jets on these four important quantities. We note that these tables would *not* have been in agreement had we stopped the jet at, say, 100 AU and measured these values then. *It is only because our jets have evolved over five orders of magnitude in length scale that we can state with some confidence that the magnetocentrifugal launching mechanism is, by itself, capable of producing jets with the observed proper motion, rotational velocity, radius, and mass outflow rate.* Indeed, our jets are still very young, having evolved to only 100 yr, and allowing them to evolve over an additional one or two orders of magnitude in time may still be useful. For example, it would be interesting to know whether $\langle\beta\rangle$ rises above unity for any of the jets (Fig. 3.2a), and thus enter into a hydrodynamically dominated regime. It would also be interesting to see how long it takes for the power laws in jet radius and mass flux as a function of B_i to reach their asymptotic limits.

Our jet widths tend to be higher than those observed, particularly when one considers that the values for r_{jet} in Table 3.2 are at $t = 20 \text{ yr}$ ⁷, and that r_{jet} continues to grow in time (*e.g.*, for the $\beta_i = 40$ jet, $2r_{\text{jet}} \sim 100 \text{ AU}$ by $t = 100 \text{ yr}$). As our jet radii mark the locations of the contact discontinuity while observed radii mark hot, emitting regions, our

⁷Some simulations had not reached $t = 100 \text{ yr}$ at the time of this writing.

widths should be considered upper limits. That our values *contain* all observed jet widths is a success of these simulations.

Similarly, our numerical mass fluxes are higher than observed values by at least an order of magnitude. Since observed mass-loss rates account only for emitting material (*e.g.*, in forbidden lines; Hartigan, Morse, & Raymond 1994), and thus temperatures in excess of 10^4 K (Dyson & Williams 1997; p. 104), our mass fluxes are necessarily upper limits as well. Indeed, if we measure our mass fluxes near the jet tip (instead of at 200 AU for Table 3.2) and restrict the integration to fluid above 10^4 K, our mass fluxes drop by a factor of 10–100, in much better agreement with Table 3.1.

Chapter 4

Additional results from simulations of protostellar jets

In this Chapter, I expand upon the results of Chapter 3 by describing the methods used to achieve those results, introducing new results and expanding on the discussion. In light of this broader picture, I revisit previous comparisons to observations in an attempt to make further connections with observed protostellar jets.

4.1 Introduction

In this work, I simulate the time-dependent equations of ideal MHD in cylindrical, axisymmetric $[(z, r, \varphi); \partial/\partial\varphi = 0]$ coordinates using the AZEuS AMR-MHD fluid code. The ideal equation of state, $\gamma = 5/3$, and the internal energy equation are used (as opposed to the total energy equation) for reasons described in Section 3.2.

The total computational domain is 4096×256 AU in size, within which we place 8 additional levels of higher resolution. Table 4.1 summarises our initial static mesh refinement set up, with the lower-left corner of each grid located at the origin. For grids at levels $l > 1$, the seemingly odd grid dimensions are a result of the desire to maximise parallel efficiency. AZEuS employs OpenMP parallelism at the do-loop level, and a noticeable increase in efficiency is observed if the number of iterations in the most

time intensive loops are tuned to a multiple of the number of CPUs being used (in this case, we almost exclusively use 16 CPUs).

| Level | $z_{\max}(AU)$ | $r_{\max}(AU)$ | $\Delta z (AU)$ |
|-------|----------------|----------------|-----------------------|
| 1 | 4096 | 256 | 1.6 |
| 2 | 508.8 | 124.8 | 0.8 |
| 3 | 254.4 | 62.4 | 0.4 |
| 4 | 127.2 | 31.2 | 0.2 |
| 5 | 63.6 | 15.6 | 0.1 |
| 6 | 31.8 | 7.8 | 5.0×10^{-2} |
| 7 | 15.9 | 3.9 | 2.5×10^{-2} |
| 8 | 7.95 | 1.95 | 1.25×10^{-2} |
| 9 | 3.975 | 0.975 | 6.25×10^{-3} |

Table 4.1 Initial static grid set up for these simulations. The zones are everywhere uniform in shape (*i.e.*, $\Delta z = \Delta r$).

In addition to static grids, which are stationary throughout the simulation lifetime, resolution is added dynamically using the criterion described in Section 4.4.

With the exception of the initial magnetic field strength, B_i , the initial conditions for all simulations are the same. B_i is measured at r_i , where $r_i = 0.05$ AU is the inner disc radius. The plasma- β at r_i is $\beta_i = 8\pi p_i/B_i^2$, where p_i is held constant in this work. Further details of the initial conditions may be found in Chapter 3.

Additional run-time parameters for the simulations presented here and in Chapter 3 include a Courant number of $\mathcal{C} = 0.5$, artificial viscosity parameters $q_{\text{con}} = 2.0$ and $q_{\text{lin}} = 0.2$, and AMR parameters $k_{\text{check}} = 100$, $i_{\text{buff}} = 2$, and $g_{\text{effcy}} = 0.5$. Definitions of these input parameters can be found in Section 2.7.1. Conversions between simulation and physical units employ the scaling relations of Section 3.2.3.

| Simulation | β_i | B_i (G) | t_{end} (yr) |
|------------|-----------|-----------|-----------------------|
| A | 0.1 | 200 | 42.37 |
| B | 0.4 | 100 | 60.53 |
| C | 1.0 | 63.2 | 74.92 |
| D | 2.5 | 40 | 92.68 |
| E | 10 | 20 | 100.0 |
| F | 40 | 10 | 100.0 |
| G | 160 | 5 | 76.18 ^a |
| H | 640 | 2.5 | 100.0 |

Table 4.2 Summary of simulation times. The simulation end time, t_{end} , denotes when the jet leaves the computational domain or $t = 100$ yr, whichever comes first.

^aAt this time of this writing, the $\beta_i = 160$ simulation is still running.

Table 4.2 summarises the simulation lifetimes for the set of simulations presented herein. The simulation lifetime, t_{end} , is defined by when the jet either leaves the computational domain, or the physical problem time reaches $t = 100$ yr. When Chapter 3 was written, most of the simulations summarised in Table 4.2 had not yet run to completion. Indeed, the motivation for discussing simulation F in detail in Section 3.3 was because it *had* run to $t = 100$ yr. In that which follows, we expand the discussion to include all of the simulations presented in Chapter 3, including an additional simulation with very weak magnetic field ($\beta_i = 640$; $B_i = 2.5$ G). Time-lapse animations of the results presented here can be found at <http://www.ica.smu.ca/zeus3d/rc10/>.

4.2 Description of simulations

Each simulation begins with the launching of a torsion Alfvén wave from the disc surface which imparts a sudden torque on the magnetic field in the atmosphere. The

propagation of this torsion wave can be described by (*e.g.*, Mouschovias & Paleologou 1980):

$$\frac{\partial^2 B_\varphi}{\partial t^2} = a_{A,\text{atm}}^2 \frac{\partial^2 B_\varphi}{\partial z^2}; \quad (4.1)$$

$$\frac{\partial B_\varphi}{\partial t} = r B_p \frac{\partial(r v_\varphi)}{\partial z}, \quad (4.2)$$

where $a_{p,\text{atm}} = B_{p,\text{atm}}/\sqrt{4\pi\rho_{\text{atm}}}$, ρ_{atm} are the Alfvén speed and density of the undisturbed atmosphere, respectively. These equations describe how the torsion wave propagates with time, as well as how B_φ is generated. Given that $B_{p,\text{atm}}$ is proportional to B_i , the speed of the torsion Alfvén wave will also be proportional to B_i .

Behind the torsion wave, a toroidal field and velocity are established which quickly results in a magnetic pinch towards the axis, and a centrifugal force in the positive r -direction. Combined with gravity and pressure forces, the net force points away from the disc, and material is accelerated into a wind. Beginning at r_i and moving radially outward with time, the flow just above the disc surface becomes super-slow, and cold disc material begins flowing into this newly-established wind.

4.2.1 Simulation A: $\beta_i = 0.1$

The initial magnetic field configuration (equations 3.5) is such that the angle the field makes with the disc is $< 60^\circ$ for $r \geq 2r_i$, and the conditions for launching a wind centrifugally from the disc are favourable right from the beginning (Blandford & Payne 1982; Section 1.2). In simulation A, because of the strong magnetic field, the critical

angle for launching at the disc surface changes very little with time, remaining satisfied for $r \geq 2r_i$ throughout the simulation.

The expansion of the slow surface at the disc occurs rapidly at first, but slows over time. By $t \simeq 42$ yr, it is located at $r_{j,d} \sim 20$ AU (Figure 4.1). Inside the slow surface, the initial atmosphere has been replaced by cold disc material with low temperature (~ 10 K) and plasma- β ($= 8\pi p/B^2 < 10^{-3}$).

Outside the slow surface, the poloidal velocity is low and little outflow takes place. Although the torsion Alfvén wave travels slowly through this region and generates a toroidal velocity and magnetic field, the initial atmosphere remains essentially stationary.

Once the initial atmosphere has been removed and the jet filled with cold disc material, the interior of the jet tends towards an approximately steady state. Between the axis and a reasonable distance inside the outer radius of the jet, I find that all quantities behave smoothly in both z and r , and only slowly in t .

Figure 4.2 shows the radial profiles of several quantities at 100 AU above the disc, demonstrating that the profiles are indeed smooth inside the outer jet radius. Other characteristic features exemplified by Figure 4.2 include absolute maxima which are located near the axis for all quantities, and centrally concentrated values of temperature, poloidal, and toroidal magnetic field. Also visible is a “backbone” of high v_p and B_p near the axis, but low v_φ and $|B_\varphi|$. Given that the global maxima are located just outside this backbone, the profiles in v_φ and B_φ experience strong gradients in both quantities as one approaches the axis.

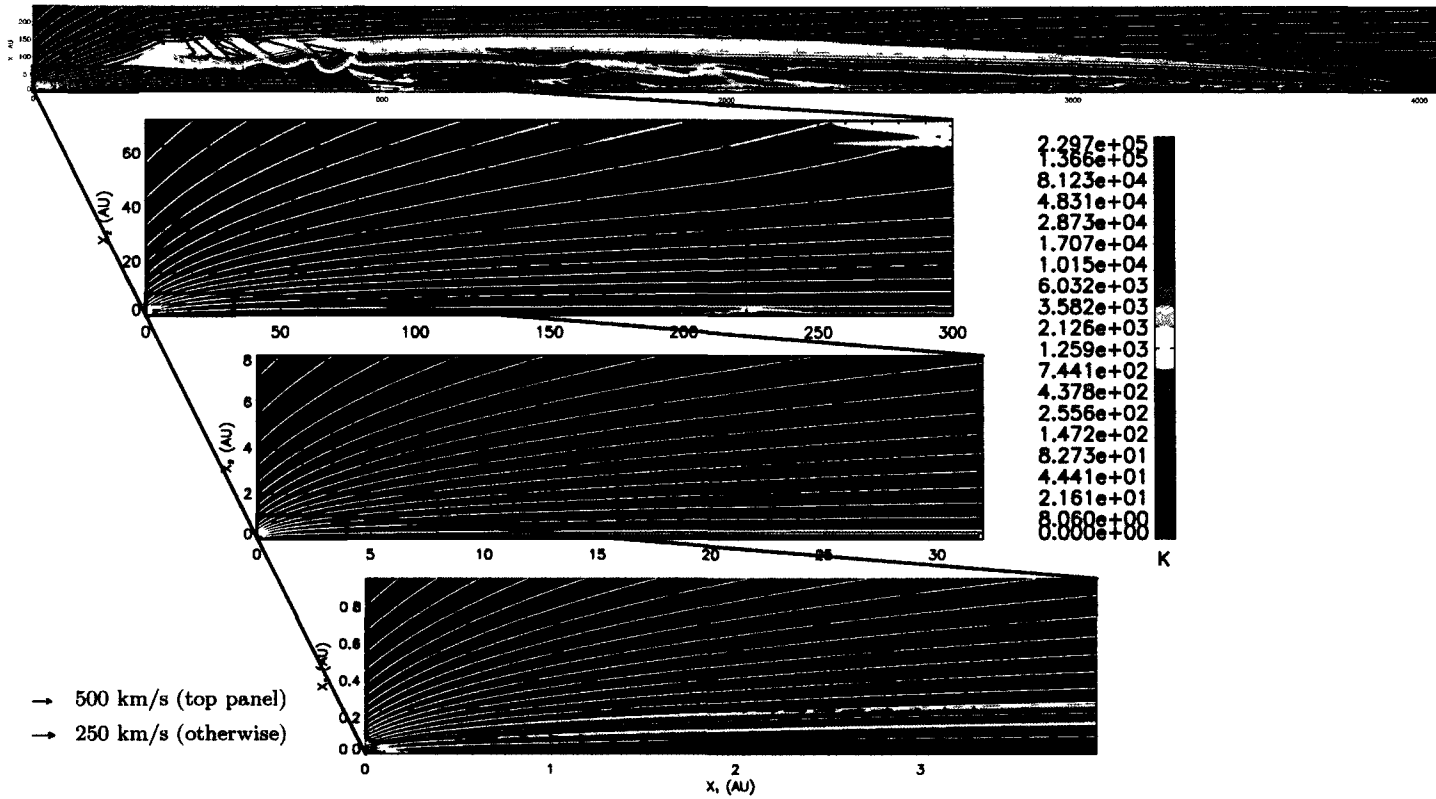


Figure 4.1 Nested images of simulation A at $t = 42.37$ yr. Colours indicate temperature, white contours magnetic field lines, black contours the slow magnetosonic surface, and arrows the poloidal velocity. Dashed lines indicate grid boundaries. The dimensions of the top panel are $z = x_1 \in [0, 4096]$ AU and $r = x_2 \in [0, 256]$ AU.

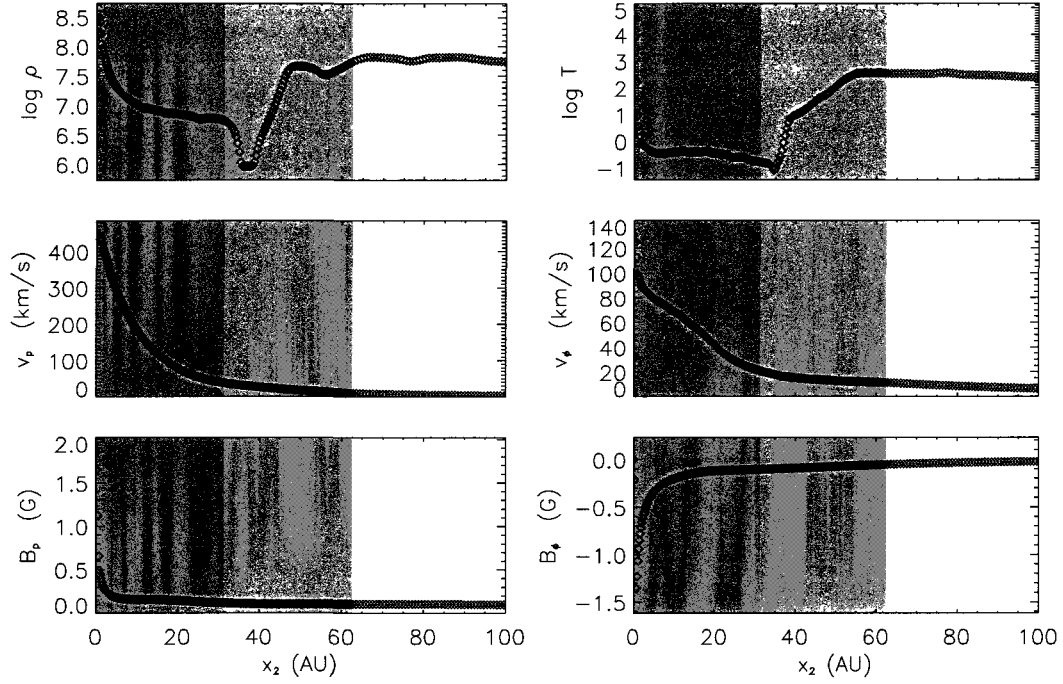


Figure 4.2 A radial slice from simulation A at $z = 100$ AU and $t = 42.37$ yr. Plotted on the left are, from top to bottom, logarithmic density, poloidal velocity, and poloidal magnetic field. Plotted on the right, from top to bottom, are logarithmic temperature, toroidal velocity, and toroidal field. Successively darker shading indicates a higher level of refinement; no shading corresponds to level $l = 2$. The highest resolution available at this height above the disc is level $l = 4$.

The outer jet radius is clearly visible in Figure 4.2 at $r \sim 40$ AU in both the density and temperature. The presence of a contact discontinuity at $r \sim 35$ AU and a global minimum in density between 35 – 40 AU is quite prominent, corresponding to just inside the outer edge of the jet. In contrast, the profiles of the other variables show no evidence of variation at the outer jet radius.

As the initial torsion wave propagates to greater z , it leaves behind it toroidal velocity and magnetic field. At t_{end} , the torsion wave at high r in simulation A extends past $z = 300$ AU. This material is clearly visible in Figure 4.2 beyond the outer jet radius, and has a small toroidal velocity and magnetic field. It also has a noticeably higher density and temperature than the majority of the jet.

At greater distances from the disc, the torsion Alfvén wave is replaced by a bow shock with the ambient medium and, as it propagates forward, heats the ambient material significantly (top panel, Figure 4.1). In fact, the highest temperatures in the simulation ($\sim 10^6$ K) occur at the head of the jet where it propagates into the undisturbed ambient medium.

The effects of the bow shock on the ambient are shown in Figure 4.3, which plots radial slices of several variables at $z = 1000$ AU above the disc. The outer jet radius (at $r \simeq 85 - 90$ AU) is clearly seen in the profiles of the hydrodynamic variables (but not B_p or B_φ) and, in particular, the sudden drop of the poloidal velocity at the outer edge of the jet and the effectively zero toroidal velocity beyond. Besides a noticeably higher temperature, the shocked ambient material ($r \simeq 90 - 95$ AU) is also characterised by a slow poloidal velocity, a result of material entrainment by the jet. Another noteworthy feature is a region of *negative* toroidal velocity just inside the jet radius which is co-spatial with a local reversal in the direction of the poloidal magnetic field (*i.e.*, change of sign in B_z ; Figure 4.3).

The jet radius initially increases with distance from the disc, but beyond some maximum, $r_{\text{jet,max}}$, it actually begins to narrow slightly with increasing distance from the disc

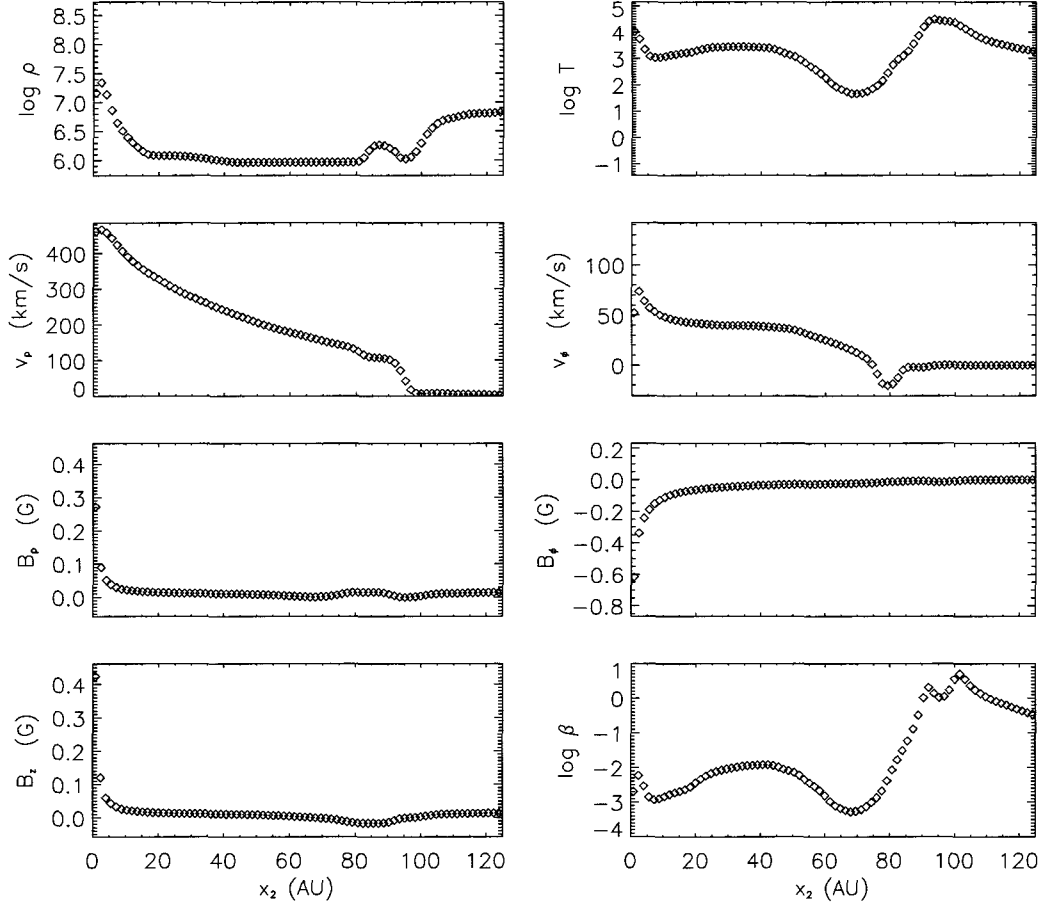


Figure 4.3 A radial slice from simulation A at $z = 1000$ AU and $t = 42.37$ yr. Plotted on the left are, from top to bottom, logarithmic density, poloidal velocity, poloidal field, and the z -component of the magnetic field. Plotted on the right, from top to bottom, are logarithmic temperature, toroidal velocity, and toroidal field, and logarithmic β . At this height above the disc, the highest resolution data available is at level $l = 1$.

(top panel of Figure 4.1). The majority of the jet momentum is forward-directed and concentrated near the symmetry axis, and so the jet propagates forward much faster than it radially expands. This is exacerbated somewhat by conditions in the ambient medium where, by the time the jet reaches $z \sim 500$ AU, the density and pressure are effectively

constant. As the now constant density and pressure require more force to displace than values which are steadily declining, the ability of the jet to expand is hampered.

Comparing Figures 4.2 and 4.3 at 100 and 1000 AU, the density has decreased while the temperature has increased, the toroidal velocity has decreased by a factor of ~ 1.5 , and the poloidal velocity profile has become shallower. However, the maximum poloidal velocity near the axis remains approximately the same.

At 100 AU above the disc, the magnitude of both the poloidal and toroidal fields are ≤ 2.0 G, significantly lower than their values at the disc surface ($B_p \gtrsim 50$ G, $B_\phi \lesssim 25$ G). At 1000 AU above the disc, the magnitude of the poloidal and toroidal field has fallen to ~ 0.3 G and ~ -0.7 G, respectively.

Figure 4.3 shows that β is low in the jet, only reaching ~ 1 in the shocked ambient medium. Thus, even though the large-scale fields appear weak relative to the values at the disc, they still dominate over thermal pressure, and the jet bow shock appears as a magnetically confined “nose-cone” (Clarke, Norman, & Burns 1986).

4.2.2 Simulation B: $\beta_i = 0.4$

The evolution of simulation B proceeds much the same as A, but the jet propagates and radially expands more slowly, taking ~ 60 yr to reach the edge of the domain (as opposed to ~ 42 yr for simulation A). The trends observed in Figures 4.2 and 4.3 remain the same, but the maxima of the different quantities decrease: *e.g.*, the strength of the fields decrease by a factor of ~ 2 at $z = 100$ AU relative to simulation A, and by a factor of ~ 1.5 at 1000 AU (notably, B_i is also a factor of 2 lower than in simulation A).

Meanwhile, the velocities decrease by a factor of $\sim 4/3$ at $z = 100$ AU and by a factor of ~ 1.5 at $z = 1000$ AU. The only qualitative difference from simulation A is the appearance of “knot”-like structures which periodically form near the origin and propagate down the length of the jet.

Figure 4.4 shows nested images of the temperature in simulation B at the simulation end time and, in the third panel, knot-like structures are clearly visible as regions of high temperature with spacing ~ 5 AU. Looking to the origin, these knots originate at $z \sim r \sim r_1 = 0.05$ AU, and propagate along the axis with the rest of the flow. In the case of simulation B, knots first appear at $t \sim 7$ yr, and are produced every ~ 0.090 yr thereafter.

As the knots (actually rings in cylindrical axisymmetry) propagate downstream, they slowly expand and diffuse in both the z and r directions, losing their original elongated shape. The spacing between knots is large enough that within ~ 60 AU of the disc surface, individual knots are easily distinguished. Beyond ~ 60 AU, the diffusion of the knots grows steadily until, around 120 AU, all that remains is a single contiguous column of hot, dense material along the jet axis.

The knots reach a maximum radius and length of only ~ 2 AU before merging into a single column of material. Even then, the maximum radial extent of the contiguous column remains well below 10 AU, and is virtually invisible on scales larger than 100 AU.

Taking an axial slice at $r = 1$ AU (Figure 4.5), oscillations associated with the knots can be seen as jumps in ρ , T , β , poloidal velocity (v_p), toroidal field (B_ϕ), Alfvénic Mach number (M_A), and fast magnetosonic Mach number (M_f). Conversely, knots are

anti-correlated with toroidal velocity v_ϕ , poloidal field (B_p), and slow magnetosonic Mach number (M_s).

In all the quantities plotted in Figure 4.5, a uniform knot spacing is evident, implying the knot generation period is constant. There is also an apparent lack of knots for $z \lesssim 10$ AU. Knots are indeed present inside $z = 10$ AU, they simply have not yet expanded to $r = 1$ AU, and thus do not show up in the axial slice.

Variations in the poloidal velocity and magnetic field components are small across the knots, while variations in density and temperature are high (factors of 10 – 1000). Hence, variations in the various Mach numbers are high, particularly for the slow speed.

In between knots, the flow is cold and magnetically-dominated (low β). In this situation, the slow speed is the analogue to the sound speed in hydrodynamics, and thus I expect the cold inter-knot regions to have small slow speeds and correspondingly high M_s , as observed in Figure 4.5.

From the trend underlying the knots, one can see that the magnetic field decreases with distance from the disc, as previously observed in Section 4.2.1. In addition, the poloidal velocity approaches an asymptotic value ($\sim 280 \text{ km s}^{-1}$) far from the disc, and the toroidal velocity first strongly increases, then gradually decreases, with height from the disc.

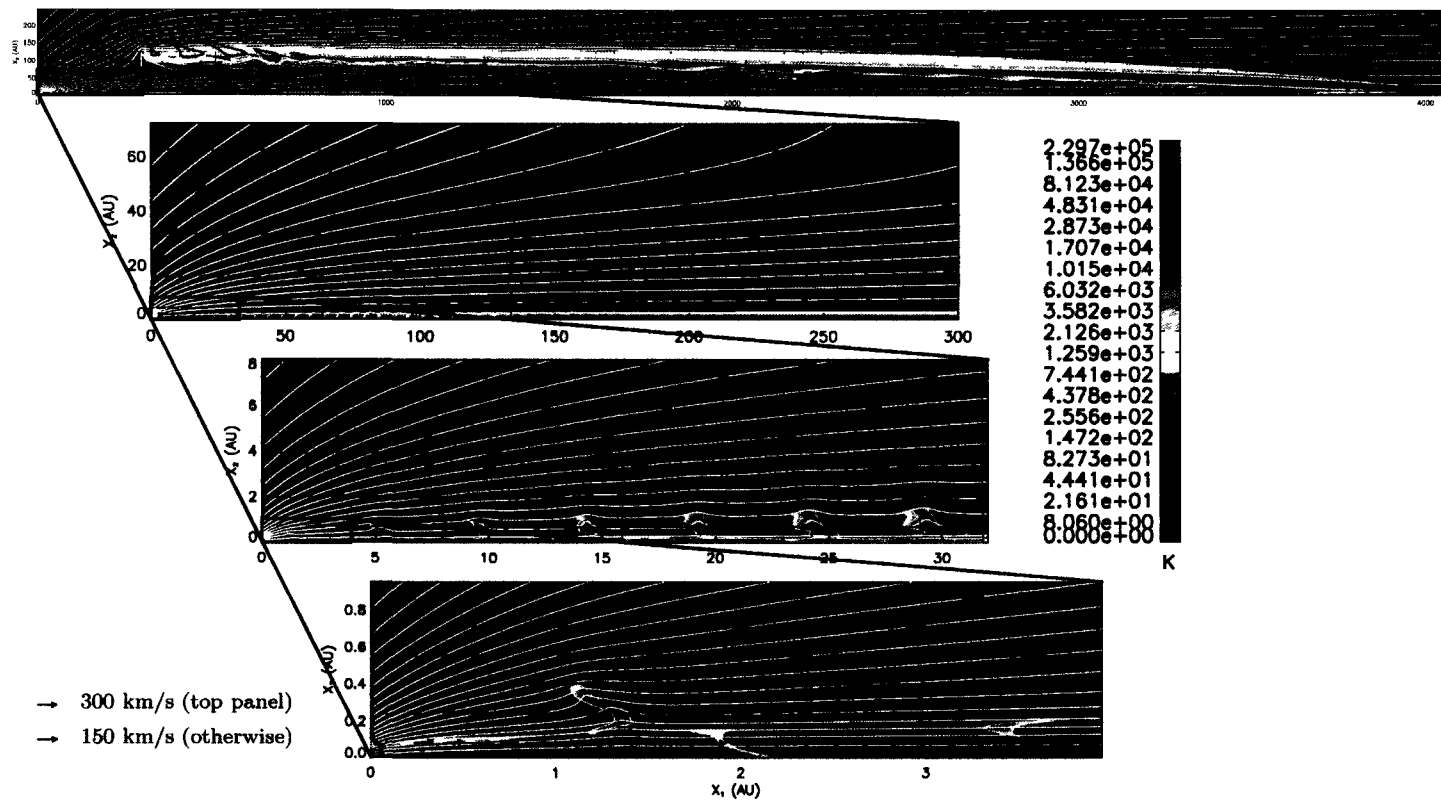


Figure 4.4 Nested images of simulation B at $t = 60.53$ yr. See Figure 4.1 for a description of the plotted quantities. The dimensions of the top panel are $z \in [0, 4096]$ AU and $r \in [0, 256]$ AU.

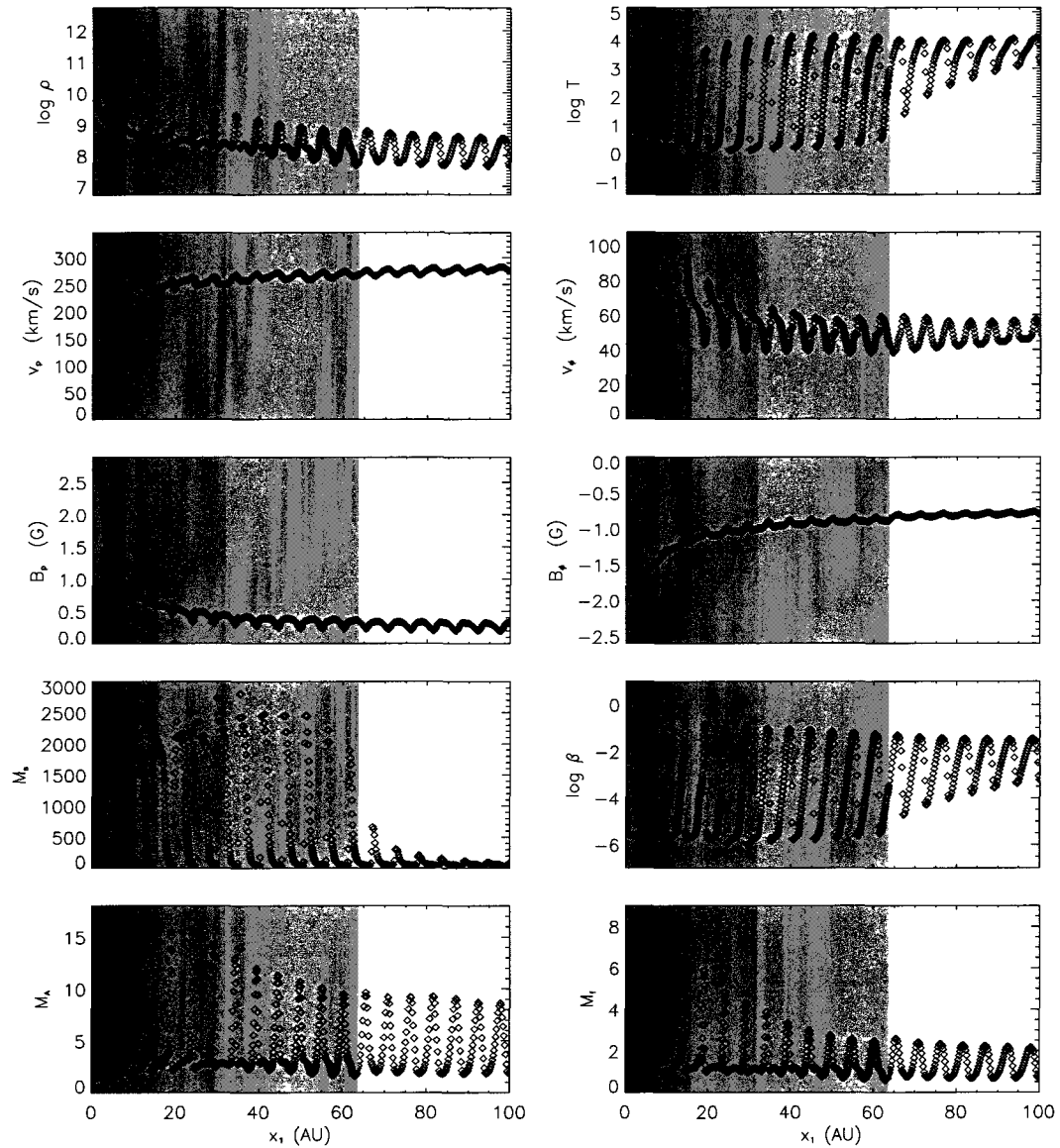


Figure 4.5 An axial slice through simulation B at $r = 1.0$ AU showing the structure of the knots. Plotted on the left, from top to bottom, are logarithmic density, poloidal velocity, poloidal field, slow magnetosonic Mach number, and Alfvénic Mach number. Plotted on the right, from top to bottom, are logarithmic temperature, toroidal velocity, toroidal field, logarithmic β , and fast magnetosonic Mach number. Successively darker shading indicates a higher level of refinement; no shading corresponds to level $l = 4$.

4.2.3 Simulation C: $\beta_i = 1.0$

Simulation C (Figure 4.6) proceeds similarly to simulation B. As was the case before, the jet propagation speed and radial expansion decrease, and it now takes the jet 74.92 yr to reach the edge of the domain. The trends from Figures 4.2 – 4.5 remain the same, and, as before, the maxima of the velocities and fields decreases relative to simulation B.

From Figure 4.6, the knot spacing has decreased to ~ 2.5 AU (see also Figure 4.15). The knots are also more elongated, taking on a characteristic “door handle” shape. Measured directly from the simulation, the knots have a period of ~ 0.056 yr.

4.2.4 Simulation D: $\beta_i = 2.5$

Simulation D continues the trend of a decrease in propagation speed, jet radii, and other quantities relative to simulation C. In keeping with this tendency, the temperature of the shocked ambient medium also decreases. In order for the bow shock to remain clearly visible in Figure 4.7 (and subsequent Figures), the contour levels have been adjusted.

The temperature of the shocked ambient medium is a function of the bow shock speed, and thus a higher propagation speed leads to a higher shocked ambient temperature. The jet propagation speed has been steadily decreasing with the value of B_i , and so too has the temperature of the shocked ambient (*e.g.*, the maximum temperature in simulation D is $\sim 10^5$ K, compared to $\sim 10^6$ K for simulation A).

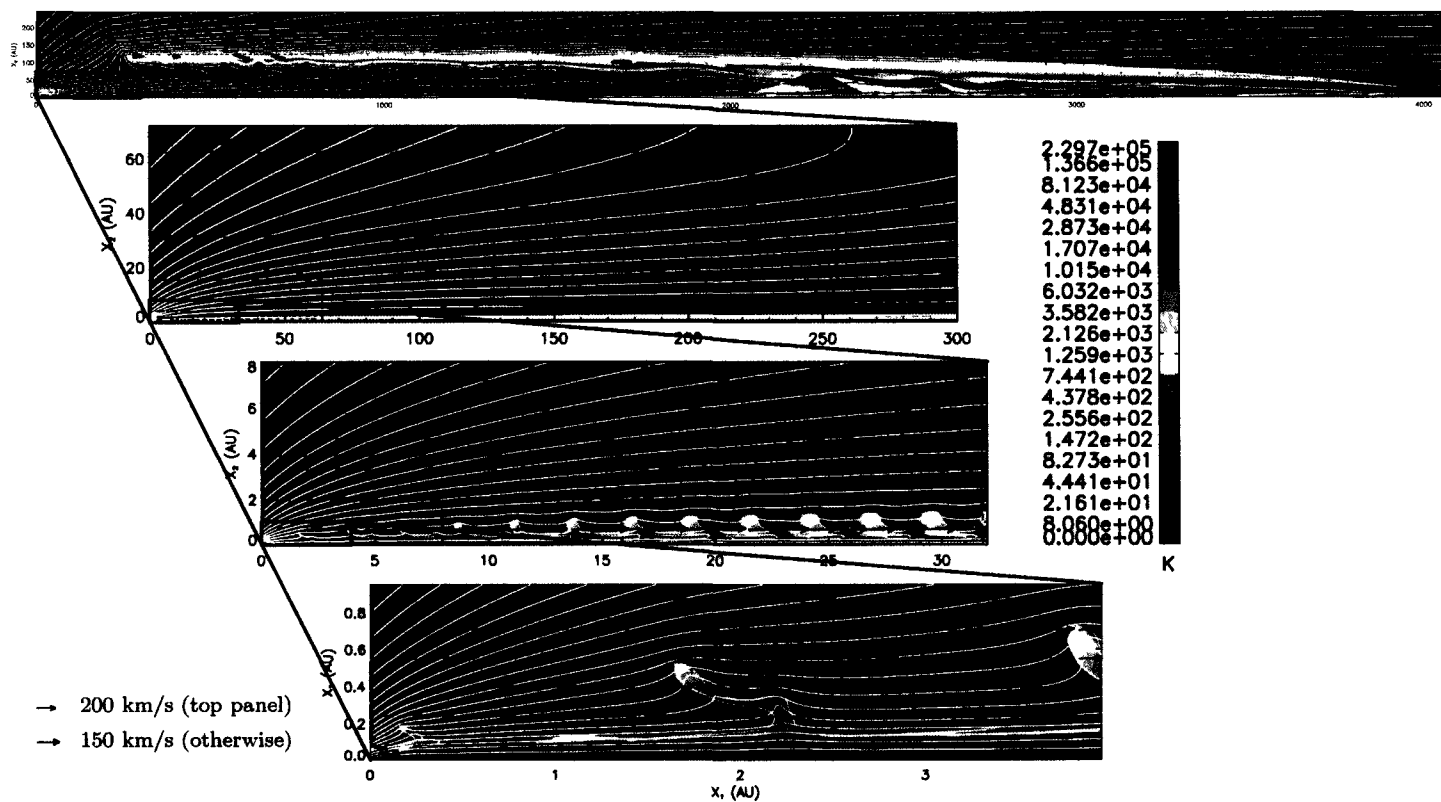


Figure 4.6 Nested images of simulation C at $t = 74.92$ yr. See Figure 4.1 for a description of the plotted quantities. The dimensions of the top panel are $z \in [0, 4096]$ AU and $r \in [0, 256]$ AU.

From Figure 4.7, the knot spacing has decreased to ~ 1.5 AU, and the knot period is measured to be ~ 0.046 yr. Relative to simulation C, the knots have become more elongated, and the “door handle” shape is even more prominent. Since the knots are now stretched in the z -direction (with lengths > 1 AU), and become more so as they propagate downstream, the rate at which they merge will increase.

This is shown in Figure 4.8, which plots a radial cut from simulation D at $z = 3.9$ AU, corresponding to the two knots just visible at the right edge of the bottom panel of Figure 4.7. There are two distinct knots at this location, and the z -velocity of the knot closer to the axis is ~ 1.4 times that of the knot at higher radius. Thus, the elongated shape of the knots results from a differential velocity between the top and bottom portions of the knot, stretching it out. In addition, there is a positive v_r between the knots, suggesting the knots will at least partially merge before passing each other by.

An additional feature which is present in all simulations with knots, but has only now become apparent enough to warrant discussion, is the “draping” of magnetic field lines over knots. For the knot in the bottom panel of Figure 4.7, located at $z = 3.8$ AU, the otherwise straight field lines are distorted by the knot, forming a loop. These loops travel along with the knot, and correspond to regions of high β .

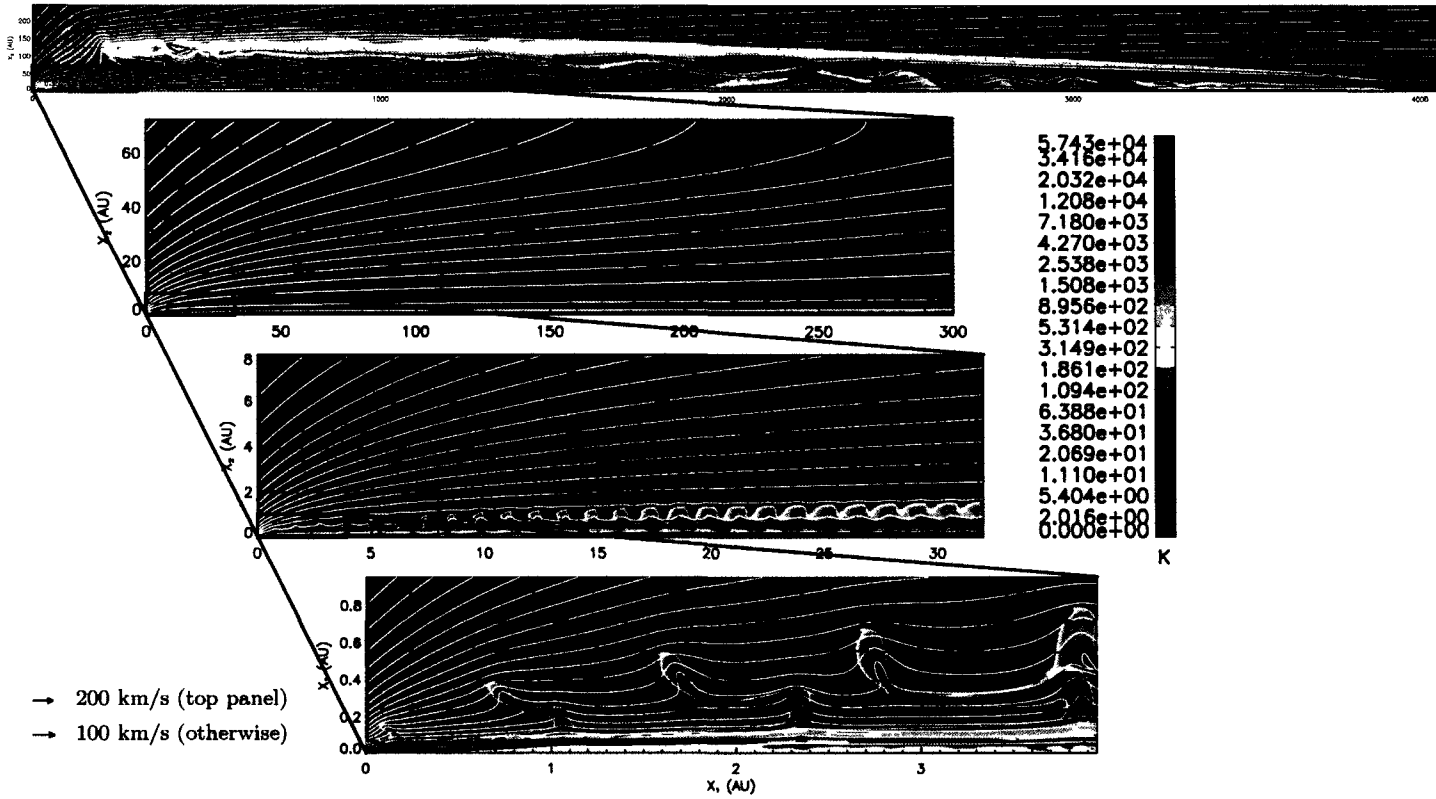


Figure 4.7 Nested images of simulation D at $t = 92.68$ yr. See Figure 4.1 for a description of the plotted quantities. Note that the contour levels for this Figure (and subsequent Figures) have changed from Figure 4.6. The dimensions of the top panel are $z \in [0, 4096]$ AU and $r \in [0, 256]$ AU.

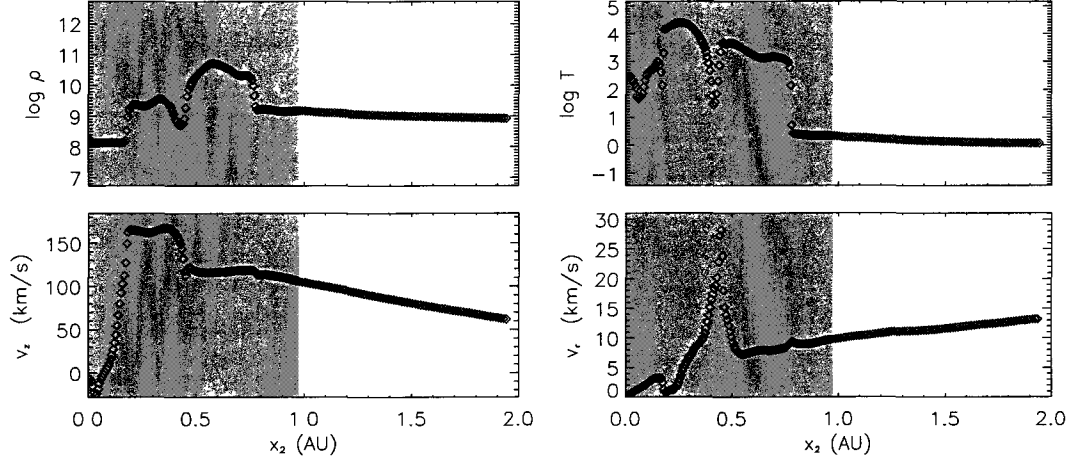


Figure 4.8 A radial cut at $z = 3.9$ AU and levels $l = 8, 9$ from simulation D. Plotted on the top are logarithmic density and temperature, and on the bottom, the z and r -components of velocity. The two knots can be seen distinctly in the density and temperature.

4.2.5 Simulation E: $\beta_i = 10$

Figure 4.9 shows simulation E at $t = 100$ yr. This is the first simulation presented which does not leave the domain within the 100 yr time limit. In fact, it only reaches a length of ~ 3000 AU from disc, continuing the trend of a slower propagation speed with decreasing B_i (increasing β_i). The other trends also still hold, with decreases in the velocities and fields relative to simulation D.

In this simulation, the knots are present in some form right from the beginning of the simulation, but ~ 5 yr elapses before they settle into a regular period. This is apparent from time-lapse animations, available at <http://www.ica.smu.ca/zeus3d/rc10/>. The time-lapse information also shows that there are periods (~ 4 yr in length) during the

evolution of the jet in which the knot generator changes its behaviour. One of these instances can be seen in the bottom panel of Figure 4.9, where the knots form downstream at ~ 2 AU, as opposed to near the origin. A more representative example of the average knot behaviour in simulation E is shown in Figure 4.10, from which I measure a knot spacing of ~ 0.4 AU and a period of ~ 0.031 yr.

4.2.6 Simulation F: $\beta_i = 40$

The jet in simulation F has previously been discussed in section 3.3 and nested images of the temperature are presented in Figure 3.1. For this simulation, I measure a knot period of ~ 0.020 yr, and a spacing of ~ 0.3 AU.

The evolution of simulation F proceeds much the same as in simulation E, with the expected decreases in jet propagation speed, radius, and velocity and magnetic field in the jet. By this stage, the maximum velocities at $z = 100$ AU have decreased by a factor ~ 6 with respect to simulation A, the poloidal field has decreased by a factor of ~ 9 , but the toroidal field has only decreased by a factor $\sim 5/2$. The situation at $z = 1000$ AU is similar, with decreases by factors of ~ 6 , ~ 10 , and ~ 3 relative to simulation A in the velocity, poloidal field, and toroidal field, respectively. For comparison, the initial magnetic field strength between simulations A and F differs by a factor of 20.

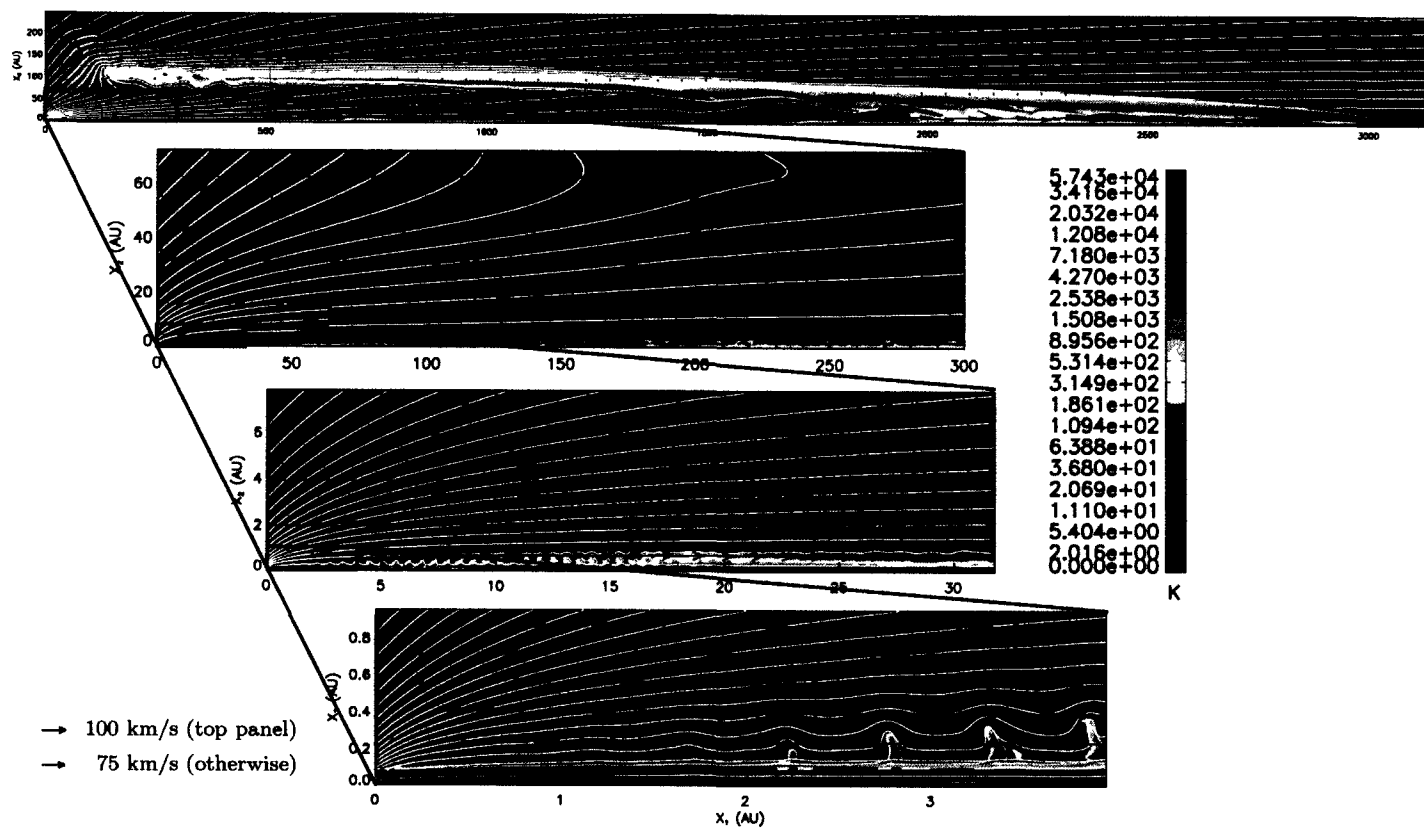


Figure 4.9 Nested images of simulation E at $t = 100$ yr. See Figure 4.1 for a description of the plotted quantities.

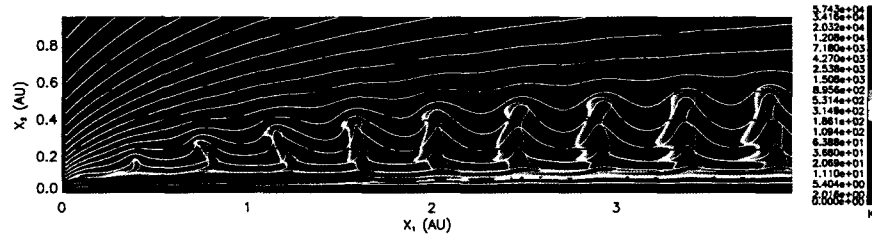


Figure 4.10 A representative example of knot production in simulation E at $t = 60.29$ yr. Temperature is plotted in colour, the slow magnetosonic surface with black contours, magnetic field lines in white, and arrows denote the poloidal velocity.

A feature which is present in all the simulations, but is just now becoming visible due to the decreasing jet radius, is a kink in the field lines at the outer jet radius (second panel of Figure 3.1). At the outer jet radius, $\beta > 1$, and hydrodynamical stresses can then bend the field lines easily (relative to $\beta < 1$). This reversal in the direction of the field line corresponds to the negative values of B_z and v_ϕ observed in simulation A (Figure 4.3).

4.2.7 Simulation G: $\beta_i = 160$

As B_i decreases even further, not only does the propagation speed and jet radius decrease, so too does the temperature of the jet bow shock. For simulation G, the maximum temperature is now only 4×10^4 K at the head of the jet.

As can be clearly seen in the bottom panel of Figure 4.11, individual knots are no longer produced, having been replaced by an unsteady, continuous stream of material. The base of the stream is located at approximately the same location as the knot generator observed in other simulations, but the conditions have changed such that the oscillatory release of material has become more or less continuous. This flow is pseudo-turbulent, has

a low magnetic field (notice the almost complete lack of field lines inside the stream), and consequently a high β . While the maximum radial extent of the knots in other simulations is restricted to ~ 2 AU, the material in simulation G is able to expand radially to $\lesssim 10$ AU as it propagates down the length of the jet.

At the time of this writing, simulation G is still running. By $t = 76.18$ yr, it has reached a height of $z \simeq 1200$ AU above the disc. Assuming the jet is traveling at a roughly constant speed, by $t = 100$ yr, it should reach a length of ~ 1600 AU.

4.2.8 Simulation H: $\beta_i = 640$

Simulation H has the weakest magnetic field of the simulations discussed here, and as such propagates the least distance with the lowest speeds. Like simulation G, it also does not exhibit knots, but rather a continuous stream of material emanating from near the origin. This stream is even more pseudo-turbulent than in simulation G, and this high temperature material results in a jet that looks qualitatively different than the others.

Figure 4.13 shows a radial slice from simulation H at $z = 100$ AU, demonstrating that even with a very weak field, the jet still manages to accelerate to super-fast speeds, and β generally remains below one. Relative to Figure 4.2, the profiles of the different quantities are no longer smooth, and the clear features at the outer jet radius are entirely washed out. The velocities in this simulation are decreased by a factor of ~ 10 relative to simulation A, as are the components of the magnetic fields.

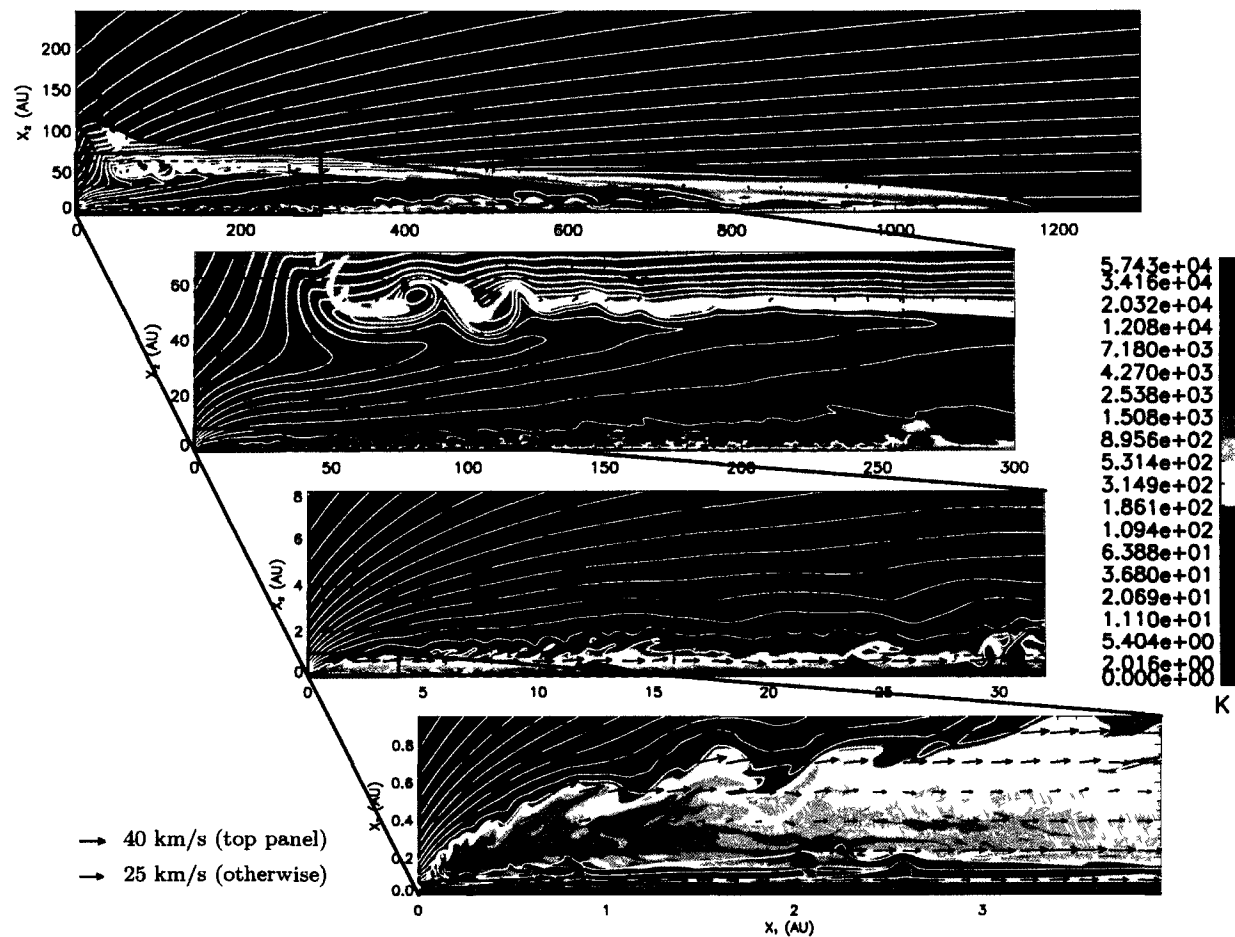


Figure 4.11 Nested images of simulation G at $t = 76.18$ yr. See Figure 4.1 for a description of the plotted quantities.

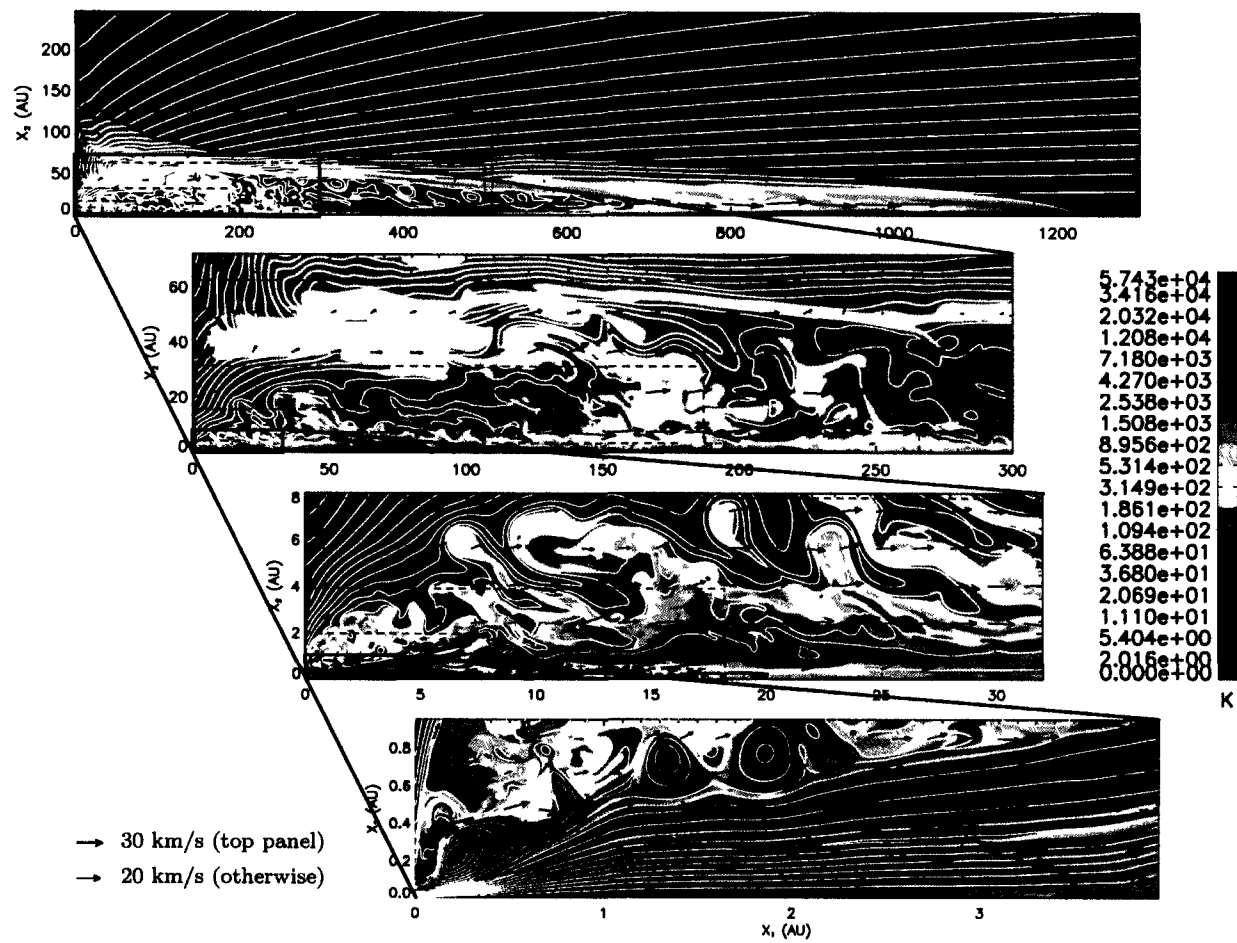


Figure 4.12 Nested images of simulation H at $t = 100$ yr. See Figure 4.1 for a description of the plotted quantities.

Simulation H exhibits a behaviour not observed in any of the other simulations: at seemingly random times, a violent eruption of high pressure (and consequently high β) material occurs near the origin. Figure 4.14 shows two snapshots in time, before and after such an eruption. Although the event disrupts the jet at small scales, the large-scale jet maintains its structure, and the jet launching mechanism is able to re-establish the flow near the disc within ~ 4 yr. These eruption events are correlated with the presence of small regions of positive B_φ near the origin, a feature which is wholly unique to simulation H. It is my suspicion that these events are numerical in origin, though the nature of these outbursts has yet to be established.

4.2.9 Qualitative trends

The behaviour of the knot-like structures as the magnetic field strength decreases from simulation A through H is summarised in Figure 4.15. For simulations which exhibit knots, the shape and size of the knots depend on B_i , with larger and more elongated knots generally corresponding to a stronger magnetic field. In addition, the knot spacing clearly increases with B_i , implying the knot frequency decreases monotonically with B_i .

Figure 4.15 also shows the locations of the plasma- $\beta = 1$ and poloidal Alfvénic Mach ($M_A = 1$) surfaces in the different simulations. With the exception of simulation H (the weakest magnetic field), the plasma- β surface is located close to the origin, and the jets are dominated by $\beta < 1$ material (*c.f.*, Figure 4.5).

The shape of the Alfvénic Mach surface also shows a dependence on B_i . For example, in simulation A, the majority of the jet near the disc is at sub-Alfvénic speeds, while the

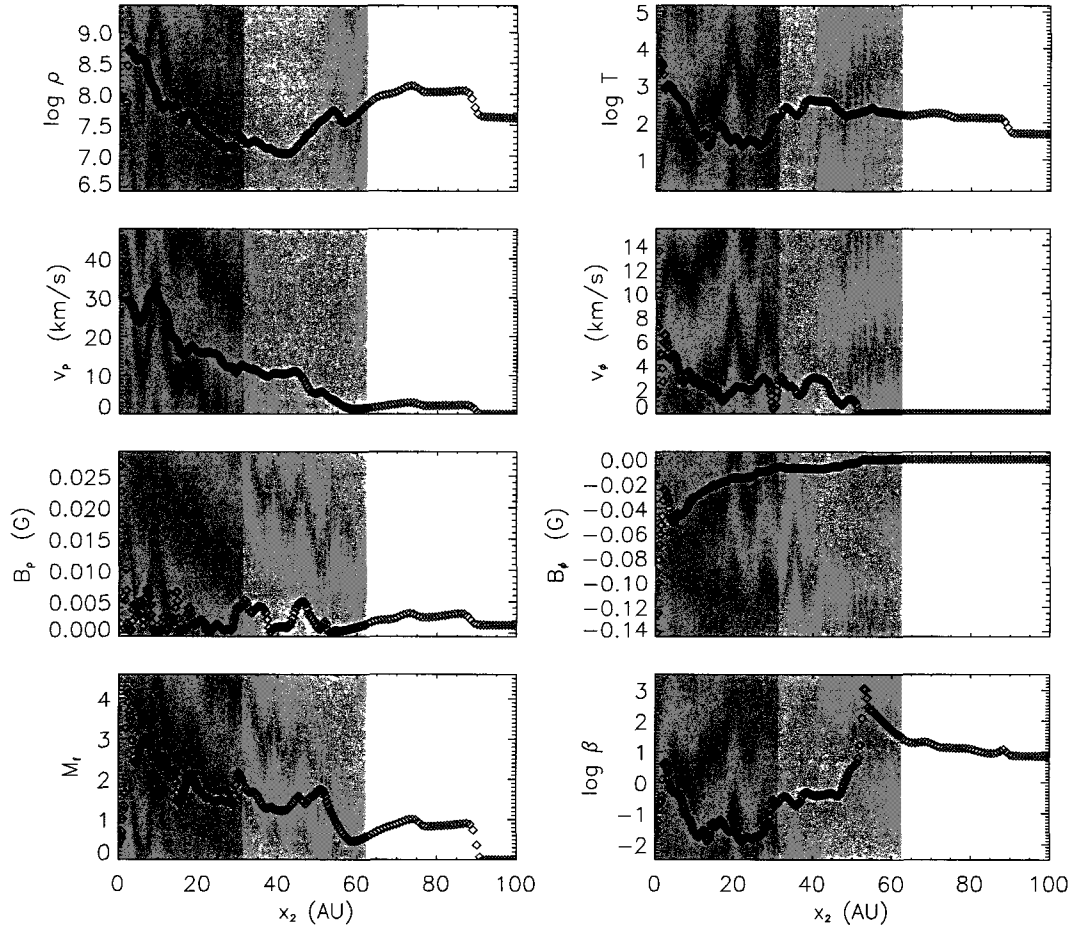


Figure 4.13 A radial slice from simulation H at $t = 100$ yr. Plotted on the left, from top to bottom, are the logarithmic density, poloidal velocity, poloidal magnetic field, and fast magnetosonic Mach number. Plotted on the right, from top to bottom, are the logarithmic temperature, toroidal velocity, toroidal field, and logarithmic β .

opposite is true for simulation G. Furthermore, the minimum height of the Alfvén surface above the disc surface increases with magnetic field strength, and is located very near the the disc surface for jets with weak fields.

At larger scales, Figure 4.16 shows the distribution of v_ϕ in simulations A – H plotted when all jets have propagated to 1000 AU above the disc. Evidently, the toroidal velocity

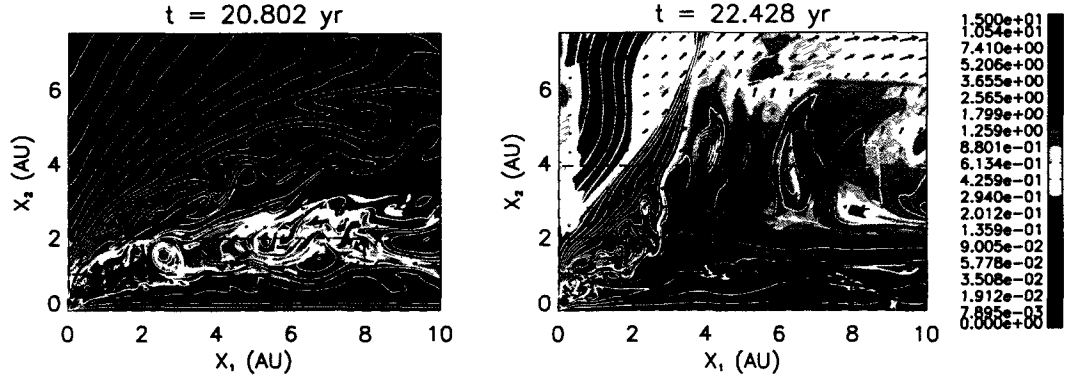


Figure 4.14 Two snapshots in time from simulation H. On the left, before an eruption event. On the right, immediately after. β is plotted in colour, magnetic field lines in white, and velocity vectors in black.

in the jet depends on the magnetic field strength, with a larger velocity corresponding to a stronger field, and a factor of ~ 20 difference between simulations A and H. Another striking feature of Figure 4.16 is the apparent self-similarity of the jets when they have the same length. Indeed, the jet radius and shape of the fast magnetosonic surface are similar, regardless of B_1 , and it is challenging to differentiate between the jets based on appearance alone.

Figure 4.17, which plots the poloidal velocity in simulations A – H at the same simulation time ($t = 42.65$ yr), very clearly shows the differences in the jet propagation speed and jet radius as the magnetic field decreases from simulations A to H (top to bottom). Indeed, both quantities increase monotonically (but not linearly) with B_1 .

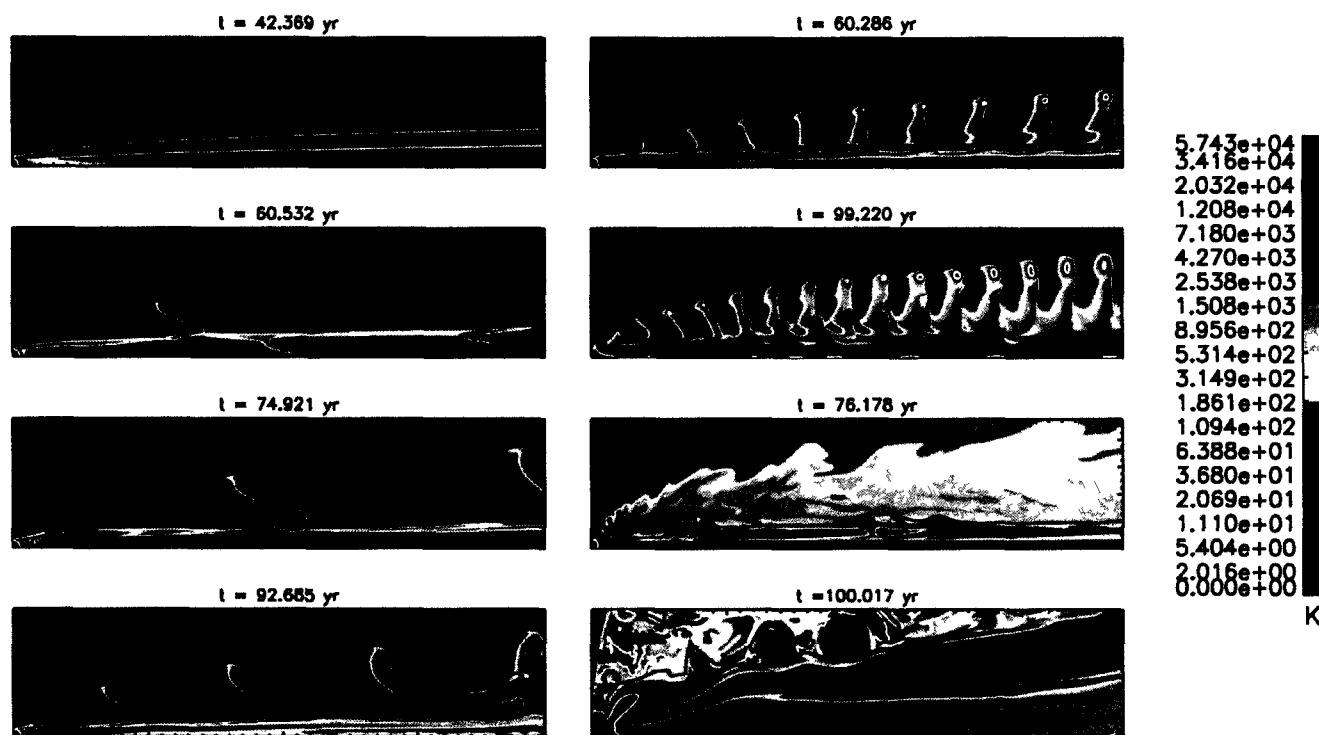


Figure 4.15 Images of the knot-like structures observed in simulations A – H on the highest resolution grid. Simulations A – D are arranged from top to bottom on the left, and simulations E – H are similarly arranged on the right. Colour contours denote the temperature, white the plasma- β surface, and black the Alfvénic Mach surface. The dimensions of each panel are $z \in [0, 4]$, $r \in [0, 1]$ AU. Unlike Figures 4.1 – 4.12, all panels use the same temperature scale.

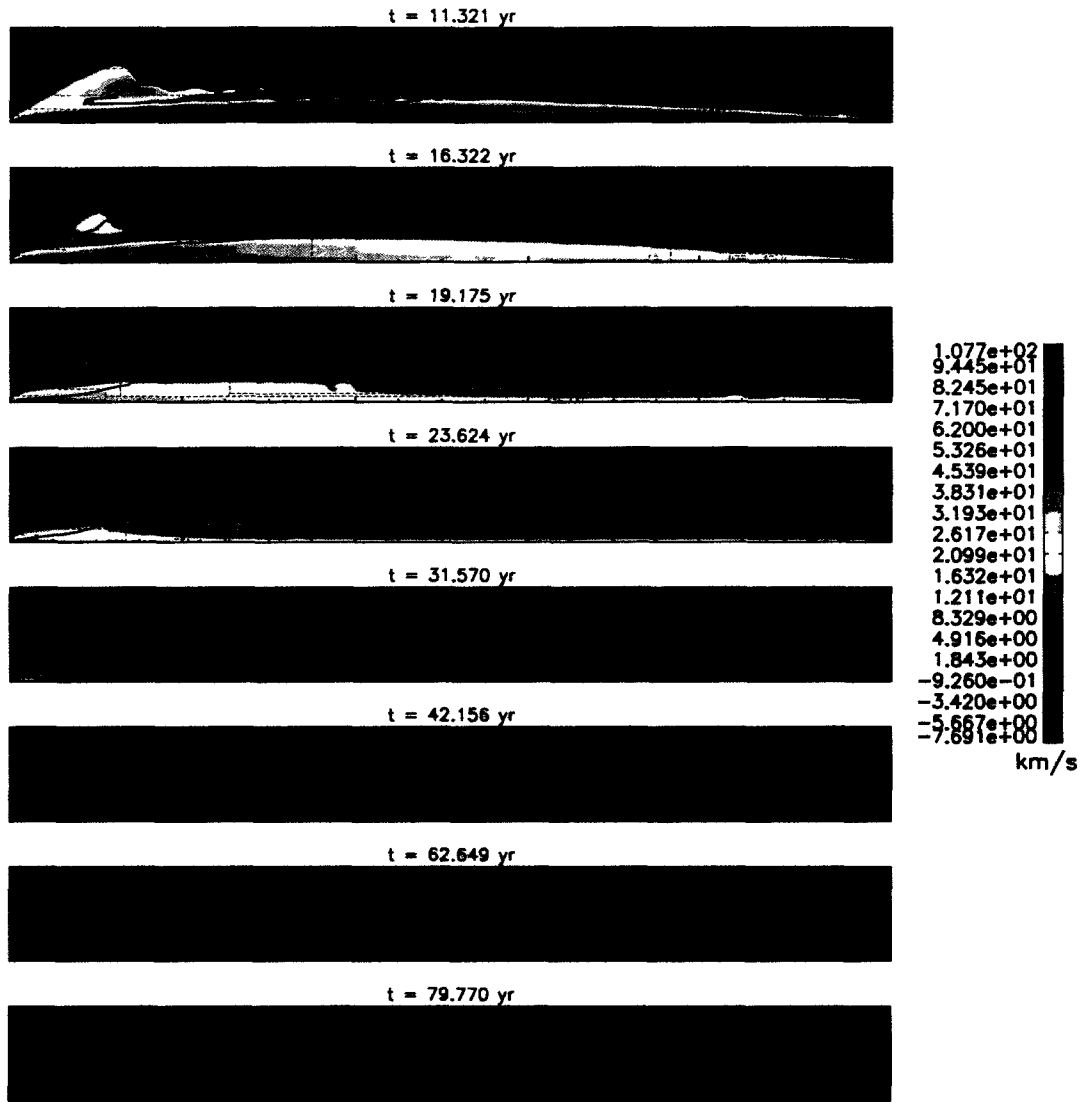


Figure 4.16 The toroidal velocity, v_ϕ , in simulations A – H (top to bottom), plotted when they reach a height of 1000 AU above the disc. Black contours denote the fast magnetosonic surface ($M_f = 1$). All plots have dimensions $z \in [0, 1025]$, $r \in [0, 110]$ AU.

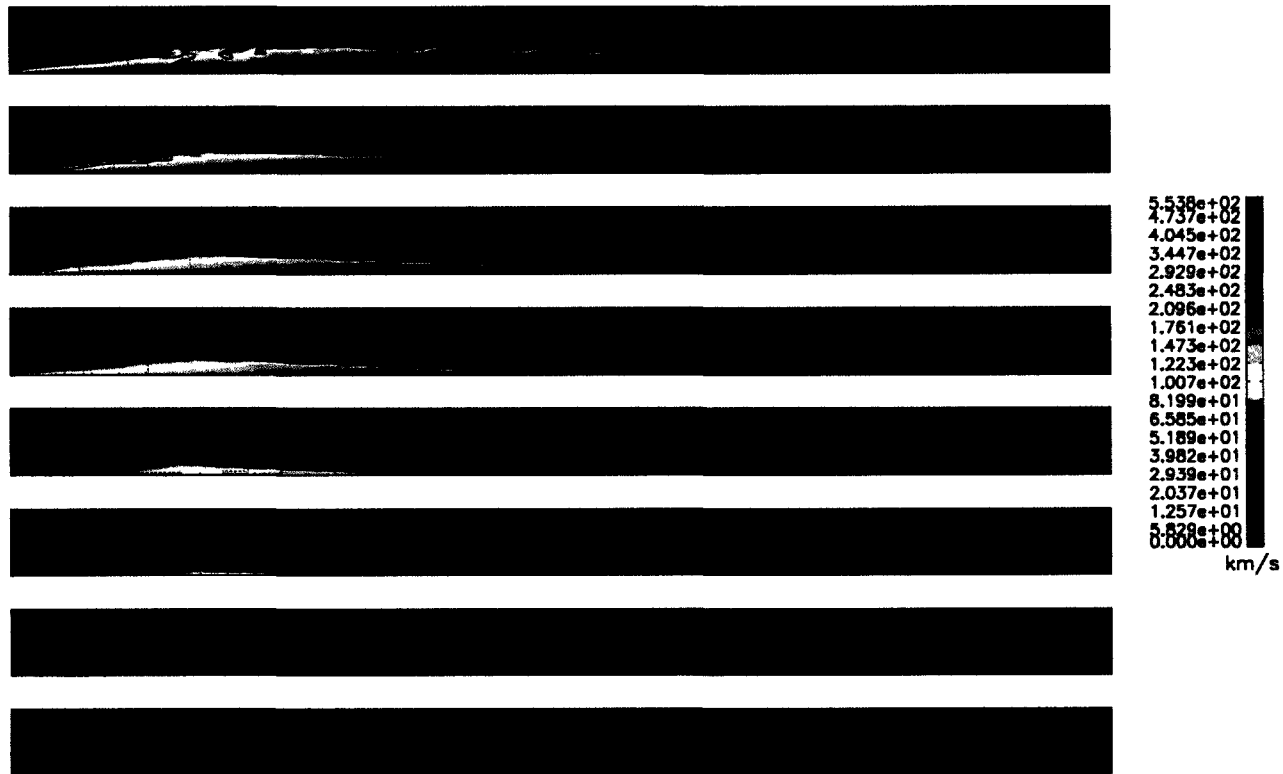


Figure 4.17 The poloidal velocity, v_p , in simulations A – H (top to bottom), plotted at simulation time $t = 42.65$ yr. Black contours denote the fast magnetosonic surface ($M_f = 1$). All plots have dimensions $z \in [0, 4070]$, $r \in [0, 245]$ AU.

4.3 The “knot” generator

The “knot”-like features observed in most of the simulations are the most striking feature of the jets on scales $\lesssim 100$ AU. As they appear to originate from the same location near the origin, it begs the question whether a single mechanism can explain their formation and varied characteristics.

Knots have previously been observed in simulations of magnetic jets and, in particular, for jets launched from a disc as a boundary condition, Ouyed & Pudritz (1997b, 1999) find episodic structures form as a result of re-collimation of the flow by a strong toroidal field and, through MHD shocks, steepen into knots (Figure 1.5). These authors speculate these knots may explain the much larger clumps of emission observed in some protostellar jets (*e.g.*, HH 111; Raga *et al.* 2002). Here, I suggest that the knots observed in the simulations presented here are instead generated by a pinch effect between outflowing and backflowing material, resulting in pressure oscillations, before being accelerated into the outflow by the magneto-centrifugal mechanism.

Using simulation F as a representative example, Figures 4.18 and 4.19 show the knot generator in the “on” and “off” positions, respectively. When the knot generator is “on”, a stream of backflowing material is present at $r \simeq 0.06$ AU, directed towards the disc surface (negative v_z ; bottom left panel of Figure 4.18). Simultaneously and at the same radius, the angle the field makes with the disc surface, θ , is less than 60° (top right panel) and material is accelerated from the disc surface. These two streams meet at $z \simeq 0.04$ AU, where material begins to accumulate. This results in a local increase in pressure, which not only increases the β (colour contours, top left panel), but also the

local slow magnetosonic speed (thus decreasing the slow Mach number at $z \simeq 0.06$ AU; black contours, top left panel).

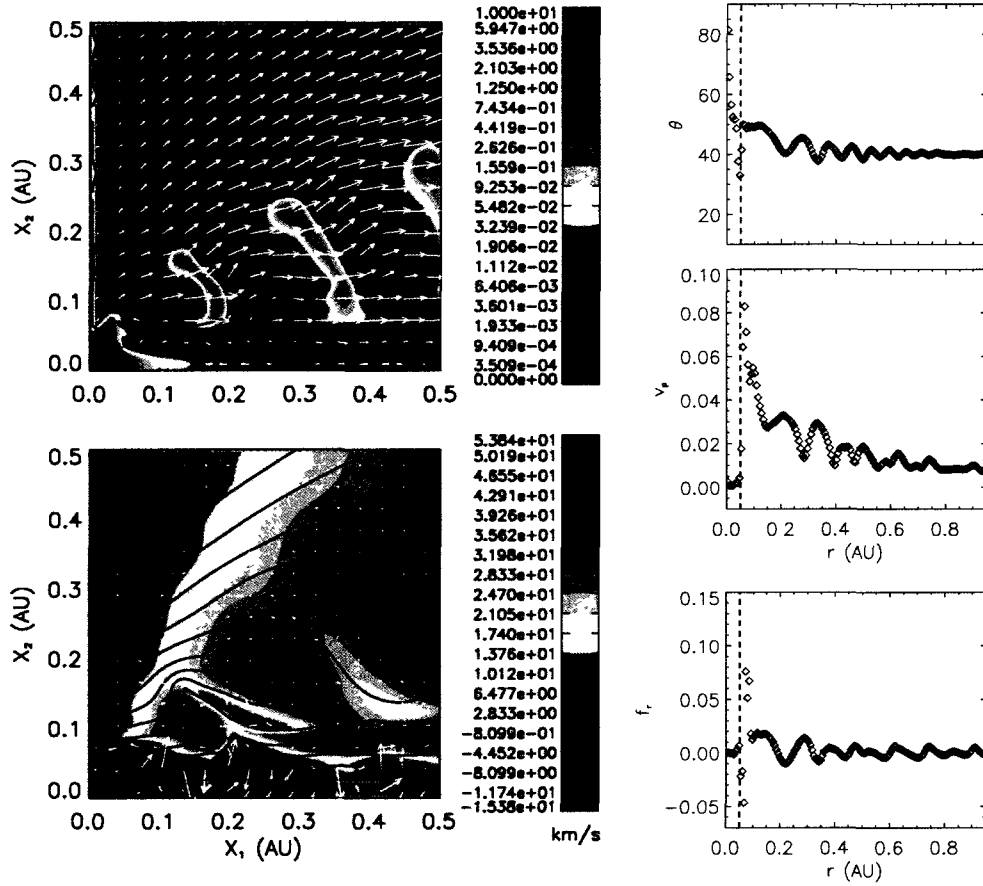


Figure 4.18 The knot generator in the “on” position. Top left panel: plasma- β is plotted in colour, the slow Mach surface in black, and velocity vectors in white. Bottom left panel: the z -component of the velocity is plotted in colour, magnetic field lines in black, and the net poloidal acceleration vectors in white. Top and middle right panels: the launching angle θ and the poloidal velocity, just above the disc surface at $z = 0.01$ AU, as a function of radius. Bottom right panel: The net radial acceleration at the location of the knot generator ($z \simeq 0.04$ AU). The dashed red line denotes the inner disc radius $r_i = 0.05$ AU.

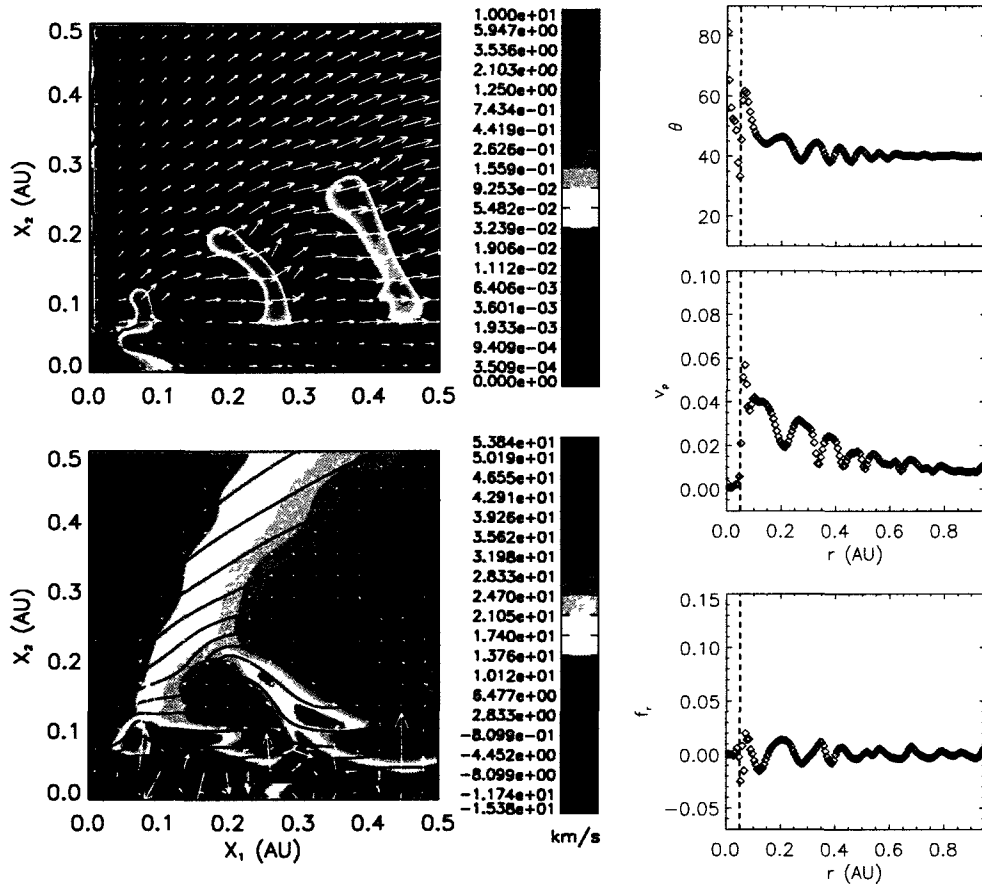


Figure 4.19 Knot generator in the “off” position. See Figure 4.18 for a description of the plotted variables.

Consequently, with a value of plasma- $\beta \sim 1$, the pressure forces are able to bend the field lines outward somewhat, further decreasing the value of θ . This increases the speed of inflow from the disc (v_p at $r \simeq 0.06$ AU; middle right panel), allowing more material to accumulate, increasing the pressure further. When the combined pressure and centrifugal forces overcome gravity and the pinch Lorentz force, material is pushed away

from the core and accelerated into the wind centrifugally, forming a knot (positive net radial acceleration at $z \simeq 0.03$ AU; bottom right panel of Figure 4.18).

The knots propagate downstream, traveling with the cold jet material, slowly diffusing and eventually merging with other knots (visible in the third panels of Figures 3.1, 4.4 – 4.9, 4.15). They are condensations of hot, high β material, and are confined by poloidal magnetic pressure (the field lines form loops around the knots; bottom left panel).

Behind the newly-formed knot, pressure and β drop, and the magnetic pressure near the disc surface pulls the field lines towards the vertical ($\theta > 60^\circ$; top right panel of Figure 4.19), causing the flow speed from the disc surface to decrease (compare the middle right panels of Figure 4.18 and 4.19). Concurrently, the knot absorbs the backflow feeding the generator as it moves away from the disc (negative v_z stops at the knot; lower left panel of Figure 4.19). Starved of material, the knot generator shuts off temporarily.

Once the knot has been carried away with the flow, a new region of backflow develops due to a loss of pressure balance behind the just-formed knot (white vectors and negative v_z , bottom left panel of Figure 4.18). Material begins to accumulate again, and as θ drops below 60° , the process starts anew.

The knot generator can be modeled as a simple harmonic oscillator in the pressure:

$$\frac{\partial^2 p}{\partial t^2} = -\omega^2 p, \quad (4.3)$$

where the angular frequency $\omega = 2\pi/\tau$, and τ is the knot generator period given by:

$$\tau \simeq \frac{\pi r_i}{a_s}, \quad (4.4)$$

where a_s is the slow magnetosonic speed, and r_i is the approximate radius of the knot generator. For simulation F, I measure a slow speed of $\sim 37 \text{ km s}^{-1}$ at the location of the knot generator. Substituting into equation (4.4), this predicts a knot generation period of $\tau_{\text{knot,calc}} \sim 0.020 \text{ yr}$, in good agreement with the period I actually observe ($\tau_{\text{knot,obs}} \simeq 0.020 \text{ yr}$).

Why should the slow speed set the period of the knot generator? In axisymmetric coordinates, if the poloidal velocity flows parallel to the poloidal magnetic, as is approximately true in the region surrounding the knot generator, then the slow and fast magnetosonic speeds reduce to the minimum and maximum of the sound ($c_s^2 = \gamma p / \rho$) and total Alfvén speeds [$a_{\text{a,tot}}^2 = (B_p^2 + B_\phi^2) / 4\pi\rho$], respectively. Empirically, I measure that the minimum of the sound and total Alfvén speeds is always c_s at the location of the knot generator. Thus, since it is the pressure that is undergoing pseudo-harmonic oscillation, the slow speed should be the characteristic speed for the knot generator.

Table 4.3 summarises the application of equations (4.3) and (4.4) to the other values of B_i , demonstrating that the suggested harmonic oscillator mechanism holds for all simulations which form knots, to within the estimated measurement uncertainties. I also find a clear correlation between $\tau_{\text{knot,obs}}$ and B_i , and fitting a power law to the data, I find that $\tau_{\text{knot,obs}} \propto B_i^{0.62 \pm 0.04}$.

The generation of knots is clearly related to the perturbation of the slow surface (compare the location of the slow surface in the top left panels of Figures 4.18 and 4.19), and thus will be some function of the pressure. As the magnetic field strength, B_i , increases, β and a_s decrease at the knot generator. At some point the field will become

| Simulation B_i (G) | H | G | F | E | D | C | B | A |
|--------------------------------|-----|---|-------|-------|-------|-------|-------|-----|
| | 2.5 | 5 | 10 | 20 | 40 | 63.2 | 100 | 200 |
| $\tau_{\text{knot,obs}}$ (yr) | — | — | 0.020 | 0.031 | 0.046 | 0.056 | 0.090 | — |
| a_s (km s ⁻¹) | — | — | 37 | 23 | 15 | 12 | 9.2 | — |
| $\tau_{\text{knot,calc}}$ (yr) | — | — | 0.020 | 0.031 | 0.049 | 0.064 | 0.080 | — |

Table 4.3 The measured and calculated periods, and the measured slow magnetosonic speed, of the knot generator, as a function of B_i . Individual knots are not produced for in simulations A, G, and H. The estimated average relative uncertainty in $\tau_{\text{knot,obs}}$ and a_s is $\sim 20\%$.

rigid enough that perturbations to the pressure will be too small to result in oscillatory behaviour. This appears to be the case for the strongest magnetic field case (simulation A), where I indeed observe no significant perturbations to the slow surface at the location of the knot generator visible in the other simulations, and no knots are generated.

In contrast, for simulation G, the values of β and a_s near the disc surface are high, and the slow surface is actually a filament which extends to $z \sim r \sim 2r_i$, from whence a nearly constant stream of material emanates. In the case of simulation H, the slow surface is even more extended, reaching $z \sim r \sim 5r_i$. Thus, in the weakest field simulations, the pressure forces are strong enough to prevent the other forces from cutting off the flow of material to the knot generator, leading to a continuous ejection of material.

At most, the knots described here are observed to extend outwards from the axis by only ~ 2 AU (*e.g.*, the third panel of Figure 4.7), and expand to widths of ~ 2 AU in the z -direction. At large heights from the disc, the knots merge with one another, resulting in a contiguous column of material rather than separate clumps. Since individual knots are resolved by ~ 20 zones in the z -direction when they begin to merge, their merger will not be strongly related to the decreasing resolution of the nested grids.

Comparing these knots to the clumpy structures observed in some protostellar jets, I find that the knots produced in these simulations are much too small (almost 2 orders of magnitude smaller in the case of HH 34; Hartigan *et al.* 2011) and, as such, are not the likely progenitors of observed knot-like structures. Unlike Ouyed & Pudritz (1997b), whose simulations extend only to 4 AU, the simulations presented here extend to observational length scales, and thus I can state with some certainty that these knots are not good candidates for explaining the observed structures on larger scales.

4.4 Numerical Challenges

As a jet propagates, a “backbone” of high poloidal field and low velocity develops along the symmetry axis. The edge of this region is well-defined by strong gradients in B_φ , and using reflecting boundary conditions at the symmetry axis, B_φ will change sign at $r = 0$. For insufficient numerical resolution near the symmetry axis, I observe that B_φ does not tend to zero as it crosses the axis, leading to a numerically induced current sheet which is unstable to perturbation. Figure 4.20 shows an early version of the simulations presented here which employed only static grids, demonstrating the effects of a perturbation at the axis. A local minimum in density, and therefore inertia, coupled with a strong inward magnetic pinch, results in material “bouncing” off the symmetry axis, manifesting as a numerical explosion.

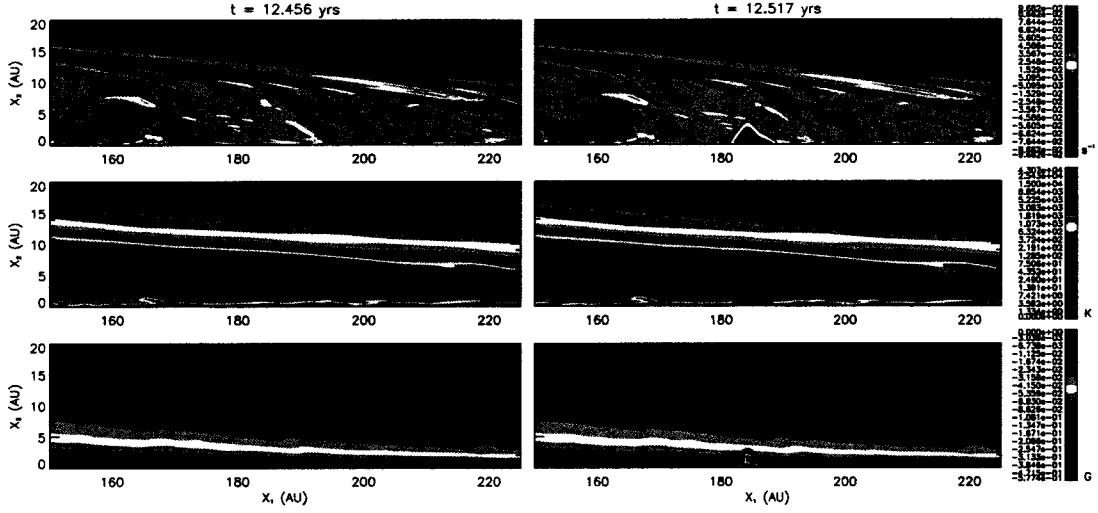


Figure 4.20 Two successive snapshots in time illustrating the numerical instability due to insufficient resolution of gradients in B_φ . From top to bottom, plotted are contours of velocity divergence, temperature, and toroidal magnetic field. The instability leads to the localised explosion observed at $z \simeq 184$ AU.

To avoid this issue, resolution is dynamically added whenever there is a change in sign in $\partial B_\varphi / \partial r$ near the axis, and the ratio of

$$\frac{\partial B_\varphi}{\partial r} \frac{\Delta t_A}{\sqrt{4\pi\langle\rho\rangle}} > \text{tolalf} = 0.15, \quad (4.5)$$

where Δt_A is the Alfvén time step ($\Delta t_A \propto a_A^{-1}$, where $a_A = B/\sqrt{4\pi\rho}$ is the Alfvén speed), tolalf is the threshold parameter set at run-time, $\langle\rho\rangle$ is the radial average of the local density, and $(1/\sqrt{4\pi\langle\rho\rangle}) \partial B_\varphi / \partial r$ is essentially the radial gradient of the toroidal Alfvén speed. If there is a change of sign in $\partial B_\varphi / \partial r$ in the first $N_{\partial B_\varphi}$ zones of the symmetry axis, where $N_{\partial B_\varphi}$ is a user-specified parameter, and equation (4.5) is greater than the threshold value, then nbuffer zones are flagged for refinement. nbuffer is typically set

to a dozen or more zones to avoid very small grids which are inefficient from a parallelism perspective.

Flagging zones for refinement based on $\partial B_\varphi/\partial r$ alone is not sufficient as a change in the sign anywhere near the symmetry axis results in refinement, even if the profile of B_φ is otherwise well-behaved. Furthermore, to prevent grids from being continually created and destroyed in regions where equation (4.5) fluctuates around the threshold value (“mesh trashing”; Khokhlov 1998), if refinement has already occurred at a location along the symmetry axis, then $2N_{\partial B_\varphi}$ zones are checked for changes in the sign of $\partial B_\varphi/\partial r$.

At the time of this writing, simulation G is, in fact, still running, having only reached a problem time of $t \simeq 76$ yr. This is in part due to time lost to results which exhibited the numerical instability just described, even though dynamic gridding was active. Reasonable results were recovered by decreasing the threshold of the refinement criterion (equation 4.5) to 0.10. As a result, simulation G has $\sim 25\%$ more zones on average than the other calculations, contributing to a longer time to completion.

Simulation H exhibits a recurring instability close to the disc surface which also involves strong gradients in B_φ . As it displays some of the same characteristics as the numerical instability just described, I speculate that it may also be numerical in origin. One way to test this hypothesis would be to perform a simulation with increased resolution at the disc surface (*e.g.*, whereas simulations A – H have a resolution of 8 zones per r_i at the disc surface, a resolution of 16 zones per r_i could be tried), and a simulation which does just that is currently underway. None of the other simulations show any evidence for this

kind of instability at the disc surface, and 8 zones per r_i is sufficient numerical resolution: employing 16 zones per r_i gives the same qualitative and integrated quantitative results.

Once knots begin to form, another numerical issue arises. Regions of extremely low density develop in between knots (*e.g.*, simulation F; Figure 4.21) which, coupled with a relatively strong magnetic field, leads to a restrictively small Alfvén time step Δt_A . To prevent these “sinkholes” from forming, a density floor is imposed which is 300 times the density obtained from equation (3.4) applied at the outer corner of the computational domain $[(z_{\max}, r_{\max}) = (4096, 256) \text{ AU}]$. This rather large floor value is only applied within a spherical radius of 20 AU from the origin where these sinkholes are observed to form. Since the Alfvén time step $\propto \sqrt{\rho}$, the chosen floor value increases the overall time step by a factor of ~ 20 . Comparisons to test simulations without this density floor show no qualitative or quantitative differences. In fact, over the simulation lifetimes, we find the total mass added in this manner for any simulation remains below 1%.

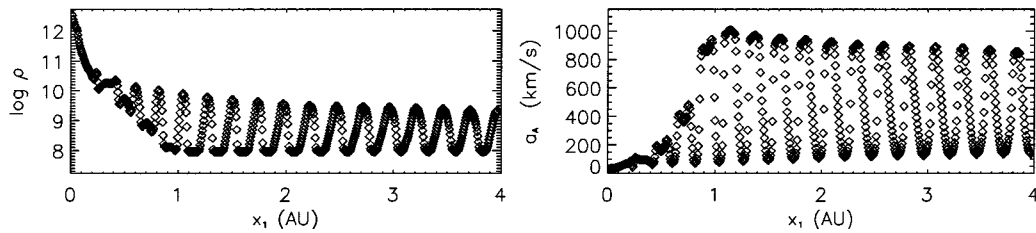


Figure 4.21 An axial slice from simulation F at $z = 0.1 \text{ AU}$ and level $l = 9$. Plotted are logarithmic density (left) and Alfvén speed (right). The highest Alfvén speeds correspond to regions between knots.

Note that this floor value should not to be confused with the constant density of $10^{-6}\rho_i$ added to the initial hydrostatic profile (Section 3.2.1). This initial constant is designed to have the density profile asymptote to an observationally realistic value, not to limit the time step.

4.5 The driving mechanism

The magneto-centrifugal theory of wind launching is commonly used to explain the launching of magnetic jets from discs (*e.g.*, Blandford & Payne 1982; Pelletier & Pudritz 1992; Spruit 1996). A requirement of this model is that $\beta < 1$, so that the field lines can be considered rigid and fluid will move along them like “beads on a wire” (Henriksen & Rayburn 1971). A prediction of this model is that acceleration of the wind should stop at the Alfvén point, where the poloidal Alfvén Mach number $M_A = v_p/a_{A,p} = 1$, and $a_{A,p} = B_p/\sqrt{4\pi\rho}$ is the poloidal Alfvén speed (henceforth simply the Alfvén speed).

For the simulations presented here which span a factor of 80 in initial magnetic field strength, can the magneto-centrifugal model explain the results, or is there a need to appeal to a different model? In the jets with weak fields, the toroidal velocity and poloidal field strength are small and the applicability of the magneto-centrifugal model should be questioned. However, jets are still present for weak poloidal fields, and if the magneto-centrifugal mechanism is not valid, how are the jets launched?

4.5.1 Steady-state constants

It is well-established that, for the equations of steady-state ($\partial/\partial t \simeq 0$), axisymmetric, ideal MHD, there exist four quantities which are constant along any given magnetic field line (Weber & Davis 1967; Mestel 1968; Spruit 1996). These constants are useful for understanding the physics of magnetic outflows, even when the assumption of steady-state is only approximately true.

The mass load $\eta(\psi)$ is an expression for the mass flux density per unit of poloidal magnetic flux, is constant along a field line ψ , and given by:

$$\eta(\psi) = \frac{\rho v_p}{B_p}, \quad (4.6)$$

which is a consequence of $\vec{v}_p \parallel \vec{B}_p$ in steady-state, ideal MHD. v_p and B_p are the poloidal velocity and magnetic field, which, in cylindrical coordinates, are components of the total magnetic field and velocity vectors:

$$\vec{B} = \vec{B}_p + B_\varphi \hat{\varphi} \quad \text{and} \quad \vec{v} = \vec{v}_p + v_\varphi \hat{\varphi}.$$

The value of the mass load for any given field line is determined at the Alfvén point; its value is $\eta(\psi) = \sqrt{\rho_A}$, where ρ_A is the density evaluated at the Alfvén point.

The apparent rotation rate $\Omega(\psi)$ is also constant along a field line, and given by:

$$\Omega(\psi) = \frac{1}{r} \left(v_\varphi - v_p \frac{B_\varphi}{B_p} \right). \quad (4.7)$$

For an accretion disc surrounding a central mass, the poloidal field lines are assumed to be anchored in the disc and, at the surface of the disc, they rotate with the disc angular velocity. Assuming the disc is Keplerian, the velocity is then $v_{K,0} = \sqrt{GM_*/r_0}$, where r_0 is the “footprint” of the field line. Indeed, the value of $\Omega(\psi)$ is determined at the field line footprint, and has the value $\Omega(\psi) = v_{K,0}/r_0$.

The third constant embodies the conservation of angular momentum, and can be written as:

$$L(\psi) = rv_\varphi - \frac{rB_\varphi}{4\pi\eta(\psi)}. \quad (4.8)$$

This equation demonstrates that the total amount of angular momentum flux per unit poloidal magnetic flux along a field line is constant. The first term on the right-hand side is the angular momentum carried by the fluid, while the second term describes the magnetic torque. The field line rotation rate and angular momentum constants are related by the value of $L(\psi)$ at the Alfvén point: $L(\psi) = \Omega(\psi)r_A^2$, where r_A is the so-called Alfvén radius and is located at the point where $M_A = 1$.

The final field line constant represents the conservation of specific energy, and is given by:

$$E(\psi) = \frac{v^2}{2} - rv_\varphi\Omega + \frac{\gamma}{\gamma - 1} \frac{p}{\rho} + \Phi, \quad (4.9)$$

where Φ is the gravitational potential, and $v^2 = v_p^2 + v_\varphi^2$. Assuming the fluid is cold and the thermal energy negligible compared to the other terms, then $E(\psi) = -3v_{K,0}^2/2$ at the disc surface.

4.5.2 Centrifugal versus magnetic mechanisms

Once the initial atmosphere has been displaced, the simulations presented here quickly approach a quasi-steady-state near the disc, notwithstanding the knot generator (Section 4.3). For poloidal field lines which vary smoothly in space and slowly in time, steady-state magnetic wind theory can then be applied to shed light on the mechanism driving the jets.

Starting at the footprint of a field line (r_0) on the disc surface, one can “follow” the field line outward from the disc along the field line coordinate \vec{s} , where $\hat{s} = \vec{B}_p/B_p$ (Staff *et al.* 2004). So long as the field line varies smoothly in space, I find that a bilinear interpolation can be used to produce reasonable results (*i.e.*, integrating both forwards and backwards along a field line gives differences of $< 0.1\%$ in \vec{s}). In so doing, quantities in the flow can be interpolated to the field line coordinate, \vec{s} , and their behaviour along field lines examined.

The left panel of Figure 4.22 shows the different velocities along a field line anchored at $r_0 \simeq 1.0$ AU for simulation A. Although the velocities are functions of the footprint, their relative importances are not, and the same trends persist as long as the steady-state approximation applies.

The right panel of Figure 4.22 plots the fractional variation of the steady-state constants (equation 4.6 – 4.9), which are a measure of the applicability of the steady-state approximation. For simulation A, with the exception of $E(\psi)$, the constants are well-behaved and remain close to their analytical values. To establish whether or not this field line can be considered steady-state, I look to a field line for which the approximation

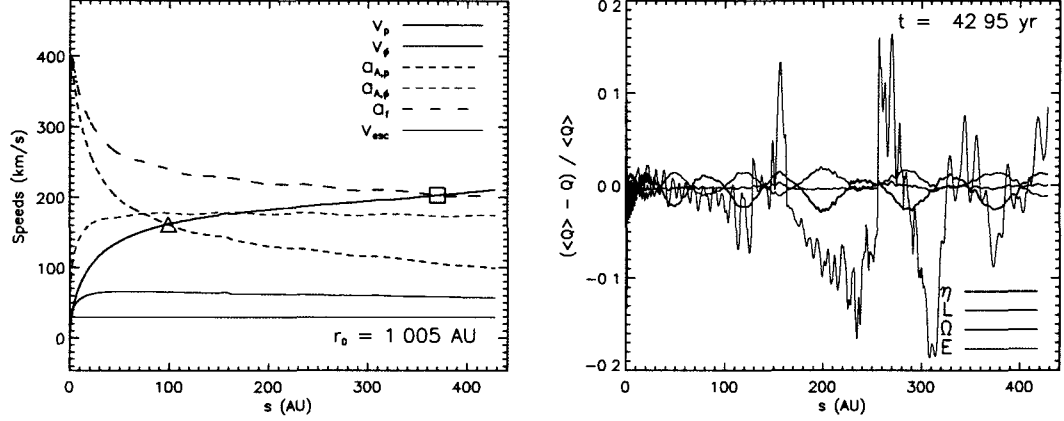


Figure 4.22 The different speeds and fractional variations of the steady-state constants along a field line anchored at $r_0 \simeq 1.0$ AU in simulation A. In the left panel, v_p is the poloidal velocity, v_ϕ is the toroidal velocity, $a_{A,p}$ is the (poloidal) Alfvén speed, $a_{A,\phi}$ is the toroidal Alfvén speed, a_f is the fast magnetosonic speed, and $v_{esc} = \sqrt{2GM/r_0}$ is the local escape speed for footprint r_0 . The triangle (square) denotes the location of the Alfvén (fast) point. Plotted in the right panel are the fractional variations of the steady-state constants from their analytical values: η is the mass load, Ω is the field line rotation rate, L is the angular momentum constant, and E is the energy constant (equations 4.6 – 4.9). These data are taken at $t = 42.95$ yr, but do not strongly vary in time.

clearly does not apply. Figure 4.23 shows a field line from simulation A, anchored at $r \simeq 0.2$ AU, which has a maximum fractional variation of $> \pm 200\%$. Further, a number of the steady-state “constants” are offset from their analytical values by as much as 120%. With this in mind, the $\pm \sim 20\%$ variation in $E(\psi)$ in Figure 4.22 (and much less for the other variables) is acceptable, and the field line is considered to be in steady-state.

In Figure 4.22, the poloidal velocity increases from effectively zero at the disc surface ($s = 0$) to more than 100 km s^{-1} within 20 AU. The majority of the acceleration of the fluid happens before the fast point ($s \simeq 370$ AU), with $\sim 80\%$ occurring between the disc surface and the Alfvén point ($s \simeq 99$ AU). From magneto-centrifugal wind theory, if the

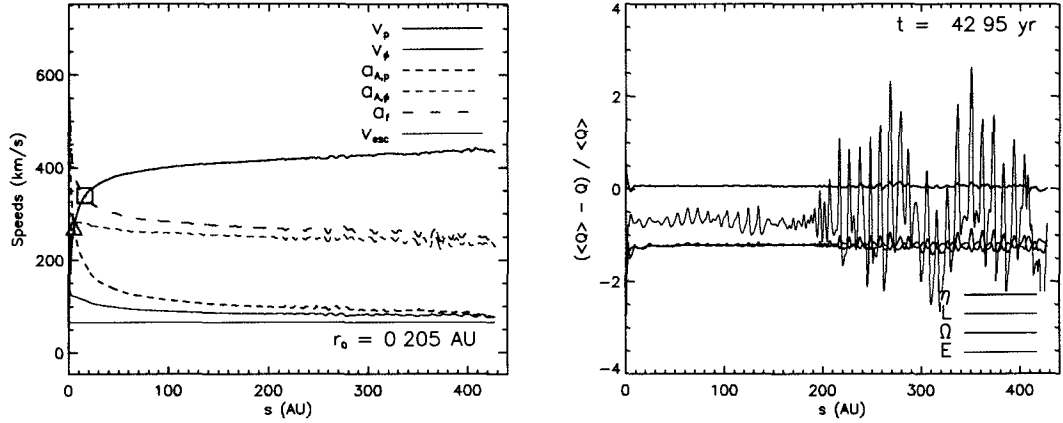


Figure 4.23 A representative example of a field line from simulation A which is *not* in steady-state ($r_0 \simeq 0.20$ AU). Note the difference in scale of the right panel relative to Figure 4.22. For a description of plotted quantities, see the caption of Figure 4.22.

magnetic field is strong ($\beta < 1$), and the kinetic energy of the fluid is low ($M_A < 1$), then the fluid will be forced to co-rotate with the field lines. Inside the Alfvén point, material will then be centrifugally flung out along field lines. Beyond the Alfvén point however, where $M_A > 1$, the kinetic energy of the fluid is greater than the poloidal magnetic energy, and co-rotation can no longer be assumed. The field becomes twisted, the toroidal field becomes dominant, and the remaining $\sim 20\%$ of the acceleration is due to gradients in the toroidal magnetic pressure (equation 1.4).

Figures 4.24 – 4.30 plot the different velocities and fractional variations of the steady-state constants for simulations B through H (and thus decreasing B_1), at footprint $r_0 \simeq 1.0$ AU. In simulation A, the poloidal field (Alfvén speed) is dominant over the toroidal field (toroidal Alfvén speed) up to the Alfvén point and, as already stated, the majority of the acceleration has occurred by the time the fluid becomes super-Alfvénic. The same is true

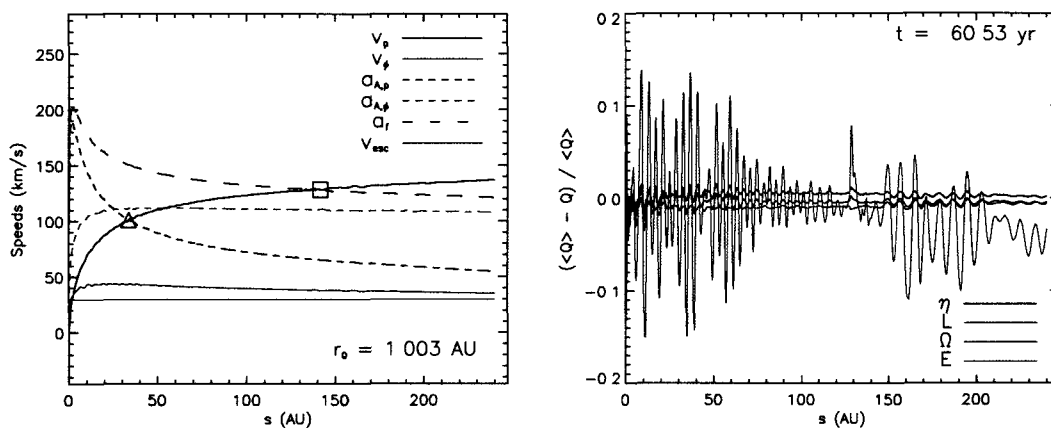


Figure 4.24 Various speeds and fractional variation of the steady-state constants along a field line with footprint at $r_0 \simeq 1.0$ AU from simulation B. See Figure 4.22 for additional information.

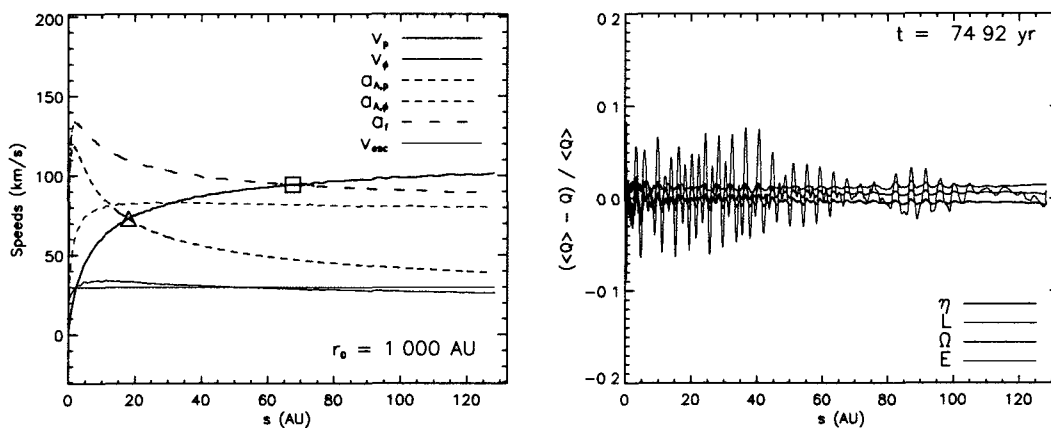


Figure 4.25 Various speeds and fractional variation of the steady-state constants along a field line with footprint at $r_0 \simeq 1.0$ AU from simulation C. See Figure 4.22 for additional information.

for simulations B and C, where almost 80% of the acceleration occurs before the Alfvén point, and beyond which the toroidal field becomes dominant.

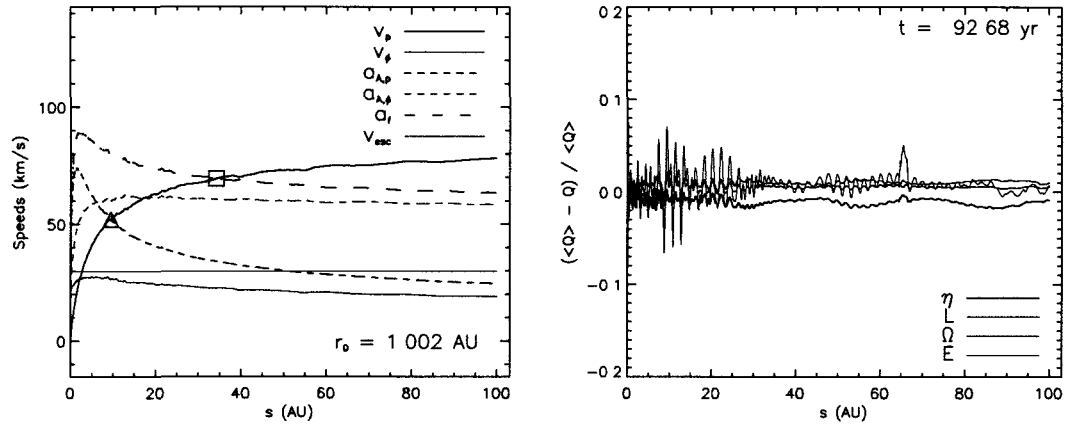


Figure 4.26 Various speeds and fractional variation of the steady-state constants along a field line with footprint at $r_0 \simeq 1.0$ AU from simulation D. See Figure 4.22 for additional information.

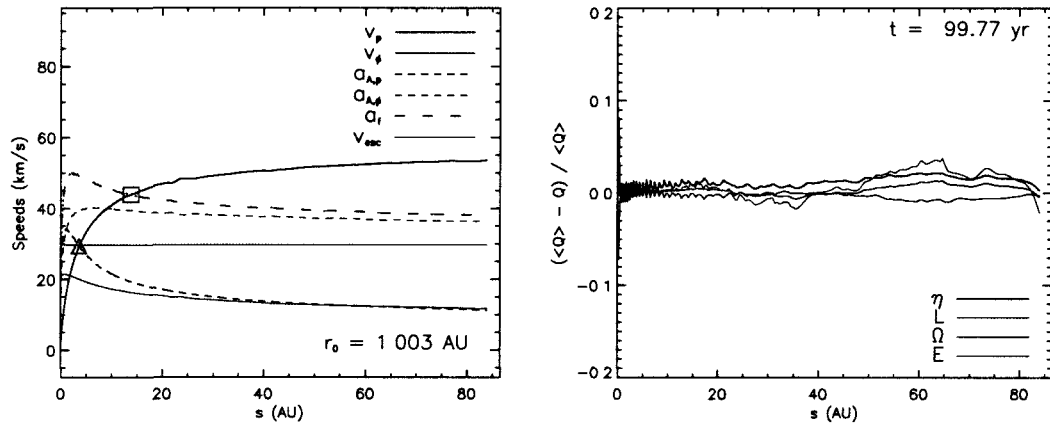


Figure 4.27 Various speeds and fractional variation of the steady-state constants along a field line with footprint at $r_0 \simeq 1.0$ AU from simulation E. See Figure 4.22 for additional information.

As the field strength decreases further, the relative importance of the Alfvén and toroidal Alfvén speeds change. In simulation D, the poloidal field is still dominant over the toroidal field, but in simulation E, the toroidal field is now stronger than the poloidal

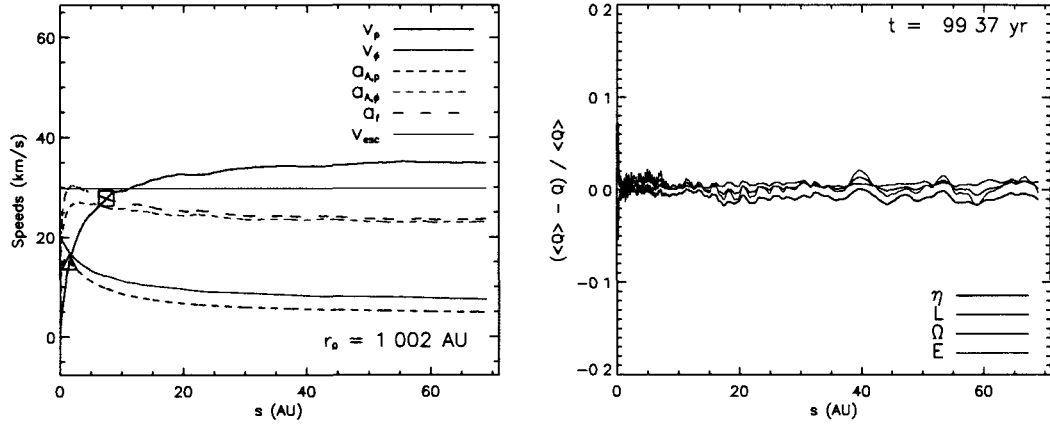


Figure 4.28 Various speeds and fractional variation of the steady-state constants along a field line with footprint at $r_0 \simeq 1.0$ AU from simulation F. See Figure 4.22 for additional information.

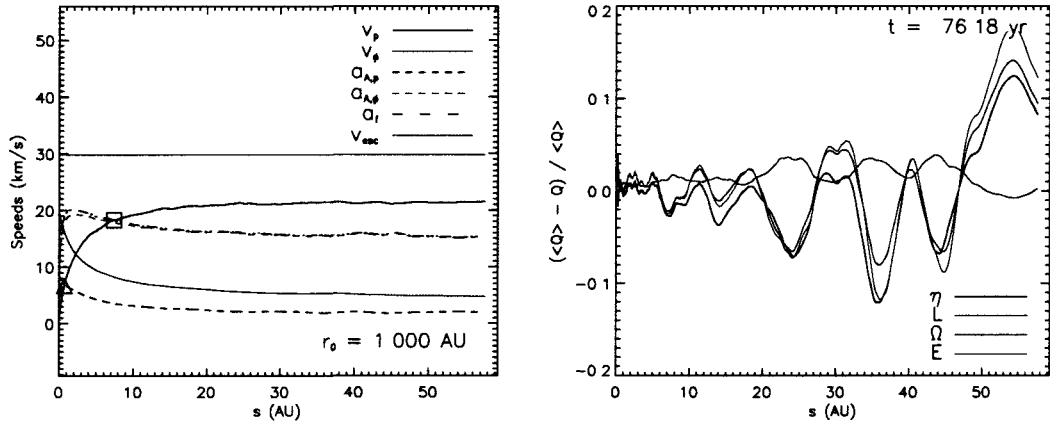


Figure 4.29 Various speeds and fractional variation of the steady-state constants along a field line with footprint at $r_0 \simeq 1.0$ AU from simulation G. See Figure 4.22 for additional information.

field at the Alfvén point, and only $\sim 67\%$ of the total acceleration has occurred at sub-Alfvénic speeds. Progressing to even weaker field strengths, only $\sim 54\%$ of the acceleration occurs before the Alfvén point in simulation F. In simulation G, only $\sim 37\%$ occurs before

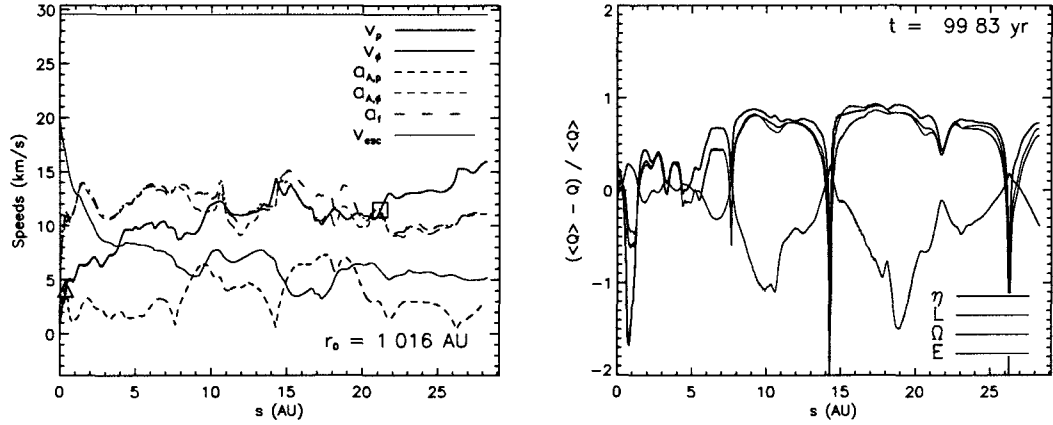


Figure 4.30 Various speeds and fractional variation of the steady-state constants along a field line with footprint at $r_0 \simeq 1.0$ AU from simulation H. See Figure 4.22 for additional information. This field line is clearly *not* in steady-state, and is only included for completeness.

the Alfvén point, and the toroidal field is dominant right from the disc surface. The amount of acceleration occurring before the Alfvén point in simulation H is similar to G, but the steady-state approximation is no longer valid (see the right panel of Figure 4.30), and I consider this result unreliable.

In the magneto-centrifugal picture, because the launching mechanism only functions efficiently up to the Alfvén point, the ability of an outflow to reach high speeds is governed by the location of the Alfvén point, or more specifically the Alfvén radius (Pelletier & Pudritz 1992). Under the assumption of rigid field lines, a large Alfvén radius provides a large lever arm for the rotating disc to supply a torque to the fluid, and thus a large Alfvén radius should correspond to a fast wind.

Figures 4.22, 4.24 — 4.29 show that, for strong magnetic fields, the Alfvén (and fast) point is far from the disc, while for weak magnetic fields, it is close to (or nearly

at) the disc surface. Subsequently, the flow along a field line anchored at $r_0 \simeq 1.0$ AU in simulation A (the strongest field) is accelerated to an asymptotic speed ~ 10 times greater than in simulation G (the second weakest field)¹.

The centrifugal mechanism of Blandford & Payne (1982) assumes that the field is strong enough to enforce co-rotation on the fluid, or equivalently that the inertia of the fluid is negligible relative to the tension in the magnetic field. If the magnetic field is weak, co-rotation no longer holds, and the rotating fluid begins to drag the field with it, resulting in a strongly wound up field. This occurs when the *toroidal* kinetic energy exceeds the poloidal magnetic energy, or equivalently when the toroidal velocity is greater than the Alfvén speed.

This first happens in simulation F (Figure 4.28), where only $\sim 54\%$ of the total acceleration occurs before the Alfvén point. Figure 4.31 plots the ratio of $|B_\varphi|/B_p$ at the disc surface as a function of r , and shows that simulation F is also the first which is dominated by B_φ right from the disc surface. Thus, for simulations F, G, and H, the assumption of co-rotation is not valid, and the centrifugal viewpoint is not efficient at launching the jet.

As noted in Section 3.4.1, the poloidal component of the Lorentz force $[(\vec{J} \times \vec{B})_p]$ along a field line is given by:

$$F_{L,\parallel} = -\frac{B_\varphi}{4\pi r} \nabla_{\parallel} (rB_\varphi) = -\frac{1}{4\pi} \left(\frac{B_\varphi^2}{r} \hat{s} \cdot \hat{r} + \frac{1}{2} \nabla_{\parallel} B_\varphi^2 \right), \quad (4.10)$$

¹Simulation H is excluded here because the steady-state approximation is not valid for the field line with $r_0 \simeq 1.0$ AU.

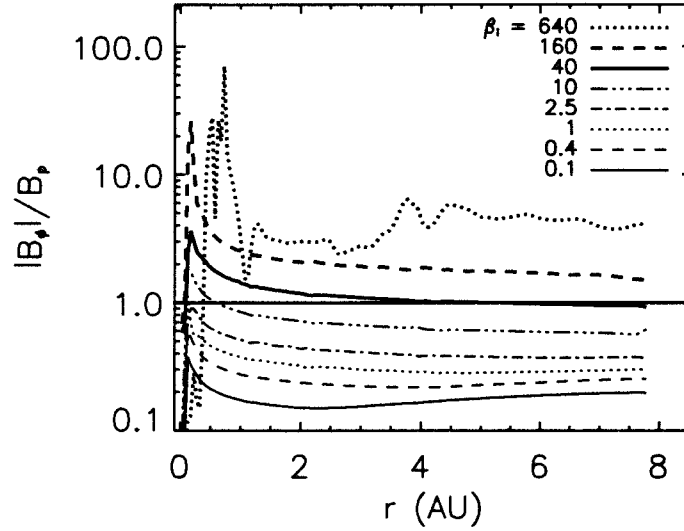


Figure 4.31 $|B_\varphi|/B_p$ as a function of radius just above the disc surface in each simulation. The data are taken at the end of the simulations (t_{end}).

where $\nabla_{\parallel} = \hat{s} \cdot \nabla$ is the gradient parallel to the field line, whereas the toroidal component of $[(\vec{J} \times \vec{B})_\varphi]$ is given by:

$$F_{L,\varphi} = \frac{B_p}{4\pi r} \nabla_{\parallel} (rB_\varphi) = \frac{B_p B_\varphi}{4\pi r} \hat{s} \cdot \hat{r} + \frac{B_p}{4\pi} \nabla_{\parallel} B_\varphi, \quad (4.11)$$

(equations 3.13, Zanni *et al.* 2007). Thus, I conclude from equation (4.10) that it is the toroidal magnetic pressure gradient $\nabla_{\parallel} B_\varphi^2$ and the magnetic tension $B_\varphi^2 \hat{s} \cdot \hat{r}/r$ which determine the acceleration along a field line for simulations F, G, H and, to a lesser extent simulations A – E where the centrifugal mechanism dominates. To use a mechanical analogy, the toroidal field acts like a “coiled spring”, storing potential energy in the field as it becomes wound up, and releasing it as kinetic energy as the jet accelerates.

Evidently, both the toroidal and poloidal Lorentz forces along a field line depend on gradients in rB_φ . The relative importance of the two components can then be assessed by taking the ratio of equations (4.10) and (4.11) (Zanni *et al.* 2007):

$$\frac{F_{L,\parallel}}{F_{L,\varphi}} = -\frac{B_\varphi}{B_p}. \quad (4.12)$$

For $|B_\varphi|/B_p < 1$, the toroidal Lorentz force $F_{L,\varphi}$ dominates, the centrifugal force will be relatively large, and the magneto-centrifugal point of view is more appropriate. Conversely, if $|B_\varphi|/B_p > 1$, the poloidal Lorentz force $F_{L,\parallel}$ will dominate, acceleration will be due to gradients in rB_φ along field lines, and the “coiled spring” viewpoint is more useful.

Appealing to a “coiled spring” of toroidal field can also help explain why the flow in some simulations experiences the majority of the acceleration between the Alfvén and fast points. Along a field line, the fast magnetosonic speed is the root-sum-square of the poloidal and toroidal Alfvén speeds. Thus, the square of the fast magnetosonic Mach number serves as a proxy for the ratio of poloidal kinetic to total magnetic energy in the flow:

$$M_f^2 = \frac{v_p^2}{a_f^2} = \frac{4\pi\rho v_p^2}{B_p^2 + B_\varphi^2}. \quad (4.13)$$

Up to the fast point, a strong toroidal magnetic field can still exert itself through the Lorentz force to accelerate the flow, thus explaining why the simulations continue accelerating beyond the Alfvén point.

For the jet with the strongest field (simulation A), Figure 4.31 shows that $|B_\varphi|/B_p < 1$, so the centrifugal viewpoint dominates. From Figure 4.22, the assumption of co-rotation

is good because the poloidal magnetic energy is much larger than the toroidal kinetic energy. The Alfvén point is far from the disc and, assuming co-rotation, the disc is provided with a large lever arm over which to apply a force. These things considered, the centrifugal point of view is most appropriate for the strong field case, and the majority of the acceleration occurs before the Alfvén point, as predicted from theory. Beyond the Alfvén point, the toroidal field can still accelerate the fluid, but provides only a minor contribution to the total acceleration.

For jets with weak fields (*e.g.*, simulation G), Figure 4.29 demonstrates that the toroidal kinetic energy dominates over poloidal magnetic energy and co-rotation is not applicable. Thus, the lever arm loses its rigidity and is unable to apply a torque efficiently to the flow. Figure 4.31 shows that $|B_\phi|/B_p > 1$, and so acceleration by gradients in the toroidal field is the dominant acceleration mechanism. In addition, the majority of the acceleration along the field line occurs beyond the Alfvén point, further implying that it is the toroidal field which accelerates the flow. Thus, it is the energy stored in the “coiled spring”, acting as a body force on the fluid, which accelerates the flow in the weak field case.

Figure 4.32 shows the net and poloidal Lorentz accelerations along the field line for simulations A and G. For the weak field case, the Lorentz acceleration traces the net acceleration closely, as it is the dominant force. For the strong field case, the Lorentz acceleration only overlies the net acceleration outside the Alfvén point, as expected for a centrifugally-driven jet.

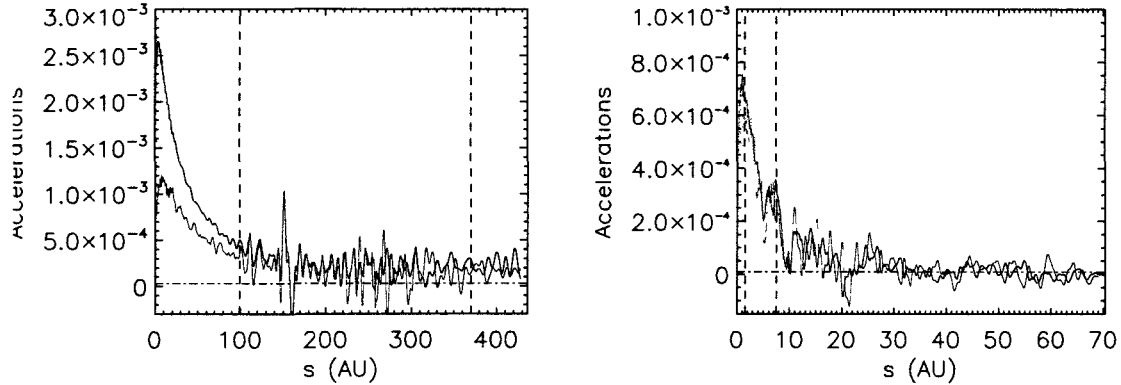


Figure 4.32 The net acceleration (black) and poloidal Lorentz acceleration (red) along a field line with foot print $r_0 \simeq 1.0$ AU for simulations A and G (left and right panels, respectively). The Alfvén and fast points are denoted by dashed lines, and 1% of the maximum acceleration is denoted by the green dash-dot line.

4.5.3 Establishing a magnetic environment

Initially, there is no toroidal field present in these simulations: only through the twisting of the poloidal field does a toroidal field become established. Once the simulations start, it does not take long for the field to become dominated by B_φ . This is demonstrated in Figure 4.33, which plots three different ways of determining the plasma- β . In all cases, the values are determined by averaging the pressure and appropriate magnetic field components over the domain, masked by v_z so that only fast-moving jet material is included in the calculation.

First, it should be pointed out that the oscillations in the simulation H ($\beta_i = 640$) profile are the direct result of the eruption events discussed in Section 4.2.8. Although these ejections of high pressure material temporarily and drastically increase the value of β , the underlying behaviour of this jet is still visible.

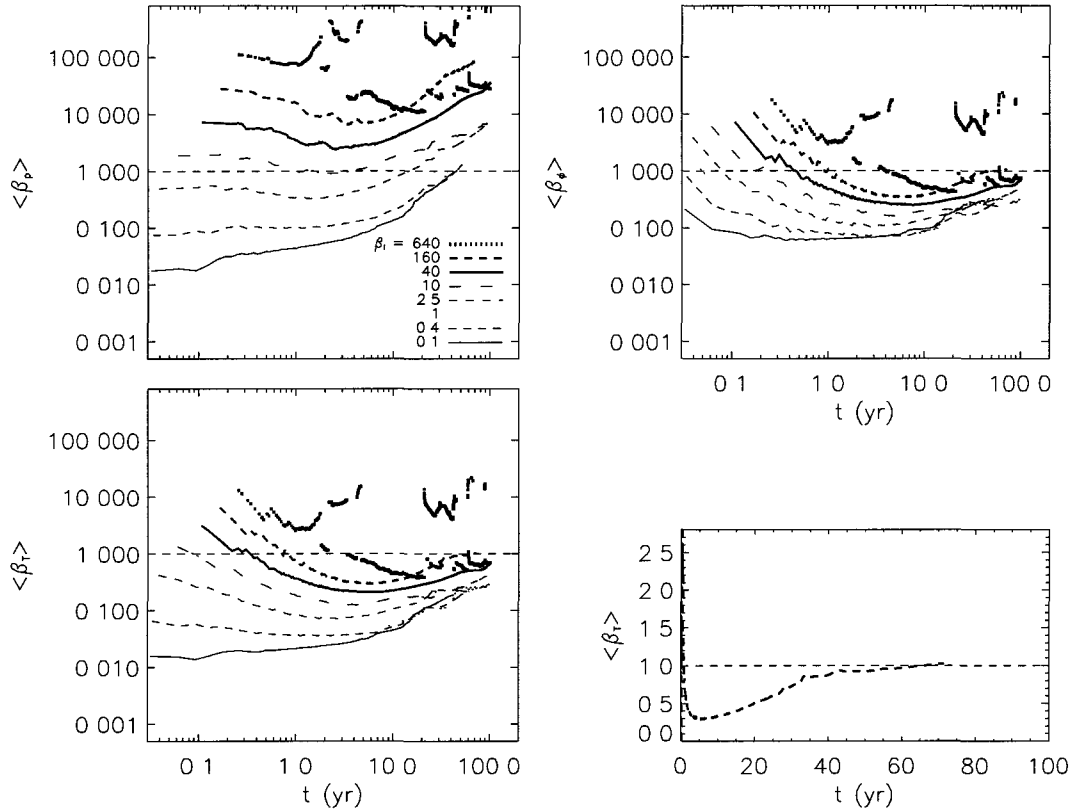


Figure 4.33 Different measures of plasma- β as a function of time. Top left panel: $\langle\beta_p\rangle = 8\pi\langle p\rangle/\langle B_p^2\rangle$ (poloidal). Top right panel: $\langle\beta_\varphi\rangle = 8\pi\langle p\rangle/\langle B_\varphi^2\rangle$ (toroidal). Bottom left panel: an updated version of Figure 3.2a for $\langle\beta_T\rangle = 8\pi\langle p\rangle/\langle B^2\rangle$ (total). Bottom right panel: a close-up of simulation G showing its asymptotic approach to $\langle\beta_T\rangle = 1$.

If only the poloidal field is included in the calculation of β ($\langle\beta_p\rangle$; top left panel of Figure 4.33), all of the simulations end with $\langle\beta_p\rangle > 1$. In contrast, if only the toroidal field is used in calculating β ($\langle\beta_\varphi\rangle$), the rapid generation of B_φ drives $\langle\beta_\varphi\rangle < 1$ for all simulations. The rate at which the toroidal field becomes dominant over the poloidal field is illustrated by comparing the toroidal $\langle\beta_\varphi\rangle$ and the total $\langle\beta_T\rangle$, which includes both

poloidal and toroidal components. Indeed, the toroidal field becomes dominant for $t \gtrsim 10$ yr, and the plots for $\langle\beta_\varphi\rangle$ and $\langle\beta_T\rangle$ become virtually indistinguishable.

As the jets evolve and fill the domain, $\langle\beta_T\rangle$ increases asymptotically towards $\langle\beta_T\rangle = 1$. In the case of simulation G, $\langle\beta_T\rangle \sim 1$ for $\sim 50\%$ of the simulation lifetime. A close-up view of this is shown in the bottom right panel of Figure 4.33, where a change in slope can be seen as it approaches, and then straddles, the $\langle\beta_T\rangle = 1$ line.

The tendency of these jets to asymptote to $\langle\beta_T\rangle = 1$ is a result of their propagation to length scales much larger than the scale at which the launching mechanism operates. As there is no additional means of strong field generation in the far-field regime, the amount of magnetic energy per unit volume decreases as the jet expands and, as nature has a tendency to do, the jets move towards equipartition between magnetic and thermal forces. It would be useful to run the simulations for much longer physical times to confirm that the jets do indeed asymptote to $\langle\beta_T\rangle = 1$ with time, regardless of the initial value of B_i .

Finally, it is worth speculating that these jets exist because the rotating accretion disc is able to establish a magnetically-dominated environment within which jets can be launched. Even the weakest field case (simulation H) is able to generate enough toroidal field to force $\langle\beta_T\rangle < 1$ and launch a jet. Thus, regardless of the environment near the surface of the disc, one might expect in general that protostellar jets on observable scales will have $\langle\beta_T\rangle \lesssim 1$, otherwise there would be no jet to observe.

4.6 Trends in B_i

4.6.1 Speeds

At the disc surface, the poloidal velocity is effectively zero. An “evaporation speed” from the disc interior is prescribed, but only to provide mass flux to the outflow (Section 2.5). By the time the flow reaches the bow shock, it is moving with a significant velocity, and this begs the question, can the velocity at the jet head be linked to conditions at the disc surface?

The first step is provided by the steady-state constants of Section 4.5.1, which can be used to derive an equation for the poloidal speed at the fast point that depends on quantities at the disc surface.

Assuming that the steady-state approximation is valid for a field line ψ , combining equations (4.7) and (4.9) gives:

$$2E(\psi) + r^2\Omega^2(\psi) = v_p^2 \left(1 + \frac{B_\varphi^2}{B_p^2} \right) + 2\Phi,$$

where I have assumed the thermal energy of the gas is negligible. Substituting the poloidal and toroidal Alfvén speeds ($B_p/\sqrt{4\pi\rho}$ and $B_\varphi/\sqrt{4\pi\rho}$, respectively) into this expression, I obtain:

$$2E + r^2\Omega^2 = v_p^2 \frac{v_f^2}{a_p^2} + 2\Phi.$$

Evaluating this expression at the fast point ($r = r_f$), and substituting for $E(\psi) = -3v_{K,0}^2/2$, $\Omega(\psi) = v_{K,0}/r_0$, and a gravitational point source, $\Phi = -GM_*/R = -v_{K,0}^2 r_0/R$,

then

$$v_{p,f}^4 = a_{p,f}^2 v_{K,0}^2 \left(\frac{r_f^2}{r_0^2} - \frac{2r_0}{R} - 3 \right),$$

where $R = \sqrt{r^2 + z^2}$ is the spherical radius. Defining the “fast moment arm” as $\xi \equiv r_f/r_0$, and replacing the spherical radius with $R = r\sqrt{1 + z^2/r^2} = r\sqrt{1 + \sigma^2}$ evaluated at the fast point, this leaves:

$$v_{p,f} = \sqrt{a_{p,f} v_{K,0}} \left(\xi^2 - \frac{2}{\xi} \frac{1}{\sqrt{1 + \sigma^2}} - 3 \right)^{1/4}, \quad (4.14)$$

which is a generalised version of equation (3.14). For the simulations presented here, it is observed that ξ and $\sigma = z_f/r_f$ are always greater than one, and thus $2/(\xi\sqrt{1 + \sigma^2})$ is small relative to ξ^2 in equation (4.14), and can be ignored. It is also observed that $\xi^2 \gg 3$, the Alfvén speed is roughly proportional to B_i , and thus:

$$v_{p,f} \propto \sqrt{B_i} \xi^{1/2}, \quad (4.15)$$

where the fast moment arm ξ is some unknown function of B_i . Applying equation 4.14 directly to the simulation data, I find that it predicts the poloidal velocity at the fast point with $< 1\%$ error, even for field lines that are not in steady-state (*e.g.*, Figure 4.23).

Table 4.4 contains the values of $v_{p,f}$ measured along different field lines in each simulation, averaged over $\gtrsim 100$ sequential slices in time. Fitting a power-law to these data, I observe that $v_{p,f} \propto B_i^{0.66 \pm 0.01}$. From equation (4.15), $v_{p,f}$ will depend on both the square root of the Alfvén speed ($\propto \sqrt{B_i}$) and ξ . As I do not have an analytical expression for ξ , I instead measure it from the simulations. Using several field lines, I find that

$\xi \propto B_i^{0.23 \pm 0.07}$ and, thus, $v_{p,f} \propto B_i^{0.62 \pm 0.03}$, in agreement with the measured values of $v_{p,f}$, to within uncertainty.

In Section 3.4.1, the power-law index on $v_{p,f}$ was stated to be 0.5, whereas here I find it to be 0.66 ± 0.01 . This discrepancy is attributable to Section 3.4.1 being biased towards the weak field simulations as the strong field simulations had not propagated very far in time². In the current discussion, the strong field simulations are given equal weight, and these results should be more robust.

| Simulation B_i (G) | H 2.5 | G 5 | F 10 | E 20 | D 40 | C 63.2 | B 100 | A 200 | α |
|---|----------|--------|---------|---------|---------|-----------|----------|----------|-----------------|
| $v_{p,f}$ (km s ⁻¹) | 14.3 | 21.0 | 30.9 | 48.9 | 75.8 | 103 | 140 | 228 | 0.66 ± 0.01 |
| v_{asympt} (km s ⁻¹) | 14.4 | 22.3 | 36.9 | 54.5 | 80.9 | 88.6 | 108 | 204 | 0.52 ± 0.04 |
| $\langle v_z \rangle$ (km s ⁻¹) | 72.3 | 77.5 | 110 | 141 | 201 | 241 | 292 | 395 | 0.45 ± 0.02 |
| v_{jet} (km s ⁻¹) | 45.3 | 67.3 | 109 | 146 | 208 | 254 | 317 | 458 | 0.48 ± 0.01 |
| $\langle v_\varphi \rangle$ (km s ⁻¹) | 1.4 | 2.6 | 3.0 | 6.2 | 10.1 | 13.1 | 18.4 | 30.6 | 0.66 ± 0.01 |

Table 4.4 The different velocities measured in simulations A – G. More detailed explanations are given in the text; see also Section 3.4.1. Although I have included simulation H results in the table, this simulation does not follow the same trends as the others, and I have elected to leave it out of the power-law fits.

Another means of measuring the dependence of the magnetic field on the flow velocity is to examine the asymptotic flow speed along a field line. Here, I approximate this by measuring the poloidal velocity where the net acceleration along a field line (*e.g.*, Figure 4.32) decreases to 1% of its maximum value. The results of this measurement are found in Table 4.4 and, fitting a power-law to the data, I find $v_{\text{asympt}} \propto B_i^{0.52 \pm 0.04}$ (Section 3.4.1).

²Indeed, simulation A had only *just* reached $t = 20$ yr at the time of submission.

The location of this “1% point” is a function of B_i , and for weak fields it is measured to be a few $\sim r_f$, while for strong fields it is located at $\sim 3r_f/4$. This is in general agreement with our interpretation of the driving mechanism (Section 4.5.2), where jets with strong fields attain the majority of their acceleration before the Alfvén point, and jets with weak fields reach their asymptotic speed well beyond the fast point. This is demonstrated in Figure 4.32, where the green dash-dot line marks 1% of the maximum acceleration along field lines with footprint $r_0 \simeq 1.0$ AU, and the dashed lines denote the location of the Alfvén (left) and fast (right) points.

Evidently and in hindsight, for the strong field cases, the flow has already nearly reached its asymptotic speed before the fast point, and thus the velocities at the “1% point” are less useful.

Moving to the far-field regime, where the steady-state approximation does not generally apply, the momentum-weighted average velocity just behind the bow shock is calculated as:

$$\langle v_z \rangle = \frac{\int \rho v_z^2 r \, dr \, dz}{\int \rho v_z r \, dr \, dz}, \quad (4.16)$$

where the integral goes from $r = 0$ to r_{\max} and $z = z_{\text{jet}} - 50$ AU to $z = z_{\text{jet}}$, and where z_{jet} is the location of the bow shock at the symmetry axis. The time-averaged results of applying equation (4.16) to the simulation data are summarised in Table 4.4, and fitting a power-law, I find that $\langle v_z \rangle \propto B_i^{0.45 \pm 0.02}$.^a

Finally, Figure 4.35 displays the height of the bow shock above the disc as a function of time for each of the simulations A – H. Beyond some initial acceleration phase, the jets propagate forward uniformly in time, and least-squares fits to the slope are performed

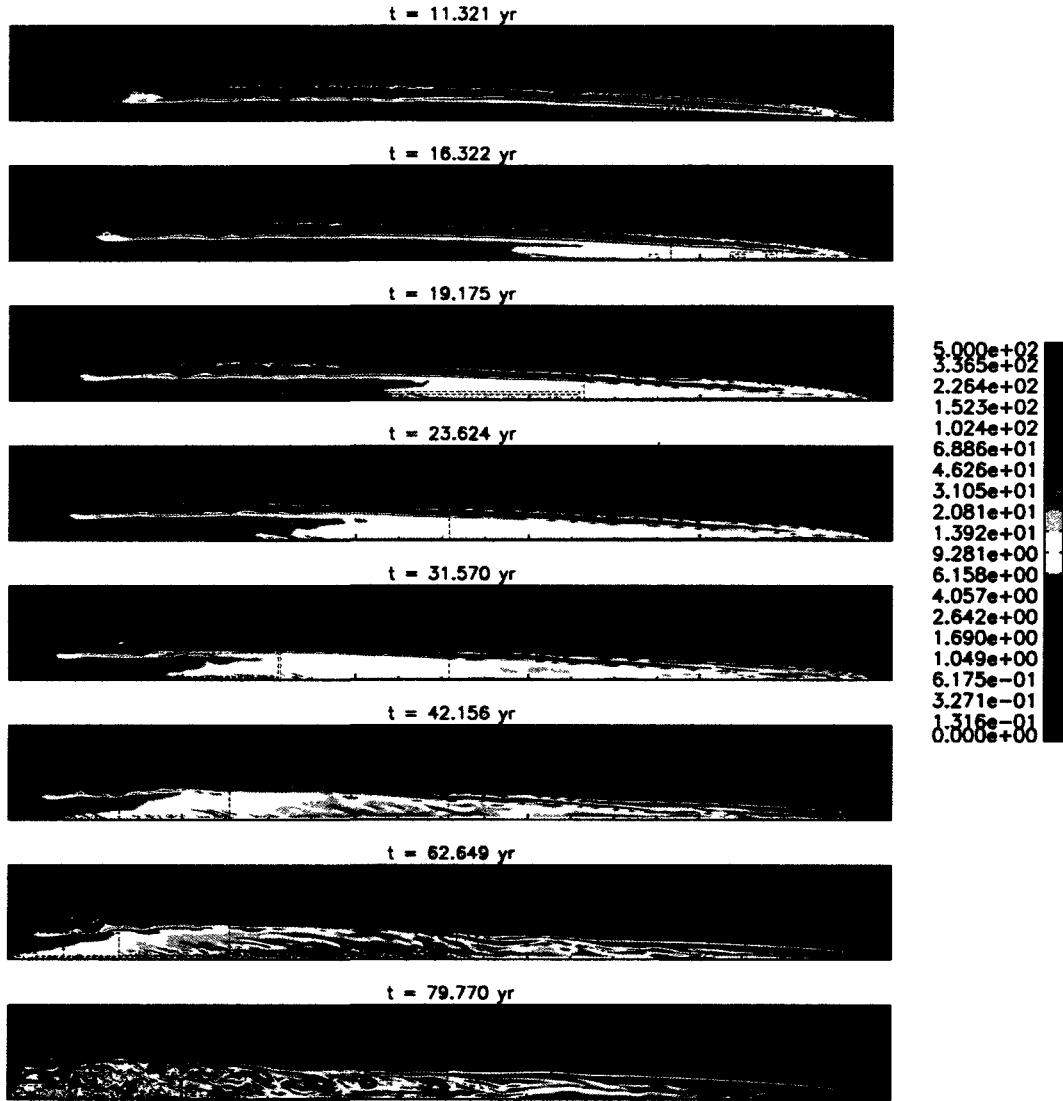


Figure 4.34 The ratio $|B_\phi|/B_p$ in simulations A – H (top to bottom), all plotted when they reach a height of 1000 AU above the disc. Black contours denote where $|B_\phi|/B_p = 1$. All plots have dimensions $z \in [0, 1025]$, $r \in [0, 110]$ AU.

to obtain the proper motions (v_{jet}) found in Table 4.4. Fitting yet another power-law then gives³ $v_{\text{jet}} \propto B_i^{0.48 \pm 0.01}$. The jet propagation speed changes only slightly ($\lesssim 15\%$ for

³The data and power-law index for v_{jet} have changed relative to Section 3.4 and Table 3.2 for the same reasons that $v_{p,f}$ has changed.

simulations A – G) from the momentum-weighted velocity immediately behind the bow shock, implying the jets are essentially ballistic.

Regardless of the initial field strength, the toroidal field becomes dominant over the poloidal field beyond the Alfvén point. Figure 4.34 plots the ratio of $|B_\varphi|/B_p$, demonstrating that, on large scales, this remains true. Appealing to the “coiled spring” mechanism, there will be some residual acceleration of the flow due to the toroidal field far from the disc surface. The amount of acceleration experienced will be a function of how “tightly wound” the spring is and, for higher values of $|B_\varphi|/B_p$, the resulting ratio between $\langle v_z \rangle / v_{\text{asympt}}$ will be larger. Thus, the discrepancy between v_{asympt} and $\langle v_z \rangle$ is the result of a small residual acceleration from the toroidal field, applied over large length scales (*e.g.*, in simulation F the “1% point” is at a few $r_f \sim 20$ AU, while $\langle v_z \rangle$ is measured beyond 2000 AU), and the size of the discrepancy will depend on the ratio $|B_\varphi|/B_p$.

The decrease in the power-law index with distance from the disc could also be a result of residual accelerations by B_φ . From Figure 4.34, the ratio $|B_\varphi|/B_p$ evidently inversely depends on B_i , and including this effect on the velocities between the “1% point” and the jet head will cause the power-law index will decrease. At the time of this writing, I have not quantified this effect, but I expect it is the dominant factor affecting the decrease in α .

For weak fields, I find that v_{jet} is always less than $\langle v_z \rangle$, while for strong fields the opposite is true. At the time of this writing, I have not uncovered a physical explanation for this effect, in particular why v_{jet} is greater than $\langle v_z \rangle$ for strong fields. However, I do note that the power-law indices are consistent with each other to within the uncertainties.

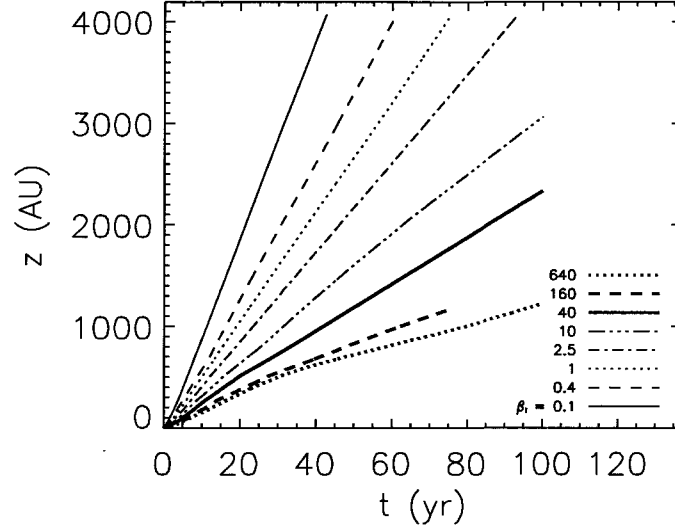


Figure 4.35 The height of the jet bow shock (z_{jet}) above the disc as a function of time and β_1 . The proper motions of Figure 3.2b and Tables 3.2 & 4.4 are determined from the asymptotic slope of these data.

A dependence on the magnetic field B_1 is not limited to the poloidal velocity. The volume-averaged toroidal velocity can also be expressed as a power-law function: $\langle v_\phi \rangle \propto B_1^{0.66 \pm 0.01}$ (see also Section 3.4.2). The volume-averaged toroidal velocity asymptotes to a constant in time, not counting an initial acceleration phase. Table 4.4 shows our results for the different simulations, where we have excluded values at $z < 100$ AU because of the presence of the torsion Alfvén wave, which has a non-negligible velocity, and is not part of the jet proper (*e.g.*, Section 4.2.1 and Figure 4.2).

Despite this rather tight power-law fit, I have yet to uncover a physical explanation for this dependence. Combining v_{jet} with $\langle v_\phi \rangle$, I find that $v_{\text{jet}} \propto \langle v_\phi \rangle^{0.73 \pm 0.02}$, a result which might be possible to confirm with observations.

In the magneto-centrifugal wind launching picture, it is the centrifugal force ($\propto v_\varphi^2$) which is responsible for accelerating the flow (Sections 1.2, 4.5.2; see also Figure 4.16). Thus, an increase in the toroidal velocity near the disc surface will lead to an increased centrifugal force, and this should result in an increase in the jet velocity, as the $\sim 3/4$ relation confirms.

4.6.2 Jet Radii

The jet radius, r_{jet} , is defined by the boundary between shocked ambient and jet material, and is visible as a sharp gradient in the temperature in Figures 4.1 – 4.11. In the top panel of Figure 4.36, the maximum jet radius is plotted as a function of time (as opposed to the jet radius at 200 AU above the disc as done in Section 3.4.3) for simulations A – G. Even at $t = 100$ yr, the jets are still expanding, and although there are signs that the jet radius will eventually asymptote (because of the asymptotically uniform ambient medium), it would take simulations of much longer duration to answer this question definitively.

In Section 3.4.3, I fit a power-law in B_1 to the jet radii at a selected time to try and draw out how the jet radius depends on conditions near the disc. Here, I instead use the maximum jet radius, and fit a power-law at several different points in time. The results are summarised in the right panel of Figure 4.36 and Table 4.5. Evidently, the power-law index for $r_{\text{jet,max}}$ decreases very slowly in time.

Given that the jet radius is determined by the interplay between the jet ram pressure (which is determined, in part, by the jet speed) and forces in the ambient medium, then a

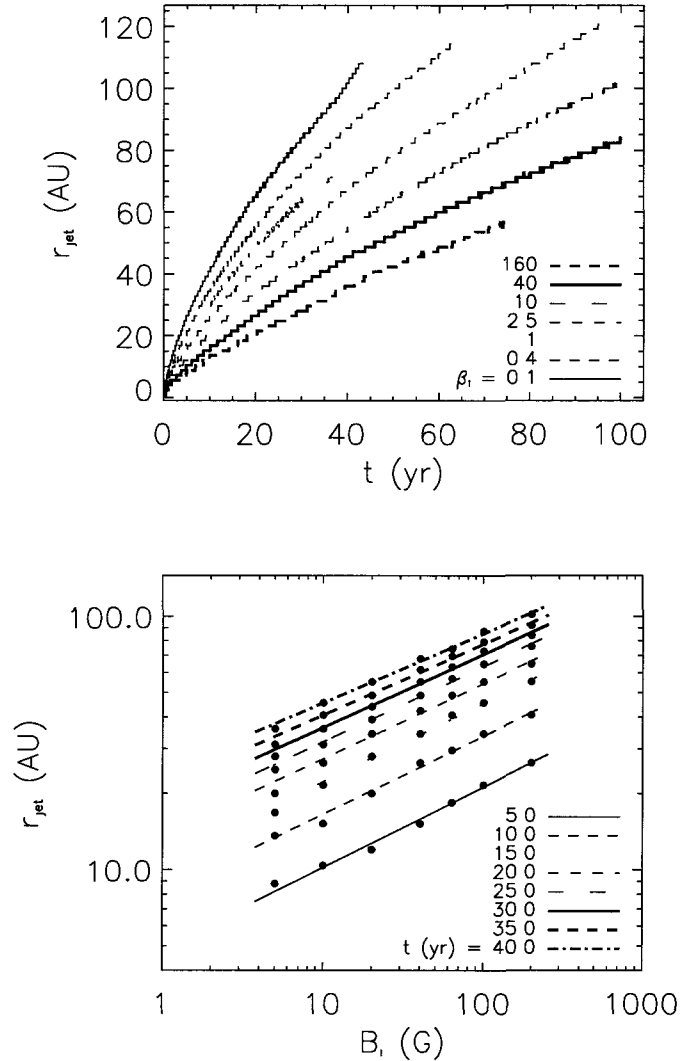


Figure 4.36 Top panel: the maximum jet radius r_{jet} as a function of time for simulations A – G. Simulation H is excluded for reasons already discussed. Bottom panel: the maximum jet radius at select times as a function of B_1 . The uncertainty for each measurement of r_{jet} is ± 1.6 AU, which is the resolution of the grid from whence these data were extracted. This is also the cause of the step-like appearance of the curves in the top panel.

correlation between $r_{\text{jet,max}}$ and B_i is expected. That the correlation is slowly decreasing in time implies that, at some point in the future, the magnetic field may no longer play a significant role in determining the jet radius. Extrapolating the decrease in the power-law index with time, the dependence of r_{jet} on B_i should disappear at ~ 250 yr, which could be confirmed by extending the duration of these simulations by a factor of 5 – 6 in time.

Figure 4.34 shows the simulations plotted at the same “propagation time”, *i.e.*, when they have all propagated to 1000 AU above the disc. As noted in Section 4.2.9, the jets all have roughly the same radius when compared at the same “propagation time”. This implies that the jet radius is not a function of B_i directly, but rather, indirectly through the ram pressure and, thus, v_{jet} . As the bow shock expands radially its area increases, but the total momentum provided by the jet launching mechanism remains the same and hence the ram pressure decreases. Meanwhile, the pressure exerted by the asymptotically uniform medium remains the same, and thus the radial expansion slows with time. Consequently, the dependence of r_{jet} on B_i also decreases with time as the momentum provided by the launching mechanism loses its ability to propel the radial expansion.

4.6.3 Fluxes

The mass, momentum, kinetic energy, and angular momentum fluxes describe the important quantities transported by the jet. In Section 3.4.3, the mass fluxes were measured at a certain time and height above the disc, noting that the power-law index was changing in time. Here, I elaborate on those statements and present the time-averaged fluxes at a few different heights above the disc, as well as fit power-law functions in B_i .

| β_i | 160 | 40 | 10 | 2.5 | 1.0 | 0.4 | 0.1 | α |
|--|-----|----|----|-----|------|-----|-----|-----------------|
| B_i (G) | 5 | 10 | 20 | 40 | 63.2 | 100 | 200 | |
| $r_{\text{jet}} @ t_{\text{slice}}$ (yr) = 5 | 8.8 | 10 | 12 | 15 | 18 | 22 | 26 | 0.32 ± 0.01 |
| 10 | 14 | 15 | 20 | 26 | 30 | 34 | 41 | 0.31 ± 0.01 |
| 15 | 17 | 22 | 28 | 34 | 41 | 46 | 55 | 0.31 ± 0.01 |
| 20 | 20 | 26 | 34 | 42 | 49 | 55 | 65 | 0.30 ± 0.01 |
| 25 | 25 | 31 | 39 | 49 | 57 | 65 | 76 | 0.30 ± 0.01 |
| 30 | 28 | 36 | 44 | 55 | 63 | 73 | 84 | 0.29 ± 0.01 |
| 35 | 31 | 41 | 49 | 62 | 70 | 79 | 92 | 0.28 ± 0.01 |
| 40 | 36 | 46 | 55 | 68 | 74 | 87 | 102 | 0.27 ± 0.01 |

Table 4.5 The variation of α in $r_{\text{jet,max}} \propto B_i^\alpha$ as a function of time. The last time slice is at $t = 40$ yr because the simulation A jet leaves the domain shortly thereafter.

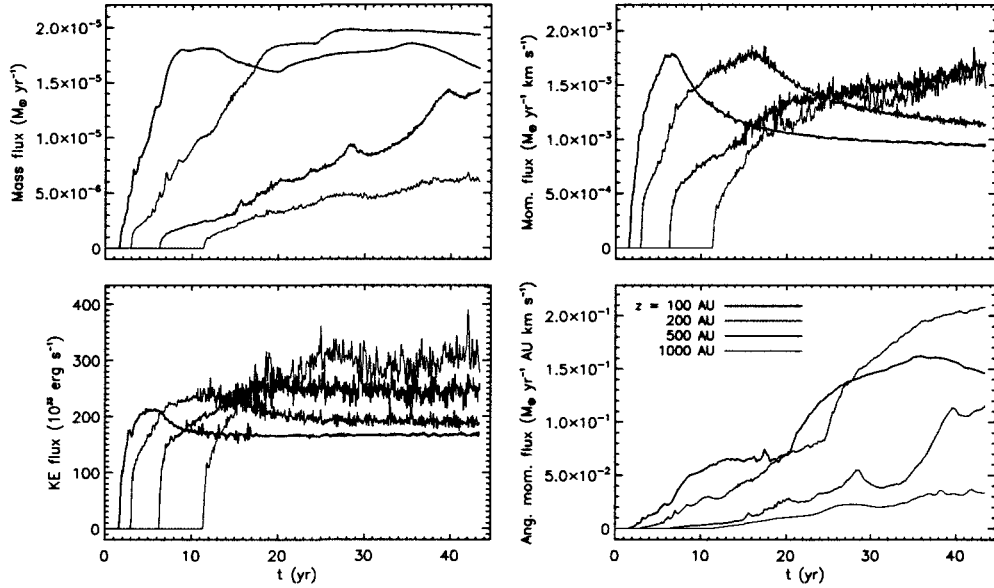


Figure 4.37 Plot of mass, momentum, kinetic energy, and angular momentum flux for simulation A as a function of time at different heights above the disc. A boxcar average width of $\simeq 0.09$ yr has been applied to the data to smooth over short-period fluctuations which can obscure the overall trends. The kinetic energy flux was smoothed with a width of $\simeq 0.21$ yr.

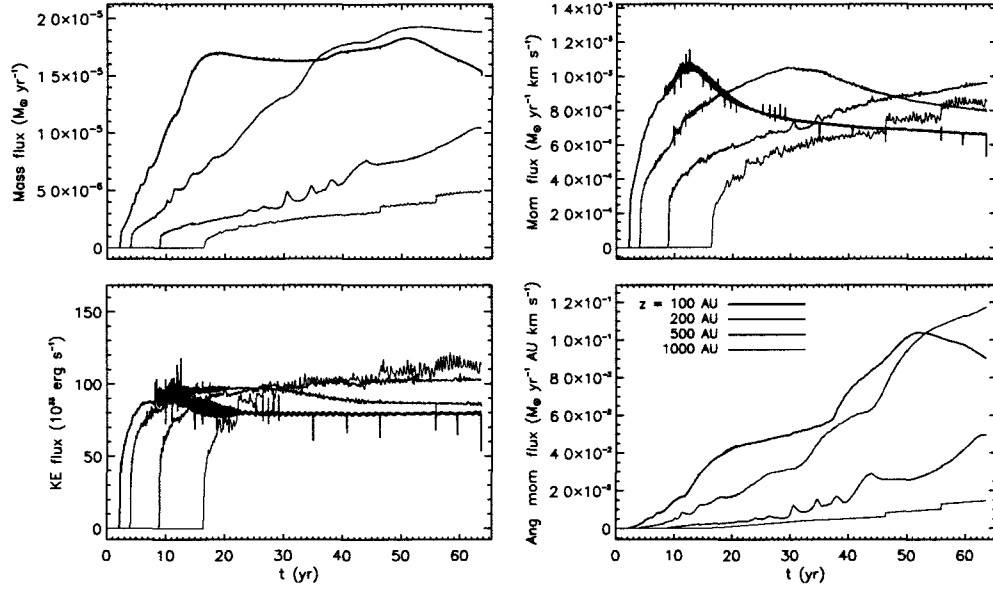


Figure 4.38 The same as Figure 4.37, but for simulation B.

Figures 4.37 – 4.44 show plots of the mass, momentum, kinetic energy, and angular momentum fluxes (\dot{M} , \dot{S} , \dot{K} , and \dot{L} , respectively) as functions of time for different heights above the disc (100 AU, 200 AU, 500 AU, and 1000 AU). The different fluxes are defined as:

$$\dot{M} = 2\pi\dot{M}_1 \int \rho v_z r dr; \quad (4.17)$$

$$\dot{S} = 2\pi\dot{S}_1 \int \rho v_z^2 r dr; \quad (4.18)$$

$$\dot{K} = 2\pi\dot{K}_1 \int \rho v_z^3 r dr; \quad (4.19)$$

$$\dot{L} = 2\pi\dot{L}_1 \int \rho v_z v_\phi r^2 dr, \quad (4.20)$$

where the integrals are from $r = 0$ to r_{\max} , and the scaling factors are

$$\dot{M}_i = (9.7 \times 10^{-7} M_{\odot} \text{yr}^{-1}) \left(\frac{\beta}{40}\right) \left(\frac{B_i}{10 \text{ G}}\right)^2 \left(\frac{r_i}{0.05 \text{ AU}}\right)^{5/2} \left(\frac{0.5 M_{\odot}}{M_*}\right)^{1/2}; \quad (4.21)$$

$$\dot{S}_i = (7.4 \times 10^{-5} M_{\odot} \text{yr}^{-1} \text{ km s}^{-1}) \left(\frac{\beta}{40}\right) \left(\frac{B_i}{10 \text{ G}}\right)^2 \left(\frac{r_i}{0.05 \text{ AU}}\right)^2; \quad (4.22)$$

$$\dot{K}_i = (3.6 \times 10^{33} \text{ erg s}^{-1}) \left(\frac{\beta}{40}\right) \left(\frac{B_i}{10 \text{ G}}\right)^2 \left(\frac{r_i}{0.05 \text{ AU}}\right)^{3/2} \left(\frac{M_*}{0.5 M_{\odot}}\right)^{1/2}; \quad (4.23)$$

$$\dot{L}_i = (3.7 \times 10^{-6} M_{\odot} \text{yr}^{-1} \text{ AU km s}^{-1}) \left(\frac{\beta}{40}\right) \left(\frac{B_i}{10 \text{ G}}\right)^2 \left(\frac{r_i}{0.05 \text{ AU}}\right)^3. \quad (4.24)$$

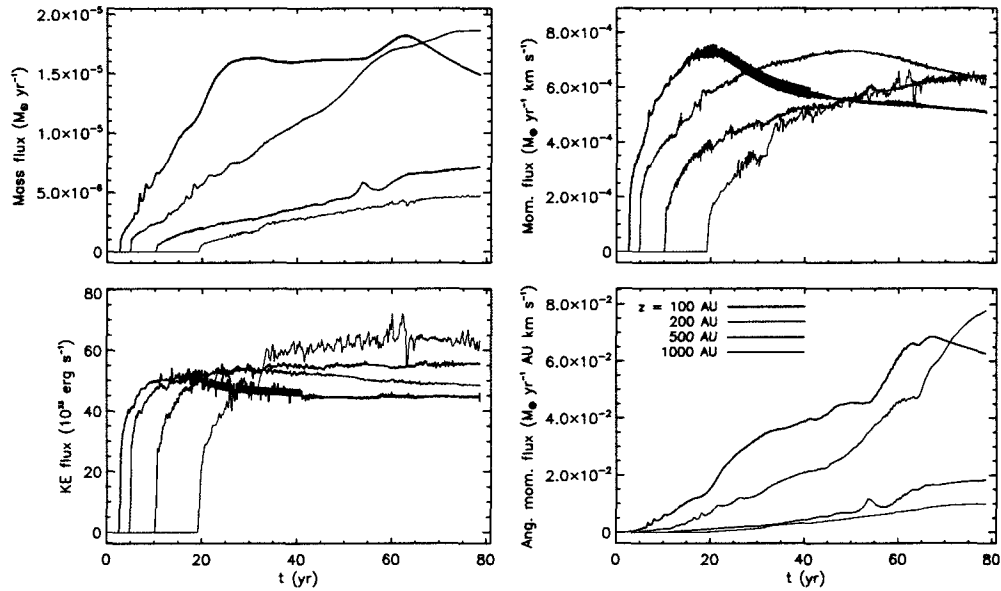


Figure 4.39 The same as Figure 4.37, but for simulation C.

Given what is already known about the relationship between the jet speed and B_i , it comes as no surprise that simulation A transports the most flux, while simulation H

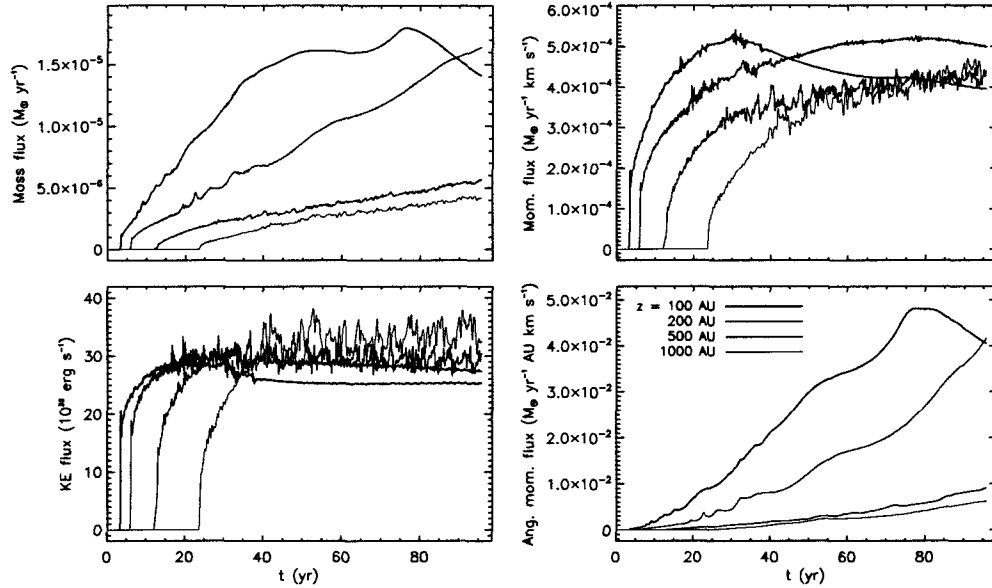


Figure 4.40 The same as Figure 4.37, but for simulation D.

transports the least. Time-averaged fluxes for the different heights, summarised in Tables 4.6 – 4.9, confirm this. Time-averaged values for the fluxes are calculated by taking the mean of the data, but excluding times for which there is a negligible signal. For example, in Figure 4.37, only fluxes at $t \gtrsim 7$ yr are considered in determining the time-averaged fluxes at $z = 500$ AU.

While the fluxes might be expected to asymptote to constant values over time, this appears to hold only for the kinetic energy fluxes and some of the momentum fluxes. As the jet is still expanding with time, larger areas are continually being included in the mass fluxes, and this could prevent the fluxes from asymptoting. This would be a particularly prominent effect in the angular momentum flux, due to the r^2 dependence in the integrand. As the radial expansion slows down over time (*e.g.*, Figure 4.36), I would

| Simulation B_i (G) | H | G | F | E | D | C | B | A | α |
|---------------------------|------|------|------|------|------|------|------|------|-----------------|
| $\langle \dot{M} \rangle$ | 4.17 | 3.26 | 6.13 | 10.1 | 13.7 | 15.1 | 16.1 | 17.3 | 0.32 ± 0.07 |
| $\langle \dot{S} \rangle$ | 0.73 | 0.87 | 1.67 | 2.91 | 4.46 | 5.94 | 7.78 | 11.1 | 0.67 ± 0.03 |
| $\langle \dot{K} \rangle$ | 0.98 | 1.77 | 4.78 | 12.2 | 26.2 | 46.3 | 81.2 | 169 | 1.19 ± 0.02 |
| $\langle \dot{L} \rangle$ | 0.96 | 0.55 | 3.05 | 11.9 | 27.7 | 40.8 | 62.9 | 108 | 1.3 ± 0.1 |

Table 4.6 Time-averaged mass $\langle \dot{M} \rangle$ ($10^{-6} M_{\odot} \text{yr}^{-1}$), momentum $\langle \dot{S} \rangle$ ($10^{-4} M_{\odot} \text{yr}^{-1} \text{km s}^{-1}$), kinetic energy $\langle \dot{K} \rangle$ ($10^{33} \text{erg s}^{-1}$), and angular momentum fluxes $\langle \dot{L} \rangle$ ($10^{-3} M_{\odot} \text{yr}^{-1} \text{AU km s}^{-1}$) with power-law fits α , measured at $z = 100$ AU above the disc for the different values of β_i . The data for simulation H is included in the table for completeness, but is excluded from the power-law fits (see Table 4.4).

also expect the angular momentum to asymptote on longer time scales. To confirm this, longer simulations would be needed.

Conversely, as shown in Figures 4.2 and 4.3, the poloidal velocity is strongly peaked near the axis at both small (100 AU) and large (1000 AU) scales. Thus, the kinetic energy flux, which is strongly weighted in v_z , will be very strongly peaked near the axis, reducing the role of the jet radius in the flux calculation and providing an explanation for why the kinetic energy fluxes asymptote to constant values more quickly than the other fluxes.

In some cases, the momentum fluxes at $z = 100$ AU reach a maximum at early times, before beginning a steady decline (*e.g.*, simulations A – D). These characteristic peaks only occur in the jets with the strongest fields and only at early times. Since these maxima do not appear at greater distances from the disc (which serve as a proxy for a later time), it is likely they are an artifact due to the jets undergoing an acceleration phase at early times ($t \lesssim 10$ yr).

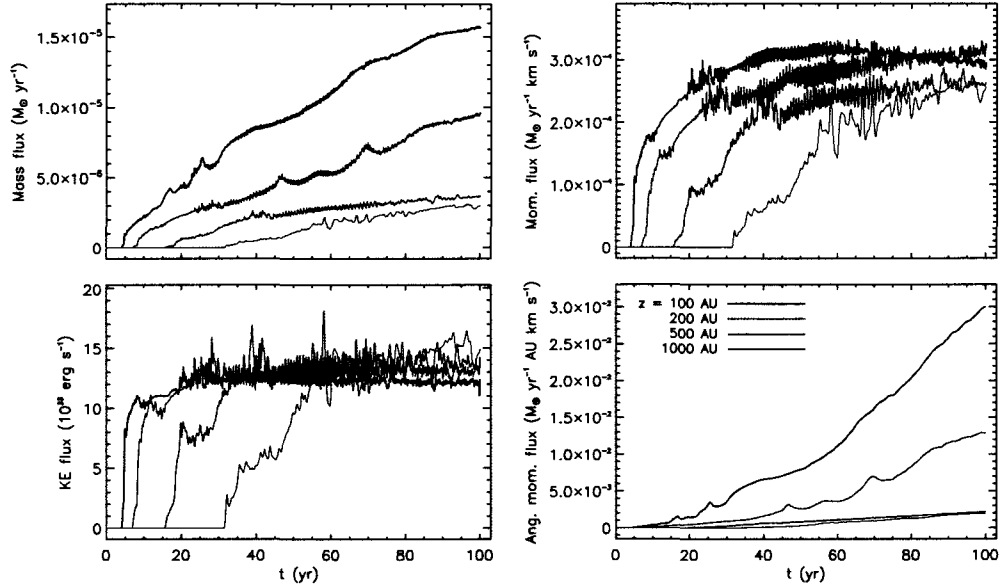


Figure 4.41 The same as Figure 4.37, but for simulation E.

As with the other quantities presented in this Section, power-laws of the form $\langle \dot{M} \rangle \propto B_i^\alpha$ have been fit to the time-averaged values and the resulting power-law indices are given in Tables 4.6 – 4.9. For a particular flux, the power-law indices do not vary drastically with height above the disc (z). At the four different heights above the disc for which fluxes are measured, the mass flux power-law index varies from 0.32 ± 0.07 – 0.56 ± 0.08 . This compares favourably with how $\langle v_z \rangle$ varies with B_i ($\langle v_z \rangle \propto B_i^{0.45 \pm 0.02}$), and thus the effect of mass-weighting this average (as is done in calculating the mass flux) is minor. The range of indices for the momentum flux is 0.67 ± 0.03 – 0.87 ± 0.05 (*c.f.* $v_{\text{jet}}^2 \propto B_i^{0.88 \pm 0.02}$), and the kinetic energy flux is 1.19 ± 0.02 – 1.38 ± 0.04 , and (*c.f.* $v_{\text{jet}}^3 \propto B_i^{1.32 \pm 0.03}$). Finally, the range of power-law indices for the angular momentum flux is 1.3 ± 0.01 – 1.66 ± 0.08 ,

whereas $v_{\text{jet}} \langle v_{\varphi} \rangle r_{\text{jet}} \propto B_i^{1.40 \pm 0.03}$ [where the average of α from Table 4.5 ($= 0.30 \pm 0.01$) has been adopted for the power-law index of r_{jet}].

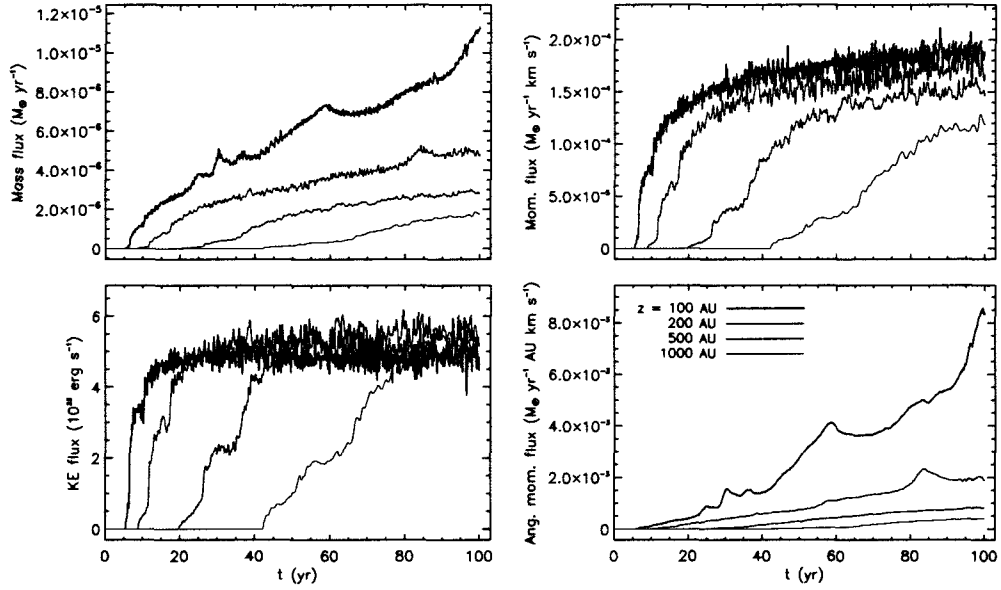


Figure 4.42 The same as Figure 4.37, but for simulation F.

Thus, simply taking the product of the constituent quantities of a flux, one can make a rough estimate of the dependence of that flux on B_i , regardless of the height above the disc where the flux is measured. Hence, I adopt the following as time-independent

approximate power-law indices for the difference fluxes:

$$\langle \dot{\mathcal{M}} \rangle \propto B_1^{0.44 \pm 0.01}, \quad (4.25)$$

$$\langle \dot{\mathcal{S}} \rangle \propto B_1^{0.88 \pm 0.02}, \quad (4.26)$$

$$\langle \dot{\mathcal{K}} \rangle \propto B_1^{1.32 \pm 0.03}, \quad (4.27)$$

$$\langle \dot{\mathcal{L}} \rangle \propto B_1^{1.40 \pm 0.03}. \quad (4.28)$$

To render these useful observational tools, one need to determine estimates for the proportionality constants, which is beyond the scope of these simulations.

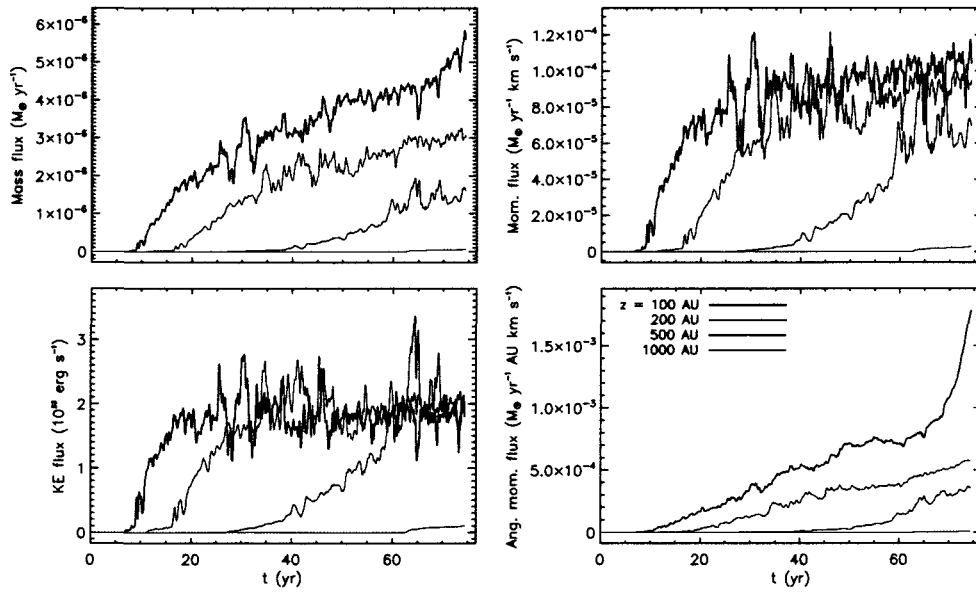


Figure 4.43 The same as Figure 4.37, but for simulation G.

| Simulation B_i (G) | H 2.5 | G 5 | F 10 | E 20 | D 40 | C 63.2 | B 100 | A 200 | α |
|---------------------------|----------|--------|---------|---------|---------|-----------|----------|----------|-----------------|
| $\langle \dot{M} \rangle$ | 2.38 | 2.14 | 3.51 | 5.74 | 9.62 | 12.5 | 15.0 | 18.2 | 0.56 ± 0.04 |
| $\langle \dot{S} \rangle$ | 0.52 | 0.76 | 1.54 | 2.74 | 4.75 | 6.71 | 9.19 | 13.9 | 0.77 ± 0.03 |
| $\langle \dot{K} \rangle$ | 0.78 | 1.82 | 5.11 | 13.0 | 28.7 | 51.2 | 91.3 | 202 | 1.25 ± 0.02 |
| $\langle \dot{L} \rangle$ | 0.48 | 0.31 | 1.11 | 5.14 | 16.4 | 32.0 | 58.7 | 125 | 1.66 ± 0.08 |

Table 4.7 The same as Table 4.6, but measured at $z = 200$ AU above the disc. $\langle \dot{M} \rangle$ has units of $10^{-6} M_{\odot} \text{yr}^{-1}$, $\langle \dot{S} \rangle$ units of $10^{-4} M_{\odot} \text{yr}^{-1} \text{km s}^{-1}$, $\langle \dot{K} \rangle$ units of $10^{33} \text{erg s}^{-1}$, and $\langle \dot{L} \rangle$ units of $10^{-3} M_{\odot} \text{yr}^{-1} \text{AU km s}^{-1}$.

| Simulation B_i (G) | H 2.5 | G 5 | F 10 | E 20 | D 40 | C 63.2 | B 100 | A 200 | α |
|---------------------------|----------|--------|---------|---------|---------|-----------|----------|----------|-----------------|
| $\langle \dot{M} \rangle$ | 0.30 | 0.86 | 2.02 | 2.62 | 3.54 | 4.43 | 5.73 | 8.22 | 0.52 ± 0.05 |
| $\langle \dot{S} \rangle$ | 0.11 | 0.43 | 1.23 | 2.21 | 3.69 | 5.33 | 7.67 | 14.0 | 0.83 ± 0.03 |
| $\langle \dot{K} \rangle$ | 0.26 | 1.38 | 5.01 | 12.9 | 29.3 | 53.9 | 98.6 | 245 | 1.31 ± 0.02 |
| $\langle \dot{L} \rangle$ | 0.06 | 0.14 | 0.48 | 1.12 | 3.56 | 7.90 | 18.3 | 46.4 | 1.57 ± 0.04 |

Table 4.8 The same as Table 4.6, but measured at $z = 500$ AU above the disc. $\langle \dot{M} \rangle$ has units of $10^{-6} M_{\odot} \text{yr}^{-1}$, $\langle \dot{S} \rangle$ units of $10^{-4} M_{\odot} \text{yr}^{-1} \text{km s}^{-1}$, $\langle \dot{K} \rangle$ units of $10^{33} \text{erg s}^{-1}$, and $\langle \dot{L} \rangle$ units of $10^{-3} M_{\odot} \text{yr}^{-1} \text{AU km s}^{-1}$.

4.7 Linking simulations to observations

4.7.1 Comparisons with current observations

One of the motivations for performing these simulations to such large-scales is to facilitate the direct comparison of simulations to observations. To this end, I now compare the simulation results to general observational characteristics of protostellar jets found in the literature.

Beginning with the proper motions of Table 4.4 and comparing them to the observed values in Table 4.10, the simulations presented here match observations quite well, with all but simulations G and H falling within the observed range of proper motions. A similar

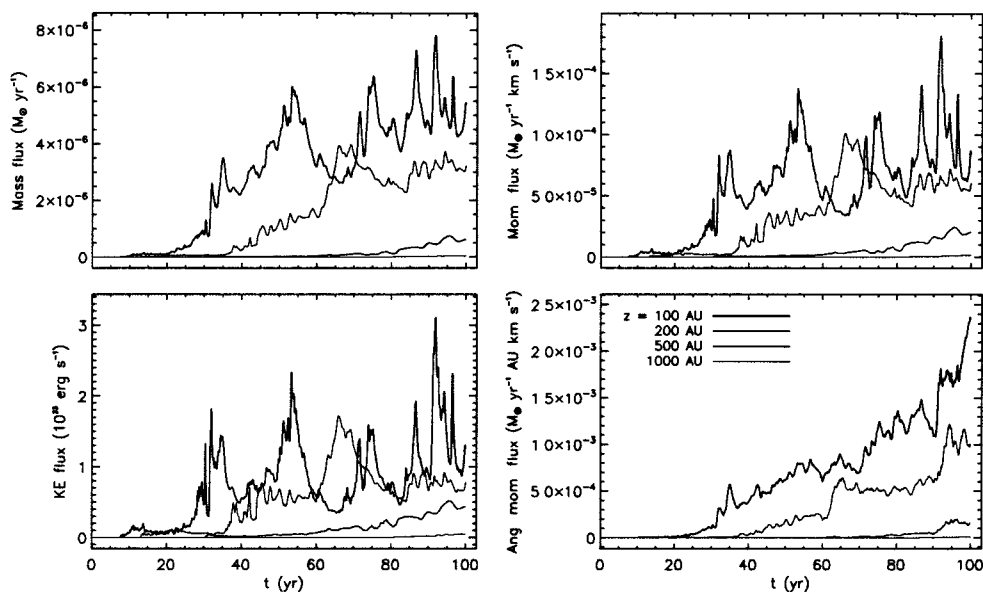


Figure 4.44 The same as Figure 4.37, but for simulation H.

statement can be made about the volume and time-averaged toroidal velocities: all of our jets fall within the observed range of rotational velocities.

Our measured jet radii are typically higher than observed values, especially when taking into account that at the end of the simulations the jets are still radially expanding. However, as measured, our radii track the discontinuity between the jet and shocked ambient medium, whereas observed radii are derived from measurements of forbidden emission lines (*e.g.*, [SII], [OI]; Ray *et al.* 2007). As we are not including any radiative effects in this work, our jet radii should thus be taken as upper limits.

Table 4.11 summarises the range of fluxes measured for simulations A – H. We find that our mass fluxes can be as much as 10 times larger than the observed range of values. Observational fluxes are typically determined using forbidden emission (*e.g.*, Hartigan,

| Simulation B_i (G) | H 2.5 | G 5 | F 10 | E 20 | D 40 | C 63.2 | B 100 | A 200 | α |
|---------------------------|----------|--------|---------|---------|---------|-----------|----------|----------|-----------------|
| $\langle \dot{M} \rangle$ | 0.03 | 0.04 | 0.89 | 1.90 | 2.70 | 3.16 | 3.05 | 4.41 | 0.42 ± 0.08 |
| $\langle \dot{S} \rangle$ | 0.01 | 0.02 | 0.68 | 1.85 | 3.45 | 5.05 | 6.49 | 13.0 | 0.87 ± 0.05 |
| $\langle \dot{K} \rangle$ | 0.03 | 0.08 | 3.50 | 12.1 | 31.2 | 57.8 | 99.8 | 283 | 1.38 ± 0.04 |
| $\langle \dot{L} \rangle$ | 0.0 | 0.0 | 0.19 | 0.95 | 2.67 | 4.97 | 6.45 | 19.7 | 1.4 ± 0.1 |

Table 4.9 The same as Table 4.6, but measured at $z = 1000$ AU above the disc. Due to fluxes from simulations G and H barely registering at 1000 AU above the disc, we exclude this data from the fits for this height only. $\langle \dot{M} \rangle$ has units of $10^{-6} M_\odot \text{ yr}^{-1}$, $\langle \dot{S} \rangle$ units of $10^{-4} M_\odot \text{ yr}^{-1} \text{ km s}^{-1}$, $\langle \dot{K} \rangle$ units of $10^{33} \text{ erg s}^{-1}$, and $\langle \dot{L} \rangle$ units of $10^{-3} M_\odot \text{ yr}^{-1} \text{ AU km s}^{-1}$.

| | |
|---|-----------------------------|
| proper motion (km s^{-1}) | 100 – 200 (500 max.) |
| rotational velocity (km s^{-1}) | $(5 - 25) \pm 5$ |
| FWHM jet radius (AU) | 15 – 40 (at 200 AU) |
| mass-loss rate ($M_\odot \text{ yr}^{-1}$) | $10^{-8} - 10^{-6}$ |
| momentum flux ($M_\odot \text{ yr}^{-1} \text{ km s}^{-1}$) | 10^{-5} |
| ang. mom. flux ($M_\odot \text{ yr}^{-1} \text{ AU km s}^{-1}$) | $10^{-6} - 10^{-5}$ |
| mechanical luminosity (erg s^{-1}) | $(2.7 - 16) \times 10^{33}$ |
| $\dot{M}_{\text{jet}}/\dot{M}_{\text{acc}}$ | 0.05 – 0.1 |

Table 4.10 A review of selected observational characteristics of protostellar jets.

References. — Hartigan, Morse, & Raymond (1994); Reipurth & Bally (2001); Podio *et al.* (2006); McKee & Ostriker (2007); Ray *et al.* (2007); Coffey *et al.* (2008, 2011).

Morse, & Raymond 1994), which require the gas to be at temperatures $\sim 10^4$ K (Dyson & Williams 1997; p, 104). Meanwhile, the jets presented here are relatively cold, and with the exception of the fastest moving $\beta_i = 0.1$ jet, the volume filling factor of gas above 10^4 K is quite small ($\lesssim 1\%$ in $\beta_i = 2.5$ and decreasing with magnetic field strength). While it is true that the mass flux in the simulations above 10^4 K is 10 – 100 times smaller, and thus in better agreement with observations, the mass fluxes from these simulations should still be taken as upper limits.

| | |
|--|-------------|
| $\langle \dot{M} \rangle$ ($10^{-6} M_{\odot} \text{ yr}^{-1}$) | 0.30 – 18.2 |
| $\langle \dot{S} \rangle$ ($10^{-4} M_{\odot} \text{ yr}^{-1} \text{ km s}^{-1}$) | 0.11 – 14.0 |
| $\langle \dot{K} \rangle$ ($10^{33} \text{ erg s}^{-1}$) | 0.26 – 283 |
| $\langle \dot{L} \rangle$ ($10^{-3} M_{\odot} \text{ yr}^{-1} \text{ AU km s}^{-1}$) | 0.06 – 125 |

Table 4.11 The ranges of fluxes in the simulations A – H. We have ignored fluxes from simulation G and H at $z = 1000$ AU in determining these values; see Table 4.9.

A commonly used ratio to describe the efficiency of outflows is the ratio of mass-loss rate to accretion rate of the protostar, $\dot{M}_{\text{jet}}/\dot{M}_{\text{acc}}$, and takes on values of 0.05 – 0.1 (Ray *et al.* 2007). Steady-state theory predicts that $\dot{M}_{\text{jet}}/\dot{M}_{\text{acc}} \simeq (r_0/r_A)^2$ (Pelletier & Pudritz 1992), where r_A/r_0 is the Alfvén lever arm. For values of the Alfvén lever arm observed in these simulations ($r_A/r_0 \sim 2 - 12$), then $\dot{M}_{\text{jet}}/\dot{M}_{\text{acc}} \sim 0.01 - 0.25$, in reasonable agreement with the observationally determined value.

As with the mass fluxes, the momentum fluxes are also larger than observed values by approximately a factor of 10. The same is true for our kinetic energy (sometimes referred to as mechanical luminosities) and angular momentum fluxes when compared to observational values. Similar to the mass fluxes, if only momentum and kinetic energy fluxes above 10^4 K are considered, the fluxes drop by a factor of 10 – 100, putting the results into better agreement with observed values.

4.7.2 Comparisons with future observations

Although the highest resolution currently attainable for the nearest star formation region is only ~ 14 AU (Ray *et al.* 2007), as telescope technology advances it will eventually become possible to resolve structures on the scale of the jet launching mechanism. As such,

it is worthwhile to use the results of the simulations presented here to provide observable proxies for physical quantities near the disc surface which are otherwise challenging to measure.

For example, equation (4.4) demonstrates that the knot period is inversely proportional to the slow speed at the location of the knot generator. By observing both the knot spacing and proper motion, the knot period, and thus the slow speed, can be determined. Assuming, as in Section 4.3, that the poloidal velocity and magnetic field are approximately parallel, and that the sound speed c_s is less than the total Alfvén speed $a_{a,tot}$, then $a_s \sim c_s$ and, using the ideal gas law, the temperature at the location of the knot generator can be written:

$$T \sim \frac{\pi^2 r_i^2 \langle m \rangle}{\gamma k \tau^2}, \quad (4.29)$$

where $\langle m \rangle$ is half a proton mass, k is the Boltzmann constant, and τ is the period of the knot generator (equation 4.4).

As already stated in Section 4.3, I find that the knot period and field strength can be related through a power-law of the form $\tau_{\text{knot,obs}} \propto B_i^{0.62 \pm 0.04}$. This is in general agreement with the temperature measured at the knot generator, where T is found to decrease with increasing B_i . In addition, I find that the magnetic field measured at the knot generator is within a factor of 2 of B_i .

The properties of the knots can also be used to qualitatively determine which launching mechanism dominates. From Figure 4.31, the transition between the “bead on a wire” and “coiled spring” mechanisms occurs at simulation E ($\beta_i = 10$). In this case, the radial extent of the knots is comparable to the knot spacing (Figure 4.10). Thus, if the

knots produced in these simulations are observed in protostellar jets, then the ratio of the radial extent of the knots to the spacing provides a simple method of determining which physical mechanism dominates near the disc surface, with $B_\varphi/B_p < 1$ (where the magneto-centrifugal mechanism dominates) corresponding to a ratio of knot radial extent to spacing of < 1 .

An alternate means of distinguishing between physical mechanisms comes from measuring the value of B_φ/B_p beyond $r \sim 1$ AU at the disc surface (*e.g.*, Figure 4.31). If the magnetic field cannot be measured directly to determine B_φ/B_p , this ratio can instead be estimated by observing the pitch angle of the field through polarimetry (and consequent modeling; *e.g.*, Chrysostomou *et al.* 2007), and then calculating B_φ/B_p from the fitted magnetic field structure.

4.8 Discussion

Taken together, the results presented here and in Chapter 3 comprise the first simulations of protostellar jets which resolve the launching mechanism at sub-AU scales, while simultaneously following the jet propagation to observational length scales of thousands of AU. The jets produced in these simulations naturally reproduce a number of general observational characteristics, demonstrating that magnetic disc winds can in fact produce realistic jets.

The knot generator observed in these simulations occurs in a region where β and the slow Mach number $M_s \sim 1$, and as such, is sensitive to the relationship between thermal pressure and magnetic forces. If β moves far enough away from equipartition in either

direction, the knots disappear. In the case of the strongest fields, oscillations are damped out and knots never form. Conversely, for the weakest fields, the oscillatory nature of the generator disappears and a continuous outward stream of material remains.

I find that two viewpoints are necessary to understand the simulations presented here which span a factor of 80 in the initial magnetic field strength, B_i . In both mechanisms, the magnetic field combines with rotation and gravity to launch the jet. When the magnetic field is strong, B_p acts as rigid wires along which centrifugally-launched beads of plasma are accelerated through the Alfvén point to form an outflow (Blandford & Payne 1982). Beyond this point, the assumption of co-rotation fails, and acceleration is largely stifled.

For weak magnetic fields, the lever arm is ineffective, and B_p becomes wound up into a dominantly toroidal field. Once B_φ has reached a sufficient strength, outward gradients in B_φ^2 accelerate material away from the disc. This “coiled spring” mechanism transfers potential energy stored in the field to kinetic energy of the outflow.

The transition between these two mechanisms is continuous, with simulation F exhibiting properties of both. Indeed, to some extent, both mechanisms are at work in each of the simulations presented here. For intermediate strength fields, the “surface force” provided by the magneto-centrifugal mechanism serves to accelerate the flow from the disc to the Alfvén point. Thereafter, the “body force” of the “coiled spring” mechanism takes over, and accelerates the flow through the fast point and beyond.

An interesting observation from these simulations is that, so long as there is a magnetic field present which couples the disc and atmosphere, in addition to a mass flux

flowing from the disc into the atmosphere, the twisting of the field into a toroidal component manages to create a significant region in which $\langle\beta_T\rangle < 1$ for $t \gtrsim 10$ yr. Thus, regardless of the initial field strength, the conditions required for magnetically launching a jet from a gravitationally-bound rotating accretion disc are always established. As the jet propagates, these conditions are at least somewhat maintained as rotational and gravitational energy are converted to magnetic energy which, in turn, is converted to kinetic energy of the outflow.

As demonstrated by Figure 4.33, all of the jets presented here, regardless of the initial magnetic field strength, first generate a region where $\langle\beta_T\rangle < 1$ before asymptoting to $\langle\beta_T\rangle \sim 1$ as they propagate to greater distances. Thus, I speculate here that protostellar jets on observable length scales will have magnetic fields which are in rough equipartition with the thermal energy density. A consequence of this is that observationally measured field strengths in the jet will have little bearing on the field strength near the jet launching mechanism. In this case, one must turn to other observable quantities such as v_{jet} and $\langle v_\varphi \rangle$ to constrain the field strength near the surface of the disc.

Comparing these simulations to observations, I find they produce jet speeds and rotational velocities which generally agree with observational values, again demonstrating the ability of disc winds to produce realistic protostellar jets. For the jet radii and fluxes, the values presented here are generally larger than observational values, and should be taken as upper limits. Given that the observational counterparts to these quantities are strongly related to line emission and radiative cooling (*e.g.*, Hartigan, Morse, & Raymond 1994), and since we do not include these effects here, the mismatch is not unexpected.

However, if we mask our fluxes to temperatures above 10^4 K, where forbidden emission is important, then we do produce more realistic values, at the cost of a low volume filling factor ($\lesssim 1\%$ for most simulations).

The most readily accessible observable from this work that is related to conditions at the disc surface is the jet propagation speed, v_{jet} . To turn this into a useful observational tool, more work needs to be done to quantify the constant of proportionality, C , in the power law $v_{\text{jet}} = C B_i^{0.44 \pm 0.01}$. This involves varying initial conditions other than B_i (such as density, pressure, *etc.*), and measuring how the jet speed responds, but this is well beyond the scope of this work.

Finally, the power-law indices for the fluxes clearly have not converged, nor has the dependence of the magnetic field strength on the jet radius. Thus, the results presented herein could benefit from simulations of significantly longer duration that extend to well beyond the current maximum extent of 4096×256 AU.

Chapter 5

Conclusions

I have investigated the formation and propagation of protostellar jets with simulations that simultaneously include both the region where the jet is launched at sub-AU scales, and much larger observational length scales of thousands of AU. These are the first simulations to accomplish this feat, and permit jet properties on observational scales to be related to conditions at the disc surface where the jet is launched.

This study is made possible through the development of a new AMR version of *ZEUS-3D*, *AZEuS*. In Chapter 2, I described in detail how the AMR method of Berger & Colella (1989) was modified for the fully-staggered mesh characteristic to the *ZEUS* family of codes. Higher-order interpolations for the prolongation of grids have been implemented, as these have proven invaluable for the propagation of waves across the boundaries of static grids, such as those employed for the simulations in Chapters 3 and 4. The prolongation and restriction operators have also been generalised for curvilinear coordinates, ensuring the conservation of the important physical quantities. *AZEuS* has been validated against a number of test problems in 1-, 2-, and 3-D, in both Cartesian and curvilinear coordinates, proving that it is capable of producing virtually identical results for non-turbulent problems whether using a single grid or AMR. To the best of my knowledge, *AZEuS* is the only fully-staggered mesh AMR-MHD code in use in astrophysics.

The first science results with AZEuS were presented in Chapters 3 and 4, where simulations of protostellar jets launched from an accretion disc as a boundary condition are followed for more than 5 orders of magnitude in length. These simulations revealed relationships between large-scale observable quantities and conditions at the disc surface where the jet is launched. Clear correlations were found to exist between the magnetic field strength near the disc surface, B_i , and the jet proper motion (v_{jet}) and average rotational velocity ($\langle v_\varphi \rangle$):

$$\left. \begin{array}{l} v_{\text{jet}} \propto B_i^{0.48 \pm 0.01}, \\ \langle v_\varphi \rangle \propto B_i^{0.66 \pm 0.01} \end{array} \right\} \Rightarrow v_{\text{jet}} \propto \langle v_\varphi \rangle^{0.73 \pm 0.02}.$$

Some analytical explanation was given for the former, whereas the latter is an entirely numerical result. I also find that fluxes transported by the jet (mass, momentum, kinetic energy, and momentum) depend on B_i , but not as tightly as v_{jet} and $\langle v_\varphi \rangle$. Indeed, the fluxes can be expressed in terms of their constituent quantities and, thus, the majority of their dependence on B_i derives from their reliance on the jet propagation speed and rotational velocity. The observed correlation between B_i and the maximum jet radius seems to be determined more by the interaction of the asymptotic ambient medium with the jet ram pressure (which, in turn, depends on v_{jet}), than an intrinsic relationship between $r_{\text{jet,max}}$ and B_i . Even $\langle \beta_T \rangle$ seems to have little correlation with B_i as it asymptotes to unity, regardless of the conditions near the disc surface and the value of B_i .

While the jet proper motions and rotational velocities in these simulations were shown to be in good agreement with observations, the values for the fluxes and jet radii are generally larger than observed values by a factor of $\sim 10 - 100$. As observed values are

derived from line emission data (which requires temperatures $\sim 10^4$ K), they necessarily only trace the high temperature regions of a jet. While I demonstrated that the measured fluxes can be reduced by a factor of 10 – 100 through masking of temperatures above 10^4 K, this results in a small volume filling factor ($\lesssim 1\%$).

Overall, the characteristics of these simulations well contain the observed properties of protostellar jets, and this work demonstrates that jets launched magnetically from discs can, by themselves, produce realistic protostellar jets. Indeed, it is only because these simulations have evolved from sub-AU length scales to thousands of AU can I make this claim with some confidence.

Knots were observed to form in these simulations near the origin, and are the result of pressure oscillations in a region where the plasma- β and the slow magnetosonic Mach number, M_s , are both near unity. Knots produced through this mechanism reach extents of only ~ 2 AU in size and are therefore not good candidates for explaining the much larger clumpy structures seen in observations of protostellar jets.

In Chapter 4, I found there are at least two distinct driving mechanisms that accelerate the jets. For strong magnetic fields ($\beta_i \leq 1$), the magneto-centrifugal model (Blandford & Payne 1982), where a rotating disc applies a torque via a rigid magnetic field, efficiently accelerates jet material through the Alfvén point after which the jet asymptotes to a more or less constant speed. When the magnetic field is weak ($\beta_i \geq 10$), magnetic field is wound up and becomes predominantly toroidal. In this case, the magnetic field acts like a “coiled spring”, in which the potential energy stored in the tightly wound toroidal magnetic field is converted to kinetic energy of the flow, and material is accelerated through the fast

point. As the toroidal field permeates the entire jet, some residual acceleration takes place throughout, and certainly beyond the fast point, independent of which mechanism is invoked near the disc surface. For intermediate field strengths ($1 < \beta_i < 10$), both mechanisms contribute significantly to the acceleration of the flow.

I observe that if the magnetic fields are initially too weak to launch a jet, the “coiled spring” mechanism taps the gravitational and rotational energy of the disc-star system and winds up the field until a magnetically-dominated environment can be established in which a jet can be launched. This is consistent with the long-held view that a magnetically-dominated region near the disc is required for a jet to be launched. Furthermore, the tendency of the simulations to asymptote to $\beta \sim 1$ or, equivalently, to equipartition between thermal and magnetic pressure, suggests that, on observational scales, observed magnetic field strengths will have little bearing on the strength of the field launching the jet. Instead, one must look to other observable quantities (such as v_{jet} and $\langle v_\varphi \rangle$) to act as proxies for the magnetic field near the disc surface.

Clearly, protostellar jets are emission-dominated objects (*e.g.*, Figure 1.1 and 1.7). However, in this work, radiative effects have been ignored due to the complexity and computational demands associated with self-consistently determining the line cooling and emission. Given that the observed properties of protostellar jets are strongly related to line emission, the comparisons to observations presented here (in particular the jet radii and fluxes) would benefit from the inclusion of radiative effects. This could also have a noticeable effect on the results at observational length scales as radiative cooling behind shocks can have significant consequences for the properties of the flow (Reipurth & Bally

2001). Thus, future work based on these simulations should self-consistently include radiative processes, and possible approaches for doing so can be found in the literature (*e.g.*, Raga *et al.* 1997; Teşileanu *et al.* 2008).

Given that several properties of the jets have not yet temporally converged by the end of these simulations (*e.g.*, the dependence of the jet radii and fluxes on B_i), and the existence of protostellar jets which span tens of thousands of AU (Section 1.1), it would also be worthwhile to extend these simulations in both duration and size (by factors of $\sim 5 - 10$). Furthermore, in order to turn the various power-laws presented in Chapters 3 and 4 into useful observational tools, additional work in the variation of initial conditions other than B_i (*e.g.*, ρ_i , p_i) is needed.

References

- Anderson, J. M., Li, Z.-Y., Krasnopolsky, R., Blandford, R. D., 2003, *ApJ*, 590, L107
- Anderson, J. M., Li, Z.-Y., Krasnopolsky, R., Blandford, R. D., 2005, *ApJ*, 630, 945
- Anderson, J. M., Li, Z.-Y., Krasnopolsky, R., Blandford, R. D., 2006, *ApJ*, 653, L33
- Anglada, G., Villuendas, E., Estalella, R., Beltrán, M. T., Rodríguez, L. F., Torrelles, J. M., Curiel, S., 1998, *AJ*, 116, 2953
- Arce, H. G., Shepherd, D., Gueth, F., Lee, C.-F., Bachiller, R., Rosen, A., Beuther, H., 2007, in *Protostars and Planets V*, eds. B. Reipurth, D. Jewitt, K. Keil (Tucson: Univ. of Arizona Press), 245
- Bacciotti, F., Eisloffel, J., 1999, *A&A*, 342, 717
- Baierlein, R., 1999, *Thermal Physics* (1st ed.; Cambridge: Cambridge University Press)
- Balbus, S. A., Hawley, J. F., 1991, *ApJ*, 376, 214
- Bally, J., Devine, D., 1994, *ApJ*, 428, L65
- Bally, J., Reipurth, B., Davis, C. J., 2007, in *Protostars and Planets V*, eds. B. Reipurth, D. Jewitt, K. Keil (Tucson: Univ. of Arizona Press), 215
- Balsara, D. S., 2001, *JCoPh*, 174, 614

- Berger, M. J., Olinger, J., 1984, JCoPh, 53, 484
- Bell, J., Berger, M., Saltzman, J., Welcome, M., 1994, SIAM J. Sci. Comput., 15, 127
- Berger, M. J., Colella, P., 1989, JCoPh, 82, 64
- Berger, M. J., Rigoutsos, I., 1991, IEEE Trans. Systems Man and Cybernet., 21, 1278
- Bergin, E.A., Tafalla, M., 2007, ARA&A, 45, 339
- Bisnovatyi-Kogan, G. S., Ruzmaikin, A. A., 1976, Ap&SS, 42, 401
- Blandford, R. D., 1976, MNRAS, 176, 465
- Blandford, R. D., Payne, D. G., 1982, MNRAS, 199, 883
- Calvet, N., Hartmann, L., Strom, S. E., 2000, in Protostars and Planets IV, eds. V. Mannings, A. P. Boss, S. S. Russell (Tucson: Univ. of Arizona Press), 377
- Carrasco-González, C., Rodríguez, L. F., Anglada, G., Martí, J., Torrelles, J. M., Osorio, M., 2010, Science, 330, 1209
- Casse, F., Keppens, R., 2004, ApJ, 601, 90
- Chrysostomou, A., Lucas, P. W., Hough, J. H., 2007, Nature, 450, 71
- Clarke, D. A., 1988, Ph.D. dissertation, The University of New Mexico
- Clarke, D. A., 1996, ApJ, 457, 291
- Clarke, D. A., 2007, *ZEUS-3D* User Manual (Version 3.5),
<http://www.ica.smu.ca/zeus3d>

- Clarke, D. A., 2010, *ApJS*, 187, 119
- Clarke, D. A., Norman, M. L., Burns, J. O., 1986, *ApJ*, 311, L63
- Coffey, D., Bacciotti, F., Podio, L., 2008, *ApJ*, 689, 1112
- Coffey, D., Bacciotti, F., Chrysostomou, A., Nisini, B., Davis, C., 2011, *A&A*, 526, A40
- Colella, P., Woodward, P. R., 1984, *JCoPh*, 54, 174
- Collins, D. C., Xu, H., Norman, M. L., Li, H., Li, S., 2010, *ApJS*, 186, 308
- Cunningham, A. J., Frank, A., Varnière, P., Mitran, S., Jones, T. W., 2009, *ApJS*, 182, 519
- Delamarter, G., Frank, A., Hartmann, L., 2000, *ApJ*, 530, 923
- Donati, J.-F., Paletou, F., Bouvier, J., Ferreira, J., 2005, *Nature*, 438, 466
- Dyson, J. E., Williams, D. A., 1997, *The Physics of the interstellar medium* (2nd ed.; Bristol: IOP Publishing)
- Evans, C. R., Hawley, J. F., 1988, *ApJ*, 332, 659
- Falle, S. A. E. G., 2002, *ApJ*, 577, L123
- Fendt, C., 2006, *ApJ*, 651, 272
- Fendt, C., 2009, *ApJ*, 692, 346
- Fendt, C., 2011, arXiv: astro-ph/1105.6232
- Fendt, C., Čemeljić, M., 2002, *A&A*, 395, 1045

- Fendt, C., Elstner, D., 2000, A&A, 363, 208
- Ferreira, J., 1997, A&A, 319, 340
- Fromang, S., Hennebelle, P., Teyssier, R., 2006, A&A, 457, 371
- Fryxell, B., *et al.*, 2000, ApJS, 131, 273
- Gardiner, T. A., Stone, J. M., 2005, JCoPh, 205, 509
- Gracia, J., Vlahakis, N., Tsinganos, K., 2006, MNRAS, 367, 201
- Haro, G., 1952, ApJ, 115, 572
- Haro, G., 1953, ApJ, 117, 73
- Hartigan, P., Edwards, S., Ghandour, L., 1996, ApJ, 452, 736
- Hartigan, P., Edwards, S., Pierson, R., 2004, ApJ, 609, 261
- Hartigan, P., Frank, A., Foster, J. M., Wilde, B. H., Douglas, M., Rosen, P. A., Coker, R. F., Blue, B. E., Hansen, J. F., 2011, arXiv: astro-ph/1104.4341
- Hartigan, P., Frank, A., Varnière, P., Blackman, E. G., 2007, ApJ, 661, 910
- Hartigan, P., Morse, J. A., Raymond, J., 1994, ApJ, 436, 125
- Hawley, J. F., 2000, ApJ, 528, 462
- Hayes, J. C., Norman, M. L., Fiedler, R. A., Bordner, J. O., Li, P. S., Clark, S. E., ud-Doula, A., Mac Low, M.-M., 2006, ApJS, 165, 188

-
- Heathcote, S., Morse, J. A., Hartigan, P., Reipurth, B., Schwartz, R. D., Bally, J., Stone, J. M., 1996, *AJ*, 112, 1141
- Henriksen, R. N., Rayburn, D. R., 1971, *MNRAS*, 152, 323
- Herbig, G. H., 1950, *ApJ*, 111, 11
- Herbig, G. H., 1951, *ApJ*, 113, 697
- Heyvaerts, J., Norman, C., 1989, *ApJ*, 347, 1055
- Igumenshchev, I. V., Narayan, R., 2002, *ApJ*, 566, 137
- Khokhlov, A. M., 1998, *JCoPh*, 143, 519
- Klein, R. I., 1999, *J. Comput. Appl. Math.*, 109, 123
- Krasnopolsky, R., Li, Z.-Y., Blandford, R., 1999, *ApJ*, 526, 631
- Krasnopolsky, R., Li, Z.-Y., Blandford, R., 2003, *ApJ*, 526, 631
- Kigure, H., Shibata, K., 2005, *ApJ*, 634, 879
- Kudoh, T., Matsumoto, R., Shibata, K., 1998, *ApJ*, 508, 186
- Lada, C. J., 1985, *ARA&A*, 23, 267
- Li, S., Li, H., 2004, *JCoPh*, 199, 1
- Livio, M., 2009, in *Protostellar Jets in Context*, eds. K. Tsinganos, T. Ray, M. Stute (Berlin: Springer), 3
- Londrillo, P., Del Zanna, L., 2000, *ApJ*, 530, 508.

-
- Lovelace, R. V. E., 1976, *Nature*, 262, 649
- Matsakos, T., Massaglia, S., Trussoni, E., Tsinganos, K., Vlahakis, N., Sauty, C., Mignone, A., 2009, *A&A*, 502, 217
- Matsakos, T., Tsinganos, K., Vlahakis, N., Massaglia, S., Mignone, A., Trussoni, E., 2008, *A&A*, 477, 521
- Matt, S., Goodson, A. P., Winglee, R. M., Böhm, K.-H., 2002, *ApJ*, 574, 232
- McKee, C. F., Ostriker, E. C., 2007, *ARA&A*, 45, 565
- Meier, D. L., Edgington, S., Godon, P., Payne, D. G., Lind, K. R., 1997, *Nature*, 388, 350
- Meliani, Z., Casse, F., Sauty, C., 2006, *A&A*, 460, 1
- Mestel, L., 1968, *MNRAS*, 138, 359
- Michel, F. C., 1969, *ApJ*, 158, 727
- Mignone, A., Bodo, G., Massaglia, S., Matsakos, T., Tesileanu, O., Zanni, C., Ferrari, A., 2007, *ApJS*, 170, 228
- Miller, K. A., Stone, J. M., 1997, *ApJ*, 489, 890
- Mouschovias, T. C. and Paleologou, E. V., 1980, *ApJ*, 237, 877
- Mundt, R., Büehrke, T., Fried, J. W., Neckel, T., Sarcander, M., Stocke, J., 1983, *A&A*, 140, 17
- Mundt, R., Fried, J. W., 1983, *ApJ*, 274, L83

- Mundt, R., Stocke, J., Stockman, H. S., 1983, *ApJ*, 265, L71
- Orszag, S. A., Tang, C.-M., 1979, *J. Fluid Mech.*, 90, 129
- O'Shea, B. W., Bryan, G., Bordner, J., Norman, M. L., Abel, T., Harkness, R., Kritsuk, A., 2004, eprint (arXiv: astro-ph/0403044)
- Ouyed, R., Clarke, D. A., Pudritz, R. E., 2003, *ApJ*, 582, 292
- Ouyed, R., Pudritz, R. E., 1997a, *ApJ*, 482, 712
- Ouyed, R., Pudritz, R. E., 1997b, *ApJ*, 484, 794
- Ouyed, R., Pudritz, R. E., 1999, *MNRAS*, 309, 233
- Pelletier, G., Pudritz, R. E., 1992, *ApJ*, 394, 117
- Podio, L., Bacciotti, F., Nisini, B., Eisloffel, J., Massi, F., Giannini, T., Ray, T. P., 2006, *A&A*, 456, 189
- Porth, O., Fendt, C., 2010, *ApJ*, 709, 1100
- Pravdo, S. H., Rodríguez, L. F., Curiel, S., Cantó, J., Torrelles, J. M., Becker, R. H., Sellgren, K., 1985, *ApJ*, 293, L35
- Press, W. H., Teukolsky, S. A., Vetterling, W. T., Flannery, B. P., 1992, *Numerical Recipes in FORTRAN: The Art of Scientific Computing* (2nd ed.; Cambridge: Cambridge Univ. Press)
- Pudritz, R. E., Norman, C. A., 1983, *ApJ*, 274, 677

-
- Pudritz, R. E., Ouyed, R., Fendt, C., Brandenburg, A., 2007, in *Protostars and Planets V*, eds. B. Reipurth, D. Jewitt, K. Keil (Tucson: Univ. of Arizona Press), 277
- Pudritz, R. E., Rogers, C., Ouyed, R., 2006, *MNRAS*, 365, 1131
- Quillen, A. C., Thorndike, S. L., Cunningham, A., Frank, A., Gutermuth, R. A., Blackman, E. G., Pipher, J. L., Ridge, N., 2005, *ApJ*, 632, 941
- Raga, A. C., Mellema, G., Lundqvist, P., 1997, *ApJS*, 109, 517
- Raga, A. C., Noriega-Crespo, A., Reipurth, B., Garnavich, P.M., Heathcote, S., Böhm, K. H., Curiel, S., 2002, *ApJ*, 565, L29
- Ramsey, J. P., Clarke, D. A., 2011, *ApJ*, 728, L11
- Ray, T., Dougados, C., Bacciotti, F., Eisloffel, J., Chrysostomou, A., 2007, in *Protostars and Planets V*, eds. B. Reipurth, D. Jewitt, K. Keil (Tucson: Univ. of Arizona Press), 231
- Ray, T. P., Mundt, R., Dyson, J. E., Falle, S. A. E. G., Raga, A. C., 1996, *ApJ*, 468, L103
- Ray, T. P., Muxlow, T. W. B., Axon, D. J., Brown, A., Corcoran, D., Dyson, J., Mundt, R., 1997, *Nature*, 385, 415
- Reipurth, B., 1999, *A general catalogue of Herbig-Haro objects*, 2nd edition, <http://casa.colorado.edu/hhcat>
- Reipurth, B., Bally, J., 2001, *ARA&A*, 39, 403
- Reipurth, B., Bally, J., Devine, D., 1997b, *AJ*, 114, 2708

-
- Reipurth, B., Hartigan, P., Heathcote, S., Morse, J. A., Bally, J., 1997a, *AJ*, 114, 757
- Reipurth, B., Heathcote, S., Morse, J., Hartigan, P., Bally, J., 2002, *AJ*, 123, 362
- Romanova, M. M., Ustyugova, G. V., Koldoba, A. V., Lovelace, R. V. E., 2005, *ApJ*, 635, L165
- Ryu, D., Jones, T. W., 1995, *ApJ*, 442, 228
- Schatzman, E., 1962, *Ann. Astrophys.*, 25, 18
- Schwartz, R. D., 1983, *ARA&A*, 21, 209
- Shibata, K., Uchida, Y., 1986, *PASJ*, 38, 631
- Shu, F., Najita, J., Ostriker, E., Wilkin, F., Ruden, S., Lizano, S., 1994, *ApJ*, 429, 781
- Snell, R. L., Loren, R. B., Plambeck, R. L., 1980, *ApJ*, 239, L17
- Soker, N., 2005, *A&A*, 435, 125
- Spruit, H.C., 1996, in *Evolutionary processes in binary stars*, eds. R. A. M. J. Wijers, M. B. Davies, C. A. Tout, (Dordrecht: Kluwer academic publishers), 249
- Staff, J. E., Jørgenson, M. A. S. G., Ouyed, R., 2004,
<http://www.capca.ucalgary.ca/software/jetget.html>
- Staff, J. E., Niebergal, B. P., Ouyed, R., Pudritz, R. E., Cai, K., 2010, *ApJ*, 722, 1325
- Stone, J. M., Norman, M. L., 1992, *ApJS*, 80, 753
- Stone, J. M., Norman, M. L., 1992, *ApJS*, 80, 791

-
- Stone, J. M., Mihalas, D., Norman, M. L., 1992, *ApJS*, 80, 819
- Stone, J. M., Gardiner, T. A., Teuben, P., Hawley, J. F., Simon, J. B., 2008, *ApJS*, 178, 137
- Stute, M., Gracia, J., Tsinganos, K., Vlahakis, N., 2010, *A&A*, 516, A6
- Stute, M., Tsinganos, K., Vlahakis, N., Matsakos, T., Gracia, J., 2008, *A&A*, 491, 339
- Teşileanu, O., Mignone, A., Massaglia, S., 2008, *A&A*, 488, 429
- Truelove, J. K., Klein, R. I., McKee, C. F., Holliman, J. H., II, Howell, L. H., Greenough, J. A., 1997, *ApJ*, 489, L179
- Truelove, J. K., Klein, R. I., McKee, C. F., Holliman, J. H., II, Howell, L. H., Greenough, J. A., Woods, D. T., 1998, *ApJ*, 495, 821
- Tzeferacos, P., Ferrari, A., Mignone, A., Zanni, C., Bodo, G., Massaglia, S., 2009, *MNRAS*, 400, 820
- Uchida, Y., Shibata, K., 1985, *PASJ*, 37, 515
- Ustyugova, G. V., Koldoba, A. V., Romanova, M. M., Chechetkin, V. M., Lovelace, R. V. E., 1995, *ApJ*, 439, 3
- Ustyugova, G. V., Koldoba, A. V., Romanova, M. M., Chechetkin, V. M., Lovelace, R. V. E., 1999, *ApJ*, 516, 221
- Vallée, J.P., 2003, *NewAR*, 47, 85
- Vitorino, B. F., Jatenco-Pereira, V., Opher, R., 2002, *A&A*, 384, 329

Vitorino, B. F., Jatenco-Pereira, V., Opher, R., 2003, *ApJ*, 592, 332

van Leer, B., 1977, *JCoPh*, 23, 276

von Neumann, J., Richtmyer, R. D., 1950, *J. Appl. Phys.*, 21, 232

von Rekowski, B., Brandenburg, A., Dobler, W., Shukurov, A., 2003, *A&A*, 398, 825

Weber, E. J., Davis, Jr., L., 1967, *ApJ*, 148, 217

Woitak, J., Bacciotti, F., Ray, T. P., Marconi, A., Coffey, D., Eisloffel, J., 2005, *A&A*,
432, 149

Wu, Y., Wei, Y., Zhao, M., Shi, Y., Yu, W., Qin, S., Huang, M., 2004, *A&A*, 426, 53

Zanni, C., Ferrari, A., Rosner, R., Bodo, G., Massaglia, S., 2007, *A&A*, 469, 811

Ziegler, U., 2008, *Comput. Phys. Comm.*, 179, 227



**Saint Mary's
University**

Halifax, Nova Scotia
Canada B3H 3C3

Patrick Power Library

tel 902.420.5534

fax 902.420.5561

web www.stmarys.ca

Copyright Permission Notice

Documentation regarding permissions for the use of copyrighted material in this thesis is on file at the Saint Mary's University Archives. Contact us if you wish to view this documentation:

Saint Mary's University, Archives
Patrick Power Library
Halifax, NS
B3H 3C3

Email: archives@smu.ca
Phone: 902-420-5508
Fax: 902-420-5561